Analysis of large antenna systems

Document Version:
Publisher's PDF, also known as Version of Record (includes final page, issue and volume numbers)

Please check the document version of this publication:

• A submitted manuscript is the version of the article upon submission and before peer-review. There can be important differences between the submitted version and the official published version of record. People interested in the research are advised to contact the author for the final version of the publication, or visit the DOI to the publisher's website.
• The final author version and the galley proof are versions of the publication after peer review.
• The final published version features the final layout of the paper including the volume, issue and page numbers.

Link to publication

Analysis of Large Antenna Systems

Analysis of Large Antenna Systems

PROEFSCHRIFT

ter verkrijging van de graad van doctor aan de
Technische Universiteit Eindhoven, op gezag van de
rector magnificus, prof.dr.ir. C.J. van Duijn, voor een
commissie aangewezen door het College voor
Promoties in het openbaar te verdedigen
op maandag 7 juni 2010 om 14.00 uur

door

Rob Maaskant

geboren te Rotterdam

Contents

Chapter 1

Introduction

This chapter describes the context and framework within which the research of this thesis has been conducted. We recall important historical facts that have led to the science field called "radio astronomy". Subsequently, we identify challenging technological problems that need to be solved to model/predict the receiver sensitivity of the next generation radio telescope: the Square Kilometre Array. To address the associated computational challenges, various innovative modeling techniques are developed throughout this thesis and are summarized in this chapter. We conclude with the thesis outline.

1.1 Historical Context

> *An antenna-receiver combination acts like a bolometer, or heat-measuring device, in which the radiation resistance of the antenna measures the equivalent temperature of distant parts of space to which it is projected by the antenna response pattern.*
>
> Reber (1942)

How were stars formed? What is the origin of the universe in which we live, how does it evolve, and what is its ultimate fate? To answer these fundamental questions, and to establish new physical laws, or to validate existing ones, astronomers hanker to perform deep-space surveys using advanced instrumentation. In early times, observations were

solely performed in the visible light using "optical telescopes", but this changed dramatically in 1932, a moment that can be marked as the beginning of a new era in astronomy.

In 1931, the radio engineer Karl Gunthe Jansky of the Bell Telephone Laboratories tried to detect thunderstorms with a 30 m long by 4 m high rotatable antenna. However, his experiments, which were published in 1932, not only showed thunderstorm statics, but also a noisy source of unknown origin whose direction of arrival changed during the day. After analyzing his results, he came to the staggering conclusion that the Milky Way not only emits electromagnetic waves in the optical frequency spectrum, but also at much lower frequencies, i.e., at radio wavelengths [1]. In 1933, he reported his findings in a paper, entitled: "Electrical Disturbances Apparently of Extraterrestrial Origin" [2].

The radio engineer Grote Reber got fascinated by Jansky's results and diligently constructed a 9.5 m parabolic reflector antenna in the backyard of his home in Wheaton, Illinois (1937) [3, Chapter 1]. He observed cosmic radiation at wavelengths of order 2 m, and devoted a considerable effort to characterize and understand the performance-limiting factors of his antenna-receiver combination. His first results were published in 1940 in the Astrophysical Journal [4]. Because of the revolutionary character of the material, the scientific community was initially undecided about the wisdom of publishing it. In 1944, he produced the first radio maps of the sky. To date, he is considered to be a pioneer who developed the first radio telescopes.

The Dutch astronomer Prof. Jan Hendrik Oort recognized the importance of Reber's activities and organized a meeting in 1944 on behalf of the Netherlands Astronomers' Club (NAC) at Leiden Observatory [5]. It was at this meeting where Hendrik van de Hulst from the Sonnenborgh Observatory (Utrecht) suggested that Reber might have detected radiation from a layer of ionized hydrogen. More importantly, van de Hulst's theoretical predictions indicated that neutral hydrogen is likely to radiate at a wavelength of 21 cm. Since its importance, Oort immediately made plans to obtain equipment for observations at these radio wavelengths. With the help of a young engineer from Delft, C. A. Muller, a sensitive receiver was developed using electronics from Philips. The first successful observations at 21 cm were performed with the aid of a 7.5 m Würzburg radar reflector in Kootwijk, and due to a destructive fire, this happened only in May 1951. Unluckily, this occurred after H. I. Ewen and E. M. Purcell had detected the 21 cm radiation using a horn antenna at Harvard University, in March 1951. Despite this setback, the reports by Ewen and Purcell and by Muller and Oort were published side by side in Nature [6, 7].

Parallel to the activities in Kootwijk, and owing to the inspiring political skills of Oort, the Dutch government founded "The Netherlands Organization for the Advancement of Pure Scientific Research (ZWO)" in 1949[1]. During the same year, the subsidiary "Stichting Radiostraling van Zon en Melkweg (SRZM)", or, "Netherlands Foundation for Radio Astronomy" was founded[2]. This new foundation, chaired by Oort, provided a broad base of knowledge, interest, and financial support to construct a novel 25 m reflector antenna near the Dwingeloo village, the home base of SRZM. This world's largest fully moveable radio telescope was constructed by Werkspoor (a company building railway bridges) under the supervision of Ben G. Hooghoudt in 1954–1955. The Dwingeloo telescope was inaugurated in April 1956 by Her Majesty Queen Juliana and remained operational until 1998. Its last major success was the discovery of the Dwingeloo-1 galaxy in 1994.

As the Dwingeloo telescope was not going to solve the very fundamental problems of the structure of the universe in which Jan Oort and many others were interested, the construction of a new instrument consisting of twelve 25 m dishes (two movable) in Westerbork along an east-west baseline began in 1966 and ended in 1968. Significant contributions to the design of the antenna-feed structure were carried out at the Eindhoven University of Technology by Dr. M. E. J. Jeuken [8, 9]. The so named "Westerbork Synthesis Radio Telescope (WSRT)" was officially opened in 1970 by Queen Juliana. Many upgrades followed throughout the lifetime of the WSRT, among which the addition of two extra moveable dishes in 1975–1980. It was the most powerful radio telescope in the world for over a decade [10], and probably still is below 1.7 GHz due to its excellent polarimetric imaging capability.

Technologically, the development of these radio telescopes kept evolving rapidly to facilitate the research demands of radio astronomers. This has caused ASTRON to grow from twenty employees in the early 1960's to about 180 staff members today.

1.2 The Square Kilometre Array Radio Telescope

The Square Kilometre Array (SKA) is a future radio telescope which will scan and map the sky with a sensitivity of two orders of magnitude higher than present-day radio tele-

---

[1]At present, ZWO has been renamed to "The Netherlands Organization for Scientific Research (NWO)".
[2]To date, SRZM has been renamed to "The Netherlands Institute for Radio Astronomy (ASTRON)".

scopes [11–13]. The SKA is planned to be operational in 2020; it will ultimately operate over a large frequency bandwidth, ranging from approximately 70 MHz to more than 25 GHz, and the receiver sensitivity metric, $A_{\text{eff}}/T_{\text{sys}}$, is required to be of order[3] 10000 m^2/K, where A_{eff} is the effective collecting area and T_{sys} is the system equivalent noise temperature [15]. Thus, for a canonical 50 K system noise temperature, the total collecting area is required to be of order 1 km^2, which is unprecedentedly large. The challenge is therefore to minimize the system-noise temperature, which is a difficult task for non-cooled antenna systems.

The SKA project is a long-term international endeavor during which a number of different antenna technologies are considered each of which operates in a certain frequency subband (see Fig. 1.1). With the aid of national and international funds, ASTRON examines both

Figure 1.1: Artist impression of the Square Kilometre Array [13].

aperture and focal plane array concepts and develops SKA pathfinding activities, among which LOFAR, APERTIF, and EMBRACE [16–18], the latter aperture array project being sponsored by the European FP6 project "SKA Design Studies (SKADS)" [19]. These instruments will cover a substantial part of the frequency spectrum ($0.01 < f < 10$ GHz). Below 300 MHz, electrically small dipole antennas are positioned over a non-uniform grid whose sparsity level increases with the distance to the center of the array. Above 300 MHz,

---

[3]The minimum required sensitivity depends on the astronomical science case, which differs per frequency subband [14].

(a)   (b)
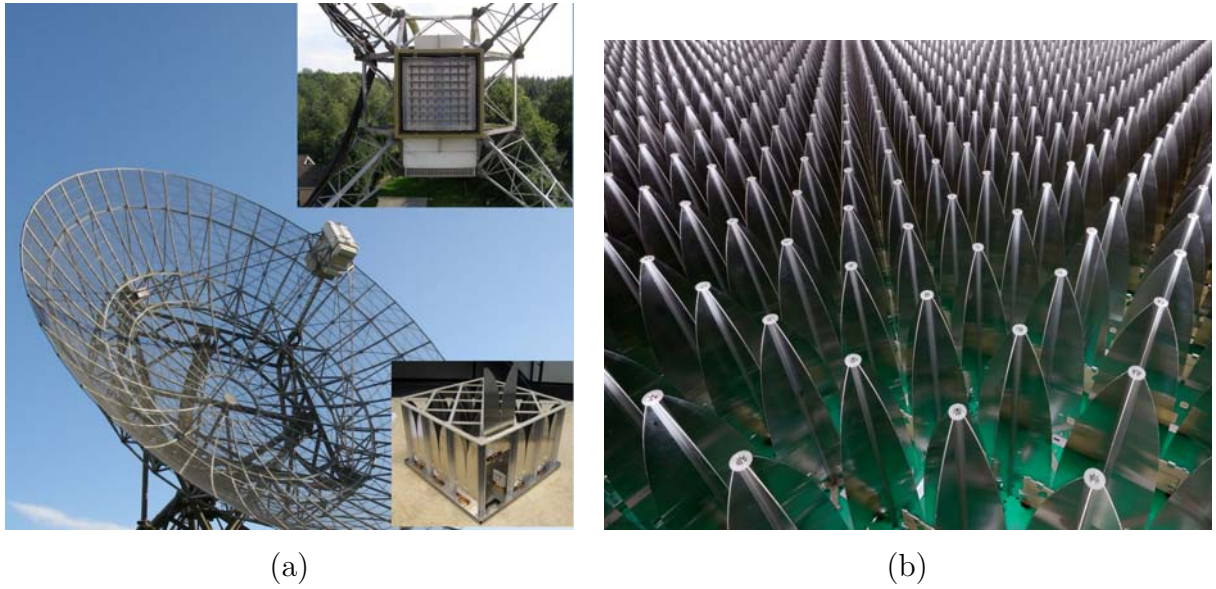
Figure 1.2: (a) The APERTIF focal-plane array antenna (72 aluminum dual-polarized tapered slot antennas), (b) The EMBRACE aperture-array antenna (10000 aluminum dual-polarized tapered slot antennas).

contiguous arrays of Tapered Slot Antennas (TSAs) are promising candidates for both the aperture- and focal-plane array concepts [see Figs. 1.2(a) and (b)]. Because the number of antenna elements is relatively large, the manufacturing cost needs to be minimized. At present, novel antenna-feed concepts have been developed of which the production cost is as low as two Euro per antenna element [20]. These low-cost technologies require a high level of integration with the attached electronics [21–23].

1.3   Challenges and Motivation of the Thesis Subject

The design and analysis of large arrays of strongly coupled TSAs constitutes a challenging task. To increase the operational frequency bandwidth, the outer edges of the TSA fins are (entirely) connected to the adjacent elements to preserve the continuity of the surface current across TSA boundaries [consider Fig. 1.2(b)]. Discontinuities introduced by slots and gaps of sufficient size tend to radiate and, consequently, disrupt the impedance and radiation characteristics. A penalty of these interconnections is that the numerical analysis of the entire array problem cannot be reduced to the analysis of a single isolated TSA element.

To date, commercial software tools cannot handle large finite antenna arrays because of memory constraints and excessively long simulation times. Alternatively, one can impose periodic boundary conditions to analyze a unit cell of an infinite phased-array antenna, but this is not possible if the edge truncation effects are significant, which is the case in our applications, and is inefficient if the excitation scheme is nonuniform. Parallelization and supercomputing technologies increase the future perspectives, but are not yet affordable to a large audience and cannot be implemented on a large scale on local hardware [24].

A major challenge is therefore to:

> *Accurately compute the impedance and radiation characteristics of large and complex antenna arrays using only moderate computing power, particularly, of single and dual-polarized arrays of 100+ TSA elements that are electrically interconnected. If the collection of these elements forms a subarray of a larger system, it is also of interest to analyze an array of disjoint subarrays as illustrated in Fig. 1.1.*

For validation purposes, a relative accuracy level of $\leq 20\%$ between the measured and simulated antenna patterns and impedances will be classified as "good", unless specified differently. Such a level of disagreement is not uncommon for very large and complex antenna structures where also the measurement errors, and in particular the manufacturing tolerances, determine the final accuracy. The manufacturing tolerances will be detailed for specific cases when necessary. The S-parameters have been measured with the Hewlett Packard 8720D network analyzer (0.05–20 GHz) which has, in combination with the available calibration kit, a measurement accuracy of order ± 0.05 dB, around the 0 dB measurement level, and about ± 0.5 dB for a -30 dB reflection measurement (output power is 0 dBm). In the absence of measurement errors and manufacturing tolerances, one may expect a relative numerical accuracy of less than a few percent; an example is the case where the accuracy of a plain method-of-moments code is compared to an enhanced version of it. Nonetheless, it is worth mentioning that relative differences in computed S-parameters can be as large as 20% if different numerical tools (formulations) are cross-validated [25].

Generally, the impact of a numerical error depends on how the overall system performance is affected by this error. To determine the maximum permissible error level, one must model the antenna system in its entirety and, subsequently, pose a requirement on the accuracy of the overall system sensitivity, as this is the primary figure of merit. However,

modeling the receiver sensitivity of an actively beamformed antenna system is a complex task.

A second major challenge is therefore to:

> *Characterize the system sensitivity of actively beamformed arrays of strongly coupled antenna elements. The antenna system should incorporate the external source environment (noise and signals), the antenna array, amplifiers, and a beamforming network, each of which may be lossy and noisy.*

In characterizing the system sensitivity, one should account for: (i) mismatch effects between antennas, amplifiers, and the beamforming circuit; (ii) an external (possibly nonuniform) noise field, superimposed by (partially) polarized celestial sources, and; (iii) noise generated by active and passive devices. Special attention must be devoted to the noise emanating from the amplifier inputs and re-entering into the system coherently through the mutually coupled antennas; this phenomenon is referred to as "noise coupling".

1.4   Novel Elements of This Dissertation

To address the above challenges, the limitations of a conventional integral-equation based method-of-moments formulation [26] need to be overcome. In such a method, a boundary integral equation is formulated for the current, which is subsequently discretized by employing a relatively large number of low-level basis and test functions, after which the resulting system of linear equation is solved for the unknown expansion coefficients. Often, a fine discretization is required to accurately represent the spatial distribution of the current. In turn, this leads to a large construction and solve time of the matrix equation. Many basis functions are required to represent the "shape" of the current well. However, the basis functions need not be all independent. In fact, from a physical point of view, the number of degrees of freedom for the current is limited, and this should correspond to the number of independent basis functions that are employed.

In this work, a conventional method-of-moments technique has been enhanced and made suitable to solve electrically large and interconnected antenna array problems on a desktop computer. Novel approaches encompass:

- A combination of the Characteristic Basis Function Method (CBFM) and the Adaptive Cross Approximation (ACA) technique[4]. The CBFM employs physics-based macro-domain basis functions to reduce the number of unknowns while maintaining the flexibility of low-level basis functions in modeling arbitrarily-shaped geometries. The ACA is used for fast construction of the corresponding reduced moment matrix.

- A meshing strategy to optimally exploit the quasi-Toeplitz symmetry in overlapping domain decomposition techniques and, in relation to that, the fast computation of element radiation patterns and input impedances.

- A derivation of a stationary formula for the antenna input *admittance* of an antenna. The antenna is excited by an RWG "voltage-gap source" and treated as a scattering problem. Consistent definitions for the voltage, current, and field relations are deduced, which are different from those published in the literature.

- A post-windowing technique for the numerical generation of partially overlapping macro-domain basis functions (CBFs). This procedure eliminates the edge-singular currents and preserves the continuity of the surface currents across subdomain interfaces while avoiding the use of an independent set of "junction basis functions".

- A perturbation approach to analyze large phase-steered antenna arrays of disjoint subarrays (*cf.* Fig. 1.1).

- A reduced-order model for microstrip-fed TSA arrays. In the literature, it was concluded that similar models could not be used to predict the radiation and impedance characteristics in a quantitative manner. However, the results of a 112 element TSA array are compared to measurements and the relative difference is found to be smaller than 20%.

- A detailed derivation of the sheet impedance of thin conductor slabs.

The techniques mentioned above have been implemented in a dedicated software analysis tool, termed CAESAR (Computationally Advanced and Efficient Simulator for ARrays, see Appendix F). Furthermore, this tool is capable of analyzing the receiver sensitivity of large antenna array systems. Novel aspects, in this respect, include:

---

[4]A detailed motivation to select these methods is given in Chapter 4.

- A framework to numerically model the antenna-receiver combination for a given set of external and internal signal and noise sources. For this purpose, existing models/methods have been combined, including the Thévenin network description of an antenna array on receive, and the connection matrix theory to numerically evaluate the signal and spectral noise power at the output of a receiver. External noise sources are represented at the antenna output ports by a noise-wave correlation matrix whose elements are expressed in terms of pattern overlap integrals and a nonuniform brightness temperature distribution of the sky.

- The accurate and numerical efficient evaluation of the radiation efficiency and noise temperature of low-loss antennas from a MoM solution. The thus computed efficiency is numerically smaller than or equal to 100%, contrary to results obtained with several commercial solvers. Furthermore, we develop a perturbation approach, which yields accurate results whenever the current resembles the PEC current.

In addition to the numerical software tool CAESAR, semi-analytical techniques have been developed to further increase our common understanding in the performance limiting factors of antenna-array receiving systems. The key elements are:

- The use of the active reflection coefficient of antenna elements to "noise decouple" the receiver channels. It is concluded that minimum receiver noise temperature is achieved by noise matching to the active reflection coefficient, rather than to the passive one.

- The modeling of the system sensitivity by representing an antenna-array receiving system by an equivalent single-channel receiver. For this purpose, the above-mentioned "noise-decoupling technique" is used.

With the above described methods implemented, CAESAR is capable of analyzing the receiver sensitivity of very large actively beamformed antenna array systems, both from a computational electromagnetics and system modeling point of view.

1.5   Outline of the Thesis

This thesis is organized as follows. In Chapter 2, the fundamental field equations are presented and a mathematical framework is developed for the subsequent chapters. Also, reciprocity relations are derived for antenna arrays on receive. In Chapter 3, the electric-field integral equation is formulated and subsequently discretized using the method of moments. Details are given on the computation aspects of the impedance and the radiation patterns. The numerical results are cross validated with commercially available simulators and with measurements. In Chapter 4, a numerical method is presented for computing the electromagnetic radiation and impedance characteristics of large dielectric-free antenna structures. Here, the Characteristic Basis Function Method (CBFM) is combined with the Adaptive Cross Approximation (ACA) algorithm to rapidly construct a reduced moment matrix, a novel method is developed to generate macro-basis functions that preserve the continuity of the current between connected antenna elements, a perturbation technique is detailed to analyze arrays of disjoint subarrays, and a combined electromagnetic en microwave circuit model of a 112-element TSA array is proposed of which the impedance characteristics are validated through measurements. In Chapter 5, the receiver sensitivity is analyzed. Both numerical and semi-analytical expressions are developed that account for the mismatch and noise coupling effects in strongly coupled antenna array systems. Results are shown for a practical 4-element antenna array system whose noise temperature is measured through the radiometric method (Y-factor method). Also, numerical results are shown for a dipole array which is validated by a semi-analytical approach. The radiation efficiency plays a vital role in the formula for the receiver sensitivity and has therefore been examined separately. Results on the radiation efficiency are shown for various cases among which a practical tapered slot antenna. Finally, the conclusions and recommendations are presented in Chapter 6.

Unless stated differently, the numerical computations have been carried out in double precision arithmetic on a Dell Inspiron 9300 Notebook, equipped with an Intel Pentium-M processor operating at 1.73 GHz, and 2.0 GB of RAM.

Chapter 2

Electromagnetic Field Equations

Various (vector) notations and identities are introduced in this chapter for the purpose of formulating the fundamental field equations. We recall the most relevant theorems that are required to develop a mathematical framework for the subsequent chapters. Maxwell's equations are first formulated in the time domain and subsequently transformed to the frequency domain. Next, the boundary conditions are presented for the electromagnetic field and used thereafter to express the radiated field in terms of equivalent currents and charges. Finally, the reaction concept and the associated reciprocity relations for antenna arrays are derived.

2.1 Maxwell's Equations and Constitutive Relations

Throughout this dissertation, vector quantities, matrices and arrays are typeset in boldface, the only difference being that the latter two are of the sans-serif font type. Calligraphic script letters are used for time-dependent field functions, and roman letters are used for frequency-dependent field functions. A double overbar indicates a dyadic operator, while a single overbar designates the time average. The short-hand notation ∂_t denotes the partial derivative $\partial/\partial t$ with respect to the real-valued time coordinate t, and may apply to any other coordinate as well. By employing a right-handed orthogonal Cartesian reference system for the spatial coordinates, the gradient operator is expressed as $\boldsymbol{\nabla} = \partial_x \hat{\boldsymbol{x}} + \partial_y \hat{\boldsymbol{y}} + \partial_z \hat{\boldsymbol{z}}$, where $\{\hat{\boldsymbol{x}}, \hat{\boldsymbol{y}}, \hat{\boldsymbol{z}}\}$ is the pertaining set of unit basis vectors that span the three-

dimensional Euclidian space $\mathbb{R}^3$. In this reference frame, the position vector $\boldsymbol{r}$ is defined as $\boldsymbol{r} = x\hat{\boldsymbol{x}} + y\hat{\boldsymbol{y}} + z\hat{\boldsymbol{z}}$ and its 2-norm length as $r = \|\boldsymbol{r}\|_2 = \sqrt{\boldsymbol{r} \cdot \boldsymbol{r}} = \sqrt{x^2 + y^2 + z^2}$, so that the unit vector is $\hat{\boldsymbol{r}} = \boldsymbol{r}/r$. Herein, the scalar product is denoted by $\cdot$ and the vector product by $\times$. Furthermore, we define that

$$\boldsymbol{\nabla} \cdot \boldsymbol{\mathcal{A}} \quad \text{is the } \textit{divergence} \text{ of a vector field } \boldsymbol{\mathcal{A}}(\boldsymbol{r})$$
$$\boldsymbol{\nabla} \times \boldsymbol{\mathcal{A}} \quad \text{is the } \textit{curl} \text{ of a vector field } \boldsymbol{\mathcal{A}}(\boldsymbol{r})$$
$$\boldsymbol{\nabla}\phi \quad \text{is the } \textit{gradient} \text{ of a scalar field } \phi(\boldsymbol{r})$$
$$\boldsymbol{\nabla} \cdot (\boldsymbol{\nabla}\phi) = \nabla^2\phi \quad \text{is the } \textit{Laplacian} \text{ of a scalar field } \phi(\boldsymbol{r}).$$

Finally, the operators $\mathfrak{Re}\{z\}$ and $\mathfrak{Im}\{z\}$ take the real and imaginary part of a complex number $z = z' + jz''$, respectively, with j as the imaginary unit defined by $j^2 = -1$. We will adopt the standard convention that $j = \sqrt{-1}$.

The formulation regarding the coupled set of hyperbolic partial differential equations that interrelate the electric and magnetic field intensities has been completed by James Clerk Maxwell in 1865 [27]. In the time domain, and in macroscopic form, Maxwell's equations read [28]

$$\boldsymbol{\nabla} \times \boldsymbol{\mathcal{E}} + \partial_t \boldsymbol{\mathcal{B}} = \boldsymbol{0}, \quad \text{(Faraday–Henry)} \tag{2.1a}$$
$$\boldsymbol{\nabla} \times \boldsymbol{\mathcal{H}} - \partial_t \boldsymbol{\mathcal{D}} = \boldsymbol{\mathcal{J}}, \quad \text{(Ampère–Maxwell)} \tag{2.1b}$$

where

$$\boldsymbol{\mathcal{E}}(\boldsymbol{r}, t) \quad \text{is called the } \textit{electric field strength} \text{ [Vm}^{-1}\text{]}$$
$$\boldsymbol{\mathcal{B}}(\boldsymbol{r}, t) \quad \text{is called the } \textit{magnetic flux density} \text{ [Vsm}^{-1}\text{]}$$

which, on account of the Lorentz force law, are regarded as the two fundamental electromagnetic force fields[1]. In addition,

$$\boldsymbol{\mathcal{H}}(\boldsymbol{r}, t) \quad \text{is called the } \textit{magnetic field strength} \text{ [Am}^{-1}\text{]}$$
$$\boldsymbol{\mathcal{D}}(\boldsymbol{r}, t) \quad \text{is called the } \textit{electric flux density} \text{ [Asm}^{-1}\text{]}$$
$$\boldsymbol{\mathcal{J}}(\boldsymbol{r}, t) \quad \text{is called the } \textit{electric current density} \text{ [Am}^{-2}\text{]}.$$

---

[1]From a mathematical point of view, however, it is advantageous to maintain the symmetry in the field equations by choosing $\boldsymbol{\mathcal{E}}$ and $\boldsymbol{\mathcal{H}}$ as the primary field quantities.

Maxwell's equations in (2.1) are complemented by the conservation law of free charges and currents. The associated law is commonly referred to as the continuity equation,

$$\boldsymbol{\nabla} \cdot \boldsymbol{\mathcal{J}} = -\partial_t \varrho \tag{2.2}$$

in which

$$\varrho(\boldsymbol{r}, t) \quad \text{is called the } \textit{electric charge density } [\text{Asm}^{-3}].$$

By taking the divergence of (2.1a) and (2.1b), and substituting (2.2), one obtains a set of auxiliary equations, which are known as the compatibility relations

$$0 = -\boldsymbol{\nabla} \cdot (\partial_t \boldsymbol{\mathcal{B}}) = -\partial_t (\boldsymbol{\nabla} \cdot \boldsymbol{\mathcal{B}}) \quad \rightarrow \quad \boldsymbol{\nabla} \cdot \boldsymbol{\mathcal{B}} = c_1 \tag{2.3a}$$

$$\partial_t \varrho = \boldsymbol{\nabla} \cdot (\partial_t \boldsymbol{\mathcal{D}}) = \partial_t (\boldsymbol{\nabla} \cdot \boldsymbol{\mathcal{D}}) \quad \rightarrow \quad \boldsymbol{\nabla} \cdot \boldsymbol{\mathcal{D}} = \varrho + c_2 \tag{2.3b}$$

where we may set the scalar functions $c_1(\boldsymbol{r}) = c_2(\boldsymbol{r}) = 0$ by imposing the initial condition that $\boldsymbol{\nabla} \cdot \boldsymbol{\mathcal{B}}$ and $\boldsymbol{\nabla} \cdot \boldsymbol{\mathcal{D}} - \varrho$ must vanish at the instant $t = t_0$ for all $\boldsymbol{r} \in \mathbb{R}^3$.

At this point, the media considered in this dissertation are assumed linear, time-invariant, and causal so that a frequency-domain representation can be used for both the sources and fields through the application of the unilateral Laplace transform

$$\boldsymbol{F}(\boldsymbol{r}, s) = \int_{t_0(\boldsymbol{r})}^{\infty} \boldsymbol{\mathcal{F}}(\boldsymbol{r}, t) e^{-st} \, \mathrm{d}t \tag{2.4a}$$

$$\boldsymbol{\mathcal{F}}(\boldsymbol{r}, t) = \frac{1}{2\pi j} \int_{-\delta - j\infty}^{\delta + j\infty} \boldsymbol{F}(\boldsymbol{r}, s) e^{st} \, \mathrm{d}s \tag{2.4b}$$

where the time-dependent field $\boldsymbol{\mathcal{F}}(\boldsymbol{r}, t)$ at the position $\boldsymbol{r}$ is assumed to be zero prior to instant $t_0(\boldsymbol{r})$. The complex frequency $s = \delta + j\omega$, in which ω is the radial frequency [rads^{-1}]. The medium is assumed to be passive, and the energy of the fields and sources remain bounded for $t \rightarrow \infty$. Hence, each field $\boldsymbol{F}(s)$ is assumed to be analytic for $\mathfrak{Re}\{s\} > 0$, i.e., poles of $\boldsymbol{F}$ only reside in the left-half of the complex s-plane ($\delta < 0$) and/or along the imaginary axis ($\delta = 0$).

For a real-valued function $\boldsymbol{\mathcal{F}}(\boldsymbol{r}, t)$, and with $s = \lim_{\delta \downarrow 0}\{\delta + j\omega\}$, it is inferred from (2.4a) that $\boldsymbol{F}(\boldsymbol{r}, -\omega) = \boldsymbol{F}^*(\boldsymbol{r}, \omega)$, so that (2.4b) simplifies to

$$\boldsymbol{\mathcal{F}}(\boldsymbol{r}, t) = \frac{1}{\pi} \int_0^{\infty} \mathfrak{Re}\left\{\boldsymbol{F}(\boldsymbol{r}, \omega) e^{j\omega t}\right\} \, \mathrm{d}\omega \tag{2.5}$$

where the angular frequency ω is nonnegative and real-valued.

The sources that generate the fields are assumed to be monochromatic for $t > t_0$, i.e., have a sinusoidal time dependence for $t > t_0$. Hence, and under steady-state conditions $[t \to \infty]$, the fields that reside in this media will also have a sinusoidal time dependence of the same frequency, provided that the higher-order turn-on transients of the fields (homogeneous solution) have sufficiently damped with respect to the instantaneous field.

We will restrict the analysis to steady-state signals (particular solution) by representing these time-harmonic fields $\boldsymbol{\mathcal{F}}$ at each of the discrete frequencies by a phasor $\boldsymbol{F}$, i.e., $\boldsymbol{\mathcal{F}}(\boldsymbol{r}, t) = \mathfrak{Re}\{\boldsymbol{F}(\boldsymbol{r}, \omega)e^{j\omega t}\}$. Note that the dimension of $\boldsymbol{F}$ has changed, since it no longer represents a spectral density, in contrast to $\boldsymbol{F}$ in (2.5). This is a result of taking only one spectral component of (2.5) through the application of the sifting property of the delta distribution function, which has the dimension of Hz^{-1}. Consequently, and as opposed to the integral representation (2.5), the total time-dependent field for a number of spectral lines is then obtained through a discrete sum of spectral components and the time factor $e^{j\omega t}$. For each of these spectral components, one can write (2.1a) in the frequency domain as[2]

$$\boldsymbol{\nabla} \times \mathfrak{Re}\{\boldsymbol{E}e^{j\omega t}\} = -\partial_t \mathfrak{Re}\{\boldsymbol{B}e^{j\omega t}\} \tag{2.6a}$$

$$\boldsymbol{\nabla} \times \boldsymbol{E} = -j\omega \boldsymbol{B} \tag{2.6b}$$

where we have used the linearity of the operators and that, if $\boldsymbol{A}$ and $\boldsymbol{B}$ are complex vectors, and $\mathfrak{Re}\{\boldsymbol{A}e^{j\omega t}\} = \mathfrak{Re}\{\boldsymbol{B}e^{j\omega t}\}$ for all t, then $\boldsymbol{A} = \boldsymbol{B}$. This can be readily observed by subsequent evaluation of the above equation at $t = 0$ and $\omega t = \pi/2$, which yields $\mathfrak{Re}\{\boldsymbol{A}\} = \mathfrak{Re}\{\boldsymbol{B}\}$ and $\mathfrak{Im}\{\boldsymbol{A}\} = \mathfrak{Im}\{\boldsymbol{B}\}$, respectively, so that $\boldsymbol{A} = \boldsymbol{B}$.

In the frequency domain, Maxwell's equations are expressed in complex phasor form as

$$\boldsymbol{\nabla} \times \boldsymbol{E} + j\omega \boldsymbol{B} = \boldsymbol{0} \tag{2.7a}$$

$$\boldsymbol{\nabla} \times \boldsymbol{H} - j\omega \boldsymbol{D} = \boldsymbol{J} \tag{2.7b}$$

$$\boldsymbol{\nabla} \cdot \boldsymbol{J} + j\omega \rho = 0 \tag{2.7c}$$

with the auxiliary set of compatibility relations

$$\boldsymbol{\nabla} \cdot \boldsymbol{B} = 0 \tag{2.8a}$$

$$\boldsymbol{\nabla} \cdot \boldsymbol{D} = \rho. \tag{2.8b}$$

---

[2]Note that one can equally well choose to work with spectral field densities.

The above set of partial differential equations is incomplete since the characteristics of the medium are yet to be specified through the constitutive relations.

In addition to assuming that the media are linear, passive, causal, and time-invariant, they are also assumed to be isotropic and locally reacting. Then, the constitutive relations for this matter are

$$\boldsymbol{B} = \mu \boldsymbol{H} \qquad\qquad \boldsymbol{D} = \varepsilon \boldsymbol{E} \qquad\qquad (2.9)$$

where the electromagnetic properties of the medium are defined by the permeability $\mu(\boldsymbol{r}, \omega)$ [VsA^{-1}m^{-1}] and the permittivity $\varepsilon(\boldsymbol{r}, \omega)$ [AsV^{-1}m^{-1}], which are complex-valued scalar functions. The conductivity $\sigma(\boldsymbol{r}, \omega)$ [AV^{-1}m^{-1}] is herein part of the permittivity, i.e.,

$$\varepsilon = \varepsilon_0 \varepsilon_r - j \frac{\sigma}{\omega} \qquad\qquad (2.10)$$

so that $\boldsymbol{J}$ in (2.7) designates a primary impressed current. By international agreement, the permeability of vacuum has been chosen as $\mu_0 = 4\pi \times 10^{-7}$ VsA^{-1}m^{-1}, and because the speed of light in vacuum is $c_0 = 1/\sqrt{\mu_0 \varepsilon_0} \approx 3 \times 10^8$ ms^{-1}, it readily follows that the permittivity in vacuum $\varepsilon_0 \approx 1/(36\pi) \times 10^{-9}$ AsV^{-1}m^{-1}. Furthermore, one can write that $\mu = \mu_0 \mu_r$ and $\varepsilon = \varepsilon_0 \varepsilon_r$, where μ_r and ε_r represent the (complex) dimensionless relative permeability and permittivity of the medium, respectively.

2.2 Boundary Conditions

For Maxwell's differential equations to have a unique solution, a suitable set of boundary conditions needs to be imposed on the fields in (2.7). We will distinguish between the interface and radiation boundary conditions. Consider for this purpose the stationary and locally smooth interface $\mathcal{S}$ that separates two homogeneous media as depicted in Fig. 2.1.

Upon taking the limit of (2.7) when crossing the interface $\mathcal{S}$, it can be derived that the tangential fields have to satisfy the interface boundary conditions

$$\begin{aligned}
\hat{\boldsymbol{n}} \times \boldsymbol{E}_2 - \hat{\boldsymbol{n}} \times \boldsymbol{E}_1 = \boldsymbol{0} \qquad &\rightarrow \qquad \hat{\boldsymbol{n}} \times \boldsymbol{D}_2 - (\varepsilon_2/\varepsilon_1)\, \hat{\boldsymbol{n}} \times \boldsymbol{D}_1 = \boldsymbol{0} \\
\hat{\boldsymbol{n}} \times \boldsymbol{H}_2 - \hat{\boldsymbol{n}} \times \boldsymbol{H}_1 = \boldsymbol{J}_S \qquad &\rightarrow \qquad \hat{\boldsymbol{n}} \times \boldsymbol{B}_2 - (\mu_2/\mu_1)\, \hat{\boldsymbol{n}} \times \boldsymbol{B}_1 = \mu_2 \boldsymbol{J}_S
\end{aligned} \qquad (2.11)$$

at $\boldsymbol{r} \in \mathcal{S}$, where the primary impressed and/or secondary induced surface current density $\boldsymbol{J}_S$ [Am^{-1}], supported by $\mathcal{S}$ has a Dirac dependence in the $\hat{\boldsymbol{n}}$-direction. Note that, on
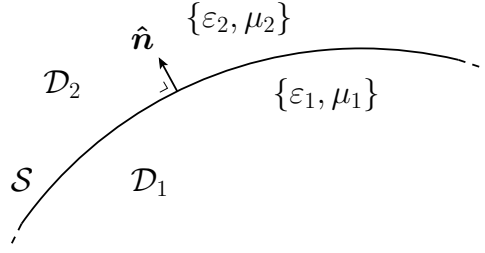
Figure 2.1: Locally smooth boundary interface $\mathcal{S}$ as the surface between two homogeneous media 1 and 2.

physical grounds, and irrespective of the medium properties, the tangential components of $\boldsymbol{E}$ are continuous across the interface. Similarly, the boundary conditions for the normal components of the fields are formulated as

$$
\begin{aligned}
\hat{\boldsymbol{n}} \cdot \boldsymbol{D}_2 - \hat{\boldsymbol{n}} \cdot \boldsymbol{D}_1 = \rho_S &\qquad \rightarrow \qquad \hat{\boldsymbol{n}} \cdot \boldsymbol{E}_2 - (\varepsilon_1/\varepsilon_2)\,\hat{\boldsymbol{n}} \cdot \boldsymbol{E}_1 = \rho_S/\varepsilon_2 \\
\hat{\boldsymbol{n}} \cdot \boldsymbol{B}_2 - \hat{\boldsymbol{n}} \cdot \boldsymbol{B}_1 = 0 &\qquad \rightarrow \qquad \hat{\boldsymbol{n}} \cdot \boldsymbol{H}_2 - (\mu_1/\mu_2)\,\hat{\boldsymbol{n}} \cdot \boldsymbol{H}_1 = 0
\end{aligned}
\tag{2.12}
$$

where, in this case, the normal component of $\boldsymbol{B}$ is continuous across the interface. Furthermore, the impressed and/or induced surface charge density ρ_S [Asm^{-2}] and the corresponding surface current $\boldsymbol{J}_S$ satisfy the surface continuity equation

$$
\boldsymbol{\nabla}_S \cdot \boldsymbol{J}_S = -j\omega\rho_S
\tag{2.13}
$$

with the surface divergence operator $\boldsymbol{\nabla}_S = \boldsymbol{\nabla} - (\hat{\boldsymbol{n}} \cdot \boldsymbol{\nabla})\,\hat{\boldsymbol{n}}$.

A specific situation occurs when medium 1 becomes electrically impenetrable, i.e., for $|\varepsilon_1| \to \infty$. Examples of such a material are a perfect polarizable medium and a perfect electric conductor (PEC). From (2.11) one has that $\hat{\boldsymbol{n}} \times \boldsymbol{E}_1 = \hat{\boldsymbol{n}} \times \boldsymbol{E}_2 = \boldsymbol{0}$, and because fields must remain finite in a PEC medium, one concludes from (2.12) that $\hat{\boldsymbol{n}} \cdot \boldsymbol{E}_1 = 0$, so that $\boldsymbol{E}_1 = \boldsymbol{0}$ as well as that $\hat{\boldsymbol{n}} \cdot \boldsymbol{E}_2 = \rho_S/\varepsilon_2$. Accordingly, $\boldsymbol{B}_1 = (j/\omega)\boldsymbol{\nabla} \times \boldsymbol{E}_1 = \boldsymbol{0}$, so that from (2.11) and (2.12) it is inferred that $\hat{\boldsymbol{n}} \times \boldsymbol{B}_2 = \mu_2\boldsymbol{J}_S$, and $\hat{\boldsymbol{n}} \cdot \boldsymbol{B}_2 = 0$, respectively. In summary, $\boldsymbol{E}_1 = \boldsymbol{H}_1 = \boldsymbol{0}$, and

$$
\begin{aligned}
\hat{\boldsymbol{n}} \times \boldsymbol{E}_2 = \boldsymbol{0} &\qquad\qquad \hat{\boldsymbol{n}} \times \boldsymbol{H}_2 = \boldsymbol{J}_S \\
\hat{\boldsymbol{n}} \cdot \boldsymbol{D}_2 = \rho_S &\qquad\qquad \hat{\boldsymbol{n}} \cdot \boldsymbol{B}_2 = 0
\end{aligned}
\tag{2.14}
$$

at $\boldsymbol{r} \in \mathcal{S}$, where $\boldsymbol{E}_2$ and $\boldsymbol{H}_2$ are the limiting field values.

In addition to the interface boundary conditions, a condition at infinity must be enforced for open-boundary problems as, e.g., in case of antennas radiating in free space. Let R be

the radius of a sphere that encloses all sources, inhomogeneities, etc. Outside the sphere the sources are assumed to radiate in a homogeneous space. When $R \to \infty$, the Sommerfeld radiation condition states that the outward-traveling fields in a point at the surface ∂S of the sphere must be vanishing small; this is a result of the free-space expansion of the fields and is essentially a statement of energy conservation. In addition, it states that $\boldsymbol{E}$ and $\boldsymbol{B}$ will be directed transversely to the propagation direction (plane-wave propagation) and will decrease as R^{-1}. In mathematical terms, the Sommerfeld radiation condition can be written as [29]

$$\hat{\boldsymbol{r}} \times \boldsymbol{H} + (\varepsilon/\mu)^{\frac{1}{2}} \boldsymbol{E} = \mathcal{O}\left(R^{-2}\right) \quad \text{as } R \to \infty \tag{2.15a}$$

$$\hat{\boldsymbol{r}} \times \boldsymbol{E} - (\mu/\varepsilon)^{\frac{1}{2}} \boldsymbol{H} = \mathcal{O}\left(R^{-2}\right) \quad \text{as } R \to \infty \tag{2.15b}$$

where $\boldsymbol{r} \in \partial S$. Here, we define the wave impedance $Z = \sqrt{\mu/\varepsilon}$ [Ω] and the wave admittance $Y = \sqrt{\varepsilon/\mu}$ [Ω^{-1}]. In vacuum, $Z_0 = \sqrt{\mu_0/\varepsilon_0} \approx 120\pi$.

2.3   Mixed Potential Formulation

Maxwell's equations (2.7) have a unique solution, provided that an appropriate set of boundary conditions is imposed and that the constitutive parameters (2.9) of the medium are known. Of particular interest is to determine the electromagnetic field that is radiated by a source current distribution $\boldsymbol{J}$ in free space, with $\varepsilon(\boldsymbol{r}) = \varepsilon_0$ and $\mu(\boldsymbol{r}) = \mu_0$. For this specific medium (vacuum), Maxwell's equations reduce to

$$\begin{aligned} \boldsymbol{\nabla} \times \boldsymbol{E} &= -j\omega\mu_0\boldsymbol{H} & \boldsymbol{\nabla} \cdot \boldsymbol{E} &= \rho/\varepsilon_0 \\ \boldsymbol{\nabla} \times \boldsymbol{H} &= \boldsymbol{J} + j\omega\varepsilon_0\boldsymbol{E} & \boldsymbol{\nabla} \cdot \boldsymbol{H} &= 0. \end{aligned} \tag{2.16}$$

Because $\boldsymbol{H}$ is solenoidal ($\boldsymbol{\nabla} \cdot \boldsymbol{H} = 0$), we may express this field in terms of a magnetic vector potential $\boldsymbol{A}$. For instance,

$$\boldsymbol{H} = \boldsymbol{\nabla} \times \boldsymbol{A} \tag{2.17}$$

which can be substituted in the left two Equations of (2.16) to yield

$$\boldsymbol{\nabla} \times (\boldsymbol{E} + j\omega\mu_0\boldsymbol{A}) = 0, \tag{2.18}$$

$$\boldsymbol{\nabla} \times \boldsymbol{\nabla} \times \boldsymbol{A} = \boldsymbol{J} + j\omega\varepsilon_0\boldsymbol{E}. \tag{2.19}$$

The curl in (2.18) is operating on a conservative (irrotational) vector field, which can mathematically be formulated as

$$\boldsymbol{E} = -j\omega\mu_0\boldsymbol{A} - \boldsymbol{\nabla}\Phi \tag{2.20}$$

where Φ is an electric scalar potential, yet to be determined. Substituting (2.20) in (2.19) and utilizing the vector identity $\boldsymbol{\nabla} \times \boldsymbol{\nabla} \times \boldsymbol{A} = \boldsymbol{\nabla}\left(\boldsymbol{\nabla} \cdot \boldsymbol{A}\right) - \boldsymbol{\nabla}^2\boldsymbol{A}$ leads to

$$\boldsymbol{\nabla}^2\boldsymbol{A} + k_0^2\boldsymbol{A} = -\boldsymbol{J} + \boldsymbol{\nabla}\left(\boldsymbol{\nabla} \cdot \boldsymbol{A} + j\omega\varepsilon_0\Phi\right) \tag{2.21}$$

where the free-space wavenumber has been introduced as $k_0 = \omega\sqrt{\mu_0\varepsilon_0}$.

A vector field $\boldsymbol{A}$ is defined uniquely if both its curl and divergence are specified, provided that $\boldsymbol{A}$ is known in a single point or vanishes at infinity. With reference to definition (2.17), and in view of (2.21), it is advantageous to set

$$\boldsymbol{\nabla} \cdot \boldsymbol{A} = -j\omega\varepsilon_0\Phi \tag{2.22}$$

which is known as the Lorenz gauge. Upon substituting this result in (2.21), one arrives at the inhomogeneous Helmholtz wave equation

$$\boldsymbol{\nabla}^2\boldsymbol{A} + k_0^2\boldsymbol{A} = -\boldsymbol{J} \tag{2.23}$$

which can be solved for a given forcing function $\boldsymbol{J}$. The radiation condition imposed on $\boldsymbol{A}$ at infinity requires that only outward traveling wave solutions are physically possible. It can be shown that the well-known general solution of (2.23) is [30, pp. 78–80]

$$\boldsymbol{A}(\boldsymbol{r}) = \iiint\limits_{\mathcal{V}} G(\boldsymbol{r} - \boldsymbol{r}')\boldsymbol{J}(\boldsymbol{r}')\,\mathrm{d}V' \quad (\boldsymbol{r}\text{ outside }\mathcal{V}) \tag{2.24}$$

with the scalar free-space Green's function $G = \exp(-jk_0R)/(4\pi R)$ and $R = \|\boldsymbol{r} - \boldsymbol{r}'\|_2$.

Upon taking the divergence of (2.20), and by using (2.22) as well as that $\boldsymbol{\nabla} \cdot \boldsymbol{E} = \rho/\varepsilon_0$, one readily arrives at the inhomogeneous wave equation for the electric scalar potential, which reads

$$\boldsymbol{\nabla}^2\Phi + k_0^2\Phi = -\frac{\rho}{\varepsilon_0} \tag{2.25}$$

and has the generic solution

$$\Phi(\boldsymbol{r}) = \frac{1}{\varepsilon_0}\iiint\limits_{\mathcal{V}} G(\boldsymbol{r} - \boldsymbol{r}')\rho(\boldsymbol{r}')\,\mathrm{d}V' \quad (\boldsymbol{r}\text{ outside }\mathcal{V}). \tag{2.26}$$

In summary, the free-space electromagnetic fields $\{\boldsymbol{E}, \boldsymbol{H}\}$ can be determined outside the source region $\mathcal{V}$ through the evaluation of the potentials $\boldsymbol{A}$ and Φ as

$$\boldsymbol{E}(\boldsymbol{r}, \boldsymbol{J}) = -j\omega\mu_0\boldsymbol{A} - \boldsymbol{\nabla}\Phi \tag{2.27a}$$

$$\boldsymbol{H}(\boldsymbol{r}, \boldsymbol{J}) = \boldsymbol{\nabla} \times \boldsymbol{A} \tag{2.27b}$$

$$\boldsymbol{A}(\boldsymbol{r}) = \iiint\limits_{\mathcal{V}} G(\boldsymbol{r} - \boldsymbol{r}')\boldsymbol{J}(\boldsymbol{r}')\,\mathrm{d}V' \tag{2.27c}$$

$$\Phi(\boldsymbol{r}) = -\frac{1}{j\omega\varepsilon_0}\iiint\limits_{\mathcal{V}} G(\boldsymbol{r} - \boldsymbol{r}')\boldsymbol{\nabla}' \cdot \boldsymbol{J}(\boldsymbol{r}')\,\mathrm{d}V' \tag{2.27d}$$

$$G(\boldsymbol{r} - \boldsymbol{r}') = \frac{e^{-jk_0\|\boldsymbol{r}-\boldsymbol{r}'\|_2}}{4\pi\|\boldsymbol{r} - \boldsymbol{r}'\|_2}. \tag{2.27e}$$

Note that we have substituted the continuity equation $\boldsymbol{\nabla}' \cdot \boldsymbol{J}(\boldsymbol{r}') = -j\omega\rho(\boldsymbol{r}')$ in (2.26) to arrive at (2.27d), with the divergence operator $\boldsymbol{\nabla}' = \boldsymbol{\nabla}_{\boldsymbol{r}'}$ operating on $\boldsymbol{r}'$.

Alternatively, by substituting (2.22) in (2.20), a single potential formulation is obtained that assumes the form

$$\boldsymbol{E}(\boldsymbol{r}, \boldsymbol{J}) = \frac{1}{j\omega\varepsilon_0}\left[\boldsymbol{\nabla}\left(\boldsymbol{\nabla} \cdot \boldsymbol{A}\right) + k_0^2\boldsymbol{A}\right]. \tag{2.28}$$

From (2.22), (2.27c), and (2.27d), it is inferred that

$$\boldsymbol{\nabla} \cdot \iiint\limits_{\mathcal{V}} G(\boldsymbol{r} - \boldsymbol{r}')\boldsymbol{J}(\boldsymbol{r}')\,\mathrm{d}V' = \iiint\limits_{\mathcal{V}} G(\boldsymbol{r} - \boldsymbol{r}')\boldsymbol{\nabla}' \cdot \boldsymbol{J}(\boldsymbol{r}')\,\mathrm{d}V'. \tag{2.29}$$

2.4 The Reaction Concept

The reaction concept has been widely used, not only in the analytical evaluation of both the self- and mutual port impedances of electromagnetic structures [31], but also in the numerical evaluation of system matrix entries arising in integral-equation-based computer methods [32] (see also Chapter 3). The reaction concept has been introduced by Rumsey [33], and quantifies the reaction of a field a, which has been generated by a source a, on a source b. This reaction is symbolically written as $\langle a, b \rangle$. It will be shown that this concept is closely related to the reciprocity theorem, which states that $\langle a, b \rangle = \langle b, a \rangle$.
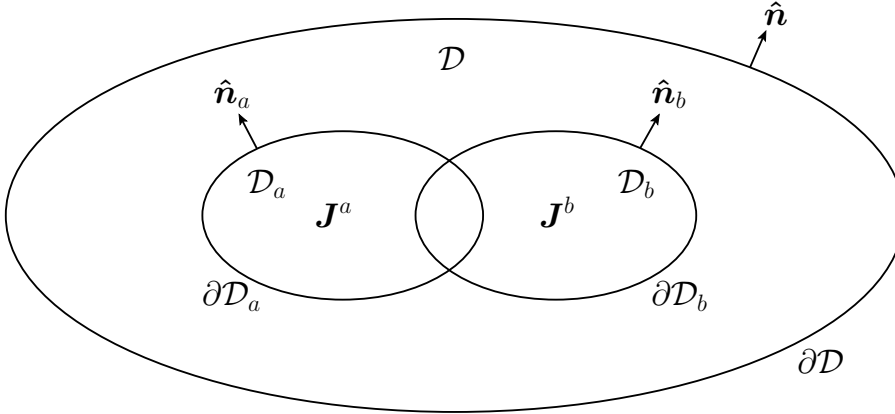
Figure 2.2: Current distributions $\boldsymbol{J}^{a,b}$, confined within the overlapping volumetric domains $\mathcal{D}_{a,b}$ and used to generate the respective fields $\{\boldsymbol{E}^{a,b}, \boldsymbol{H}^{a,b}\}$ throughout the entire volume $\mathcal{D}$.

Figure 2.2 specifies the situation of two electric currents distributions $\boldsymbol{J}^{a,b}$, which are confined within the (possibly) overlapping volumetric domains $\mathcal{D}_{a,b}$. Each source is considered in the absence of the other to independently generate the respective fields $\{\boldsymbol{E}^{a,b}, \boldsymbol{H}^{a,b}\}$ throughout the entire volume $\mathcal{D}$.

The fields in $\mathcal{D}$ satisfy either

$$
\begin{aligned}
\boldsymbol{\nabla} \times \boldsymbol{E}^a &= -j\omega\mu\boldsymbol{H}^a \\
\boldsymbol{\nabla} \times \boldsymbol{H}^a &= \boldsymbol{J}^a + j\omega\varepsilon\boldsymbol{E}^a
\end{aligned}
\quad \text{or} \quad
\begin{aligned}
\boldsymbol{\nabla} \times \boldsymbol{E}^b &= -j\omega\mu\boldsymbol{H}^b \\
\boldsymbol{\nabla} \times \boldsymbol{H}^b &= \boldsymbol{J}^b + j\omega\varepsilon\boldsymbol{E}^b
\end{aligned}
\tag{2.30}
$$

depending upon whether source a, or source b has been used to generate the fields. From (2.30), and the vector identity $\boldsymbol{\nabla} \cdot (\boldsymbol{A} \times \boldsymbol{B}) = \boldsymbol{B} \cdot (\boldsymbol{\nabla} \times \boldsymbol{A}) - \boldsymbol{A} \cdot (\boldsymbol{\nabla} \times \boldsymbol{B})$, one can readily verify that

$$
\begin{aligned}
\boldsymbol{\nabla} \cdot \left(\boldsymbol{E}^b \times \boldsymbol{H}^a\right) &= \boldsymbol{H}^a \cdot \left(\boldsymbol{\nabla} \times \boldsymbol{E}^b\right) - \boldsymbol{E}^b \cdot (\boldsymbol{\nabla} \times \boldsymbol{H}^a) \\
&= -j\omega\mu\boldsymbol{H}^a \cdot \boldsymbol{H}^b - \boldsymbol{E}^b \cdot \boldsymbol{J}^a - j\omega\varepsilon\boldsymbol{E}^b \cdot \boldsymbol{E}^a.
\end{aligned}
\tag{2.31}
$$

Interchanging the superscripts a and b, and subtracting the resulting equation from (2.31), yields

$$
\boldsymbol{\nabla} \cdot \left(\boldsymbol{E}^b \times \boldsymbol{H}^a - \boldsymbol{E}^a \times \boldsymbol{H}^b\right) = \boldsymbol{E}^a \cdot \boldsymbol{J}^b - \boldsymbol{E}^b \cdot \boldsymbol{J}^a
\tag{2.32}
$$

Next, (2.32) is integrated over the volume $\mathcal{D}$ and Gauss' divergence theorem is used, which states that

$$
\iiint\limits_{\mathcal{D}} \boldsymbol{\nabla} \cdot \boldsymbol{A} \, \mathrm{d}V = \oiint\limits_{\partial\mathcal{D}} \boldsymbol{A} \cdot \hat{\boldsymbol{n}} \, \mathrm{d}S
\tag{2.33}
$$

so that one arrives at

$$\oiint_{\partial \mathcal{D}} \left(\boldsymbol{E}^b \times \boldsymbol{H}^a - \boldsymbol{E}^a \times \boldsymbol{H}^b \right) \cdot \hat{\boldsymbol{n}} \, \mathrm{d}S = \langle a, b \rangle - \langle b, a \rangle \tag{2.34}$$

with the reactions defined by:

$$\langle a, b \rangle = \iiint_{\mathcal{D}_b} \boldsymbol{E}^a \cdot \boldsymbol{J}^b \, \mathrm{d}V \qquad\qquad \langle b, a \rangle = \iiint_{\mathcal{D}_a} \boldsymbol{E}^b \cdot \boldsymbol{J}^a \, \mathrm{d}V. \tag{2.35}$$

Through cyclic rotation, the left-hand side of (2.34) can be rewritten as

$$\oiint_{\partial \mathcal{D}} \left(\boldsymbol{E}^b \times \boldsymbol{H}^a - \boldsymbol{E}^a \times \boldsymbol{H}^b \right) \cdot \hat{\boldsymbol{n}} \, \mathrm{d}S = \oiint_{\partial \mathcal{D}} \left(\hat{\boldsymbol{n}} \times \boldsymbol{E}^b \right) \cdot \boldsymbol{H}^a - \left(\hat{\boldsymbol{n}} \times \boldsymbol{E}^a \right) \cdot \boldsymbol{H}^b \, \mathrm{d}S. \tag{2.36}$$

If $\partial \mathcal{D}$ represents the surface of a sphere with radius R, which is centered around the origin of the coordinate system, then $\hat{\boldsymbol{n}} = \hat{\boldsymbol{r}}$. In addition, for $R \to \infty$, and on account of the radiation conditions as listed in (2.15), one has that $\hat{\boldsymbol{r}} \times \boldsymbol{E}^{a,b} = Z_0 \boldsymbol{H}^{a,b}$, where the intrinsic impedance of the medium (free-space) is given by $Z_0 = \sqrt{\mu_0/\varepsilon_0}$. Upon substituting the latter expressions in (2.36), one observes that, at infinity, the integrand in (2.36) vanishes because $Z_0 \boldsymbol{H}^b \cdot \boldsymbol{H}^a - Z_0 \boldsymbol{H}^a \cdot \boldsymbol{H}^b = 0$. Hence, as $R \to \infty$, Eq. (2.34) simplifies to

$$\oiint_{\partial \mathcal{D}} \left(\boldsymbol{E}^b \times \boldsymbol{H}^a - \boldsymbol{E}^a \times \boldsymbol{H}^b \right) \cdot \hat{\boldsymbol{n}} \, \mathrm{d}S = 0 \tag{2.37}$$

which is the Lorentz reciprocity theorem in integral form.

With reference to (2.35), Eq. (2.37) also holds if $\boldsymbol{J}^a = \boldsymbol{J}^b = \boldsymbol{0}$ in the volume outside $\mathcal{D}$, which is bounded between the finite-sized surface $\partial \mathcal{D}$ (see Fig. 2.2) and a third imaginary surface placed at infinity as the outer shell. Since the integration at infinity yields zero for outward traveling fields, the integral over $\partial \mathcal{D}$ must vanish as well. The implication of this result is that the Lorentz theorem holds for any regular, closed surface ∂S surrounding the sources a and b. Hence, and on account of (2.34), one concludes that $\langle a, b \rangle = \langle b, a \rangle$, which is commonly known as the reciprocity theorem.

2.5   Antenna Reciprocity for Finite Arrays

Over the past decades, the application of the reciprocity and reaction theorem has become common practice in solving various types of antenna and scattering problems. In this

respect, a particularly important result in the characterization of the electrical properties of receiving array antennas has already been reported by de Hoop in 1975 [34]. In this reference, a rigorous proof is presented which justifies the use of a Thévenin circuit representation of an antenna array on receive. This equivalent electrical network has internal (voltage) sources whose strengths depend on the amplitude, phase and state of polarization of the radiation that is incident upon the antenna in the receiving situation. Since this circuit representation is of great importance in the analysis of entire antenna array systems (Chapter 5), an approach based on [34] will be followed for deriving the relevant components of the Thévenin network.

Transmit situation

Figure 2.3 illustrates an N-port antenna array on transmit. The array is excited by N current sources to generate the total transmitted fields $\{\boldsymbol{E}^T, \boldsymbol{H}^T\}$. Domains $\mathcal{D}_1$ and $\mathcal{D}_3$ have constitutive parameters μ_0 and ε_0 (vacuum). The antenna structure occupies a (possibly lossy) domain $\mathcal{D}_2$, with complex-valued constitutive parameters μ and ε, and is bounded by the interior and exterior, sufficiently regular, closed surfaces $\partial\mathcal{D}_1$ and $\partial\mathcal{D}_2$, respectively. Domain $\mathcal{D}_1$ contains the current sources $\{I_1^T, I_2^T, \ldots, I_N^T\}$, each of which is interconnected to a pair of perfectly electrically conducting (lossless) leads that penetrate the surface $\partial\mathcal{D}_1$.
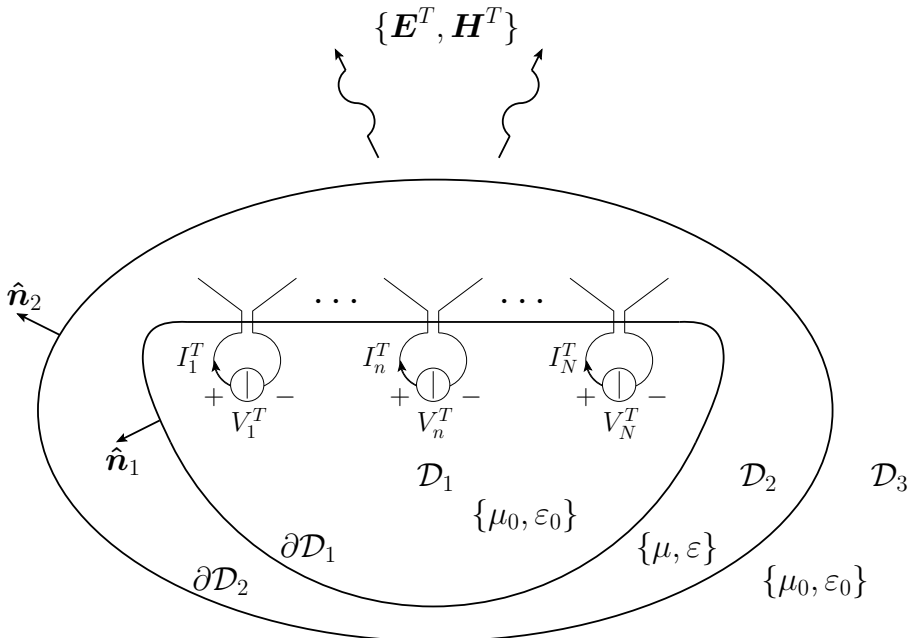
Figure 2.3: N-port antenna array on transmit.

Receive situation

Figure 2.4 illustrates the N-port antenna array on receive, where a plane electromagnetic wave is assumed to be incident on the array from direction $\hat{\boldsymbol{r}}_i$, i.e.,

$$
\begin{aligned}
\boldsymbol{E}^i &= \boldsymbol{E}_0 e^{j(\boldsymbol{k}_0 \cdot \boldsymbol{r})} \\
\boldsymbol{H}^i &= Z_0^{-1} \boldsymbol{E}^i \times \hat{\boldsymbol{r}}_i = Y_0 \boldsymbol{E}_0 \times \hat{\boldsymbol{r}}_i e^{j(\boldsymbol{k}_0 \cdot \boldsymbol{r})}.
\end{aligned}
\tag{2.38}
$$

where $\boldsymbol{k}_0 = k_0 \hat{\boldsymbol{r}}_i$. The complex-valued vector $\boldsymbol{E}_0$ specifies the polarization state of the plane wave at the origin $\mathcal{O}$, and the intrinsic admittance of free space is denoted by $Y_0 = Z_0^{-1} = (\varepsilon_0/\mu_0)^{-1/2}$. The incident fields $\{\boldsymbol{E}^i, \boldsymbol{H}^i\}$ are defined in the absence of the scatterer (antenna system). On account of the linearity of Maxwell's equations, we define the total fields on receive as

$$
\begin{aligned}
\boldsymbol{E}^R &= \boldsymbol{E}^i + \boldsymbol{E}^s \\
\boldsymbol{H}^R &= \boldsymbol{H}^i + \boldsymbol{H}^s
\end{aligned}
\tag{2.39}
$$

for $\boldsymbol{r} \in \mathbb{R}^3$, where the fields $\{\boldsymbol{E}^s, \boldsymbol{H}^s\}$ that scatter from the antenna structure have been added to the incident fields and satisfy Sommerfeld's radiation condition, Eq. (2.15). The configuration in Fig. 2.4 also shows that the antenna port currents $\{I_1^R, I_2^R, \ldots, I_N^R\}$ induce the voltages $\{V_1^R, V_2^R, \ldots, V_N^R\}$ across the corresponding terminals, each of which is loaded with a finite impedance.

Figure 2.4: N-port antenna array on receive.

Inside the source-free region $\mathcal{D}_2$, the fields must satisfy (2.37), that is,

$$\oiint_{\partial\mathcal{D}_1} \left(\boldsymbol{E}^T \times \boldsymbol{H}^R - \boldsymbol{E}^R \times \boldsymbol{H}^T\right) \cdot \hat{\boldsymbol{n}}_1 \, \mathrm{d}S = \oiint_{\partial\mathcal{D}_2} \left(\boldsymbol{E}^T \times \boldsymbol{H}^R - \boldsymbol{E}^R \times \boldsymbol{H}^T\right) \cdot \hat{\boldsymbol{n}}_2 \, \mathrm{d}S. \quad (2.40)$$

The left- and right-hand sides of (2.40) will be evaluated separately and will be expressed in terms of the current excitation sources on transmit and the plane wave source on receive, respectively.

In the feed region of an antenna it is often required to interrelate the vector field description $\{\boldsymbol{E}, \boldsymbol{H}\}$ to the scalar circuit description $\{V, I\}$. For simplicity, consider the single-port feed region $\mathcal{D}_1$ in Fig. 2.5. The accessible port is excited by a current source on transmit, whereas it is terminated with a port impedance across the gap on receive. The gap size is assumed to be electrically small, so that the current distributions $\boldsymbol{J}^{T,R}$ within the cylindrically shaped gaps may be assumed uniform and directed along the axis of the cylinder as shown in Fig. 2.5; the same assumption will hold for $\boldsymbol{E}^{T,R}$.
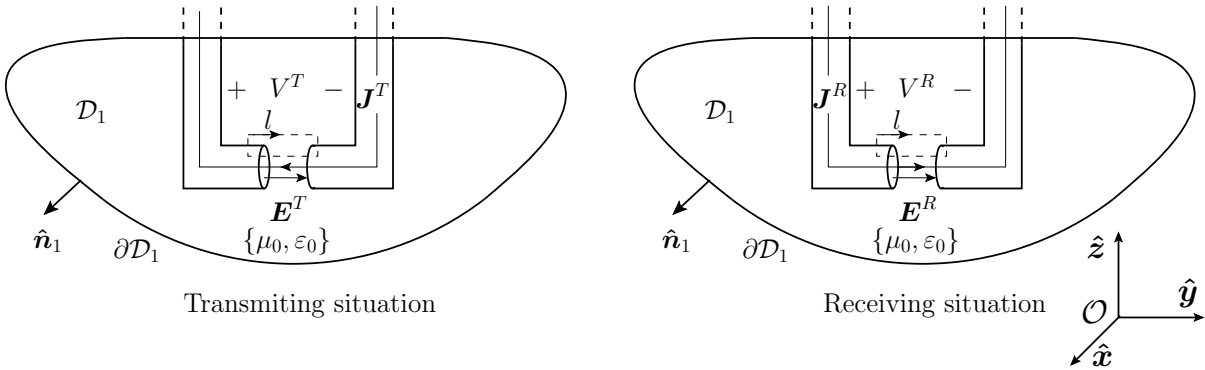
Figure 2.5: Electric fields $\boldsymbol{E}^{T,R}$ and total currents $\boldsymbol{J}^{T,R}$ defined in the feed region $\mathcal{D}_1$.

The application of (2.34) inside the volume $\mathcal{D}_1$ yields

$$\oiint_{\partial\mathcal{D}_1} \left(\boldsymbol{E}^T \times \boldsymbol{H}^R - \boldsymbol{E}^R \times \boldsymbol{H}^T\right) \cdot \hat{\boldsymbol{n}}_1 \, \mathrm{d}S = \iiint_{\mathcal{D}_1} \left(\boldsymbol{E}^R \cdot \boldsymbol{J}^T - \boldsymbol{E}^T \cdot \boldsymbol{J}^R\right) \, \mathrm{d}V \quad (2.41)$$

where $\boldsymbol{J}^{T,R}$ is the *total* current, which combines the induced and impressed current, that is, $\boldsymbol{J}^{T,R} = \sigma\boldsymbol{E}^{T,R} + \boldsymbol{J}^{T,R}_{\text{prim}}$. Next, since $\left(\boldsymbol{E}^T \times \boldsymbol{H}^R - \boldsymbol{E}^R \times \boldsymbol{H}^T\right) \cdot \hat{\boldsymbol{n}}_1 = \left(\hat{\boldsymbol{n}}_1 \times \boldsymbol{E}^T\right) \cdot \boldsymbol{H}^R - \left(\hat{\boldsymbol{n}}_1 \times \boldsymbol{E}^R\right) \cdot \boldsymbol{H}^T$, and since $\hat{\boldsymbol{n}}_1 \times \boldsymbol{E}^T = \hat{\boldsymbol{n}}_1 \times \boldsymbol{E}^R = \boldsymbol{0}$ on the perfect electrical conducting surfaces within $\mathcal{D}_1$ (vanishing integrand), the surface $\partial\mathcal{D}_1$ can be shrunk to exclude the

cylindrically shaped leads of the terminals. Furthermore, since σ and $\boldsymbol{J}^{T,R}_{\mathrm{prim}}$ are assumed to attain non-zero values only within the gaps and metallic leads, the corresponding volume $\mathcal{D}_1$ can be reduced further to contain only the gap volume representing the accessible port.

Finally, within the electrically small gap we may introduce an electric scalar potential Φ through the locally quasi-static relation $\boldsymbol{E}^{T,R} = -\boldsymbol{\nabla}\Phi$. The voltage $V^{T,R}$ is the potential difference $\Phi_b - \Phi_a$ between the terminals a and b, so that $V^{T,R} - \int_a^b \boldsymbol{E}^{T,R} \cdot \mathrm{d}\hat{\boldsymbol{y}} = 0$ along both of the contours in Fig. 2.5. Also, since the integrand on the right-hand side of (2.41) is a constant function within the gap volume, it can be further evaluated as

$$
\begin{aligned}
\iiint_{\mathcal{D}_1} \left(\boldsymbol{E}^R \cdot \boldsymbol{J}^T - \boldsymbol{E}^T \cdot \boldsymbol{J}^R\right) \mathrm{d}V &= \iiint_{\mathrm{gap}} \left(\boldsymbol{E}^R \cdot \boldsymbol{J}^T - \boldsymbol{E}^T \cdot \boldsymbol{J}^R\right) \mathrm{d}V \\
&= \int \boldsymbol{E}^R \cdot \mathrm{d}(-\hat{\boldsymbol{y}}) \iint \boldsymbol{J}^T \cdot \mathrm{d}\boldsymbol{S} - \int \boldsymbol{E}^T \cdot \mathrm{d}\hat{\boldsymbol{y}} \iint \boldsymbol{J}^R \cdot \mathrm{d}\boldsymbol{S} \\
&= -V^R I^T - V^T I^R
\end{aligned}
\tag{2.42}
$$

where we accounted for the directions of $\boldsymbol{J}^{T,R}$ when integrating the E-field inside the gap region, and where the flux of the current through a cross section of the cylinder equals the total port current I^T or I^R.

Substituting (2.42) in (2.41) leads to the following port–field relation within $\mathcal{D}_1$:

$$
\oiint_{\partial\mathcal{D}_1} \left(\boldsymbol{E}^T \times \boldsymbol{H}^R - \boldsymbol{E}^R \times \boldsymbol{H}^T\right) \cdot \hat{\boldsymbol{n}}_1 \, \mathrm{d}S = -V^R I^T - V^T I^R.
\tag{2.43}
$$

Analogously, for multi-port antennas, the left-hand side of (2.40) is evaluated as

$$
\oiint_{\partial\mathcal{D}_1} \left(\boldsymbol{E}^T \times \boldsymbol{H}^R - \boldsymbol{E}^R \times \boldsymbol{H}^T\right) \cdot \hat{\boldsymbol{n}}_1 \, \mathrm{d}S = -\sum_{m=1}^{N} \left(V^R_m I^T_m + V^T_m I^R_m\right).
\tag{2.44}
$$

The right-hand side of (2.40) is rewritten with the aid of (2.39) as

$$
\begin{aligned}
\oiint_{\partial\mathcal{D}_2} \left(\boldsymbol{E}^T \times \boldsymbol{H}^R - \boldsymbol{E}^R \times \boldsymbol{H}^T\right) \cdot \hat{\boldsymbol{n}}_2 \, \mathrm{d}S &= \oiint_{\partial\mathcal{D}_2} \left(\boldsymbol{E}^T \times \boldsymbol{H}^i - \boldsymbol{E}^i \times \boldsymbol{H}^T\right) \cdot \hat{\boldsymbol{n}}_2 \, \mathrm{d}S \\
&+ \oiint_{\partial\mathcal{D}_2} \left(\boldsymbol{E}^T \times \boldsymbol{H}^s - \boldsymbol{E}^s \times \boldsymbol{H}^T\right) \cdot \hat{\boldsymbol{n}}_2 \, \mathrm{d}S.
\end{aligned}
\tag{2.45}
$$

Substituting $b = T$ and $a = s$ in (2.37), and by applying this theorem outside $\mathcal{D}_2$, leads to the conclusion that, on account of the radiation condition, the surface integral over the

scattered and transmitted fields at an imaginary closed surface at infinity amounts to zero. Hence, the second term on the right-hand side of (2.45) must vanish as well. Using this, and substituting (2.38) in (2.45), one obtains

$$
\oiint_{\partial \mathcal{D}_2} \left(\boldsymbol{E}^T \times \boldsymbol{H}^i - \boldsymbol{E}^i \times \boldsymbol{H}^T \right) \cdot \hat{\boldsymbol{n}}_2 \, \mathrm{d}S = \oiint_{\partial \mathcal{D}_2} \boldsymbol{H}^i \cdot \left(\hat{\boldsymbol{n}}_2 \times \boldsymbol{E}^T \right) + \boldsymbol{E}^i \cdot \left(\hat{\boldsymbol{n}}_2 \times \boldsymbol{H}^T \right) \, \mathrm{d}S
$$

$$
= Y_0 \oiint_{\partial \mathcal{D}_2} \left([\boldsymbol{E}_0 \times \hat{\boldsymbol{r}}_i] \cdot [\hat{\boldsymbol{n}}_2 \times \boldsymbol{E}^T] + \boldsymbol{E}_0 \cdot [\hat{\boldsymbol{n}}_2 \times Z_0 \boldsymbol{H}^T] \right) e^{j(\boldsymbol{k}_0 \cdot \boldsymbol{r})} \, \mathrm{d}S
$$

$$
= Y_0 \boldsymbol{E}_0 \cdot \left(\hat{\boldsymbol{r}}_i \times \oiint_{\partial \mathcal{D}_2} \left([\hat{\boldsymbol{n}}_2 \times \boldsymbol{E}^T] - \hat{\boldsymbol{r}}_i \times [\hat{\boldsymbol{n}}_2 \times Z_0 \boldsymbol{H}^T] \right) e^{j(\boldsymbol{k}_0 \cdot \boldsymbol{r})} \, \mathrm{d}S \right) \tag{2.46}
$$

where we applied the cyclic rotation

$$
[\boldsymbol{E}_0 \times \hat{\boldsymbol{r}}_i] \cdot [\hat{\boldsymbol{n}}_2 \times \boldsymbol{E}^T] = \boldsymbol{E}_0 \cdot \left(\hat{\boldsymbol{r}}_i \times [\hat{\boldsymbol{n}}_2 \times \boldsymbol{E}^T] \right). \tag{2.47}
$$

Moreover, we used that, for an arbitrary vector $\boldsymbol{B}$,

$$
\boldsymbol{E}_0 \cdot [\hat{\boldsymbol{r}}_i \times (\hat{\boldsymbol{r}}_i \times \boldsymbol{B})] = \boldsymbol{E}_0 \cdot (\hat{\boldsymbol{r}}_i \cdot \boldsymbol{B})\hat{\boldsymbol{r}}_i - \boldsymbol{E}_0 \cdot (\hat{\boldsymbol{r}}_i \cdot \hat{\boldsymbol{r}}_i)\boldsymbol{B} = -\boldsymbol{E}_0 \cdot \boldsymbol{B} \tag{2.48}
$$

since $\boldsymbol{E}_0 \cdot \hat{\boldsymbol{r}}_i = 0$ and $\hat{\boldsymbol{r}}_i \cdot \hat{\boldsymbol{r}}_i = 1$.

Finally, one can rewrite (2.46) as

$$
\oiint_{\partial \mathcal{D}_2} \left(\boldsymbol{E}^T \times \boldsymbol{H}^i - \boldsymbol{E}^i \times \boldsymbol{H}^T \right) \cdot \hat{\boldsymbol{n}}_2 \, \mathrm{d}S = -\frac{1}{j\omega\mu_0} \boldsymbol{E}_0 \cdot \boldsymbol{e}^T \tag{2.49}
$$

with

$$
\boldsymbol{e}^T = -jk_0 \hat{\boldsymbol{r}}_i \times \oiint_{\partial \mathcal{D}_2} \left([\hat{\boldsymbol{n}}_2 \times \boldsymbol{E}^T] - \hat{\boldsymbol{r}}_i \times [\hat{\boldsymbol{n}}_2 \times Z_0 \boldsymbol{H}^T] \right) e^{j(\boldsymbol{k}_0 \cdot \boldsymbol{r})} \, \mathrm{d}S. \tag{2.50}
$$

The far-field amplitude vector $\boldsymbol{e}^T(\hat{\boldsymbol{r}}_i)$ is a result of a surface integration of the tangential parts of both the electric and magnetic fields on $\partial \mathcal{D}_2$. In fact, the electric field $\boldsymbol{E}^T(r, \hat{\boldsymbol{r}}_i) = \boldsymbol{e}^T \exp\left(-jk_0 r\right)/(4\pi r)$ represents the electric far-field function that has been generated by these tangential field components on $\partial \mathcal{D}_2$ and serves as a mathematical realization of Huygens' surface equivalence principle, evaluated in the far field. The general (Fresnel) form is known as Franz' formula (1948), see e.g. the exposition in [35], where a comparison is made with the well-known Stratton-Chu formulas [36, pp. 464–470].

Equations (2.49) and (2.45) are combined and subsequently substituted, along with (2.44), in Eq. (2.40) to arrive at

$$\sum_{m=1}^{N} \left(V_m^R I_m^T + V_m^T I_m^R\right) = \frac{1}{j\omega\mu_0} \boldsymbol{E}_0 \cdot \boldsymbol{e}^T. \tag{2.51}$$

Next, the far-field pattern $\boldsymbol{e}^T$ can be decomposed into N antenna element patterns according to $\boldsymbol{e}^T = \sum_{m=1}^{N} \boldsymbol{e}_m^T I_m^T$. In addition, one can write that $V_m^T = \sum_{n=1}^{N} Z_{mn}^{\mathrm{ant}} I_n^T$ for $m = 1\ldots N$, where Z_{mn}^{ant} denotes an element of the antenna input impedance matrix. Hence, upon substituting these expressions in (2.51), and rearranging the result, one obtains

$$\sum_{m=1}^{N}\sum_{n=1}^{N} \left(V_m^R I_m^T + Z_{mn}^{\mathrm{ant}} I_n^T I_m^R\right) = \frac{1}{j\omega\mu_0} \boldsymbol{E}_0 \cdot \sum_{m=1}^{N} \boldsymbol{e}_m^T(\hat{\boldsymbol{r}}_i) I_m^T$$

$$\sum_{n=1}^{N}\sum_{m=1}^{N} \left(V_m^R I_m^T + Z_{nm}^{\mathrm{ant}} I_m^T I_n^R\right) = \frac{1}{j\omega\mu_0} \sum_{m=1}^{N} \left[\boldsymbol{E}_0 \cdot \boldsymbol{e}_m^T(\hat{\boldsymbol{r}}_i)\right] I_m^T$$

$$\sum_{m=1}^{N} \left(\sum_{n=1}^{N} Z_{nm}^{\mathrm{ant}} I_n^R + V_m^R\right) I_m^T = \frac{1}{j\omega\mu_0} \sum_{m=1}^{N} \left[\boldsymbol{E}_0 \cdot \boldsymbol{e}_m^T(\hat{\boldsymbol{r}}_i)\right] I_m^T. \tag{2.52}$$

Equation (2.52) should hold for any choice of $\{I_m^T\}$, so that for each linear combination of port currents

$$\sum_{n=1}^{N} Z_{nm}^{\mathrm{ant}} I_n^R + V_m^R = \frac{1}{j\omega\mu_0} \boldsymbol{E}_0 \cdot \boldsymbol{e}_m^T(\hat{\boldsymbol{r}}_i), \qquad \text{for } m = 1\ldots N. \tag{2.53}$$

This equation is recognized as a Thévenin circuit description. The interpretation of this equation is graphically illustrated in Fig. 2.6. It should be noted that the transpose of the antenna impedance matrix $\mathbf{Z}^{\mathrm{ant}}$ is taken and that the mth open-circuit terminal voltage on receive is specified as

$$V_m^{\mathrm{oc}} = (j\omega\mu_0)^{-1} \boldsymbol{E}_0 \cdot \boldsymbol{e}_m^T(\hat{\boldsymbol{r}}_i). \tag{2.54}$$

Each voltage generator is an elementary source in the Thévenin network and this voltage is therefore commonly referred to as the "equivalent electromotive force". We conclude by stating that $\boldsymbol{e}_m^T$ can be deduced from the elemental far-field pattern $\boldsymbol{E}_m^T$ through the relation $\boldsymbol{e}_m^T = 4\pi \exp\left(jk_0\right)\boldsymbol{E}_m^T$, with the far-field distance $r = 1$ m. This normalized pattern
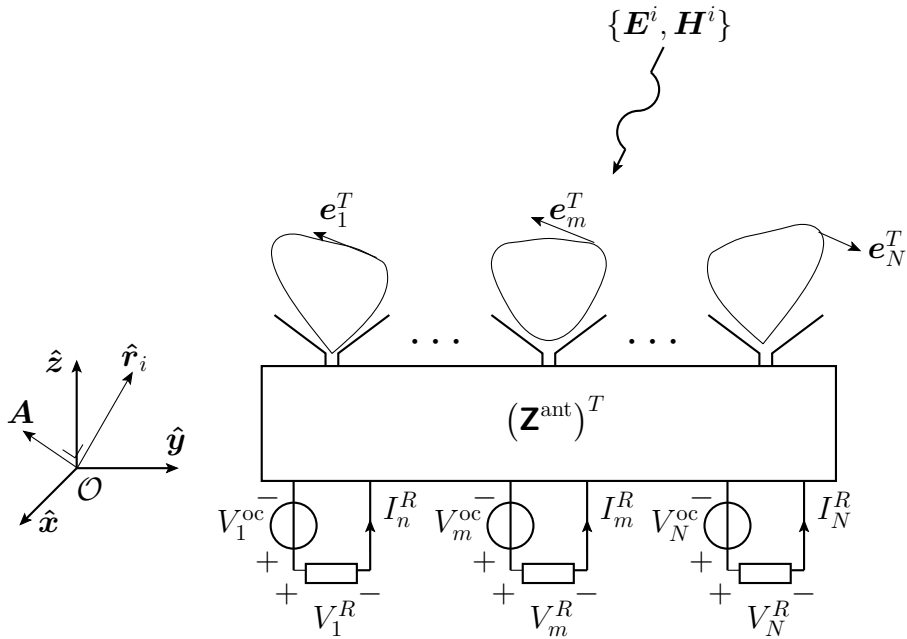
Figure 2.6: Thévenin circuit representation for an N-port terminated antenna array on receive.

is obtained by exciting the mth element with an impressed current of 1 Ampère, while the other ports are open-circuited.

It is important to realize that the Thévenin circuit representation of an array on receive can readily be added to the library of standard multi-port components available to microwave circuit simulators. Furthermore, because the internal voltage sources are a function of the plane-wave field that is incident upon the array, also the received noise power as a result of an external noise field, such as the cosmic microwave background noise, can be represented by the internal voltage sources of the Thévenin circuit. This property will be further elaborated in Chapter 5, where the external noise field in the far-field region of the antenna system is described in terms of a stochastic plane-wave spectrum which is generated by a black body. In that chapter, we will also present an analysis methodology to analyze the receiver sensitivity of antenna array systems.

Chapter 3

Galerkin's Moment Method for the Analysis of Antennas

In this chapter, a numerical method is presented for computing the electromagnetic radiation and impedance characteristics of dielectric-free antenna structures[1]. The volumetric currents inside electrically thin and imperfectly conducting metals will be modeled by average surface currents on infinitely thin sheets. After a surface impedance boundary condition is imposed for the total electric field on these sheets, an integro-differential equation is formulated, discretized and solved to subsequently obtain the sheet currents, antenna input impedance matrix, and element radiation patterns for various numerical examples.

3.1   Surface Impedance Boundary Condition

The numerical computation of volumetric currents inside imperfectly conducting surfaces of finite thickness, as e.g. shown in Fig. 3.1(a), is a burdensome task when straightforward volume integral equation formulations are employed that require fine spatial discretizations. The computational burden can be significantly relaxed when the conductor can be

---

[1]This chapter is partly based on:

[37]: <u>R. Maaskant</u>, D. J. Bekers, M. J. Arts, W. A. van Cappellen, and M. V. Ivashina, "Evaluation of the radiation efficiency and the noise temperature of low-loss antennas," *IEEE Antennas Wireless Propag. Lett.*, vol. 8, pp. 1536-1225, Jan. 2009.

[38]: <u>R. Maaskant</u> and M. J. Arts, "Reconsidering the voltage-gap source model used in moment methods," *IEEE Antennas Propag. Mag.*, accepted for publication.

approximated by an infinitesimally thin impedance sheet supporting an average surface current which can be determined through solving a surface integral equation. The pertaining configuration, which entails both geometrical and electrical approximations, has been depicted in Fig. 3.1(b).
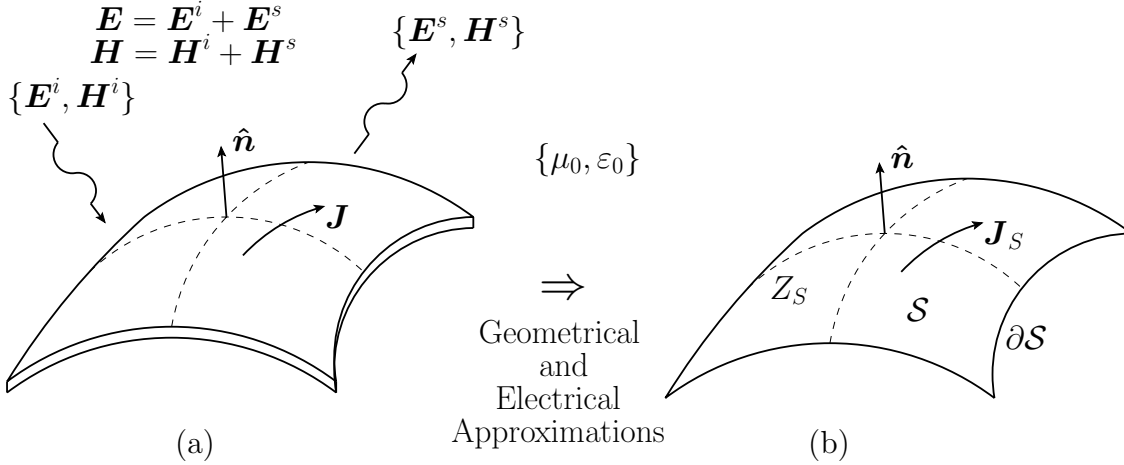
Figure 3.1: Induced conductor current due to an incident electromagnetic field: (a) the volumetric current $\boldsymbol{J}$ in the actual configuration; (b) the averaged surface current $\boldsymbol{J}_S$ supported by a sheet with an appropriate surface impedance $Z_S(\boldsymbol{r})$.

Similar to the interface boundary conditions in (2.11), the impedance sheet is also characterized by: (i) a jump discontinuity of the tangential magnetic field components across the sheet interface, and; (ii) continuous tangential components of the electric field (no magnetic currents), i.e.,

$$\hat{\boldsymbol{n}} \times \boldsymbol{E}_2 - \hat{\boldsymbol{n}} \times \boldsymbol{E}_1 = \boldsymbol{0} \tag{3.1a}$$

$$\hat{\boldsymbol{n}} \times \boldsymbol{H}_2 - \hat{\boldsymbol{n}} \times \boldsymbol{H}_1 = \boldsymbol{J}_S \tag{3.1b}$$

where $\{\boldsymbol{E}_1, \boldsymbol{H}_1\}$ and $\{\boldsymbol{E}_2, \boldsymbol{H}_2\}$ are the fields on the negative and positive sides of the outward unit vector normal to the surface $\mathcal{S}$, respectively. In addition to (3.1), the amplitude of the tangential electric field $\boldsymbol{E}_1|_{\tan} = \boldsymbol{E}_2|_{\tan}$ at the sheet interface is required to be proportional to the sheet current $\boldsymbol{J}_S$. The complex-valued surface impedance Z_S represents this proportionality constant in Ohms per square, and is known to satisfy [39]

$$-\hat{\boldsymbol{n}} \times (\hat{\boldsymbol{n}} \times \boldsymbol{E}_1) = \boldsymbol{E}_1|_{\tan} = \boldsymbol{E}_2|_{\tan} = Z_S \boldsymbol{J}_S. \tag{3.2}$$

3.2 Determination of the Sheet Impedance Z_S

3.2.1 Field Impedance Relations for Slab Configurations

An appropriate formula for the sheet impedance Z_S will be derived rigorously and pertains to the fields across the boundaries of a material slab region (see also [40, Chapter 2]). The mathematical and physical approximations that are subsequently required to arrive at an effective surface as shown in Fig. 3.1(b), as well as at the effective boundary condition (3.2), will be introduced systematically.

Consider Fig. 3.2, which illustrates the locally enlarged cross section of Fig. 3.1(a). We will assume that the smallest curvature radius $R_{\min}$ of the actual curved surface in Fig. 3.1 is much larger than the conductor thickness d, i.e., $R_{\min} \gg d$. This implies that the surface is locally planar as well as that the fields within this slab are primarily determined by the tangential components of the fields along the bottom and top surfaces (locality principle, end-effects neglected).
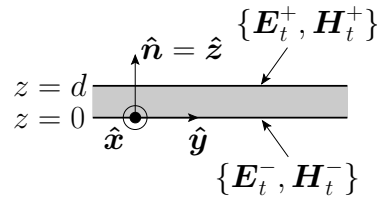
Figure 3.2: Locally enlarged cross section of the conducting slab.

Inside the conducting slab region, the electromagnetic fields satisfy

$$\boldsymbol{\nabla} \times \boldsymbol{E} = -j\omega\mu\boldsymbol{H}, \qquad \boldsymbol{\nabla} \times \boldsymbol{H} = j\omega\varepsilon\boldsymbol{E}. \tag{3.3}$$

It is convenient to decompose the fields and the gradient operator into tangential and normal components with respect to the conductor surfaces, that is,

$$\boldsymbol{E} = \boldsymbol{E}_t + E_z\hat{\boldsymbol{z}}, \qquad \boldsymbol{H} = \boldsymbol{H}_t + H_z\hat{\boldsymbol{z}}, \qquad \boldsymbol{\nabla} = \boldsymbol{\nabla}_t + \partial_z\hat{\boldsymbol{z}} \tag{3.4}$$

which can be substituted in the first equation of (3.3) to yield

$$\boldsymbol{\nabla}_t \times \boldsymbol{E}_t + \partial_z\hat{\boldsymbol{z}} \times \boldsymbol{E}_t + \boldsymbol{\nabla}_t \times E_z\hat{\boldsymbol{z}} = -j\omega\mu\boldsymbol{H}_t - j\omega\mu H_z\hat{\boldsymbol{z}} \tag{3.5}$$

where we have used that $\partial_z E_z \hat{\boldsymbol{z}} \times \hat{\boldsymbol{z}} = \mathbf{0}$. By collecting the transverse and normal field components, one obtains

$$H_z \hat{\boldsymbol{z}} = -(j\omega\mu)^{-1} \boldsymbol{\nabla}_t \times \boldsymbol{E}_t \tag{3.6a}$$

$$\boldsymbol{H}_t = -(j\omega\mu)^{-1} \left(\partial_z \hat{\boldsymbol{z}} \times \boldsymbol{E}_t + \boldsymbol{\nabla}_t \times E_z \hat{\boldsymbol{z}}\right). \tag{3.6b}$$

Similarly, using duality, we find

$$E_z \hat{\boldsymbol{z}} = (j\omega\varepsilon)^{-1} \boldsymbol{\nabla}_t \times \boldsymbol{H}_t \tag{3.7a}$$

$$\boldsymbol{E}_t = (j\omega\varepsilon)^{-1} \left(\partial_z \hat{\boldsymbol{z}} \times \boldsymbol{H}_t + \boldsymbol{\nabla}_t \times H_z \hat{\boldsymbol{z}}\right). \tag{3.7b}$$

Substituting (3.7a) in (3.6b) yields

$$\partial z \hat{\boldsymbol{z}} \times \boldsymbol{E}_t = -j\omega\mu \boldsymbol{H}_t - (j\omega\varepsilon)^{-1} \boldsymbol{\nabla}_t \times (\boldsymbol{\nabla}_t \times \boldsymbol{H}_t) \tag{3.8}$$

which is locally valid inside the conducting slab. Next, Eq. (3.8) is averaged over the conductor thickness d by integrating the fields over the conductor thickness d and subsequently dividing this integral by d. This yields

$$\frac{\hat{\boldsymbol{z}} \times \boldsymbol{E}_t|_{z=d} - \hat{\boldsymbol{z}} \times \boldsymbol{E}_t|_{z=0}}{d} = -\frac{j\omega\mu}{d} \int_0^d \boldsymbol{H}_t \, \mathrm{d}z - \frac{1}{j\omega\varepsilon d} \boldsymbol{\nabla}_t \times \left(\boldsymbol{\nabla}_t \times \int_0^d \boldsymbol{H}_t \, \mathrm{d}z\right). \tag{3.9}$$

Upon taking the cross product of (3.9) with $-\hat{\boldsymbol{z}}$, and by introducing the short-hand notations $\boldsymbol{E}_t|_{z=d} = \boldsymbol{E}_t^+$ and $\boldsymbol{E}_t|_{z=0} = \boldsymbol{E}_t^-$, and subsequently making use of the vector identity

$$-\boldsymbol{z} \times \boldsymbol{\nabla}_t \times (\boldsymbol{\nabla}_t \times \boldsymbol{A}_t) = \boldsymbol{\nabla}_t \boldsymbol{\nabla}_t \cdot (\hat{\boldsymbol{z}} \times \boldsymbol{A}_t) \tag{3.10}$$

one obtains the compact form

$$\boldsymbol{E}_t^+ - \boldsymbol{E}_t^- = j\omega\mu \left(\overline{\overline{\mathcal{I}}}_t + \frac{\boldsymbol{\nabla}_t \boldsymbol{\nabla}_t}{k^2}\right) \cdot \left(\hat{\boldsymbol{z}} \times \int_0^d \boldsymbol{H}_t \, \mathrm{d}z\right) \tag{3.11}$$

where dyadic $\overline{\overline{\mathcal{I}}}_t$ is the 2×2 unit diagonal matrix. The objective is to express (3.11) solely in terms of the tangential field components at $z = 0$ and $z = d$. To this end, we remark that the integral in (3.11) can be evaluated analytically when plane-wave fields are considered, or, more generally, for a spectral plane-wave representation of the fields.

A plane-wave representation for the transverse fields is obtained through the application of the 2-D spatial Fourier transform pair

$$\breve{\boldsymbol{F}}_t(\boldsymbol{k}_t, z) = FT\{\boldsymbol{F}_t(\boldsymbol{r})\} = \iint\limits_{-\infty}^{\infty} \boldsymbol{F}_t(\boldsymbol{r}) e^{j\boldsymbol{k}_t \cdot \boldsymbol{r}} \, \mathrm{d}x \, \mathrm{d}y \tag{3.12a}$$

$$\boldsymbol{F}_t(\boldsymbol{r}) = FT^{-1}\{\breve{\boldsymbol{F}}_t(\boldsymbol{k}_t, z)\} = \frac{1}{4\pi^2} \iint\limits_{-\infty}^{\infty} \breve{\boldsymbol{F}}_t(\boldsymbol{k}_t, z) e^{-j\boldsymbol{k}_t \cdot \boldsymbol{r}} \, \mathrm{d}\boldsymbol{k}_t \tag{3.12b}$$

with $\boldsymbol{k}_t = k_x \hat{\boldsymbol{x}} + k_y \hat{\boldsymbol{y}}$. Note that the following useful properties hold:

$$FT\{\boldsymbol{\nabla}_t \cdot \boldsymbol{F}_t(\boldsymbol{r})\} = -j\boldsymbol{k}_t \cdot \breve{\boldsymbol{F}}_t(\boldsymbol{k}_t, z) \tag{3.13a}$$

$$FT\{\boldsymbol{\nabla}_t^2 \boldsymbol{F}_t(\boldsymbol{r})\} = -k_t^2 \breve{\boldsymbol{F}}_t(\boldsymbol{k}_t, z) \tag{3.13b}$$

$$FT\{\boldsymbol{\nabla}^2 \boldsymbol{F}_t(\boldsymbol{r})\} = \left(-k_t^2 + \partial_z^2\right) \breve{\boldsymbol{F}}_t(\boldsymbol{k}_t, z) \tag{3.13c}$$

The magnetic field $\boldsymbol{H}_t$ in the interior slab region satisfies the source-free Helmholtz equation $\nabla^2 \boldsymbol{H}_t + k^2 \boldsymbol{H}_t = \boldsymbol{0}$. Hence, in the spectral domain, this equation transforms into

$$\partial_z^2 \breve{\boldsymbol{H}}_t + k_z^2 \breve{\boldsymbol{H}}_t = 0 \tag{3.14}$$

where $k_z^2 = k^2 - k_t^2$. The general solution to (3.14) is given as

$$\breve{\boldsymbol{H}}_t(z) = \boldsymbol{A}_t e^{-jk_z z} + \boldsymbol{B}_t e^{jk_z z} \tag{3.15}$$

where $\boldsymbol{A}_t$ and $\boldsymbol{B}_t$ are vectorial constants that can be determined through the boundary conditions

$$\breve{\boldsymbol{H}}_t(d) = \breve{\boldsymbol{H}}_t^+, \qquad \breve{\boldsymbol{H}}_t(0) = \breve{\boldsymbol{H}}_t^-. \tag{3.16}$$

This yields

$$\boldsymbol{A}_t = \frac{1}{2j} \left(\frac{e^{jk_z d} \breve{\boldsymbol{H}}_t^- - \breve{\boldsymbol{H}}_t^+}{\sin(k_z d)} \right), \qquad \boldsymbol{B}_t = \frac{1}{2j} \left(\frac{\breve{\boldsymbol{H}}_t^+ - e^{-jk_z d} \breve{\boldsymbol{H}}_t^-}{\sin(k_z d)} \right). \tag{3.17}$$

With the aid of this result, the integral of the transverse magnetic field components in (3.15) can be evaluated analytically, i.e.,

$$\int_0^d \breve{\boldsymbol{H}}_t \, \mathrm{d}z = \frac{1}{jk_z} \left[\boldsymbol{A}_t \left(1 - e^{-jk_z d}\right) + \boldsymbol{B}_t \left(e^{jk_z d} - 1\right) \right]$$

$$= \frac{1 - \cos(k_z d)}{k_z \sin(k_z d)} \left(\breve{\boldsymbol{H}}_t^+ + \breve{\boldsymbol{H}}_t^- \right) = \frac{\tan(k_z d/2)}{k_z} \left(\breve{\boldsymbol{H}}_t^+ + \breve{\boldsymbol{H}}_t^- \right) \tag{3.18}$$

where the constants $\boldsymbol{A}_t$ and $\boldsymbol{B}_t$ have been substituted. Taking the spectral representation of (3.11), and by substituting (3.18) in the corresponding result, gives

$$\breve{\boldsymbol{E}}_t^+ - \breve{\boldsymbol{E}}_t^- = j\omega\mu f \overline{\overline{A}} \cdot \hat{\boldsymbol{z}} \times \left(\breve{\boldsymbol{H}}_t^+ + \breve{\boldsymbol{H}}_t^- \right) \tag{3.19a}$$

$$\breve{\boldsymbol{H}}_t^+ - \breve{\boldsymbol{H}}_t^- = -j\omega\varepsilon f \overline{\overline{A}} \cdot \hat{\boldsymbol{z}} \times \left(\breve{\boldsymbol{E}}_t^+ + \breve{\boldsymbol{E}}_t^- \right) \tag{3.19b}$$

where the latter expression has been obtained through duality, and where the dyadic

$$\overline{\overline{A}} = \left(\overline{\overline{I}}_t - \frac{\boldsymbol{k}_t \boldsymbol{k}_t}{k^2} \right) \qquad \text{and function} \qquad f(k_z, d) = \frac{\tan(k_z d/2)}{k_z}. \tag{3.20}$$

Equations (3.19) can be written in matrix form by using impedance operators which relate $\breve{\boldsymbol{E}}_t^+$ and $\breve{\boldsymbol{E}}_t^-$ (equivalent vector voltages) to both $\hat{\boldsymbol{z}} \times \breve{\boldsymbol{H}}_t^+$ and $\hat{\boldsymbol{z}} \times \breve{\boldsymbol{H}}_t^-$ (equivalent vector currents). To this end, we multiply (3.19b) by $(j\omega\varepsilon f)^{-1} \hat{\boldsymbol{z}} \times \overline{\overline{A}}^{-1}$, which yields

$$(j\omega\varepsilon f)^{-1} \hat{\boldsymbol{z}} \times \overline{\overline{A}}^{-1} \cdot \left(\breve{\boldsymbol{H}}_t^+ - \breve{\boldsymbol{H}}_t^- \right) = \breve{\boldsymbol{E}}_t^+ + \breve{\boldsymbol{E}}_t^- \tag{3.21}$$

and then add this equation to (3.19a), to obtain

$$2\breve{\boldsymbol{E}}_t^+ = j\omega\mu f \overline{\overline{A}} \cdot \hat{\boldsymbol{z}} \times \left(\breve{\boldsymbol{H}}_t^+ + \breve{\boldsymbol{H}}_t^- \right) + (j\omega\varepsilon f)^{-1} \hat{\boldsymbol{z}} \times \overline{\overline{A}}^{-1} \cdot \left(\breve{\boldsymbol{H}}_t^+ - \breve{\boldsymbol{H}}_t^- \right) \tag{3.22}$$

with the dyadic (see Appendix A)

$$\overline{\overline{A}}^{-1} = k_z^{-2} \left[k^2 \overline{\overline{I}}_t - (\hat{\boldsymbol{z}} \times \boldsymbol{k}_t)(\hat{\boldsymbol{z}} \times \boldsymbol{k}_t) \right]. \tag{3.23}$$

Substituting (3.23) in (3.22) and using the identities

$$\hat{\boldsymbol{z}} \times (\hat{\boldsymbol{z}} \times \boldsymbol{k}_t) = -\boldsymbol{k}_t \tag{3.24a}$$

$$(\hat{\boldsymbol{z}} \times \boldsymbol{k}_t) \cdot \left(\breve{\boldsymbol{H}}_t^+ - \breve{\boldsymbol{H}}_t^- \right) = -\boldsymbol{k}_t \cdot \hat{\boldsymbol{z}} \times \left(\breve{\boldsymbol{H}}_t^+ - \breve{\boldsymbol{H}}_t^- \right), \tag{3.24b}$$

one observes that the last term in (3.22) can be expressed as

$$
\begin{aligned}
\hat{\boldsymbol{z}} \times \overline{\overline{A}}^{-1} \cdot \left(\breve{\boldsymbol{H}}_t^+ - \breve{\boldsymbol{H}}_t^- \right) &= \frac{k^2}{k_z^2} \hat{\boldsymbol{z}} \times \left(\breve{\boldsymbol{H}}_t^+ - \breve{\boldsymbol{H}}_t^- \right) - \frac{1}{k_z^2} \boldsymbol{k}_t (\hat{\boldsymbol{z}} \times \boldsymbol{k}_t) \cdot \left(\breve{\boldsymbol{H}}_t^+ - \breve{\boldsymbol{H}}_t^- \right) \\
&= \frac{k^2}{k_z^2} \left(\overline{\overline{I}}_t - \frac{\boldsymbol{k}_t \boldsymbol{k}_t}{k^2} \right) \cdot \hat{\boldsymbol{z}} \times \left(\breve{\boldsymbol{H}}_t^+ - \breve{\boldsymbol{H}}_t^- \right) \\
&= \frac{k^2}{k_z^2} \overline{\overline{A}} \cdot \hat{\boldsymbol{z}} \times \left(\breve{\boldsymbol{H}}_t^+ - \breve{\boldsymbol{H}}_t^- \right).
\end{aligned} \tag{3.25}
$$

By substituting this latter result in (3.22), and by collecting the $\breve{\boldsymbol{H}}_t^+$ and $\breve{\boldsymbol{H}}_t^-$ terms, one arrives at

$$2\breve{\boldsymbol{E}}_t^+ = j\omega\mu f\left(1 - \frac{1}{k_z^2 f^2}\right)\overline{\overline{A}}\cdot\hat{\boldsymbol{z}}\times\breve{\boldsymbol{H}}_t^+ + j\omega\mu f\left(1 + \frac{1}{k_z^2 f^2}\right)\overline{\overline{A}}\cdot\hat{\boldsymbol{z}}\times\breve{\boldsymbol{H}}_t^- \tag{3.26}$$

where

$$f\left(1 - \frac{1}{k_z^2 f^2}\right) = \frac{\sin^2(k_z d/2) - \cos^2(k_z d/2)}{k_z\cos(k_z d/2)\sin(k_z d/2)} = \frac{-\cos(k_z d)}{k_z\sin(k_z d)/2} = -\frac{2}{k_z\tan(k_z d)} \tag{3.27}$$

and

$$f\left(1 + \frac{1}{k_z^2 f^2}\right) = \frac{\sin^2(k_z d/2) + \cos^2(k_z d/2)}{k_z\cos(k_z d/2)\sin(k_z d/2)} = \frac{1}{k_z\sin(k_z d)/2} = \frac{2}{k_z\sin(k_z d)}. \tag{3.28}$$

Hence, in matrix notation, we find that

$$\breve{\boldsymbol{E}}_t^+ = \overline{\overline{Z}}_{11}\cdot\hat{\boldsymbol{z}}\times\breve{\boldsymbol{H}}_t^+ + \overline{\overline{Z}}_{12}\cdot\hat{\boldsymbol{z}}\times\breve{\boldsymbol{H}}_t^- \tag{3.29}$$

where the impedance operators are given as

$$\overline{\overline{Z}}_{11} = -j\frac{Zk}{k_z}\frac{1}{\tan(k_z d)}\overline{\overline{A}} \qquad \text{and} \qquad \overline{\overline{Z}}_{12} = j\frac{Zk}{k_z}\frac{1}{\sin(k_z d)}\overline{\overline{A}} \tag{3.30}$$

with the wave impedance of the medium defined by $Z = \sqrt{\mu/\varepsilon}$. Analogously, one can find that

$$\breve{\boldsymbol{E}}_t^- = \overline{\overline{Z}}_{21}\cdot\hat{\boldsymbol{z}}\times\breve{\boldsymbol{H}}_t^+ + \overline{\overline{Z}}_{22}\cdot\hat{\boldsymbol{z}}\times\breve{\boldsymbol{H}}_t^- \tag{3.31}$$

where $\overline{\overline{Z}}_{21} = -\overline{\overline{Z}}_{12}$ and $\overline{\overline{Z}}_{22} = -\overline{\overline{Z}}_{11}$. Both minus signs can be explained from symmetry and the orientation of $\hat{\boldsymbol{z}}$.

From the above elimination procedure, one finally obtains

$$\begin{pmatrix} \breve{\boldsymbol{E}}_t^+ \\ \breve{\boldsymbol{E}}_t^- \end{pmatrix} = \begin{pmatrix} \overline{\overline{Z}}_{11} & \overline{\overline{Z}}_{12} \\ \overline{\overline{Z}}_{21} & \overline{\overline{Z}}_{22} \end{pmatrix}\begin{pmatrix} \hat{\boldsymbol{z}}\times\breve{\boldsymbol{H}}_t^+ \\ \hat{\boldsymbol{z}}\times\breve{\boldsymbol{H}}_t^- \end{pmatrix} \tag{3.32}$$

with

$$\overline{\overline{Z}}_{11} = -\overline{\overline{Z}}_{22} = -j\frac{Zk}{k_z}\frac{1}{\tan(k_z d)}\overline{\overline{A}} \tag{3.33a}$$

$$\overline{\overline{Z}}_{12} = -\overline{\overline{Z}}_{21} = j\frac{Zk}{k_z}\frac{1}{\sin(k_z d)}\overline{\overline{A}} \tag{3.33b}$$

where $Z = \sqrt{\mu/\varepsilon}$ is the wave impedance of the slab medium. It is evident that for each spectral component a different k_z has to be computed, however; it will be shown in the next section that only one spectral component is of interest in the case of good conductors and a field distribution which can locally be represented by a plane wave.

3.2.2   Good Conductors Fulfilling the Condition $\sigma \gg \omega\varepsilon_0|\varepsilon_r|$

Equation (3.32) can be approximated such that it solely applies to materials for which $\sigma \gg \omega\varepsilon_0|\varepsilon_r|$ (electrically good conductors). Furthermore, the curvature radius of the phase front of the incident field will be assumed much larger than the skin depth of the material, and because $\boldsymbol{k}_t$ has to be continuous across a boundary surface (*cf.* Snell's law), $k_t = \|\boldsymbol{k}_t\|_2$ will be smaller than the wavenumber k_0 of the surrounding free-space medium, i.e., $k_t \leq k_0$. Furthermore, for good conductors, one has that $k_0 \ll |k|$, so that $k_t \ll |k|$. This implies that $\overline{\overline{A}} \approx \overline{\overline{I}}_t$ and $k_z = \sqrt{k^2 - k_t^2} \approx k$, which simplifies the analysis to the case of normal incidence (Leontovich IBC). Equation (3.32) then reads

$$\begin{pmatrix} \breve{\boldsymbol{E}}_t^+ \\ \breve{\boldsymbol{E}}_t^- \end{pmatrix} = \begin{pmatrix} Z_{11} & Z_{12} \\ Z_{21} & Z_{22} \end{pmatrix} \begin{pmatrix} \hat{\boldsymbol{z}} \times \breve{\boldsymbol{H}}_t^+ \\ \hat{\boldsymbol{z}} \times \breve{\boldsymbol{H}}_t^- \end{pmatrix} \tag{3.34}$$

with

$$Z_{11} = -Z_{22} = \frac{-jZ}{\tan(kd)} \quad \text{and} \quad Z_{12} = -Z_{21} = \frac{jZ}{\sin(kd)}. \tag{3.35}$$

In addition, for good conductors one may write that

$$Z = \sqrt{\frac{j\omega\mu}{\sigma + j\omega\varepsilon_0\varepsilon_r}} \approx \sqrt{j\frac{\omega\mu}{\sigma}} = \sqrt{\frac{\omega\mu}{2\sigma}}(1+j) = \frac{1+j}{\delta\sigma} \tag{3.36}$$

and that

$$k = \omega\sqrt{\mu\varepsilon} = \omega\sqrt{\mu\left(\varepsilon_0\varepsilon_r - j\frac{\sigma}{\omega}\right)} \approx (1-j)\sqrt{\frac{\omega\mu\sigma}{2}} = \frac{1-j}{\delta} \tag{3.37}$$

where δ is the skin depth of the metal defined by

$$\delta = \sqrt{\frac{2}{\omega\mu\sigma}} \tag{3.38}$$

so that the impedance matrix elements in (3.35) can be approximated as

$$Z_{11} = -Z_{22} \approx \frac{1-j}{\delta\sigma\tan[(1-j)\,d/\delta]} \quad \text{and} \quad Z_{12} = -Z_{21} \approx -\frac{1-j}{\delta\sigma\sin[(1-j)\,d/\delta]}. \tag{3.39}$$

From (3.34) and (3.39) it follows that, in the spatial domain,

$$\boldsymbol{E}_t^+ = \frac{1-j}{\delta\sigma\tan[(1-j)\,d/\delta]}\left[\hat{\boldsymbol{z}} \times \boldsymbol{H}_t^+ - \frac{1}{\cos[(1-j)d/\delta]}\hat{\boldsymbol{z}} \times \boldsymbol{H}_t^-\right] \tag{3.40a}$$

$$\boldsymbol{E}_t^- = \frac{1-j}{\delta\sigma\tan[(1-j)\,d/\delta]}\left[\frac{1}{\cos[(1-j)d/\delta]}\hat{\boldsymbol{z}} \times \boldsymbol{H}_t^+ - \hat{\boldsymbol{z}} \times \boldsymbol{H}_t^-\right] \tag{3.40b}$$

Adding the two equations and using that

$$\frac{1}{\tan(z)}\left(1+\frac{1}{\cos(z)}\right)=\frac{1+\cos(z)}{\sin(z)}=\frac{2\cos^2(z/2)}{\sin(z)}=\frac{2\cos^2(z/2)}{2\sin(z/2)\cos(z/2)}=\cot(z/2)$$

(3.41)

yields [37, 41]

$$\boldsymbol{E}_t^+ + \boldsymbol{E}_t^- = \frac{1-j}{\delta\sigma\tan\left[(1-j)\,d/(2\delta)\right]}\left[\hat{\boldsymbol{z}}\times\boldsymbol{H}_t^+ - \hat{\boldsymbol{z}}\times\boldsymbol{H}_t^-\right].$$

(3.42)

To arrive at the surface impedance boundary condition, Eq. (3.2), we need to model the slab as infinitely thin and assume that $\boldsymbol{E}_t^+ = \boldsymbol{E}_t^-$ at the transition. We then find that

$$\boldsymbol{E}_t^+ = \boldsymbol{E}_t^- = \frac{1-j}{2\delta\sigma\tan\left[(1-j)\,d/(2\delta)\right]}\left[\hat{\boldsymbol{z}}\times\boldsymbol{H}_t^+ - \hat{\boldsymbol{z}}\times\boldsymbol{H}_t^-\right]$$

(3.43)

where the right-hand-side (RHS) can be viewed as a constant times the surface current, i.e.,

$$Z_S = \frac{1-j}{2\delta\sigma\tan\left[(1-j)\,d/(2\delta)\right]}.$$

(3.44)

Equation (3.44) is the approximate surface impedance of a good conductor. It has been implemented in the FEKO software [42, p. 10-112], and has been tested on a conducting spherical shell. After illuminating the sphere by a plane electromagnetic wave, the shielding factor was computed and turned out to be in good agreement with the exact solution (through a Mie series representation of the fields). An alternative derivation based on the volume equivalence principle can be found in [43], and a detailed dimensional analysis to approximate a conductor of finite thickness and conductivity by an infinitely thin perfectly conducting sheet can be found in [44].

As derived above, the formula for Z_S entails a number of approximations, in summary:

- the minimum curvature radius R_{min} of the curved slab is much larger than the skin depth of the slab material, i.e., $R_{\mathrm{min}} \gg \delta$;

- the curvature radius of the phase front of the incident field is much larger than the skin depth of the slab material, i.e., $R_{\mathrm{ph}} \gg \delta$;

- end/edge effects are neglected;

- the conductor is electrically thin, i.e., $|k|d \ll 1$;

- the conductor has a high conductivity, such that $\sigma \gg \omega\varepsilon_0|\varepsilon_r|$.

3.2.3 Approximations of Z_S for $d \ll \delta$ and $d \gg \delta$

For electrically thin conducting slabs for which the conductor thickness d is much smaller than the skin depth δ, i.e., $d \ll \delta$, one concludes with the aid of the MacLaurin series approximation $\tan(z) = z + z^3/3 + \mathcal{O}(z^5)$ that (3.44) can be approximated as [37, 41]

$$
Z_S = \frac{1-j}{2\delta\sigma \left[(1-j)\,d/(2\delta) + ((1-j)d/(2\delta))^3/3 + \mathcal{O}\left((d/\delta)^5\right)\right]}
$$
$$
= \frac{1}{\sigma d \left[1 - j(d/\delta)^2/6 + \mathcal{O}\left((d/\delta)^4\right)\right]} = \frac{1}{\sigma d}\left\{1 + \frac{jd^2}{6\delta^2} + \mathcal{O}\left((d/\delta)^4\right)\right\}. \tag{3.45}
$$

Hence, the relative error of approximating Z_S by $1/(\sigma d)$ is mainly described by $jd^2/(6\delta^2)$. The first-order term indicates a relative error of this approximation of less than 0.5% for $d/\delta \leq 0.17$. The zero-order term $1/(\sigma d)$ in this expression is the low-frequency approximation [40, pp. 38-40] of Z_S.

For $d \gg \delta$ (and $|k|d \ll 1$), we use the geometric series representation $1/(1-x) = \sum_{n=0}^{\infty} x^n$ for $|x| < 1$ and write

$$
\frac{1}{\tan\left[(1-j)\,d/(2\delta)\right]} = j\left(1 + e^{-(1+j)d/\delta}\right)/\left(1 - e^{-(1+j)d/\delta}\right)
$$
$$
= j\left(1 + e^{-(1+j)d/\delta}\right)\left(1 + e^{-(1+j)d/\delta} + e^{-2(1+j)d/\delta} + \ldots\right)
$$
$$
= j\left(1 + 2e^{-(1+j)d/\delta} + \mathcal{O}\left(e^{-2d/\delta}\right)\right) \tag{3.46}
$$

so that, for $d \gg \delta$, the following approximation is found for Z_S [37, 41]:

$$
Z_S = \frac{1+j}{2\delta\sigma}\left\{1 + 2e^{-(1+j)d/\delta} + \mathcal{O}\left(e^{-2d/\delta}\right)\right\}. \tag{3.47}
$$

When Z_S is approximated as $(1+j)/(2\delta\sigma)$, the first-order term $2e^{-(1+j)d/\delta}$ in (3.47) indicates a relative error of less than 0.5% for $d/\delta \geq 6$.

One can also derive a jump condition for the fields pertaining to an electrically thick conductor ($|k|d \gg 1$), provided that the fields across one of the sides of the conductor

are known. For example, the fields in the exterior region of a waveguiding structure may be assumed zero when the electric walls are impenetrable from the interior $(d \gg \delta)$. Accordingly, assuming that the fields only exist across the upper interface of the slab (see Fig. 3.2 with $\{\boldsymbol{E}_t^-, \boldsymbol{H}_t^-\} = \boldsymbol{0}$), reduces Eq. (3.34) to the boundary condition $\boldsymbol{E}_t^+ = Z_{11}\hat{\boldsymbol{z}} \times \boldsymbol{H}_t^+ + Z_{12}\hat{\boldsymbol{z}} \times \boldsymbol{H}_t^- \approx Z_S\hat{\boldsymbol{z}} \times \boldsymbol{H}_t^+$, with the surface impedance across the upper boundary

$$Z_S = \lim_{|k|d \to \infty} \{Z_{11}\} = \frac{1+j}{\delta\sigma} \tag{3.48}$$

where, as in (3.47), the surface resistance is seen to equal the surface reactance and the effective thickness equals the skin depth only once, as opposed to (3.47). The above formula has been implemented in the HFSS software (finite element method), which is particularly suitable to analyze closed-boundary problems (waveguides, transmission lines, etc.).

The zero-order term in Eq. (3.47) has been applied to estimate the losses and the associated noise contribution of antenna arrays [45]. A footnote in [46] states that the factor 2 in the denominator of the zero-order term results from the assumption that, in good approximation, the current is evenly distributed on the two faces of the metallic antenna. However, this is a too stringent requirement, because in the above derivation of Z_S we were not forced to assume a symmetric current distribution inside the conductor, except that $\boldsymbol{E}_t^+ = \boldsymbol{E}_t^-$.

Strong currents are often observed along edges when open surfaces are considered that are highly conductive. Consequently, the edge effects may be strong and the above approximations for Z_S may cease to hold near edges and corners. Higher-order impedance boundary conditions have been developed to account for both the edge effects and the actual curvature of the conductor, see e.g. [47] and [48] and references cited therein. Depending upon the required solution accuracy, some uncertainty in the surface impedance may be acceptable. For instance, when the antenna parameter of interest is the radiation efficiency, η_{rad}, a relatively large variation of Z_S (say a factor of 2) will not cause η_{rad} to change much, provided that $\eta_{\text{rad}} \approx 100\%$. Hence, some degree of uncertainty may be acceptable in practice, particularly in worst-case analyses of low-loss antenna systems. On the contrary, for low values of η_{rad}, a small variation of Z_S can lead to significant variations in η_{rad}. As a result, errors in Z_S may be pronounced strongly, and hence; care has to be exercised in applying the above impedance boundary conditions for a general class of problems.

In this dissertation, we will mostly employ PEC surfaces, although the power absorption

losses of metals, which causes the antenna's radiation efficiency to decrease, will be examined in a quantitative manner in Chapter 5. It will turn out that these losses contribute only moderately to the total antenna system noise temperature (determine e.g. η_{rad} from Figs. 5.13 and 5.14 for $\sigma = 3 \times 10^7$, and substitute its value in Eq. (5.95) for $T_{\mathrm{amb}} = 300$ K).

3.3   The Electric Field Integral Equation

When the piecewise-smooth impedance sheet of Fig. 3.1(b) is illuminated by an incident electromagnetic field $\{\boldsymbol{E}^i, \boldsymbol{H}^i\}$, which is defined in the absence of the sheet, a current $\boldsymbol{J}_S$ is induced on the surface of the scatterer/antenna which, in turn, generates the scattered/radiated field $\{\boldsymbol{E}^s, \boldsymbol{H}^s\}$. On account of the linearity of both the constitutive relations and Maxwell's equations, the total electric field $\boldsymbol{E}$ is given as

$$\boldsymbol{E} = \boldsymbol{E}^i + \boldsymbol{E}^s(\boldsymbol{J}_S) \tag{3.49}$$

for $\boldsymbol{r} \in \mathbb{R}^3$. By inserting (3.49) in boundary condition (3.2), a functional equation is obtained for $\boldsymbol{J}_S$ at the surface of the impedance sheet, i.e.,

$$-\boldsymbol{E}^i_{\mathrm{tan}} = \boldsymbol{E}^s_{\mathrm{tan}}(\boldsymbol{J}_S) - Z_S \boldsymbol{J}_S, \quad \text{for } \boldsymbol{r} \in \mathcal{S} \tag{3.50}$$

where the scattered/radiated electric field $\boldsymbol{E}^s$, due to a current-carrying volume, is given by (2.27). To arrive at the field expressions that are generated by currents on surfaces, the appropriate limiting process of (2.27) has to be taken [49, pp. 147–150]. Accordingly, the potential formulas are substituted in (3.50) to yield

$$-\boldsymbol{E}^i_{\mathrm{tan}} = -\left(j\omega\mu_0 \boldsymbol{A} + \boldsymbol{\nabla}\Phi\right)_{\mathrm{tan}} - Z_S \boldsymbol{J}_S \tag{3.51}$$

with $\boldsymbol{r} \in \mathcal{S}$ and

$$\boldsymbol{A}(\boldsymbol{r}) = \lim_{\delta \downarrow 0} \iint\limits_{\mathcal{S}-\mathcal{S}_\delta} G(\boldsymbol{r} - \boldsymbol{r}')\boldsymbol{J}_S(\boldsymbol{r}')\,\mathrm{d}S' \tag{3.52a}$$

$$\Phi(\boldsymbol{r}) = -\lim_{\delta \downarrow 0} \frac{1}{j\omega\varepsilon_0} \iint\limits_{\mathcal{S}-\mathcal{S}_\delta} G(\boldsymbol{r} - \boldsymbol{r}')\boldsymbol{\nabla}'_t \cdot \boldsymbol{J}_S(\boldsymbol{r}')\,\mathrm{d}S' \tag{3.52b}$$

$$G(\boldsymbol{r} - \boldsymbol{r}') = \frac{e^{-jk_0\|\boldsymbol{r}-\boldsymbol{r}'\|_2}}{4\pi\,\|\boldsymbol{r} - \boldsymbol{r}'\|_2} \tag{3.52c}$$

where $\boldsymbol{\nabla}'_t = \boldsymbol{\nabla}' - \partial_n\hat{\boldsymbol{n}}$ denotes the surface divergence operator with respect to the primed coordinates, and where $\mathcal{S}_\delta$ represents a small area of arbitrary shape that contains the

singular point $\boldsymbol{r} = \boldsymbol{r}'$ and has a maximum chord length δ. Hence, the potential integrals should be understood in terms of Cauchy principal values [50, pp. 86–88]. The integrals are improper, although convergent, since the residual term contained in $\mathcal{S}_\delta$ can be shown to vanish in the limiting case. Equation (3.51) is recognized as the well-known Electric Field Integral Equation (EFIE); it is herein classified as a Fredholm boundary value integral equation of the second kind, and occasionally referred to as the third type [51, p. 311].

3.4 Discretization and Solution of the EFIE

The objective in this section is to transform the continuous functional (3.51) into a matrix equation so that it can be solved by standard algebraic techniques. In this, so-called, weighted residual method, or moment method approach [32], the surface current $\boldsymbol{J}_S$ is approximated by a finite set of basis functions.

3.4.1 Method of Weighted Residuals

Suppose that N independent vector basis functions $\{\boldsymbol{f}_n\}_{n=1}^N$ are employed on $\mathcal{S}$, then

$$\boldsymbol{J}_S(\boldsymbol{r}) \approx \sum_{n=1}^N I_n \boldsymbol{f}_n(\boldsymbol{r}) \tag{3.53}$$

where the sequence of complex-valued amplitudes $\{I_n\}$ are the unknown expansion coefficients to be determined. Clearly, the numerical convergence of the above approximation depends upon: (i) the specific choice of the subsectional and/or entire domain basis functions $\{\boldsymbol{f}_n\}$, and; (ii) the number of independent basis functions N. The specific choice of basis, and its implications on the solution accuracy and stability, are discussed in e.g. [49, 52–54]. In the following, only the most relevant aspects will be emphasized.

Let the EFIE in (3.51) be cast in the compact form

$$-\boldsymbol{E}_{\text{tan}}^i(\boldsymbol{r}) = L\left\{\boldsymbol{J}_S(\boldsymbol{r})\right\} \tag{3.54}$$

where L is a linear operator, which maps functions in the domain of L, denoted by $\mathcal{D}(L)$,

onto functions in the range of L, denoted by $\mathcal{R}(L)$. Substituting (3.53) in (3.54) gives

$$-\boldsymbol{E}^i_{\tan}(\boldsymbol{r}) \approx \sum_{n=1}^{N} I_n L\left\{\boldsymbol{f}_n(\boldsymbol{r})\right\} = -\boldsymbol{E}^i_N = -\mathcal{P}_N\left(\boldsymbol{E}^i_{\tan}\right), \qquad (3.55)$$

where $\boldsymbol{E}^i_N$ is the approximant of $\boldsymbol{E}^i_{\tan}$, and where $\mathcal{P}_N$ is the projection operator which projects the excitation $\boldsymbol{E}^i_{\tan}$ onto the space spanned by $L\{\boldsymbol{f}_n\}$ for $n = 1, \ldots, N$. The space that is spanned by the set of basis functions $\{\boldsymbol{f}_n\}$ will be denoted by $X_N = \mathrm{span}\{\boldsymbol{f}_1, \ldots, \boldsymbol{f}_n\}$. For ultimate convergence, it is required that $\boldsymbol{E}^i_N \to \boldsymbol{E}^i_{\tan}$ for $N \to \infty$ and, hence, $\{\boldsymbol{f}_n\}$ must form a complete basis for $\mathcal{D}(L)$, so that also $\{L\{\boldsymbol{f}_n\}\}$ forms a complete basis for the operator range $\mathcal{R}(L)$. The latter is most desired as it spans a basis for $\boldsymbol{E}^i_{\tan}$, and may be achieved even when the basis $\{\boldsymbol{f}_n\}$ is incomplete in $\mathcal{D}(L)$. In any case, the basis functions should be chosen such that X_N is contained in $D(L)$, which means that each of the basis functions must be suitable to be subjected to the various operations involved (e.g. differentiations), and that each of the basis functions satisfies the boundary conditions (classical solution). When only a weighted sum of basis functions satisfies the boundary conditions, and/or the differentiability conditions are satisfied in a distributional sense, a distributional solution is obtained. We will, however, consider only the classical solution.

By substituting (3.53) in (3.54), the field approximation error, or residual field function $\boldsymbol{R}$, can be defined as

$$\boldsymbol{R}(\boldsymbol{r}) = \boldsymbol{E}^i_{\tan}(\boldsymbol{r}) + \sum_{n=1}^{N} I_n L\left\{\boldsymbol{f}_n(\boldsymbol{r})\right\} \qquad (3.56)$$

which has to be minimized, and most preferably in regions on $\mathcal{S}$ where the field intensities are significant. One could enforce that $\boldsymbol{R} = \boldsymbol{0}$ at N given points $\{\boldsymbol{r}_1, \ldots, \boldsymbol{r}_N\}$; this specific form of (strong) "testing" is referred to as the collocation method, or point-matching method [32].

The more general (weak) form of testing is achieved through multiplication (weighting) of the residual function by N suitable testing functions. More specifically, we require a vanishing norm of $\boldsymbol{R}$ through the inner product[2]

$$\langle \boldsymbol{R}, \boldsymbol{w}_m \rangle = \iint\limits_{\mathcal{S}_m} \boldsymbol{R}(\boldsymbol{r}) \cdot \boldsymbol{w}^*_m(\boldsymbol{r}) \, \mathrm{d}S = 0 \qquad (3.57)$$

---

[2]Note that the inner product reduces to a symmetric product for real-valued testing functions.

over the mth support $\mathcal{S}_m$ of the mth conjugated weighting function $\boldsymbol{w}_m$, for $m = 1, 2, \ldots, N$. Note that, in the collocation method, the testing functions are real-valued and simply taken as $\boldsymbol{w}_m(\boldsymbol{r}) = \delta(\boldsymbol{r} - \boldsymbol{r}_m)$, where $\boldsymbol{r}_m$ represents the mth test point. However, this method is often not preferred since the accuracy of the collocation method strongly depends upon the choice of the matching points. Also note that, on the basis of $\langle \boldsymbol{E}^i_{\mathrm{tan}} - \boldsymbol{E}^i_N, \boldsymbol{w}_m \rangle = 0$, each of the weighting functions $\boldsymbol{w}_m$ is chosen orthogonal to the field approximation error $\boldsymbol{E}^i_{\mathrm{tan}} - \boldsymbol{E}^i_N$. Furthermore, the weighting functions $\{\boldsymbol{w}_m\}$ should be contained in $\mathcal{R}(L)$ and form a basis, or, more generally, this basis has to be contained in the domain of the adjoint operator L^*, viz. $\mathcal{D}(L^*)$, because $\mathcal{R}(L) \subset \mathcal{D}(L^*)$. The adjoint operator L^* is defined as

$$\langle y, L\{x\} \rangle = \langle L^*\{y\}, x \rangle \tag{3.58}$$

for all $x, y \in H$, where H denotes the Hilbert space, used herein to define inner products between square-summable vector tuples of infinite dimensions (continuous functions) belonging to $\mathcal{L}^2$. When $L = L^*$, the operator is self-adjoint (Hermitian) so that $\mathcal{D}(L^*) = \mathcal{D}(L) = \mathcal{R}(L)$, which suggests that the testing functions can be chosen equal to the basis functions, i.e., $\boldsymbol{w}_m = \boldsymbol{f}_m$ for all m. This specific choice is known as Galerkin's method. In electromagnetics, however, the operators are generally not self-adjoint. In fact, the EFIE operator is symmetric [55], that is, $\langle y, L\{x\} \rangle = \langle L\{y\}, x \rangle$ for all $x, y \in \mathcal{D}(L)$ and the choice of Galerkin's scheme needs more justification, as further detailed below.

When Galerkin's method is invoked, Eq. (3.56) transforms into the matrix equation

$$V_m = \sum_{n=1}^{N} Z_{mn} I_n \quad \text{for } m = 1, 2, \ldots, N \tag{3.59}$$

with

$$V_m = -\langle \boldsymbol{E}^i, \boldsymbol{f}_m \rangle \quad \text{and} \quad Z_{mn} = \langle L\{\boldsymbol{f}_n\}, \boldsymbol{f}_m \rangle \tag{3.60}$$

where the subscripts "tan" have been omitted since the vector test functions are chosen tangential to the surface $\mathcal{S}$. It turns out that, when Galerkin's method is applied to discretize EFIE operators, symmetry in $\mathbf{Z}$ is preserved if

$$Z_{mn} = \langle L\{\boldsymbol{f}_n\}, \boldsymbol{f}_m \rangle = \langle L\{\boldsymbol{f}_m\}, \boldsymbol{f}_n \rangle = Z_{nm} \tag{3.61}$$

which is generally only true for real-valued functions $\{\boldsymbol{f}_m, \boldsymbol{f}_n\}$. For complex-valued functions, symmetry is preserved if the test functions are chosen equal to the conjugate of the basis functions, that is, $\boldsymbol{w}_m = \boldsymbol{f}_m^*$ for all m. The latter choice is a non-Galerkin approach for which the energy norm in (3.57) becomes mathematically identical to replacing

this inner product by a symmetric product and choosing the basis functions equal to the test functions (Galerkin's approach). Neither from a practical point of view, nor from a mathematical point of view, has it been shown that Galerkin's method is the "best" choice [56, 57]. Moreover, about a factor of 2 in matrix-fill time can be gained when the matrix is known to be symmetric. Henceforth, we will indeed remove the conjugate in (3.57) to maintain symmetry, even when complex-valued basis and testing functions are involved. Also, it is worthwhile to point out that this is in accordance with the reaction concept and reciprocity theorem (no conjugations involved). In this respect, for PEC surfaces, the matrix element Z_{mn} can then be interpreted as the reaction integral of a basis function $\boldsymbol{f}_n$, which generates an electric field whose inner product is taken with the mth test function (current) $\boldsymbol{f}_m$, after which the result is integrated over the support of the mth test function. In addition, and regardless of whether or not testing functions are identical to basis functions, it is known that field reactions (defined through a symmetric product), and therefore also the computed moment matrix entries, are of a variational form and are second-order accurate in the electric fields that are tested by the basis functions [56, 58].

However, without knowledge of the specific type of basis functions, Galerkin's approach does not necessarily guarantee accurate solutions for the current. Despite this, it will be shown in Section 3.5.1 that the antenna port impedance characteristics can be conveniently computed through a stationary impedance formula whenever a solution vector of the current is available which has been obtained through Galerkin's approach, in conjunction with a symmetric product for testing.

Finally, the above linear system of N equations with N unknown expansion coefficients can be solved through standard matrix factorization methods. However, to obtain a unique solution, or to avoid spurious solutions from occurring, the matrix $\mathbf{Z}$ is required to be of full rank, i.e., the null space $\mathcal{N}(\mathbf{Z})$ has to be empty. In numerical practice, we require that the condition number of $\mathbf{Z}$ is sufficiently small, or, equivalently, that the range of singular values of $\mathbf{Z}$ is limited. Without preconditioning, an ill-conditioned matrix equation may lead to inaccurate solutions and poorly converging iterative solvers. We remark that the matrix condition number depends on the choice of basis and test functions, and increases for an increasingly larger discretization level N. This occurs because the columns of the moment matrix $\mathbf{Z}$ become almost linearly dependent for finer discretization levels.

3.4.2   Selection of Basis and Testing Functions

Not only the above outlined mathematical considerations are of importance in choosing appropriate basis and testing functions, but the computational aspects are equally important. In fact, the analytical and numerical evaluation of matrix elements may become a difficult and tedious task when, for instance, complicated (higher-order) basis and testing functions are selected. Furthermore, a basis may be required to conform, at least in a piecewise-continuous manner, to arbitrary shaped geometries; this particularly applies to multi-purpose codes. This flexibility may be reduced when entire-domain basis functions are employed, so that in general a subsectional basis is preferred, even though this may give rise to a larger moment matrix.

We will employ Galerkin's scheme in conjunction with a real-valued subsectional basis to maintain and exploit the symmetry of the moment matrix and to achieve a high degree of flexibility in modeling arbitrarily shaped structures. Although no rigorous mathematical proof exists to justify the use of a Galerkin's scheme for a general EFIE case, it has been widely accepted and demonstrated that, for plate structures, the Galerkin approach is capable to yield accurate solutions.

The current $\boldsymbol{J}_S$ in the EFIE (3.51) will be expanded according to (3.53), and subsequently be tested using Galerkin's method, to yield

$$-j\omega\mu_0\langle\boldsymbol{A},\boldsymbol{f}_m\rangle - \langle\boldsymbol{\nabla}\Phi,\boldsymbol{f}_m\rangle - \sum_{n=1}^{N}I_n\langle Z_S\boldsymbol{f}_n,\boldsymbol{f}_m\rangle = -\langle\boldsymbol{E}^i,\boldsymbol{f}_m\rangle \tag{3.62}$$

for $m = 1, 2, \ldots N$, with

$$\boldsymbol{A}(\boldsymbol{r}) = \sum_{n=1}^{N}I_n\iint\limits_{\mathcal{S}_n}G(\boldsymbol{r}-\boldsymbol{r}')\boldsymbol{f}_n(\boldsymbol{r}')\,\mathrm{d}S' \tag{3.63a}$$

$$\Phi(\boldsymbol{r}) = -\frac{1}{j\omega\varepsilon_0}\sum_{n=1}^{N}I_n\iint\limits_{\mathcal{S}_n}G(\boldsymbol{r}-\boldsymbol{r}')\boldsymbol{\nabla}'_t\cdot\boldsymbol{f}_n(\boldsymbol{r}')\,\mathrm{d}S' \tag{3.63b}$$

where $\mathcal{S}_n$ is the support of the nth basis function, and where the principal value limits have been omitted for conciseness.

Note that $\langle \nabla\Phi, \boldsymbol{f}_m \rangle$ in (3.62) can be written as

$$
\begin{aligned}
\langle \nabla\Phi, \boldsymbol{f}_m \rangle &= \boldsymbol{\nabla}_t \cdot \langle \Phi, \boldsymbol{f}_m \rangle - \langle \Phi, \boldsymbol{\nabla}_t \cdot \boldsymbol{f}_m \rangle \\
&= \iint_{\mathcal{S}_m} \boldsymbol{\nabla}_t \cdot (\Phi \boldsymbol{f}_m)\, \mathrm{d}S - \iint_{\mathcal{S}_m} \Phi\,(\boldsymbol{\nabla}_t \cdot \boldsymbol{f}_m)\, \mathrm{d}S.
\end{aligned} \tag{3.64}
$$

Next, we recall the 2-D variant of Gauss' theorem (Green's theorem for planar surfaces) for a vector field $\boldsymbol{w}$ defined on a piecewise planar surface $\mathcal{S}$ with boundary $\partial\mathcal{S}$ and $\boldsymbol{w} \cdot \hat{\boldsymbol{n}} = 0$, i.e., $\boldsymbol{w}$ has no component normal to the surface $\mathcal{S}$. Then,

$$
\iint_{\mathcal{S}} (\boldsymbol{\nabla}_t \cdot \boldsymbol{w})\, \mathrm{d}S = \oint_{\partial\mathcal{S}} \boldsymbol{w} \cdot \hat{\boldsymbol{\nu}}\, \mathrm{d}l \tag{3.65}
$$

where $\hat{\boldsymbol{\nu}}$ denotes an outward pointing unit vector, which has an orientation normal to the edge $\partial\mathcal{S}$. Applying this surface divergence theorem to (3.64), one obtains

$$
\langle \boldsymbol{\nabla}\Phi, \boldsymbol{f}_m \rangle = \oint_{\partial\mathcal{S}_m} \Phi\,(\boldsymbol{f}_m \cdot \hat{\boldsymbol{\nu}}_m)\, \mathrm{d}l - \iint_{\mathcal{S}_m} \Phi\,(\boldsymbol{\nabla}_t \cdot \boldsymbol{f}_m)\, \mathrm{d}S. \tag{3.66}
$$

This leads to another requirement for the basis functions, namely that $\boldsymbol{f}_m \cdot \hat{\boldsymbol{\nu}}_m = 0$ along the boundary $\partial\mathcal{S}_m$, i.e., the vector basis function has only a component of the current which is parallel to the boundaries of its support. If this physics-based property is satisfied, it is observed from (3.66) that (3.64) simplifies to

$$
\langle \boldsymbol{\nabla}\Phi, \boldsymbol{f}_m \rangle = -\langle \Phi, \boldsymbol{\nabla}_t \cdot \boldsymbol{f}_m \rangle. \tag{3.67}
$$

Hence, Eq. (3.62) can then be written as

$$
-j\omega\mu_0 \langle \boldsymbol{A}, \boldsymbol{f}_m \rangle + \langle \Phi, \boldsymbol{\nabla}_t \cdot \boldsymbol{f}_m \rangle - \sum_{n=1}^{N} I_n \langle Z_S \boldsymbol{f}_n, \boldsymbol{f}_m \rangle = -\langle \boldsymbol{E}^i, \boldsymbol{f}_m \rangle \quad \text{for } m = 1, 2, \ldots N. \tag{3.68}
$$

It is evident from (3.68) and (3.63b) that the gradient operator only acts on the vector basis/test function $\boldsymbol{f}$, and because $\boldsymbol{\nabla}' \cdot \boldsymbol{f}_n = -j\omega\rho_S$, we require that $\{\boldsymbol{f}_n\}$ is chosen such that both the surface charges and surface currents are associated with electromagnetic fields of finite energy in order to be in the range of the operator and be able to satisfy the boundary condition for the electric field on $\mathcal{S}$. More specifically, we require the solution space of current densities $\{\boldsymbol{f}_n\}$ to be a subset of the, so-called, continuous space $H(\mathrm{div}, \partial\mathcal{S})$

of div-conforming vector functions, which is defined as [59]

$$H\left(\mathrm{div}, \partial\mathcal{S}\right) = \left\{ \forall \boldsymbol{f} \in \mathbb{C}^3 \,\middle|\, \iint\limits_{\mathcal{S}} \|\boldsymbol{f}\|_2^2 + \|\boldsymbol{\nabla} \cdot \boldsymbol{f}\|_2^2 \,\mathrm{d}S < \infty; \ \boldsymbol{f} \cdot \hat{\boldsymbol{\nu}}_n = 0 \ \mathrm{on} \ \partial\mathcal{S} \right\}. \quad (3.69)$$

The widely used Rao-Wilton-Glisson (RWG) basis functions are an appropriate choice in the context of a div-conforming discretization, since they are contained in $H\left(\mathrm{div}, \partial\mathcal{S}\right)$ and satisfy the aforementioned geometrical requirements [26]. Furthermore, they are also of low order and therefore lead to a moment matrix whose elements can be evaluated with relative ease.

Consider the nth (non-planar) RWG basis function $\boldsymbol{f}_n$ in Fig. 3.3(a), whose support consists of a pair of planar triangular patches, T_n^+ and T_n^-, that share a common edge with length ℓ_n.
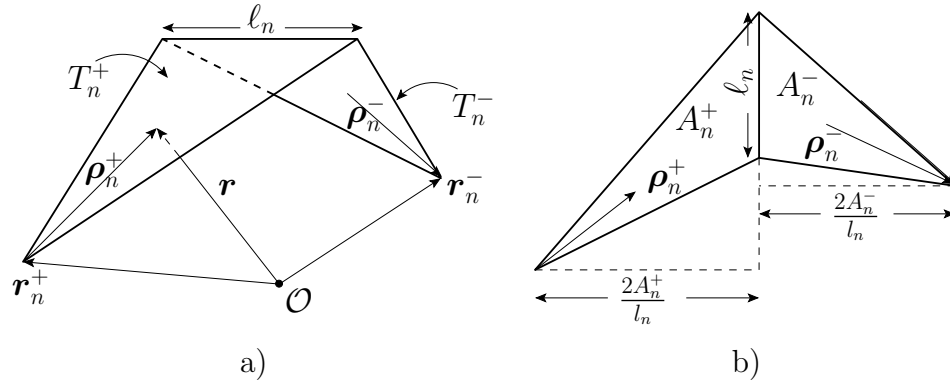

Figure 3.3: Parameters for defining the geometry and the current of a RWG function.

With reference to the nth RWG, the surface-current density $\boldsymbol{f}_n^\pm$ at position $\boldsymbol{r} \in T_n^\pm$ is defined by $\boldsymbol{r}$ and the corner vertex $\boldsymbol{r}_n^\pm$ through the linear relation $\boldsymbol{f}_n^\pm = C^\pm \boldsymbol{\rho}_n^\pm$, where $C^\pm$ is a normalization constant, yet to be specified, and $\boldsymbol{\rho}_n^\pm = \pm\left(\boldsymbol{r} - \boldsymbol{r}_n^\pm\right)$.

Figure 3.3(b) illustrates that, when $A_n^\pm$ designates the area of triangle $T^\pm$ with base length ℓ_n, the height of the triangle is given as $2A_n^\pm/\ell_n$. This height is used to normalize $\boldsymbol{\rho}_n^\pm$ such that its component normal to the common edge equals unity. The latter applies to both triangles. Hence, the normal component of $\boldsymbol{f}_n^\pm$ is continuous across the common edge (for a planar pair of triangular supports constituting the support of a RWG function), while the tangential part is discontinuous for non-equal and non-equilateral triangles. In summary,

the function description reads

$$\boldsymbol{f}_n(\boldsymbol{r}) = \begin{cases} \dfrac{\ell_n}{2A_n^+}\boldsymbol{\rho}_n^+ & \boldsymbol{r} \in T_n^+ \\ \dfrac{\ell_n}{2A_n^-}\boldsymbol{\rho}_n^- & \boldsymbol{r} \in T_n^- \\ 0 & \text{otherwise} \end{cases} \quad \text{so that} \quad \boldsymbol{\nabla}_t \cdot \boldsymbol{f}_n(\boldsymbol{r}) = \begin{cases} +\dfrac{\ell_n}{A_n^+} & \boldsymbol{r} \in T_n^+ \\ -\dfrac{\ell_n}{A_n^-} & \boldsymbol{r} \in T_n^- \\ 0 & \text{otherwise} \end{cases} \quad (3.70)$$

Note that the magnitude of the vector field $\boldsymbol{\rho}_n^+(\boldsymbol{r})$ is linearly increasing in T_n^+ when the observation point moves from the corner vertex $\boldsymbol{r}_n^+$ towards the common edge, whereas the magnitude of $\boldsymbol{\rho}_n^-(\boldsymbol{r})$ linearly decreases towards the corner vertex of T_n^-. Furthermore, the vector field has no component normal to the outer boundaries of its domain except along the inner edge, where the normal component has unit length. Hence, for a current distribution $\boldsymbol{J}_S(\boldsymbol{r}) = \sum_{n=1}^N I_n \boldsymbol{f}_n(\boldsymbol{r})$, the scalar product $I_n\ell_n$ equals the total current passing through the nth common edge. This basis function is said to be edge-based; the number of basis functions N equals the number of inner edges (assuming no multiple joints between surfaces). On account of (3.70), it is observed that the surface charge densities on the triangular patches are constant and have opposite signs so that they are in the form of pulse doublets.

Finally, it is worthwhile to mention that the above discretization of the EFIE operator L lead to an ill-conditioned problem since it suffers from a low-frequency breakdown for static or quasi-static conditions. In fact, currents tend to circulate on electrically large surfaces, so that the basis functions have to be able to correctly describe the solenoidal (zero-divergence) part of this current. This has led to the introduction of the "loop"-type basis functions, and their dual complement, the "star"-type basis functions, used to describe the irrotational part. It was demonstrated that combining the low-order RWG basis functions into a "loop-star" or "loop-tree" basis virtually annihilates the growth of the matrix condition number for increasing N, thereby improving the converge rates of iterative solvers [60, 61].

3.4.3   Mesh Representation

The RWG basis needs to be accommodated on a triangular mesh, which is preferably nearly equilateral in order to minimize the total number of triangular facets while achieving a relatively high solution accuracy and good condition number of the moment matrix

(see e.g. [62]). Figure 3.4 shows a possible triangulation of an exponentially Tapered Slot Antenna (TSA) composed of two (mirror-symmetric) polygons whose outlines are described by a set of polygonal boundary nodes (black dots). To automatically mesh the structure

$$Z_{mn} = \iint_{\mathcal{S}_m} \boldsymbol{E}^s \left(\boldsymbol{f}_n \right) \cdot \boldsymbol{f}_m \, \mathrm{d}S$$
$$\text{(if } Z_S = 0, \text{ or } \mathcal{S}_m \cap \mathcal{S}_n = \emptyset)$$
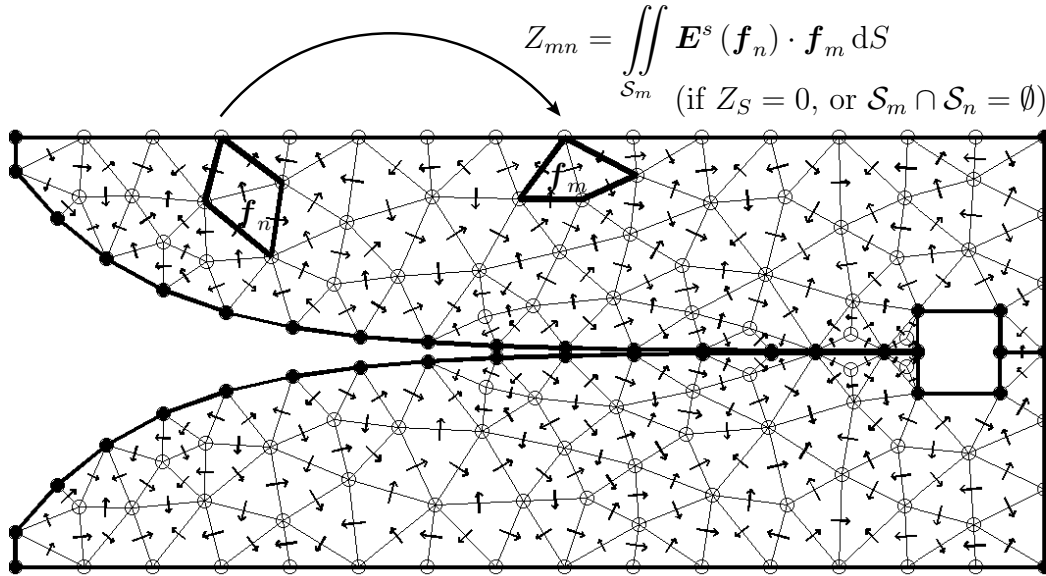
Figure 3.4: Triangular mesh representation used to partition RWGs.

using CAESAR, each of the polygons is first mapped into a 2-D plane and supplied with a uniform grid of nodes (visualized as open circles). During this phase, additional nodes are inherited from adjacent polygons that are common to the polygon under consideration. Afterwards, the coinciding nodes, as well as those that are in the exterior polygon region, are removed. Subsequently, a Delaunay triangulation is carried out [63], and the triangles that appear in the exterior polygon region are removed. Finally, each of the internal nodes is centered with respect to the surrounding nodes through an iterative routine as a result of which an almost equilateral triangular mesh is obtained.

After storing all the nodes, as well as the associated node indices of the triangles, into arrays, the various RWGs are identified by considering each of the inner edges of the mesh in conjunction with the associated triangles that share this internal edge. Figure 3.4 illustrates a possible polarity distribution of RWGs. One observes that, typically, one internal edge belongs to one RWG; however, we point out that an edge may belong to several RWGs when it concerns a line along which multiple polygons are connected. This is shown pictorially in Fig. 3.5, where the superposition of the in- and outgoing currents to and from such a "junction edge" naturally satisfies Kirchoff's current law; this follows from

the fact that the in- and outgoing current to and from a common edge of a single RWG already obeys this law (thus no local charge accumulation occurs). However, it should be noted that, when the number of interconnected polygons at a junction equals N_j, the number of independent junction basis functions only equals $N_j - 1$. This readily follows from Fig. 3.5 by realizing that an arbitrary expansion set $\{I_1, I_2, I_3, I_4\}$ yields an identical junction current as, e.g., choosing the set $\{I_1 - I_4, I_2 + I_4, I_3 - I_4, 0\}$, where, effectively, only three expansion coefficients are used.
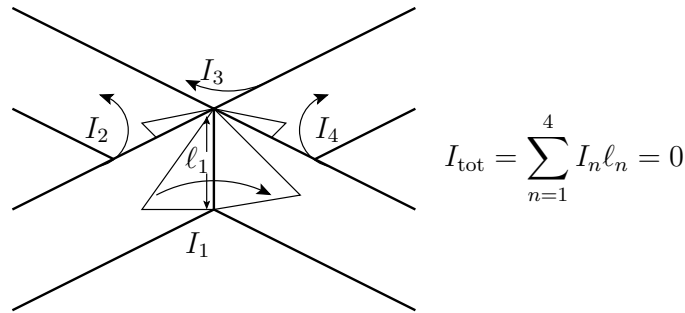

$$I_{\mathrm{tot}} = \sum_{n=1}^{4} I_n \ell_n = 0$$

Figure 3.5: Mesh representation at junctions.

a)   b)   c)
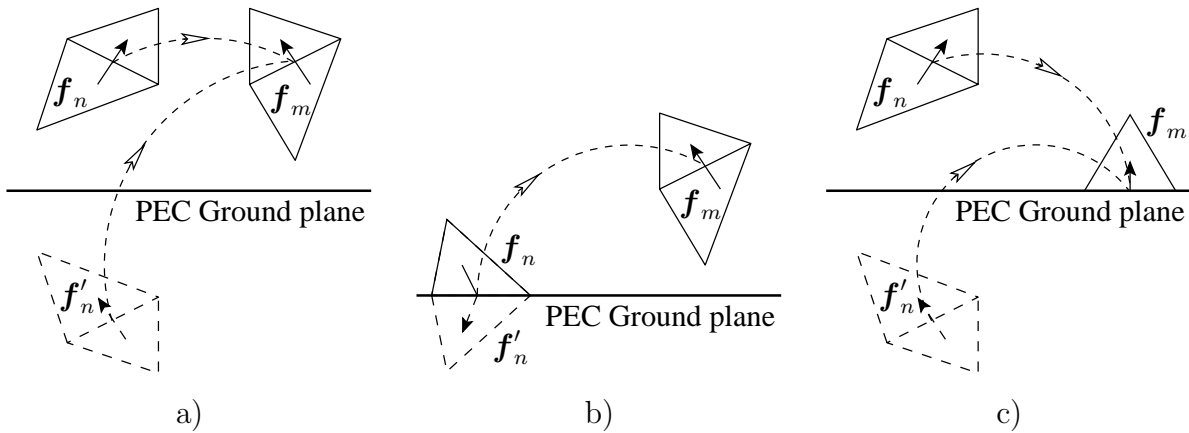
Figure 3.6: Field reaction between the source RWG $\boldsymbol{f}_n$ and the observation RWG $\boldsymbol{f}_m$. a) Source and observation RWGs above the ground plane. b) Half of a source RWG connected to the ground plane. c) Half of an observation RWG connected to a ground plane.

Another type of junction may be encountered at infinite PEC ground planes. As an example, Fig. 3.6(a) illustrates that, in order to determine matrix element Z_{mn}, the electric field that is generated by both the source RWG $\boldsymbol{f}_n$ and its mirrored counterpart $\boldsymbol{f}'_n$ need to be tested over the mth observation RWG $\boldsymbol{f}_m$. On the contrary, when the source RWG

is connected to the ground plane as in Fig. 3.6(b), only half of the source RWG and its mirrored counterpart contribute to the mth observation RWG. Similarly, when half of the observation RWG is connected to the PEC plane, both the mirrored and non-mirrored source RWG contribute to only half of the observation RWG.

3.4.4   Evaluation of the Moment Matrix Elements

As indicated in Fig. 3.4 for the PEC case (or if $\mathcal{S}_m \cap \mathcal{S}_n = 0$ in the lossy case), the moment matrix element Z_{mn} can be interpreted as a reaction integral of the electric field $\boldsymbol{E}^s\left(\boldsymbol{f}_n\right)$ that is generated and subsequently tested by real-valued basis functions $\boldsymbol{f}_n$ and $\boldsymbol{f}_m$, respectively. This integral may be evaluated accurately and effectively with the aid of Gaussian quadrature rules of sufficient high order, provided that $\boldsymbol{E}^s\left(\boldsymbol{f}_n\right)$ is a sufficiently smooth function over the support of the testing function. The latter is dependent upon the electrical separation distance between the pair of RWGs as well as the size and mutual orientation of the triangular patches. Typically, to obtain an accurate phase representation of the currents on surfaces, the minimum mesh density is $N \sim 10/\lambda_0$, but a larger density may be required near edges or geometries entailing tiny details. It will be demonstrated that a relatively low-order quadrature scheme suffices for this typical level of discretization.

We recall the discretized EFIE, Eq. (3.68),

$$-j\omega\mu_0\langle\boldsymbol{A}, \boldsymbol{f}_m\rangle + \langle\Phi, \boldsymbol{\nabla}_t\cdot\boldsymbol{f}_m\rangle - \sum_{n=1}^{N} I_n\langle Z_S\boldsymbol{f}_n, \boldsymbol{f}_m\rangle = -\langle\boldsymbol{E}^i, \boldsymbol{f}_m\rangle \quad \text{for } m = 1, 2, \dots N,$$

(3.71)

with

$$\boldsymbol{A}(\boldsymbol{r}) \approx \sum_{n=1}^{N} I_n \iint_{\mathcal{S}_n} G(\boldsymbol{r} - \boldsymbol{r}')\boldsymbol{f}_n(\boldsymbol{r}')\,\mathrm{d}S', \tag{3.72a}$$

$$\Phi(\boldsymbol{r}) \approx -\frac{1}{j\omega\varepsilon_0}\sum_{n=1}^{N} I_n \iint_{\mathcal{S}_n} G(\boldsymbol{r} - \boldsymbol{r}')\boldsymbol{\nabla}'_t\cdot\boldsymbol{f}_n(\boldsymbol{r}')\,\mathrm{d}S', \tag{3.72b}$$

and numerically evaluate the moment matrix elements (reaction integrals) corresponding to non-overlapping basis and testing functions. Since the surface divergence of a RWG basis function is proportional to its surface charge density [see Eq. (3.70)], the second term

of (3.71) is readily evaluated as

$$
\langle \Phi, \boldsymbol{\nabla}_t \cdot \boldsymbol{f}_m \rangle = \iint\limits_{\mathcal{S}_m} \Phi \boldsymbol{\nabla}_t \cdot \boldsymbol{f}_m \, \mathrm{d}S = \ell_m \left(\frac{1}{A_m^+} \iint\limits_{T_m^+} \Phi \, \mathrm{d}S - \frac{1}{A_m^-} \iint\limits_{T_m^-} \Phi \, \mathrm{d}S \right)
$$

$$
\approx \ell_m \sum_{p=1}^{P} w_p \left[\Phi\left(\boldsymbol{r}_{m;p}^+ \right) - \Phi\left(\boldsymbol{r}_{m;p}^- \right) \right] \tag{3.73}
$$

where a P-point Gaussian quadrature rule for triangles has been used that takes a weighted sum of sampled field values at P locations $\{\boldsymbol{r}_{m;p}^\pm\}_{p=1}^P$ inside the $T_m^\pm$ triangles of the mth test RWG (*cf.* Appendix B). The order of the quadrature rule, $P-1$, can be chosen adaptively and depends on the electrical distance between the basis and test functions (see Section 3.6).

Similarly, the symmetric products in (3.71) that involve the magnetic vector potential $\boldsymbol{A}$ and the incident field $\boldsymbol{E}^i$ are evaluated as

$$
\left\langle \left\{ \begin{array}{c} \boldsymbol{E}^i \\ \boldsymbol{A} \end{array} \right\}, \boldsymbol{f}_m \right\rangle = \iint\limits_{\mathcal{S}_m} \left\{ \begin{array}{c} \boldsymbol{E}^i \\ \boldsymbol{A} \end{array} \right\} \cdot \boldsymbol{f}_m \, \mathrm{d}S
$$

$$
= \ell_m \left(\frac{1}{2A_m^+} \iint\limits_{T_m^+} \left\{ \begin{array}{c} \boldsymbol{E}^i \\ \boldsymbol{A} \end{array} \right\} \cdot \boldsymbol{\rho}_m^+ \, \mathrm{d}S + \frac{1}{2A_m^-} \iint\limits_{T_m^-} \left\{ \begin{array}{c} \boldsymbol{E}^i \\ \boldsymbol{A} \end{array} \right\} \cdot \boldsymbol{\rho}_m^- \, \mathrm{d}S \right)
$$

$$
\approx \frac{\ell_m}{2} \sum_{p=1}^{P} w_p \left[\left\{ \begin{array}{c} \boldsymbol{E}^i(\boldsymbol{r}_{m;p}^+) \\ \boldsymbol{A}(\boldsymbol{r}_{m;p}^+) \end{array} \right\} \cdot \boldsymbol{\rho}_{m;p}^+ + \left\{ \begin{array}{c} \boldsymbol{E}^i(\boldsymbol{r}_{m;p}^-) \\ \boldsymbol{A}(\boldsymbol{r}_{m;p}^-) \end{array} \right\} \cdot \boldsymbol{\rho}_{m;p}^- \right]. \tag{3.74}
$$

The remaining term in (3.71) concerns the surface impedance and is evaluated as

$$
\sum_{n=1}^{N} I_n \langle Z_S \boldsymbol{f}_n, \boldsymbol{f}_m \rangle = \sum_{n=1}^{N} I_n Z_{mn}^{\mathrm{IBC}} \tag{3.75}
$$

where the matrix $\mathbf{Z}^{\mathrm{IBC}}$ equals a constant times the Gram matrix of the basis functions whenever Z_S is chosen constant. Furthermore, $\mathbf{Z}^{\mathrm{IBC}}$ is a sparse matrix when RWG basis functions are employed and the segments $\mathcal{S}_m \cap \mathcal{S}_n$ are triangular domains. If Z_S can be assumed constant over each triangle [and is e.g. given by (3.44)], then

$$
Z_{mn}^{\mathrm{IBC}} = \sum_{x,y \in \{+,-\}} Z_S(T_m^x \cap T_n^y) \iint\limits_{T_m^x \cap T_n^y} \boldsymbol{f}_m \cdot \boldsymbol{f}_n \, \mathrm{d}S \tag{3.76}
$$

where $Z_S(T)$ is the value of Z_S on triangle T and $Z_S(\emptyset) = 0$. On its plus and minus triangles an RWG is linearly ascending and descending, respectively, in its vectorial direction. The integrals in (3.76) can be evaluated in closed form. For a triangle T on which both $\boldsymbol{f}_m$ and $\boldsymbol{f}_n$ are non-trivial, let $\boldsymbol{r}^{[T,m]}$ and $\boldsymbol{r}^{[T,n]}$ be the vertices of T in which the mth and nth RWG function are equal to zero, respectively, let $\ell^{[T,n]}$ for $x \in \{m, n\}$ be the length of the edge opposite of the vertex $\boldsymbol{r}^{[T,x]}$, let A be the area of T, let $\{\boldsymbol{r}_1^{[T]}, \boldsymbol{r}_2^{[T]}, \boldsymbol{r}_3^{[T]}\}$ be the vertices of the triangle, and let $\boldsymbol{r}_c^{[T]}$ be the centroid of the triangle given by $(\boldsymbol{r}_1^{[T]} + \boldsymbol{r}_2^{[T]} + \boldsymbol{r}_3^{[T]})/3$. Then (*cf.* Appendix C),

$$\iint\limits_T \boldsymbol{f}_n \cdot \boldsymbol{f}_m \, dS = \pm \frac{\ell^{[T,m]} \ell^{[T,n]}}{2A} \left\{ \frac{9}{12} \|\boldsymbol{r}_c^{[T]}\|_2^2 - \frac{1}{12} \left(\boldsymbol{r}_1^{[T]} \cdot \boldsymbol{r}_2^{[T]}\right) - \frac{1}{12} \left(\boldsymbol{r}_1^{[T]} \cdot \boldsymbol{r}_3^{[T]}\right) - \frac{1}{12} \left(\boldsymbol{r}_2^{[T]} \cdot \boldsymbol{r}_3^{[T]}\right) \right.$$

$$\left. - \frac{1}{2} \left(\boldsymbol{r}^{[T,n]} \cdot \boldsymbol{r}_c^{[T]}\right) - \frac{1}{2} \left(\boldsymbol{r}^{[T,m]} \cdot \boldsymbol{r}_c^{[T]}\right) + \frac{1}{2} \left(\boldsymbol{r}^{[T,n]} \cdot \boldsymbol{r}^{[T,m]}\right) \right\} \qquad (3.77)$$

The plus sign in (3.77) applies in case both $\boldsymbol{f}_m$ and $\boldsymbol{f}_n$ are linearly increasing or decreasing with respect to their vectorial directions, respectively, and the minus sign otherwise. The computation of Z_{mn}^{IBC} can also be carried out numerically, since the integrand $\boldsymbol{f}_n \cdot \boldsymbol{f}_m$ represents a quadratic function whose integral is determined exactly using Gaussian quadrature rules for triangles employing at least 3 quadrature points.

Upon substituting Eqs. (3.73)–(3.75) in (3.71), one obtains

$$-j\omega\mu_0 \ell_m \sum_{p=1}^{P} w_p \left[\boldsymbol{A}\left(\boldsymbol{r}_{m;p}^+\right) \cdot \frac{\boldsymbol{\rho}_{m;p}^+}{2} + \boldsymbol{A}\left(\boldsymbol{r}_{m;p}^-\right) \cdot \frac{\boldsymbol{\rho}_{m;p}^-}{2}\right] + \ell_m \sum_{p=1}^{P} w_p \left[\Phi\left(\boldsymbol{r}_{m;p}^+\right) - \Phi\left(\boldsymbol{r}_{m;p}^-\right)\right]$$

$$- \sum_{n=1}^{N} I_n Z_{mn}^{\mathrm{IBC}} = -\ell_m \sum_{p=1}^{P} w_p \left[\boldsymbol{E}^i\left(\boldsymbol{r}_{m;p}^+\right) \cdot \frac{\boldsymbol{\rho}_{m;p}^+}{2} + \boldsymbol{E}^i\left(\boldsymbol{r}_{m;p}^-\right) \cdot \frac{\boldsymbol{\rho}_{m;p}^-}{2}\right] \quad m = 1, 2, \ldots N. \tag{3.78}$$

Next, we substitute (3.72a) and (3.72b) in (3.78). This gives us a system of linear equations in the form of $\mathbf{ZI} = \mathbf{V}$, i.e.,

$$-\sum_{n=1}^{N} I_n \left[\ell_m \sum_{p=1}^{P} w_p \left(j\omega\mu_0 \left[\boldsymbol{A}_{mn;p}^+ \cdot \frac{\boldsymbol{\rho}_{m;p}^+}{2} + \boldsymbol{A}_{mn;p}^- \cdot \frac{\boldsymbol{\rho}_{m;p}^-}{2}\right] + \left[\Phi_{mn;p}^- - \Phi_{mn;p}^+\right]\right) + Z_{mn}^{\mathrm{IBC}}\right]$$

$$= -\ell_m \sum_{p=1}^{P} w_p \left[\boldsymbol{E}_{m;p}^+ \cdot \frac{\boldsymbol{\rho}_{m;p}^+}{2} + \boldsymbol{E}_{m;p}^- \cdot \frac{\boldsymbol{\rho}_{m;p}^-}{2}\right] \quad m = 1, 2, \ldots N \tag{3.79}$$

where element Z_{mn} of the system matrix **Z** is computed as

$$
Z_{mn} = Z_{mn}^{\text{PEC}} - Z_{mn}^{\text{IBC}} = \langle \boldsymbol{E}^s(\boldsymbol{f}_n), \boldsymbol{f}_m \rangle - \langle Z_S \boldsymbol{f}_n, \boldsymbol{f}_m \rangle
$$

$$
= -\ell_m \sum_{p=1}^{P} w_p \left(j\omega\mu_0 \left[\boldsymbol{A}_{mn;p}^{+} \cdot \frac{\boldsymbol{\rho}_{m;p}^{+}}{2} + \boldsymbol{A}_{mn;p}^{-} \cdot \frac{\boldsymbol{\rho}_{m;p}^{-}}{2} \right] + \left[\Phi_{mn;p}^{-} - \Phi_{mn;p}^{+} \right] \right) - Z_{mn}^{\text{IBC}}
$$

$$(3.80)$$

and where element V_m of the excitation vector **V** is computed as

$$
V_m = -\langle \boldsymbol{E}^i, \boldsymbol{f}_m \rangle = -\ell_m \sum_{p=1}^{P} w_p \left[\boldsymbol{E}_{m;p}^{+} \cdot \frac{\boldsymbol{\rho}_{m;p}^{+}}{2} + \boldsymbol{E}_{m;p}^{-} \cdot \frac{\boldsymbol{\rho}_{m;p}^{-}}{2} \right], \tag{3.81}
$$

with

$$
\boldsymbol{A}_{mn;p}^{\pm} = \pm \iint_{\mathcal{S}_n} G\left(\boldsymbol{r}_{m;p}^{\pm} - \boldsymbol{r}' \right) \boldsymbol{f}_n(\boldsymbol{r}') \, \mathrm{d}S' \tag{3.82a}
$$

$$
\Phi_{mn;p}^{\pm} = \mp \frac{1}{j\omega\varepsilon_0} \iint_{\mathcal{S}_n} G\left(\boldsymbol{r}_{m;p}^{\pm} - \boldsymbol{r}' \right) \boldsymbol{\nabla}_t' \cdot \boldsymbol{f}_n(\boldsymbol{r}') \, \mathrm{d}S' \tag{3.82b}
$$

$$
G\left(\boldsymbol{r}_{m;p}^{\pm} - \boldsymbol{r}' \right) = \frac{e^{-jk_0 \left\| \boldsymbol{r}_{m;p}^{\pm} - \boldsymbol{r}' \right\|_2}}{4\pi \left\| \boldsymbol{r}_{m;p}^{\pm} - \boldsymbol{r}' \right\|_2} \tag{3.82c}
$$

$$
\boldsymbol{E}_{m;p}^{\pm} = \boldsymbol{E}^i\left(\boldsymbol{r}_{m;p}^{\pm} \right). \tag{3.82d}
$$

Finally, using (3.70), we can carry out a direct numerical Gaussian quadrature evaluation of the potential integrals (3.82a) and (3.82b):

$$
\boldsymbol{A}_{mn;p}^{\pm} \approx \pm \frac{\ell_n}{2} \sum_{q=1}^{P} w_q \left[G\left(\boldsymbol{r}_{m;p}^{\pm} - \boldsymbol{r}_{n;q}^{+} \right) \boldsymbol{\rho}_{n;q}^{+} + G\left(\boldsymbol{r}_{m;p}^{\pm} - \boldsymbol{r}_{n;q}^{-} \right) \boldsymbol{\rho}_{n;q}^{-} \right] \tag{3.83a}
$$

$$
\Phi_{mn;p}^{\pm} \approx \mp \frac{\ell_n}{j\omega\varepsilon_0} \sum_{q=1}^{P} w_q \left[G\left(\boldsymbol{r}_{m;p}^{\pm} - \boldsymbol{r}_{n;q}^{+} \right) - G\left(\boldsymbol{r}_{m;p}^{\pm} - \boldsymbol{r}_{n;q}^{-} \right) \right] \tag{3.83b}
$$

$$
G\left(\boldsymbol{r}_{m;p}^{\pm} - \boldsymbol{r}_{n;q}^{\pm} \right) = \frac{e^{-jk_0 \left\| \boldsymbol{r}_{m;p}^{\pm} - \boldsymbol{r}_{n;q}^{\pm} \right\|_2}}{4\pi \left\| \boldsymbol{r}_{m;p}^{\pm} - \boldsymbol{r}_{n;q}^{\pm} \right\|_2} \tag{3.83c}
$$

where the order of the quadrature rule, $P - 1$, can be chosen identical to the one used to test the electric field. This does not automatically imply that symmetry in **Z** can be preserved, as this predominantly depends on P.

In the process of constructing the matrix **Z**, the electric fields that are generated by both triangles contained in $\boldsymbol{f}_n$ have to be tested by the triangle pair contained in $\boldsymbol{f}_m$ through a

reaction integral (four cross terms). As correctly noted in [26], it is inefficient to compute the matrix elements by a subsequent consideration of pairs of internal edges that form a RWG basis and testing function, since triangles typically belong to three overlapping RWGs and, hence, some computations are unnecessarily repeated. It would therefore be beneficial to loop over triangular facets, rather than over edges, as this saves, approximately, a factor of nine in the total number of surface-integral evaluations.

However, when the objective is to construct the matrix $\mathbf{Z}$ only partially, and such that most of the triangles are considered only once, then it is advantageous to consider edge pairs rather than triangle pairs. This occurs, e.g., for electrically large structures when off-diagonal blocks of $\mathbf{Z}$, representing the far-interactions between groups of RWGs, are computed only partially with the aid of lower-order quadrature rules, while the remaining block matrix elements are approximated through an interpolation technique (see Chapter 4). Henceforth, we will employ the above proposed EFIE discretization to retain a sufficient amount of flexibility and therefore accept a less efficient scheme for constructing the (relatively low amount of) self blocks. Despite this drawback, we can still exploit that the Green's function evaluations are identical in both the vector and scalar potentials (3.83a) and (3.83b), so that the triangle-by-triangle approach in [26] has no additional advantage in this respect.

The numerical evaluation of the potential integrals (3.82a) and (3.82b) for the case that $R = \left\| \boldsymbol{r}_{m;p}^{\pm} - \boldsymbol{r}' \right\|_2 = 0$ will be treated in Section 3.4.6.

3.4.5 Evaluation of the Excitation Vector for Plane-Wave Fields

For plane-wave incidence [see Eq. (2.38)], the mth forcing term (3.81) is computed as

$$V_m = -\langle \boldsymbol{E}^i, \boldsymbol{f}_m \rangle = -\iint\limits_{\mathcal{S}_m} \boldsymbol{E}_0 \cdot \boldsymbol{f}_m e^{j(\boldsymbol{k}_0 \cdot \boldsymbol{r})} \, \mathrm{d}S. \tag{3.84}$$

With the aid of Green's second identity, it is straightforward to show that this integral can be evaluated analytically. In $\mathbb{R}^2$ Green's second identity reads

$$\iint\limits_{\mathcal{S}} \left(\psi_1 \boldsymbol{\nabla}_t^2 \psi_2 - \psi_2 \boldsymbol{\nabla}_t^2 \psi_1 \right) \, \mathrm{d}S = \oint\limits_{\partial\mathcal{S}} \left[\psi_1 \left(\boldsymbol{\nabla}_t \psi_2 \cdot \hat{\boldsymbol{\nu}} \right) - \psi_2 \left(\boldsymbol{\nabla}_t \psi_1 \cdot \hat{\boldsymbol{\nu}} \right) \right] \, \mathrm{d}\ell \tag{3.85}$$

where the scalar functions ψ_1 and ψ_2 are twice continuously differentiable on $\mathcal{S}$, and where $\hat{\boldsymbol{\nu}}$ denotes the outward pointing vector along the contour of the planar surface $\mathcal{S}$. Here

we have used that $\partial \psi_{1,2}/\partial \hat{\nu} = (\boldsymbol{\nabla}_t \psi_{1,2} \cdot \hat{\boldsymbol{\nu}})$. By substituting $\psi_1 = (\boldsymbol{E}_0 \cdot \boldsymbol{f}_m)/k_t^2$ and $\psi_2 = \exp(j\boldsymbol{k}_0 \cdot \boldsymbol{r})$ in the LHS of (3.85), it is verified that Eq. (3.84) is obtained because $\boldsymbol{\nabla}_t^2 \psi_1 = 0$ and $\boldsymbol{\nabla}_t^2 \psi_2 = -k_t^2 \exp(j\boldsymbol{k}_0 \cdot \boldsymbol{r})$. Furthermore, with the function description of the RWG basis, Eq. (3.70), one observes that $\boldsymbol{\nabla}_t \psi_1 = \pm \ell_m \boldsymbol{E}_{t,0}/(2A_m^\pm k_t^2)$ and $\boldsymbol{\nabla}_t \psi_2 = j\boldsymbol{k}_{t,0} \exp(j\boldsymbol{k}_0 \cdot \boldsymbol{r})$, so that the surface integration in (3.84) equals the simpler contour integration [RHS of (3.85)]

$$-\iint\limits_{\mathcal{S}_m} \boldsymbol{E}_0 \cdot \boldsymbol{f}_m e^{j(\boldsymbol{k}_0 \cdot \boldsymbol{r})} \, \mathrm{d}S = \frac{\ell_m}{2k_t^2} \left[\frac{1}{A_m^-} \oint\limits_{\partial T_m^-} \left[\boldsymbol{E}_0 \cdot \hat{\boldsymbol{\nu}} + (\boldsymbol{E}_0 \cdot \boldsymbol{\rho}_m^-)(j\boldsymbol{k}_0 \cdot \hat{\boldsymbol{\nu}}) \right] e^{j(\boldsymbol{k}_0 \cdot \boldsymbol{r})} \, \mathrm{d}\ell \right.$$

$$\left. - \frac{1}{A_m^+} \oint\limits_{\partial T_m^+} \left[\boldsymbol{E}_0 \cdot \hat{\boldsymbol{\nu}} - (\boldsymbol{E}_0 \cdot \boldsymbol{\rho}_m^+)(j\boldsymbol{k}_0 \cdot \hat{\boldsymbol{\nu}}) \right] e^{j(\boldsymbol{k}_0 \cdot \boldsymbol{r})} \, \mathrm{d}\ell \right] \quad (3.86)$$

where we have used that $\boldsymbol{k}_{t,0} \cdot \hat{\boldsymbol{\nu}} = \boldsymbol{k}_0 \cdot \hat{\boldsymbol{\nu}}$ and $\boldsymbol{E}_{t,0} \cdot \hat{\boldsymbol{\nu}} = \boldsymbol{E}_0 \cdot \hat{\boldsymbol{\nu}}$.

The contour integrals in (3.86) are evaluated for the planar triangles T_m^+ and T_m^- as

$$\iint\limits_{T_m^\pm} \boldsymbol{E}_0 \cdot \boldsymbol{f}_m e^{j(\boldsymbol{k}_0 \cdot \boldsymbol{r})} \, \mathrm{d}S = \pm \frac{\ell_m}{2A_m^\pm k_t^2} \oint\limits_{\partial T_m^\pm} \left[\boldsymbol{E}_0 \cdot \hat{\boldsymbol{\nu}} - (\boldsymbol{E}_0 \cdot [\boldsymbol{r} - \boldsymbol{r}_m^\pm])(j\boldsymbol{k}_0 \cdot \hat{\boldsymbol{\nu}}) \right] e^{j(\boldsymbol{k}_0 \cdot \boldsymbol{r})} \, \mathrm{d}\ell$$

$$= \pm \frac{\ell_m}{2A_m^\pm k_t^2} \sum_{i=1}^{3} \left[\left[\boldsymbol{E}_0 \cdot \hat{\boldsymbol{\nu}}^{[T,i]} + j(\boldsymbol{E}_0 \cdot \boldsymbol{r}_m^\pm)(\boldsymbol{k}_0 \cdot \hat{\boldsymbol{\nu}}^{[T,i]}) \right] \int\limits_{\ell^{[T,i]}} e^{j(\boldsymbol{k}_0 \cdot \boldsymbol{r})} \, \mathrm{d}\ell \right.$$

$$\left. - j\boldsymbol{k}_0 \cdot \hat{\boldsymbol{\nu}}^{[T,i]} \int\limits_{\ell^{[T,i]}} \boldsymbol{E}_0 \cdot \boldsymbol{r} e^{j(\boldsymbol{k}_0 \cdot \boldsymbol{r})} \, \mathrm{d}\ell \right] \quad (3.87)$$

where the contour integral has been subdivided into line integrals along the three edges of triangle T. The corresponding ith edge length is denoted by $\ell^{[T,i]}$ and the outward pointing vector normal to this edge as $\hat{\boldsymbol{\nu}}^{[T,i]}$, with $i \in \{1, 2, 3\}$. Next, let $\boldsymbol{r}_b^{[T,i]}$ and $\boldsymbol{r}_e^{[T,i]}$ denote the begin and end points of line segment $\ell^{[T,i]}$ of triangle T, respectively, and let $\varphi^{[T,i]} = \boldsymbol{k}_0 \cdot \left(\boldsymbol{r}_e^{[T,i]} - \boldsymbol{r}_b^{[T,i]} \right)$, then the line integrals are evaluated in closed form as

$$\int\limits_{\ell^{[T,i]}} e^{j(\boldsymbol{k}_0 \cdot \boldsymbol{r})} \, \mathrm{d}\ell = \frac{\ell^{[T,i]}}{j\varphi^{[T,i]}} \left[e^{j(\boldsymbol{k}_0 \cdot \boldsymbol{r}_e^{[T,i]})} - e^{j(\boldsymbol{k}_0 \cdot \boldsymbol{r}_b^{[T,i]})} \right] \quad (3.88)$$

and

$$\int\limits_{\ell^{[T,i]}} (\boldsymbol{E}_0 \cdot \boldsymbol{r}) e^{j(\boldsymbol{k}_0 \cdot \boldsymbol{r})} \, \mathrm{d}\ell = \frac{\ell^{[T,i]}}{(\varphi^{[T,i]})^2} \left[\left[(1 - j\varphi^{[T,i]})(\boldsymbol{E}_0 \cdot \boldsymbol{r}_e^{[T,i]}) - (\boldsymbol{E}_0 \cdot \boldsymbol{r}_b^{[T,i]}) \right] e^{j(\boldsymbol{k}_0 \cdot \boldsymbol{r}_e^{[T,i]})} \right.$$

$$\left. + \left[(1 + j\varphi^{[T,i]})(\boldsymbol{E}_0 \cdot \boldsymbol{r}_b^{[T,i]}) - (\boldsymbol{E}_0 \cdot \boldsymbol{r}_e^{[T,i]}) \right] e^{j(\boldsymbol{k}_0 \cdot \boldsymbol{r}_b^{[T,i]})} \right]. \quad (3.89)$$

Obviously, the analytical result only requires the evaluation of a number of exponential functions and dot products, and because the RWG functions partially overlap, most edges and vertices are considered multiple times when evaluating (3.87) for all RWGs. Therefore, it is advantageous to first construct a database holding the function values $\{e^{j(\boldsymbol{k}_0 \cdot \boldsymbol{r}_n^{[T]})}\}_{n=1}^{N_v}$ and $\{\boldsymbol{E}_0 \cdot \boldsymbol{r}_n\}_{n=1}^{N_v}$ for all the N_v vertices $\{\boldsymbol{r}_n\}_{n=1}^{N_v}$. In addition, the phase values $\{\varphi^{[T]}\}_n^{N_\ell}$ and the terms involving $\hat{\boldsymbol{\nu}}$ can be pre-computed for all the N_ℓ edges. The latter unit vectors are often directly available, or can otherwise be expressed in terms of the vertices.

Care has to be exercised when evaluating (3.88) and (3.89) numerically for the case that $\varphi^{[T,i]} \approx 0$. This situation occurs if the incident field vector $\boldsymbol{E}_0$ is almost normal to one of the edges $i = 1, 2, 3$. In the limiting case, the integrals are evaluated as

$$\lim_{\varphi^{[T,i]} \to 0} \left\{ \int_{\ell^{[T,i]}} e^{j(\boldsymbol{k}_0 \cdot \boldsymbol{r})} \, \mathrm{d}\ell \right\} = \ell^{[T,i]} e^{j(\boldsymbol{k}_0 \cdot \boldsymbol{r}_b^{[T,i]})} \tag{3.90}$$

and

$$\lim_{\varphi^{[T,i]} \to 0} \left\{ \int_{\ell^{[T,i]}} \boldsymbol{E}_0 \cdot \boldsymbol{r} e^{j(\boldsymbol{k}_0 \cdot \boldsymbol{r})} \, \mathrm{d}\ell \right\} = \ell^{[T,i]} (\boldsymbol{E}_0 \cdot \boldsymbol{r}_e^{[T,i]}) e^{j(\boldsymbol{k}_0 \cdot \boldsymbol{r}_b^{[T,i]})}. \tag{3.91}$$

Still, Eq. (3.87) remains poorly conditioned for a numerical evaluation whenever $k_t \approx 0$. This corresponds to the case that the field vector $\boldsymbol{E}_0$ is almost tangential to the surface of a triangular patch (normal incidence). Then, the phase gradient of the incident field is zero over the triangular patch. In the limiting case, the surface integral on the RHS of (3.87) is therefore evaluated as

$$\lim_{k_t \to 0} \left\{ \iint_{T_m^\pm} \boldsymbol{E}_0 \cdot \boldsymbol{f}_m e^{j(\boldsymbol{k}_0 \cdot \boldsymbol{r})} \, \mathrm{d}S \right\} = e^{j(\boldsymbol{k}_0 \cdot \boldsymbol{r}_0^{[T,\pm]})} \iint_{T_m^\pm} \boldsymbol{E}_0 \cdot \boldsymbol{f}_m \, \mathrm{d}S \tag{3.92a}$$

$$= \pm \frac{\ell_m}{2} \boldsymbol{E}_0 \cdot (\boldsymbol{r}_c^{[T,\pm]} - \boldsymbol{r}_m^{[T,\pm]}) e^{j(\boldsymbol{k}_0 \cdot \boldsymbol{r}_c^{[T,\pm]})} \tag{3.92b}$$

where $\boldsymbol{r}_0^{[T,\pm]}$ is an arbitrary point on the triangle $T_m^\pm$, $\boldsymbol{r}_m^{[T,\pm]}$ is the corner vertex of the triangle $T_m^\pm$ from which the vector basis function is linearly ascending, and $\boldsymbol{r}_c^{[T,\pm]}$ is the centroid of the triangle $T_m^\pm$. Note that a single point $\boldsymbol{r}_0^{[T,\pm]}$ in (3.92a) directly determines the constant phase term of the incident field over the triangular surface. The last integral in (3.92b) is easily evaluated by choosing $\boldsymbol{r}_0^{[T,\pm]} = \boldsymbol{r}_c^{[T,\pm]}$ and subsequently performing the integration analytically using the local coordinates and the integration strategy as outlined in Appendix C.

However, an exact integration is not required since the desired accuracy can be reached by taking a relatively small number of Gaussian quadrature points. In fact, through the application of the vector Taylor series expansion [64]

$$f\left(\boldsymbol{r} + \boldsymbol{a}\right) = \sum_{n=0}^{\infty}\left[\frac{1}{n!}\left(\boldsymbol{a}\cdot\nabla_{\boldsymbol{r}'}\right)^{n}f\left(\boldsymbol{r}'\right)\right]_{\boldsymbol{r}'=\boldsymbol{r}} \tag{3.93}$$

the complex-valued exponential function $f(\boldsymbol{r}) = \exp\left[j\left(\boldsymbol{k}_0\cdot\boldsymbol{r}\right)\right]$ in (3.84) is written as

$$f(\boldsymbol{r}_0 + \Delta\boldsymbol{r}) = \exp\left[j\left(\boldsymbol{k}_0\cdot\boldsymbol{r}_0\right)\right]\left[1 + j\left(\boldsymbol{k}_0\cdot\Delta\boldsymbol{r}\right) - \frac{1}{2}(\boldsymbol{k}_0\cdot\Delta\boldsymbol{r})^2 + \mathcal{O}\left([\boldsymbol{k}_0\cdot\Delta\boldsymbol{r}]^3\right)\right] \tag{3.94}$$

with $\boldsymbol{r}_0$ being the center point along the common edge of the pertaining RWG. Hence, the phase is a slowly varying function in $(\boldsymbol{k}_0\cdot\Delta\boldsymbol{r})$, since $|\boldsymbol{k}_0\cdot\Delta\boldsymbol{r}| \ll 2\pi$ over the electrically small triangles $T_m^{\pm}$. Moreover, when $\boldsymbol{E}^i$ is normally incident on $\mathcal{S}_m$, that is, $(\boldsymbol{k}_0\cdot\Delta\boldsymbol{r}) = 0$, the integrand in (3.84) becomes proportional to the linear vector function $\boldsymbol{E}_0\cdot\boldsymbol{f}_m$, and the integration is already exact for a 1-point quadrature rule. The latter can be concluded from (3.92b), whose analytical result is identical to a direct numerical evaluation using a midpoint integration rule. Even for oblique incidence, a low-order integration rule will be relatively accurate with respect to the computed moment matrix elements (near-field integrals).

Consider the triangular support of half of a RWG basis function in Fig. 3.7. The illustrated triangle is equilateral and each edge has a length of 1 m. The triangular surface is illuminated by a plane electromagnetic field from the direction (θ_0,ϕ_0) with an amplitude (polarization) vector $\boldsymbol{E}_0 = \hat{\boldsymbol{\theta}}(\theta_0,\phi_0)$. We set $\|\boldsymbol{k}_0\|_2 = 2\pi/10$, so that each edge has an electrical length of $\lambda_0/10$. The surface integral (3.84) has been evaluated analytically
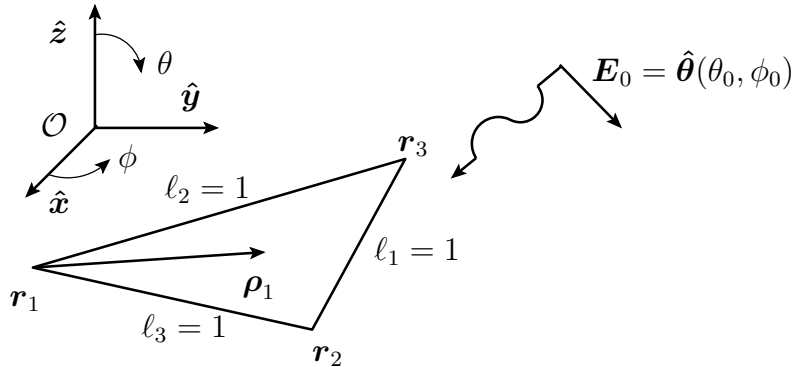

Figure 3.7: Equilateral triangle in the xy-plane illuminated by a plane-wave field.

for the single triangle and has been compared to the results obtained through Gaussian quadrature (*cf.* Appendix B), for several different (θ_0, ϕ_0) directions. The corresponding results are shown in Table 3.1.

Table 3.1: Computation of (3.84) by both evaluating the analytical formula (3.87) and by a numerical integration through a 1, 3, and 7 point Gaussian quadrature rule for triangles. The angles of incidence are $\theta_0 = 0^o, 45^o, 89^o$, and $\phi_0 = 90^o$.

θ_0	Analytical Integration	$P = 1$ point/triangle
0°	**0.288675135** - **0.000000000j**	**0.288675135** - **0.000000000j**
45°	**0.195137918** - **0.057941280j**	**0.19**7445471 - **0.05**1787573j
89°	**0.004598520** - **0.001988885j**	**0.004**710302 - **0.001**787530j

θ_0	$P = 3$ points/triangle	$P = 7$ points/triangle
0°	**0.288675135** - **0.000000000j**	**0.288675135** - **0.000000000j**
45°	**0.195**175346 - **0.0579**63148j	**0.195137919** - **0.05794127**7j
89°	**0.004**600148 - **0.001**990373j	**0.0045985**20 - **0.00198888**5j

The bold-faceted fonts indicate the correctly computed digits with respect to the analytical result. It is concluded that the quadrature rule has to be increased for oblique incidence to maintain a certain level of accuracy. It is also observed that it suffices to employ only three quadrature points to achieve a four-digit accuracy. Furthermore, because the three-point rule represents a relatively inexpensive scheme, it justifies a direct numerical approach to compute (3.84).

3.4.6 Singular and Near-Singular Potential Integral Kernels

Thus far, only distant field reactions between source and observation RWGs have been considered and these are adequately computed with the aid of standard Gaussian quadrature rules. As stated earlier, the potential integrals in (3.52) have singular kernels and need to be interpreted in terms of Cauchy principle values in order to be meaningful. In the context of the present RWG discretization, the potential integrals exhibit a singularity at $\boldsymbol{r} = \boldsymbol{r}'$ which becomes pronounced when the observation and integration points (almost) coincide, i.e., when the source and observation RWGs share edges or vertices (near singular), or even overlap (fully singular). In the mixed-potential formulation, the singularity is of a weak form, that is, $1/R = 1/\|\boldsymbol{r} - \boldsymbol{r}'\|_2$, and the exclusion area $\mathcal{S}_\delta$ in (3.52) is taken

equal to the size of a triangular patch. Gaussian quadrature rules that are based on poly-nomial function approximations are not adequate for computing the self-reactions, unless the singularity can be extracted to a sufficient level as described below.

Reaction integrals need to be computed that pertain to a triangular source domain T_m and observation domain T_n (see Fig. 3.8). In abstract form, the involved 4-D integrals are of
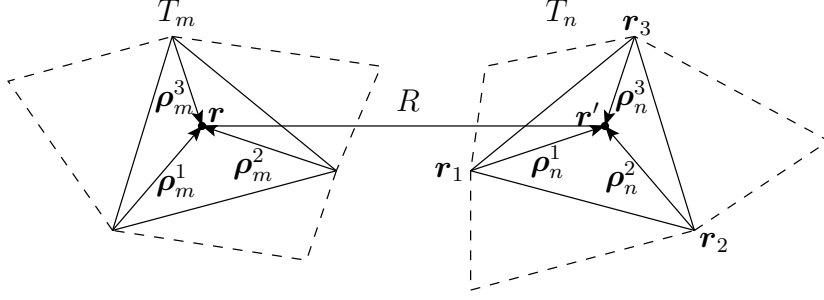

Figure 3.8: Closely separated triangular source and observation regions T_n and T_m, respectively, with uniform and linear source distributions.

the type

$$I_1 = \iint\limits_{T_m} \iint\limits_{T_n} \frac{e^{-jk_0 R}}{R}\, \mathrm{d}S'\, \mathrm{d}S \tag{3.95a}$$

$$I_2^{i;i'} = \iint\limits_{T_m} \boldsymbol{\rho}_m^i(\boldsymbol{r}) \cdot \iint\limits_{T_n} \frac{e^{-jk_0 R}}{R}\, \boldsymbol{\rho}_n^{i'}(\boldsymbol{r}')\, \mathrm{d}S'\, \mathrm{d}S \quad (i, i') \in \{1, 2, 3\}\,. \tag{3.95b}$$

Over the past decades, numerous approximations to the integrals in (3.95) have been de-veloped, both numerical and (semi)-analytical, and for various types of source distribution functions on polygonal and polyhedral domains. In the early days, approximate analytical expressions were reported only for canonical problems employing simple types of basis and testing functions [32]. Later on, simplified formulas were presented for the inner 2-D po-tential integrals in (3.95) for uniform and linear-varying source distributions on polygonal surfaces, evaluated at any point in space [65]; therein, the singularity extraction method was applied which expresses the potential integrals in (3.95) as

$$\iint\limits_{T_n} \frac{e^{-jk_0 R}}{R}\, \mathrm{d}S' = \iint\limits_{T_n} \left(\frac{e^{-jk_0 R} - 1}{R} \right) \mathrm{d}S' + \iint\limits_{T_n} \frac{1}{R}\, \mathrm{d}S' \tag{3.96a}$$

$$\iint\limits_{T_n} \boldsymbol{\rho}_n^{i'}(\boldsymbol{r}')\frac{e^{-jk_0 R}}{R}\, \mathrm{d}S' = \iint\limits_{T_n} \boldsymbol{\rho}_n^{i'}(\boldsymbol{r}') \left(\frac{e^{-jk_0 R} - 1}{R} \right) \mathrm{d}S' + \iint\limits_{T_n} \frac{\boldsymbol{\rho}_n^{i'}(\boldsymbol{r}')}{R}\, \mathrm{d}S' \tag{3.96b}$$

for $(i, i') \in \{1, 2, 3\}$. Since the static potential has been subtracted from the time-harmonic potential, the residual becomes a regular bounded function, so that it can be integrated numerically (although its first-order derivative is still discontinuous at $R = 0$), whereas the subtracted static term is singular and can be evaluated analytically. Note that the time-harmonic and static potentials are indeed integrable since [66]

$$\left\| \iint_{T_n} \begin{pmatrix} 1 \\ \boldsymbol{\rho}_n^{i'} \end{pmatrix} \frac{e^{-jk_0 R}}{R} \, dS' \right\|_2 \leq \iint_{T_n} \left\| \begin{pmatrix} 1 \\ \boldsymbol{\rho}_n^{i'} \end{pmatrix} \frac{1}{R} \right\|_2 dS' < \iint_{S_{\min}} \begin{pmatrix} 1 \\ \|\boldsymbol{\rho}_{\max}\|_2 \end{pmatrix} d\rho \, d\varphi < \infty \tag{3.97}$$

where $S_{\min}$ designates the minimum circular area containing T_n. The integrands of the static potentials can each be written as the gradient (or divergence) of some (vector) function, and such that the surface divergence theorem can be applied to transform the surface integrals into manageable contour integrals along the edges of the triangle.

Alternatively, in [67], a nonlinear transformation for the integration variables is proposed by Graglia that permits a partial analytic integration of two- and three-dimensional singularity-free potential integrals whose integration formulas for triangles are given in [68]. Yet another method expresses Green's function in terms of a power series and then invokes the surface divergence theorem to integrate each of the terms along the contour of the triangle [69]. This method turned out to be particularly efficient and accurate for small and closely spaced triangles (dense meshes). A particularly important contribution has been made by the authors of [70], who published closed-form expressions for the 4-D integrals in (3.95), concerning both the potential and testing integrals in the static self-patch case, i.e., $T_m = T_n$. Each of the 2-D surface integrations required the evaluation of three logarithmic functions. This method has been improved upon in [71], where formulas are given that are significantly simpler (three logarithmic functions in total) and are well-suited for numerical implementation, as these involve only the length of the edges, the perimeter, and the area of the triangle.

A conceptually simple and effective technique to solve the weakly singular potential integrals is known as the singularity cancellation method [66]. In this method, the Jacobian of the polar coordinate system cancels the $1/R$ singularity so that it leads to a numerically integrable integrand [*cf.* Eq. (3.97)]. This method is a special case of Duffy's coordinate transformation which generalizes the removal of such singularities to higher dimensions [72]. In a sense, this method also compares to Graglia's nonlinear coordinate-transformation method mentioned above. Following these concepts, it was shown in [73]

that through a successive application of appropriate coordinate transformations, including a Duffy transform, the original 4-D integrals can be transformed into a 1-D integral that can be evaluated via Gaussian quadrature (see also [74]).

Recently, an increased interest has arisen to obtain purely numerical schemes based upon the singularity cancellation method for integrating singular and near-singular kernels [75]. This methodology fits well within the object-oriented programming paradigms and suits multi-purpose codes. In this method, the "standard" Gaussian quadrature points and associated weights that are employed in the transformed singular-free domain, translate (map back) into new quadrature rules corresponding to the original triangle coordinates. Results have shown, however, that a relatively large number of integration points is required to achieve good accuracy. Based on this philosophy, a scheme has been proposed to numerically integrate a rational representation of the integrands using standard library routines for Gauss quadrature of rational functions [76].

In this dissertation, we will employ the well-established singularity extraction method as presented in [77]. Therein, a complete set of formulas is provided by which any number of terms can be extracted from Green's function to obtain a residual function which is sufficiently regular. Starting from the analytical result that was published in [65], each successive extracted integral term is solved in closed form through a recursive formula. In view of future extensions, it is pointed out that the formulas are readily applicable to problems dealing with homogeneous dielectric objects that are solved through a Combined Field Integral Equation (CFIE).

The semi-analytical evaluation of the electric potential integral in (3.82b) due to a uniform source distribution on a single triangular domain T_n, observed in the pth quadrature near-field point $\boldsymbol{r}_{m;p}^{\pm}$ on triangle $T_m^{\pm}$ of the mth RWG, can be computed by extracting and adding both a static and dynamic term according to

$$\Phi_{mn;p}^{\pm} = \mp \frac{\ell_n}{4\pi A_n j\omega\varepsilon_0} \iint\limits_{T_n} \frac{e^{-jk_0R}}{R}\,\mathrm{d}S' \tag{3.98a}$$

$$= \mp \frac{\ell_n}{4\pi A_n j\omega\varepsilon_0} \iint\limits_{T_n} \left(\frac{e^{-jk_0R}-1}{R} + \frac{k_0^2}{2}R \right)\mathrm{d}S'$$

$$\mp \frac{\ell_n}{4\pi A_n j\omega\varepsilon_0} \iint\limits_{T_n} \left(\frac{1}{R} - \frac{k_0^2}{2}R \right)\mathrm{d}S' \tag{3.98b}$$

where $R = \left\| \boldsymbol{r}_{m;p}^{\pm} - \boldsymbol{r}' \right\|_2$. Note that only the odd powers in R are subtracted because these

can be evaluated analytically as discussed below. Compared to the single term extraction in (3.96), the first integrand on the right-hand side of (3.98b) has now *two* continuous derivatives, so that a Gaussian integration routine will be more effective and accurate [77]. In Appendix D it is described that for a midpoint integration rule (single quadrature point), the self term can already be computed with a four-digit accuracy.

Similarly, one writes for the magnetic vector potential in (3.82a)

$$\boldsymbol{A}_{mn;p}^{\pm} = \pm \frac{\ell_n}{8\pi A_n} \iint\limits_{T_n} \boldsymbol{\rho}_n' \frac{e^{-jk_0 R}}{R}\, \mathrm{d}S' \tag{3.99a}$$

$$= \pm \frac{\ell_n}{8\pi A_n} \iint\limits_{T_n} \boldsymbol{\rho}_n' \left(\frac{e^{-jk_0 R}-1}{R} + \frac{k_0^2}{2} R \right) \mathrm{d}S'$$

$$\pm \frac{\ell_n}{8\pi A_n} \iint\limits_{T_n} \boldsymbol{\rho}_n' \left(\frac{1}{R} - \frac{k_0^2}{2} R \right) \mathrm{d}S' \tag{3.99b}$$

where we remark that, if the pth observation quadrature point $\boldsymbol{r}_{m;p}^{\pm}$ coincides with the qth source quadrature point $\boldsymbol{r}_{n;q}$, one should use that

$$\lim_{R\to 0} \left\{ \frac{e^{-jk_0 R}-1}{R} \right\} = -jk. \tag{3.100}$$

Even though closed-form expressions are known for the 4-D integrals pertaining to the $1/R$ terms in (3.98b) and (3.99b) [71], there are still good reasons to test each of the above integral terms numerically since: (i) analytical expressions are only known in the fully overlapping case, and; (ii) this is consistent with the numerical evaluation of the other terms which better suits the object-oriented programming paradigms. Now that the testing is performed numerically, the remaining 2-D potential integral terms are computed analytically and are of the type (*cf.* ref. [77]):

$$K_1^\alpha = \iint\limits_{T_n} R^\alpha\, \mathrm{d}S' \tag{3.101}$$

$$\boldsymbol{K}_2^\alpha = \iint\limits_{T_n} R^\alpha (\boldsymbol{r}' - \boldsymbol{q})\, \mathrm{d}S' \tag{3.102}$$

for $\alpha = \{-1, 1, 3, \ldots\}$, and for any arbitrary observation point $\boldsymbol{r}$ with $R^\alpha = \|\boldsymbol{r} - \boldsymbol{r}'\|_2^\alpha$. Furthermore, $\boldsymbol{q}$ denotes a corner vertex of triangle T_n such that $\boldsymbol{\rho}_n' = \boldsymbol{r}' - \boldsymbol{q}$.

In order to express (3.101) and (3.102) in a convenient analytic form, it is necessary to introduce a number of geometrical quantities. Note that, with reference to Fig. 3.9, a local
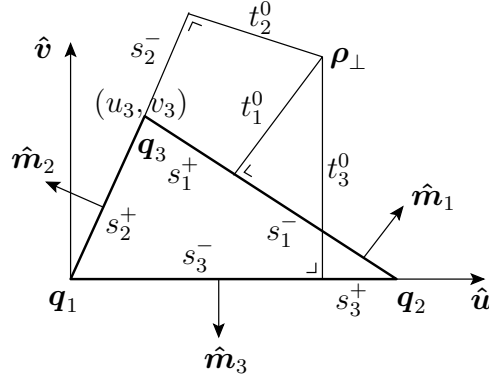
Figure 3.9: Geometrical notations used in the analytical integration of uniform and linear-varying (vector) functions over triangular supports.

cartesian coordinate system $\{\hat{\boldsymbol{u}}, \hat{\boldsymbol{v}}, \hat{\boldsymbol{w}}\}$ is employed with $\hat{\boldsymbol{u}} = (\boldsymbol{q}_2 - \boldsymbol{q}_1)/\ell_3$. The segment length ℓ_i is the length of the ith edge opposing the corner vertex $\boldsymbol{q}_i$, and $\hat{\boldsymbol{n}}$ denotes the unit normal to the triangle, so that $\hat{\boldsymbol{v}} = \hat{\boldsymbol{n}} \times \hat{\boldsymbol{u}}$. The triangle is positioned in the uv-plane with its base oriented along the u-axis whose end points are given by $\boldsymbol{q}_1 = (0, 0, 0)$ and $\boldsymbol{q}_2 = (\ell_3, 0, 0)$. The corner vertex $\boldsymbol{q}_3$ is located at $(u_3, v_3, 0)$, with $u_3 = (\boldsymbol{q}_3 - \boldsymbol{q}_1) \cdot \hat{\boldsymbol{u}}$ and $v_3 = 2A/\ell_3$, where A is the area of the triangle. Since $\boldsymbol{q}_1$ represents the local origin, the position vector $\boldsymbol{r}$ is readily expressed in local coordinates (u_0, v_0, w_0) by $u_0 = (\boldsymbol{r} - \boldsymbol{q}_1) \cdot \hat{\boldsymbol{u}}$, $v_0 = (\boldsymbol{r} - \boldsymbol{q}_1) \cdot \hat{\boldsymbol{v}}$, and $w_0 = (\boldsymbol{r} - \boldsymbol{q}_1) \cdot \hat{\boldsymbol{n}}$. Finally, the projection of the vector $\boldsymbol{r}$ on the plane of the triangle is defined by $\boldsymbol{\rho}_\parallel = \boldsymbol{r} - w_0 \hat{\boldsymbol{n}}$, with w_0 representing the height above the plane of the triangle.

With the aid of the preceding geometrical quantities, we define the relevant quantities

$$R_1^+ = R_2^- = \|\boldsymbol{r} - \boldsymbol{q}_3\|_2 \qquad R_2^+ = R_3^- = \|\boldsymbol{r} - \boldsymbol{q}_1\|_2 \qquad R_3^+ = R_1^- = \|\boldsymbol{r} - \boldsymbol{q}_2\|_2 \qquad (3.103)$$

which are the distance metrics from the begin and end points of the line sections to the observation point $\boldsymbol{r}$. The perpendicular distances t_i^0, for $i = 1, 2, 3$, measured from the projected point $\boldsymbol{\rho}_\parallel$ to the ith line segment (or its extension), are given as (see Fig. 3.9)

$$t_1^0 = \frac{v_0 (u_3 - \ell_3) + v_3 (\ell_3 - u_0)}{\ell_1} \qquad t_2^0 = \frac{u_0 v_3 - v_0 u_3}{\ell_2} \qquad t_3^0 = v_0 \qquad (3.104)$$

and are readily derived by using similarity rules between triangles. The proper signs have been incorporated to ensure that the associated normals $\{\hat{\boldsymbol{m}}_i\}$ point in the outward direction. Also, it is defined that

$$R_i^0 = \sqrt{\left(t_i^0\right)^2 + w_0^2} \qquad i \in \{1, 2, 3\}. \qquad (3.105)$$

The contours are parameterized by the arc length variables $\{\ell'_i\}$, measured from the plane which is perpendicular to the ith line segments (or their extensions) and passes through the point $\boldsymbol{r}$. The unit vectors $\{\hat{\boldsymbol{m}}_i\}$ and $\{\hat{\boldsymbol{\ell}}_i\}$ represent a local reference frame for the corresponding line segment, with end points $\{s_i^-\}$ and $\{s_i^+\}$. By accounting for the specified directions of $\{\hat{\boldsymbol{s}}_i\}$, the end points in terms of arc lengths can also be derived from triangle similarities. These are given by (*cf.* Fig. 3.9)

$$s_1^- = -\frac{(\ell_3 - u_0)(\ell_3 - u_3) + v_0 v_3}{\ell_1} \qquad s_2^- = -\frac{u_3 (u_3 - u_0) + v_3 (v_3 - v_0)}{\ell_2} \qquad s_3^- = -u_0 \tag{3.106}$$

together with

$$s_1^+ = s_1^- + \ell_1 \qquad s_2^+ = s_2^- + \ell_2 \qquad s_3^+ = s_3^- + \ell_3. \tag{3.107}$$

From Eqs. (3.103)–(3.107), it is derived in [65] that for the ith edge,

$$I_i^{-1} = \iint\limits_{\partial_i T_n} \frac{1}{R} \, \mathrm{d}\ell' = \ln\left(\frac{R_i^+ + s_i^+}{R_i^- + s_i^-}\right) \tag{3.108}$$

and with the recursive relation in [77], higher-order terms in α are computed as

$$I_i^\alpha = \iint\limits_{\partial_i T_n} R^\alpha \, \mathrm{d}\ell' = \frac{1}{1 + \alpha}\left(s_i^+ (R_i^+)^\alpha - s_i^- (R_i^-)^\alpha + \alpha (R_i^0)^2 I_i^{\alpha-2}\right) \tag{3.109}$$

for $\alpha = 1, 3, 5, \ldots$ Also, from [68], it is known that

$$w_0 K_1^{-3} = w_0 \iint\limits_{T_n} \frac{1}{R^3} \, \mathrm{d}S' = \begin{cases} 0 & w_0 = 0 \\ \dfrac{w_0}{|w_0|} \displaystyle\sum_{i=1}^{3} \beta_i & \text{otherwise} \end{cases} \tag{3.110}$$

where, for $w_0 \neq 0$,

$$\beta_i = \begin{cases} \arctan\left(\dfrac{t_i^0 s_i^+}{(R_i^0)^2 + |w_0| R_i^+}\right) - \arctan\left(\dfrac{t_i^0 s_i^-}{(R_i^0)^2 + |w_0| R_i^-}\right) & t_i^0 \neq 0 \\ 0 & \text{otherwise} \end{cases} \tag{3.111}$$

so that the integrals in (3.101) and (3.102) can be evaluated analytically by means of the

relations [77]

$$K_1^\alpha = \begin{cases} \dfrac{1}{2+\alpha} \displaystyle\sum_{i=1}^{3} t_i^0 I_i^\alpha & w_0 = 0 \\[4mm] \dfrac{1}{2+\alpha} \left(\alpha w_0^2 K_1^{\alpha-2} + \displaystyle\sum_{i=1}^{3} t_i^0 I_i^\alpha \right) & \text{otherwise} \end{cases} \tag{3.112}$$

$$\boldsymbol{K}_2^\alpha = \left(\boldsymbol{\rho}_\parallel - \boldsymbol{q}\right) K_1^\alpha + \frac{1}{2+\alpha} \sum_{i=1}^{3} I_i^{2+\alpha} \boldsymbol{m}_i. \tag{3.113}$$

3.4.7   Numerical Stability of the Singularity Subtraction Method

In order to obtain a highly accurate moment matrix, it is advised to analytically integrate the singular terms whenever the source and observation triangles have at least one edge (or even a vertex) in common [71], i.e., for the self patch and the nearest neighbors. Mathematically, the above equations are well-suited for this purpose as these are valid at any observation point $\boldsymbol{r} \in \mathbb{R}^3$. However, in practice, close-to-machine-precision evaluation of the integrals is usually not required. For instance, in [75], it has been conjectured that three to four correctly computed significant digits are sufficient in the numerical solution of the potentials, and this is consistent with the evaluation of the remaining terms and the approximation leading to the MoM matrix system. It will be shown in Section 3.6 that the desired accuracy of the moment matrix elements can indeed be reached by employing a low-order quadrature integration rule, without using singularity subtraction techniques for non-coincident triangles. Moreover, we found that the singularity substraction method yields numerically unstable solutions for certain specific observation points outside of the source triangle. This problem has been detailed below and a possible remedy is proposed to overcome this numerical instability.

A numerical instability is encountered when (3.112) is evaluated for a quadrature point $\boldsymbol{r}$ inside an observation triangle T near the edges of the source triangle T' or its extensions (dashed line in Fig. 3.10).

The geometrical notations of the previous section will be applied to the triangle T' to orient it in the uv-plane. To expose the problem, it is sufficient to evaluate Eq. (3.112) only for the edge $i = 3$ (opposite of $\boldsymbol{q}_3$) and for $\alpha = -1$. For the sake of generality, the quadrature point $\boldsymbol{r}$ has been lifted $w_0 = (\boldsymbol{r} - \boldsymbol{q}_1) \cdot \hat{\boldsymbol{n}}$ out of the plane of the source triangle, as indicated
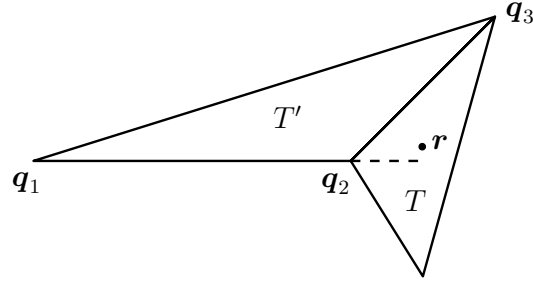
Figure 3.10: Quadrature point $\boldsymbol{r}$ near the edge extension of the source triangle T'.
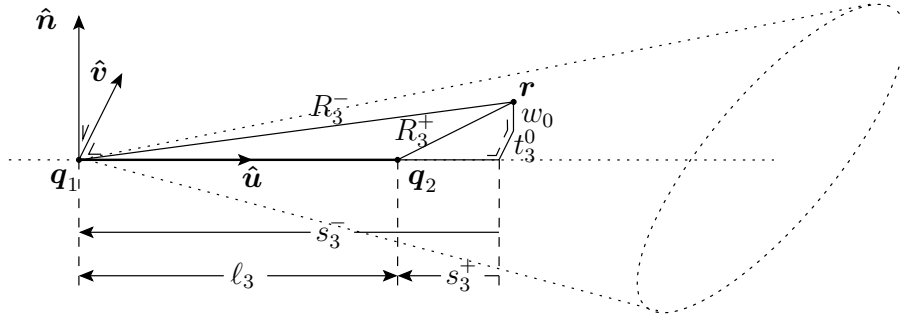
Figure 3.11: Quadrature point $\boldsymbol{r}$ near the extension of the edge $i = 3$.

in Fig. 3.11. We then have that: $t_3^0 = (\boldsymbol{r} - \boldsymbol{q}_1) \cdot \hat{\boldsymbol{v}}$; $s_3^- = -(\boldsymbol{r} - \boldsymbol{q}_1) \cdot \hat{\boldsymbol{u}}$; $s_3^+ = s_3^- + \ell_3$ and; $R_3^\pm = \sqrt{(s_3^\pm)^2 + (t_3^0)^2 + w_0^2}$. Note that $R_3^\pm \geq 0$, as opposed to t_3^0 as well as the arc lengths $s_3^\pm$, which may become negative. From Eq. (3.112), with $i = 3$ and $\alpha = -1$, one observes that in the limiting case

$$\lim_{t_3^0 \to 0, w_0 \to 0} \left\{ t_3^0 \ln \left(\frac{\sqrt{(s_3^+)^2 + (t_3^0)^2 + w_0^2} + s_3^+}{\sqrt{(s_3^-)^2 + (t_3^0)^2 + w_0^2} + s_3^-} \right) \right\} = 0 \qquad (3.114)$$

but the evaluation of this function becomes numerically unstable when t_3^0 and w_0 are almost zero. The elliptically shaped cone in Fig. 3.11 represents the region of instability. The cone increases in the positive direction of $\hat{\boldsymbol{u}}$ inside of which a term $\ln(0/0)$ or $\ln(./0)$ is encountered. We conclude that the region of instability is not biconically shaped since the numerical instability does not occur along the left edge extension where $s_3^\pm$ are both positive. The region of instability increases for increasing $\hat{\boldsymbol{u}}$ because $|s_3^\pm|$ increases, which implies that $|t_3^0|$ and $|w_0|$ have to be increased as well in order to avoid numerical instabilities. Finally, the conical region is elliptically shaped because the instability is more pronounced for small $|w_0|$. The above statements have been validated by the numerical evaluation of (3.114) for various observation points.

Since the numerical inaccuracies are only encountered in the positive $\hat{\boldsymbol{u}}$ direction, these instabilities may be reduced by numbering the triangle vertices not in a clockwise but counterclockwise direction as illustrated in Fig. 3.12. Nonetheless, this (rather cumbersome)

(a)   (b)
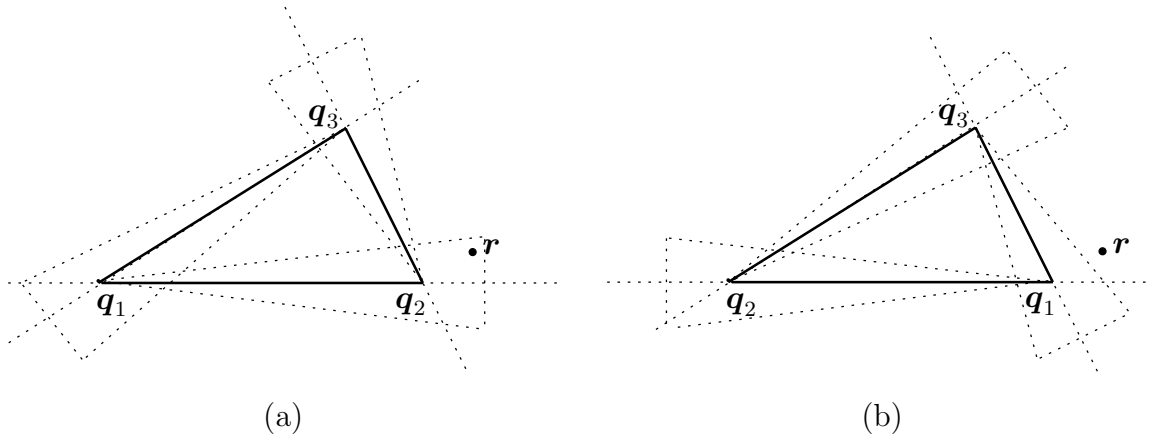
Figure 3.12: Numerically instable regions for anticlockwise and clockwise vertex numbering schemes, respectively.

solution has not been implemented since the singularity subtraction method turns out to be sufficiently adequate when solely applied to fully overlapping triangles (*cf.* Section 3.6).

Often, the associated residual integral terms as well as the reaction integrals are computed by means of a $P = 7$ points Gaussian quadrature rule. When the separation distance d between a pair of RWGs becomes sufficiently large, an adaptive numerical integration scheme can be employed, so that the total number of correctly computed most significant digits of each of the moment matrix elements remains constant as a function of the RWG separation distance d. This reduces the total matrix fill time and prevents that the smaller matrix entries are computed too accurately with respect to those having a larger magnitude. For instance, to compute the moment matrix elements with an accuracy that exceeds 4–6 digits accuracy, which is generally considered (more than) adequate, it suffices to select a numerical integration scheme with $P = 7$ when $d < \lambda_0/10$, $P = 3$ when $\lambda_0/10 \leq d < \lambda_0/5$, and $P = 1$ when $d \geq \lambda_0/5$. The latter criteria have been determined empirically as described in Appendix D.

3.4.8   Solution of the Matrix Equation

From the preceding sections, we are now left with the matrix equation $\mathbf{ZI} = \mathbf{V}$. The matrix $\mathbf{Z}$ is a square, complex symmetric matrix, i.e., $\mathbf{Z} = \mathbf{Z}^T \in \mathbb{C}^{N \times N}$ with T the transposition operator. The unknown expansion coefficient vector $\mathbf{I}$ is of size $N \times 1$ and can, for relatively small matrices (depending upon the RAM memory), be determined in a non-iterative manner through Gaussian elimination. In that case, the matrix $\mathbf{Z}$ is factored into $\mathbf{L}$ and $\mathbf{U}$ to obtain the matrix system

$$\mathbf{LUI} = \mathbf{V} \tag{3.115}$$

which is a convenient form when evaluating (3.115) for multiple right-hand sides (MRHS), that is, for a large number of excitation vectors $\mathbf{V}$. Thus, instead of explicitly forming the inverse of $\mathbf{Z}$, one solves the two triangular systems $\mathbf{LX} = \mathbf{V}$ for the unknown vector $\mathbf{X}$ (forward substitution), and then $\mathbf{UI} = \mathbf{X}$ for the unknown vector $\mathbf{I}$ (backward substitution). The LU-factorization requires $\sim \frac{2}{3}N^3$ flops, while the forward and backward substitution each require $\sim N^2$ flops (per excitation vector) [78, p. 152].

The matrix $\mathbf{Z}$ is assumed to be invertable (nonsingular), which implies that $\mathrm{rank}\,(\mathbf{Z}) = N$, that the range $\mathcal{R}\,(\mathbf{Z}) = \mathbb{C}^N$, that the nullspace $\mathcal{N}\,(\mathbf{Z}) = \{0\}$, that 0 is not an eigenvalue or singular value of $\mathbf{Z}$, and that the determinant $\det\,(\mathbf{Z}) \neq 0$. For diagnostic reasons, and to assure a numerically stable solution for $\mathbf{I}$, it is sometimes convenient to monitor the invertibility of $\mathbf{Z}$ through its condition number by applying the Singular Value Decomposition (SVD) as explained below.

The SVD is used to factorize a matrix $\mathbf{A} \in \mathbb{C}^{M \times N}$ (not necessarily square) into a product chain of the three matrices [78, p. 29],

$$\mathbf{A} = \mathbf{UDQ}^H \tag{3.116}$$

where the superscript H denotes the complex conjugate transpose and where $\mathbf{U} \in \mathbb{C}^{M \times M}$ is a unitary matrix, so that $\mathbf{U}^{-1} = \mathbf{U}^H$, which implies that the columns in U are orthonormal. Furthermore, $\mathbf{Q} \in \mathbb{C}^{N \times N}$ is unitary, and $\mathbf{D} = \mathrm{diag}\{\sigma_1, \sigma_2, \ldots, \sigma_N\}$ is a rectangular diagonal matrix of size $M \times N$ whose nonnegative real-valued entries are the singular values of $\mathbf{A}$ which can be required to be ordered as $\sigma_1 \geq \sigma_2 \geq \cdots \geq \sigma_N \geq 0$. Applying the SVD to Eq. (3.115), and using the fact that $\mathbf{A} = \mathbf{A}^T$ is complex symmetric, yields

$$\mathbf{I} = \mathbf{QD}^{-1}\mathbf{U}^H\mathbf{V} = \sum_{n=1}^{N} \frac{1}{\sigma_n}\,(\mathbf{u}_n^* \cdot \mathbf{V})\,\mathbf{q}_n \tag{3.117}$$

where $\mathbf{u}_n$ are the left-singular vectors of $\mathbf{A}$ (columns of $\mathbf{U}$) and $\mathbf{q}_n$ are the right-singular vectors of $\mathbf{A}$ (columns of $\mathbf{Q}$). Singular values of zero or near-zero magnitude indicate that the matrix $\mathbf{Z}$ is singular or ill-conditioned and, consequently, the solution $\mathbf{I}$ may be inaccurate since the projection of $\mathbf{V}$ on each of the conjugated basis vectors $\{\mathbf{u}_n^*\}$ is divided by its corresponding singular value [see Eq. (3.117)]. Obviously, the relative magnitude of the vectors in (3.117) depends on the structure of $\mathbf{Z}$ as well as on the excitation vector $\mathbf{V}$ through the inner product term $(\mathbf{u}_n^* \cdot \mathbf{V})$, which may be small for large n due to cancellation effects. The latter depends on the physics of the problem [79].

The condition number $\kappa(\mathbf{Z})$ of the matrix $\mathbf{Z}$ is an important measure to quantify the solution stability of $\mathbf{I}$ in terms of perturbations in $\mathbf{Z}$ [78, p. 95]. The 2-norm condition number is defined as

$$\kappa(\mathbf{Z}) = \|\mathbf{Z}\|_2 \|\mathbf{Z}^{-1}\|_2 = \frac{\sigma_{\max}(\mathbf{Z})}{\sigma_{\min}(\mathbf{Z})} \tag{3.118}$$

and is a measure of the spread in the singular values. It is worthwhile to mention that one should expect losing $\log_{10}\kappa(\mathbf{Z})$ digits in computing the solution vector $\mathbf{I}$. For instance, when using double-precision floating-point arithmetic, which has a machine precision $\epsilon \approx 10^{-16}$, the condition number should not exceed 10^M in order to retain at least $16 - M$ correctly computed significant digits[3].

3.5 Generalized Scattering Matrix of an Antenna

To obtain the numerical approximation of the surface current $\boldsymbol{J}_S$, we substitute (3.115) in (3.53) and this, in turn, enables us to compute the relevant antenna characteristics. Fig. 3.13 depicts the generalized scattering-matrix representation of antennas [80, pp. 123–133], one identifies: (i) the power reflection characteristics at the antenna ports (upper-left matrix block); (ii) the radiated power waves from the antenna (through fictitious ports in the sky, lower-left matrix block); (iii) the scattering or reradiation power characteristics from the antenna (lower-right matrix block), and; (iv) the transfer characteristics of the power waves that are incident on the antenna to those that emanate from the antenna output ports on receive (upper-right matrix block). The first two pertain to the transmit

---

[3]The machine epsilon must be enlarged by a factor on the order of $2^{5/2}$ when dealing with complex floating point arithmetic [78, p. 100]
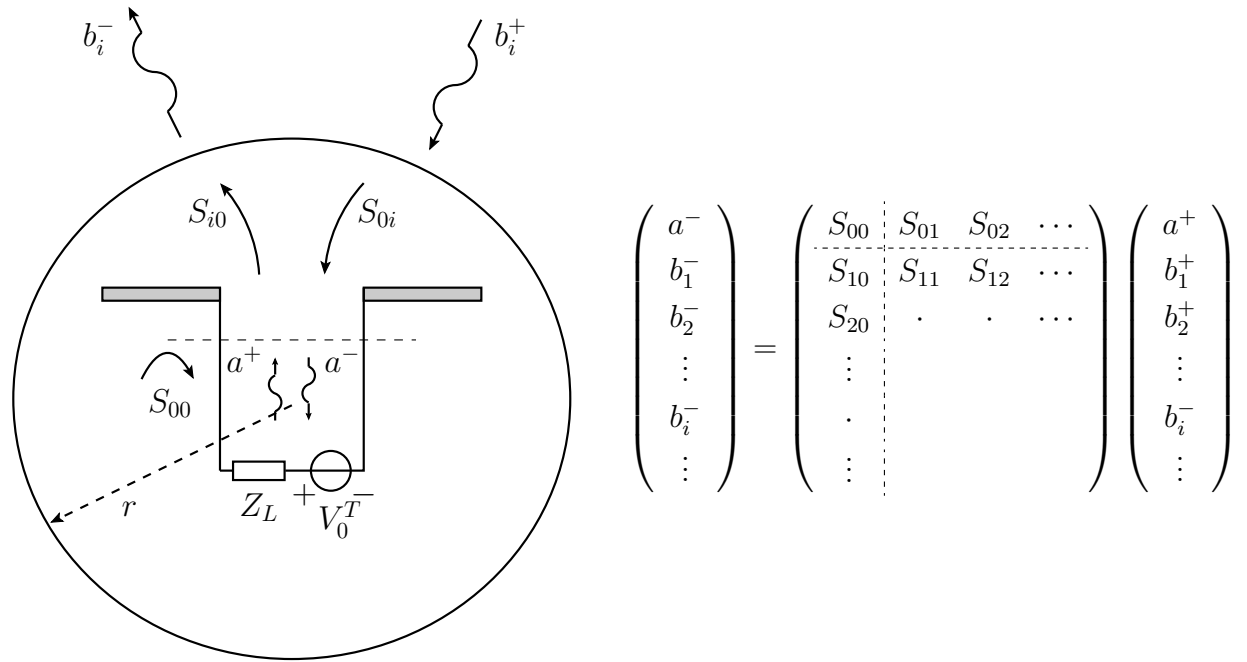
Figure 3.13: Generalized scattering-matrix representation of a single antenna element.

situation and are elaborated below, while the latter two are receive characteristics which are examined in Chapter 5 by exploiting electromagnetic reciprocity principles.

The amplitudes $\{b_i^+\}$ and $\{b_i^-\}$ are the modal amplitudes for the inward and outward traveling vector wave functions, respectively. Depending on the application, it is often convenient to choose for a spherical-mode or plane-wave spectral representation. In the far field ($r \to \infty$), we prefer a plane-wave representation, so that $1/2(b_i^-)(b_i^-)^*$ directly represents the total emitted (or reflected) power into one specific solid angle or direction. The radiation (or scattering) patterns are obtained by computing the radiated (or scattered/reradiated) power over angle.

3.5.1   Antenna Transmit Characteristics

Antenna Input Admittance Characteristics

We will analyze two methods to compute the input admittance of an antenna: (i) through a direct division of the induced port current by the voltage amplitude of the source, and;

(ii) through an integral expression which is of a variational form (reaction) and known to be stationary for perturbed solutions of the currents. Even though the direct gap impedance calculation may be considered inaccurate and unstable, it will be demonstrated that both methods yield identical results once the current has been computed. In EFIE formulations, the surface currents are computed by exciting the antennas with voltage sources (incident electric field), while all other terminals are then short-circuited so that the admittance matrix is obtained naturally, without additional manipulations. In order to obtain the antenna impedance matrix, one simply inverts the admittance matrix.

Consider the circuit source model in Fig. 3.14(a). By definition, the positive direction of the current is defined such that the current exits the plus terminal of a voltage source. The voltage source is assumed to have no internal impedance, so that the incident and scattered electric fields inside the voltage source are oppositely directed (total internal $\boldsymbol{E}$ field is zero). However, external to the voltage source, the incident and scattered electric fields point in the same direction. Also, the direction of the magnetic current $\boldsymbol{M}$ is chosen such that it generates an incident electric field in the positively defined direction of the port current (see also Appendix E). A voltage V^{ant} can be defined if the port region is much smaller than the free-space wavelength λ_0, and such that within this electrically small region we may introduce an electric scalar potential Φ through the locally quasi-static relation $\boldsymbol{E} = \boldsymbol{E}^i + \boldsymbol{E}^s = -\boldsymbol{\nabla}\Phi$, where the potential difference $\Phi^+ - \Phi^-$ between the plus and minus terminals equals the port voltage V^{ant}.
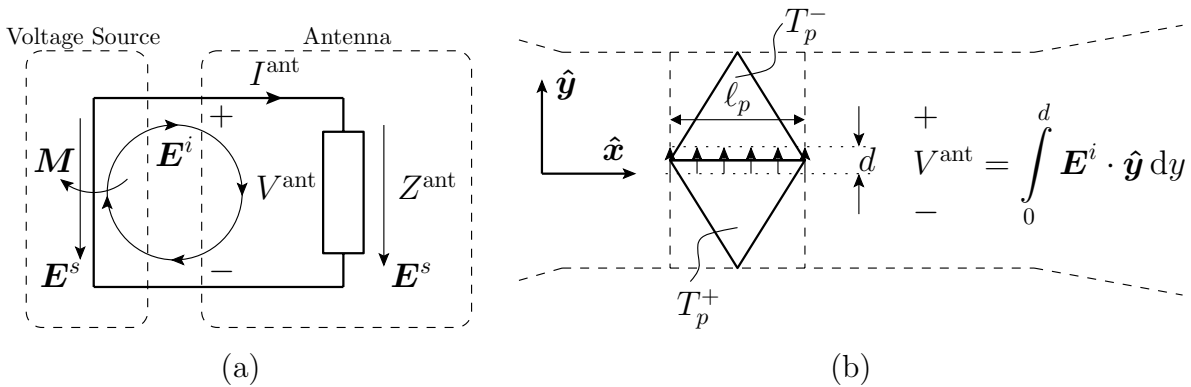

Figure 3.14: Voltage source model for feeding a metallic structure: (a) circuit model; (b) RWG model.

The electric field, which is generated in Fig. 3.14(a) by a magnetic-frill current, will henceforth be approximated by an artificial incident electric field that exists only inside the port

region across a pair of triangular facets [see Fig. 3.14(b)], i.e.,

$$\boldsymbol{E}^i = \begin{cases} \dfrac{V^{\mathrm{ant}}}{d} \hat{\boldsymbol{y}} & \boldsymbol{r} \in \text{port region} \\ \boldsymbol{0} & \text{elsewhere.} \end{cases} \tag{3.119}$$

Furthermore, Fig. 3.14(b) illustrates that the port current can be synthesized by a single RWG basis function and that the plus and minus polarity of the voltage source corresponds to the T_p^+ and T_p^- triangle of the pth RWG (the port RWG), respectively. As the incident electric field is assumed to exist only across the conductor surface for $0 \leq y \leq d$, the total electric field just external to the source region is $\boldsymbol{E} = \boldsymbol{E}^s$ (since $\boldsymbol{E}^i = \boldsymbol{0}$ there). Consequently, $\boldsymbol{E} = \boldsymbol{E}^s = -\nabla \Phi = -\boldsymbol{E}^i$, where the latter equality follows on account of the boundary condition for PEC surfaces (the voltage source has a zero-internal impedance). Note that this is in agreement with the circuit model in Fig. 3.14(a), albeit that $\boldsymbol{E}^i = \boldsymbol{0}$ across the load impedance for a localized incident field. Similar voltage-current and field relations have been presented in [81, p. 61], although the current is therein defined to exit the minus terminal of the voltage source, which may lead to a sign inconsistency in the antenna input impedance calculations.

In case $d \to 0$, the so-called voltage-gap model is obtained [*cf.* Fig. 3.14(b)], i.e.,

$$\boldsymbol{E}^i = V^{\mathrm{ant}} \delta\left(y\right) \left[U\left(x\right) - U\left(x - \ell_p\right)\right] \left[U\left(z + 0^+\right) - U\left(z - 0^+\right)\right] \hat{\boldsymbol{y}} \qquad \boldsymbol{r} \in \mathbb{R}^3 \tag{3.120}$$

which satisfies the voltage definition in Fig. 3.14(b). The Heaviside-step function is denoted by U. The electric field $\boldsymbol{E}^i$ is only associated to the common edge of the RWG that is shown in Fig. 3.14(b), i.e., it represents a combination of a pulse function along the direction of the common edge (x direction), and a delta function across (normal to) this edge (y direction). The unit of the electric field must be [Vm^{-1}], and because the unit of the delta-distribution function is [m^{-1}], the electric field should not have a delta dependence in the z direction.

The term "gap" may be misleading as one could think of a physical gap consisting of air (or vacuum). However, the voltage source has no internal impedance and does not represent a capacitor, but a short circuit. The mth element of the voltage excitation vector $\mathbf{V}$ on the right-hand side of (3.62) is evaluated as

$$V_m = -\langle \boldsymbol{E}^i, \boldsymbol{f}_m \rangle = -V^{\mathrm{ant}} \iint\limits_{\mathcal{S}_m} \left(\boldsymbol{f}_m \cdot \hat{\boldsymbol{y}}\right) \delta\left(\boldsymbol{r} - \boldsymbol{r}_{\mathrm{gap}}\right) \mathrm{d}S = \begin{cases} -V^{\mathrm{ant}} \ell_p & m = p \\ 0 & \text{otherwise} \end{cases}$$

$$\tag{3.121}$$

where we used that $(\boldsymbol{f}_m \cdot \hat{\boldsymbol{y}}) = 1$ at the common edge of the pth RWG. Since the voltage vector is given by $\mathbf{V} = [0, \ldots, -V^{\mathrm{ant}}\ell_p, \ldots, 0]^T$, the current expansion coefficient vector $\mathbf{I} = [I_1, \ldots, I_p, \ldots, I_N]^T$ is obtained through the mapping $\mathbf{I} = \mathbf{Z}^{-1}\mathbf{V}$. Because the total port current is given by $I^{\mathrm{ant}} = I_p\ell_p$, the self-admittance Y_{11}^{ant} of the antenna is directly computed as

$$Y_{11}^{\mathrm{ant}} = \frac{I^{\mathrm{ant}}}{V^{\mathrm{ant}}} = \frac{I_p\ell_p}{V^{\mathrm{ant}}} = -\frac{I_p\ell_p^2}{V_p}. \tag{3.122}$$

To compute the admittance matrix of a N_p-port antenna array, we sequentially excite each port by a unit-voltage amplitude, while the other ports are short-circuited, and then compute the N_p resulting expansion coefficient vectors through repeatedly solving the matrix system $\mathbf{ZI} = \mathbf{V}$, or directly for multiple RHS as $\mathbf{I} = \mathbf{Z}^{-1}\mathbf{V}$. In the latter case, the columns of the matrix $\mathbf{V}$ are the N_p excitation vectors, while the matrix $\mathbf{I}$ holds the N_p resulting expansion coefficient vectors. Upon taking the N_p rows of $\mathbf{I}$ that correspond to the RWG port indices, and by multiplying these with their associated common-edge lengths, the $N_p \times N_p$ admittance matrix $\mathbf{Y}^{\mathrm{ant}}$ is obtained, which holds the self and mutual admittances between all accessible ports.

Alternatively, the mutual admittance Y_{ab}^{ant} between two accessible ports a and b can also be computed in terms of a reaction integral, which is of a variational form. Suppose that $\boldsymbol{J}_S^a$ is the array surface current distribution that results from exciting terminal a with a voltage source of amplitude V_a, while all other terminals are short-circuited. Likewise, $\boldsymbol{J}_S^b$ is a result of exciting terminal b with V_b, while all other terminals are short-circuited. A stationary formula for the mutual antenna admittance Y_{ab}^{ant} has been derived in Appendix E with the aid of the Lorentz reciprocity theorem; the resulting expression is

$$Y_{ab}^{\mathrm{ant}} = \frac{-1}{V_a V_b} \iint\limits_{\mathcal{S}_a} \boldsymbol{E}^s(\boldsymbol{J}_S^b) \cdot \boldsymbol{J}_S^a \, \mathrm{d}S. \tag{3.123}$$

It is important to note that a minus sign appears in front of (3.123); this is contrary to the plus sign presented in [32, p. 109], which may be explained from the observation that the total electric field is meant in [32], not the scattered field.

Next, we expand the current for both excitations $i = \{a, b\}$ in terms of N RWGs, i.e.,

$$\boldsymbol{J}_S^i(\boldsymbol{r}) = \sum_{n=1}^{N} I_n^i \boldsymbol{f}_n(\boldsymbol{r}) \tag{3.124}$$

and substitute this expansion in (3.123) to obtain

$$
Y_{ab}^{\text{ant}} = \frac{-1}{V_a V_b} \sum_{n=1}^{N} \sum_{m=1}^{N} I_n^b \left[\iint_{\mathcal{S}_a} \boldsymbol{E}^s(\boldsymbol{f}_n) \cdot \boldsymbol{f}_m \, dS \right] I_m^a = \frac{1}{V_a V_b} \sum_{n=1}^{N} \sum_{m=1}^{N} I_n^b Z_{mn}^{\text{PEC}} I_m^a \quad (3.125a)
$$

$$
= \frac{-1}{V_a V_b} (\mathbf{I}^b)^T (\mathbf{Z}^{\text{PEC}})^T \mathbf{I}^a \quad (3.125b)
$$

where we have used the linearity of the operators contained in $\boldsymbol{E}^s$, and where $\{\mathbf{I}^{i \in \{a,b\}}\}$ are the expansion coefficient vectors of $\boldsymbol{J}_S^{i \in \{a,b\}}$. Since we will determine the solution $\mathbf{I}^a$ from the linear equation $\mathbf{I}^a = (\mathbf{Z}^{\text{PEC}})^{-1} \mathbf{V}^a$, with $\mathbf{V}^a = [0, \ldots, -V_p^a \ell_p, \ldots, 0]^T$, and because $\mathbf{Z}^{\text{PEC}} = (\mathbf{Z}^{\text{PEC}})^T$, the latter expression readily simplifies to

$$
Y_{ab}^{\text{ant}} = \frac{-1}{V_a V_b} (\mathbf{I}^b)^T \mathbf{V}^a = \frac{I_p^b V_p^a \ell_p}{V_a V_b} = \left. \frac{I_a}{V_b} \right|_{V_a = 0} \quad (3.126)
$$

since $I_p^b \ell_p = I_a$ is the total current through port a due to a voltage excitation at port b. Clearly, Eq. (3.126) has an identical form to that of (3.122), which means that it suffices to simply take the current-voltage ratio directly at the port. The success of this approach may be explained by recognizing the field reactions in (3.125a) as the moment matrix elements for PEC surfaces, which are also defined through reactions. This is a result of testing the EFIE by a symmetric product, which can also be viewed as testing it through an inner product with conjugated test functions or, otherwise, by taking real-valued basis and test functions. Furthermore, the port current is readily available from the solution when the voltage-source model in Fig. 3.14(b) is used. The respective post-processing step in the moment-method formulation is therefore of a variational form since the stationary integral formula, Eq. (3.123), does not lead to a more stable/accurate scheme for computing the input admittance than the direct approach in (3.122), in fact; the results are identical.

Far-Field Radiation From Surface Currents

This section addresses the numerical computation of the radiated electromagnetic field at a large distance from a surface current $\boldsymbol{J}_S$ which is of finite extent and located in the vicinity of the coordinate origin. The radiated magnetic field outside the source region is obtained by combining Eqs. (2.27a)–(2.27e); it takes the form

$$
\boldsymbol{H}(\boldsymbol{r}) = \frac{1}{4\pi} \boldsymbol{\nabla} \times \iint_{\mathcal{S}} \boldsymbol{J}_S(\boldsymbol{r}') \frac{e^{-jk_0 \|\boldsymbol{r} - \boldsymbol{r}'\|_2}}{\|\boldsymbol{r} - \boldsymbol{r}'\|_2} \, dS'. \quad (3.127)
$$

In the far field it is assumed that the condition $r = \|\boldsymbol{r}\|_2 \gg \|\boldsymbol{r}'\|_2 = r'$ holds, such that both $R = \|\boldsymbol{r} - \boldsymbol{r}'\|_2 \approx r - (\hat{\boldsymbol{r}} \cdot \boldsymbol{r}')$ and $R \approx r$ are sufficiently good approximations for the respective phase and amplitude terms. Furthermore, it is convenient to introduce the spherical coordinates $\boldsymbol{r}(r, \theta, \phi) = r\hat{\boldsymbol{r}} + \theta\hat{\boldsymbol{\theta}} + \phi\hat{\boldsymbol{\phi}}$ along with $\hat{\boldsymbol{r}}(\theta, \phi) = \sin(\theta)\cos(\phi)\hat{\boldsymbol{x}} + \sin(\theta)\sin(\phi)\hat{\boldsymbol{y}} + \cos(\theta)\hat{\boldsymbol{z}}$, and subsequently utilize that, for outward traveling plane waves, the curl operator $\boldsymbol{\nabla} \times$ can be replaced by $-j\boldsymbol{k}_0 \times$ where $\boldsymbol{k}_0 = k_0\hat{\boldsymbol{r}}$ is the outward pointing wave vector. Then, by subjecting (3.127) to the aforementioned approximations, which are exact for $R \to \infty$, it is observed that the magnetic far field $\boldsymbol{H}^{\text{far}}(r, \theta, \phi)$ can be written as

$$\boldsymbol{H}^{\text{far}}(r, \theta, \phi) = \frac{-jk_0 e^{-jk_0 r}}{4\pi r} \hat{\boldsymbol{r}} \times \iint_{\mathcal{S}} \boldsymbol{J}_S(\boldsymbol{r}') e^{j(\boldsymbol{k}_0 \cdot \boldsymbol{r}')} \, \mathrm{d}S'. \tag{3.128}$$

Accordingly, we substitute the basis function expansion (3.53) in conjunction with (3.70) in (3.128), and use the numerical efficient midpoint integration rule

$$\iint_{T} \boldsymbol{f}(\boldsymbol{r}) \, \mathrm{d}S \approx A\boldsymbol{f}(\boldsymbol{r}_c) \tag{3.129}$$

where A is the area of a triangle T, and $\boldsymbol{r}_c$ is the centroid of the triangle. As a result, Eq. (3.128) is discretized as

$$\boldsymbol{H}^{\text{far}} \approx \frac{-jk_0 e^{-jk_0}}{8\pi} \sum_{n=1}^{N} I_n \ell_n \, \hat{\boldsymbol{r}} \times \left[\frac{1}{A_n^+} \iint_{T_n^+} \boldsymbol{\rho}_n^+ e^{j(\boldsymbol{k}_0 \cdot \boldsymbol{r}')} \, \mathrm{d}S' + \frac{1}{A_n^-} \iint_{T_n^-} \boldsymbol{\rho}_n^- e^{j(\boldsymbol{k}_0 \cdot \boldsymbol{r}')} \, \mathrm{d}S' \right]$$

$$\approx \frac{-jk_0 e^{-jk_0}}{8\pi} \sum_{n=1}^{N} I_n \ell_n \, \hat{\boldsymbol{r}} \times \left[\boldsymbol{\rho}_{n,c}^+ e^{j(\boldsymbol{k}_0 \cdot \boldsymbol{r}_{n,c}^+)} + \boldsymbol{\rho}_{n,c}^- e^{j(\boldsymbol{k}_0 \cdot \boldsymbol{r}_{n,c}^-)} \right] \tag{3.130}$$

with the far-field distance normalized to $r = 1$ m. A similar expression can be derived through a series representation of the current by equivalent dipole moments (one per RWG) whose sum is evaluated rapidly for all angles because the dipole radiation patterns are known in analytic form [81, p. 43]. Either way, the pattern calculation time of electrically large antennas grows quadratically with the total number of equivalent dipole sources. Therefore, we will present an acceleration technique in Chapter 4 to relax the computational burden for moderately sized antenna arrays.

3.6 Validation and Representative Numerical Results

As discussed in Section 3.4.7, the moment matrix elements are computed through an adaptive integration scheme. The number of quadrature points has been determined empirically

by solving different antenna and scattering problems while maintaining good accuracy and computational efficiency. We will briefly motivate the final choice of quadrature rule after which the numerical accuracy of the present moment method will be assessed. All computations have been carried out in double precision arithmetic on a Dell Inspiron 9300 Notebook, equipped with an Intel Pentium-M processor operating at 1.73 GHz, and 2.0 GB of RAM. The C++ source code has been compiled on a Linux platform using the GNU C++ compiler version 4.1.1.

It is worth mentioning that Makarov has implemented and compared two moment methods: (i) a fully numerical scheme which avoids coinciding source and observation points. This scheme is based on a barycentric subdivision of the source triangle (9 subtriangles) where the midpoint integration rule is used for each of the subtriangles, while the field is tested at the centroid of the larger compound triangle using a single midpoint integration rule; (ii) the second scheme employs the singularity subtraction technique [70] in combination with the barycentric subdivision for the non-"self-terms". Makarov concludes that only a minor improvement is observed compared to the case of a full 9-point quadrature scheme; the difference between the methods was found to be less than 1% in the surface current magnitudes [81, p. 268].

However, we found that a fixed quadrature rule becomes unnecessary accurate for increasing separation distance between the source and observation triangles. In Appendix D, it is revealed that the moment matrix entries can be determined with ~ 4 digits accuracy if the midpoint rule (single quadrature point) is employed for both the source and observation triangles, provided that the RWG separation distance $d \geq \lambda_0/10$. For a $\lambda_0/10$ discretization it turned out to be sufficiently adequate to apply the singularity subtraction technique to the self terms only, and to compute the residual integral term for a single quadrature point. Provided that the condition number of the moment matrix is sufficiently low (*cf.* Section 3.4.8), accuracy and symmetry are preserved in both the moment and antenna input impedance matrices up to 4 digits. It has been demonstrated that this scheme is sufficiently accurate for all our planar antenna and scattering problems. However, the accuracy deteriorates when metals are bent and/or parallel oriented surfaces face each other due to both edge singularities and a strong interaction between RWGs. For a general class of problems, it has been demonstrated that a robust compromise between accuracy and computational efficiency can be realized by increasing the number of quadrature points to 7, but only in the source triangle and when $d \leq \lambda_0/2$.

3.6.1   Scattering by a Square Metallic Plate

As a first step in validating the moment method for scattering problems, it is customary to examine the induced surface current distribution on a square metallic plate with dimensions $\lambda_0 \times \lambda_0$. The flat plate is perfectly conducting and is exposed to an x-polarized plane electromagnetic wave of 1 V/m at normal incidence.
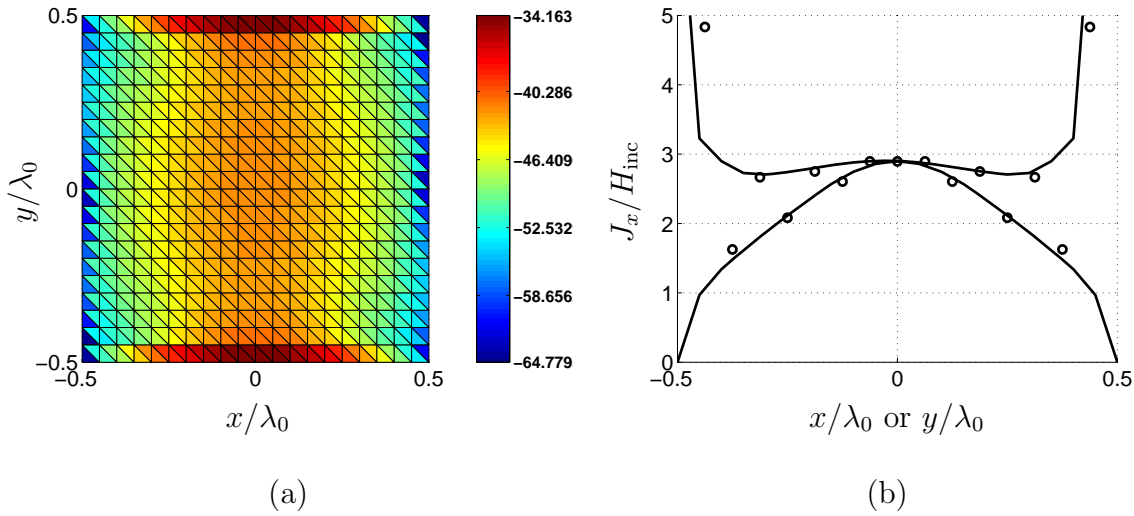

(a)   (b)

Figure 3.15: (a) Magnitude of $\boldsymbol{J}_S$ [dBA/m] for an x-polarized plane electromagnetic wave of 1 V/m at normal incidence (1160 edge elements). (b) Normalized modulus of J_x along the two principal cuts crossing the plate center (solid line). The solution is compared to [82, Fig. 4] (circles)

The solution for the current is shown in Fig. 3.15 when synthesized by 1160 RWG basis functions (20 triangles/λ_0). The simulation took about 12 seconds to construct the moment matrix and 9 seconds to solve the resulting MoM equation. The magnitude of $\boldsymbol{J}_S$ is shown in Fig. 3.15(a) in [dBA/m] and resembles the typical "saddle" type of function with strong edge effects along two of its sides. The normalized modulus $|J_x/H_{\text{inc}}|$ is shown in Fig. 3.15(b) along the two principal cuts crossing the plate center. The solid line designates the present MoM solution, which is in good agreement with the solution presented in [82, Fig. 4] (circles). The edge effect is seen to occupy a single row of edge cells; this occurs when the cell size is chosen relatively large with respect to the actual extent of the edge singularity. As a result, a difference between the two solutions is observed in Fig. 3.15(b) regarding the slope of the current near the edges. This discrepancy does not

pose a severe problem when the integral over the current is of interest as e.g. in case of far-field pattern calculations. Also, the mesh in Fig. 3.15(a) is point symmetric with respect to the plate center which causes the current to be point symmetric as well. The symmetry can be improved by choosing a 90 degree rotation-symmetric mesh such as the rhombic discretization shown in [83, p. 123].

A random discretization may improve the error cancellation in the global solution for the current. However, the current in Fig. 3.15 is probed at discrete positions whose local solutions depend strongly on the relative positions inside (and shape of) each of the corresponding triangles. Consequently, a random mesh would deteriorate the symmetry in Fig. 3.15(b).

3.6.2 Input Impedance of a Half Wavelength Dipole Antenna

The computed results for the current and input impedance of a half-wavelength dipole antenna are shown in Fig. 3.16. The dipole is operated at 75 MHz, has a length of 2 m, a strip width of 2 cm, and is excited by a delta-gap voltage source of 1 V at its center. The input impedance has been computed for various mesh densities and was subsequently compared to the reference data published in [81, p. 66] and [84].
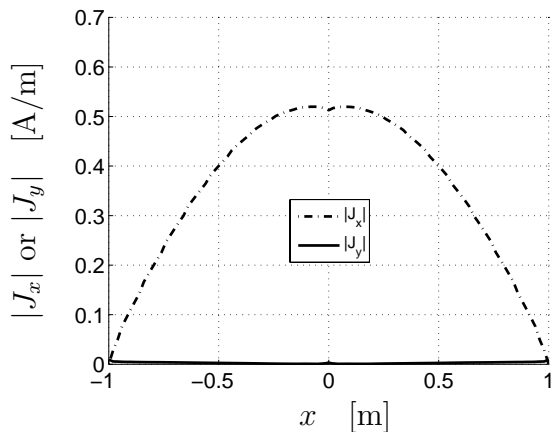
Triangles	[81, p. 66]	Present MoM
20	$88 + 34j$	$82 + 35j$
40	$88 + 41j$	$84 + 41j$
80	$87 + 44j$	$85 + 44j$
244	$88 + 47j$	$86 + 46j$

A WIPL-D simulation: $85 + 44j$ [84]

Figure 3.16: Current and input impedance of a half-wavelength dipole strip oriented along the x-axis (width/length=0.01).

For this specific strip width, it is observed in Fig. 3.16 that the modulus of the longitudinal component of the current, $|J_x|$, dominates over the transverse component by a factor of about 200, which is in accordance with the current distribution reported in [81, Fig. 4.7].

The second and third columns of the table in Fig. 3.16 indicate that the antenna input impedance converges to a fixed impedance value for increasing triangulation densities. The relative variation is 6% for the second column, and 9% for the third column. This difference is probably caused by the non-uniform mesh density that has been employed by Makarov, whereas we have used a uniform triangulation.

3.6.3 Base-Driven Monopole on an Infinite Ground Plane

The inclusion of an infinite and perfectly conducting ground plane is validated through comparing the impedance and radiation characteristics of a base-driven monopole antenna to the respective characteristics of a dipole antenna. The monopole antenna has a length

(a)   (b)
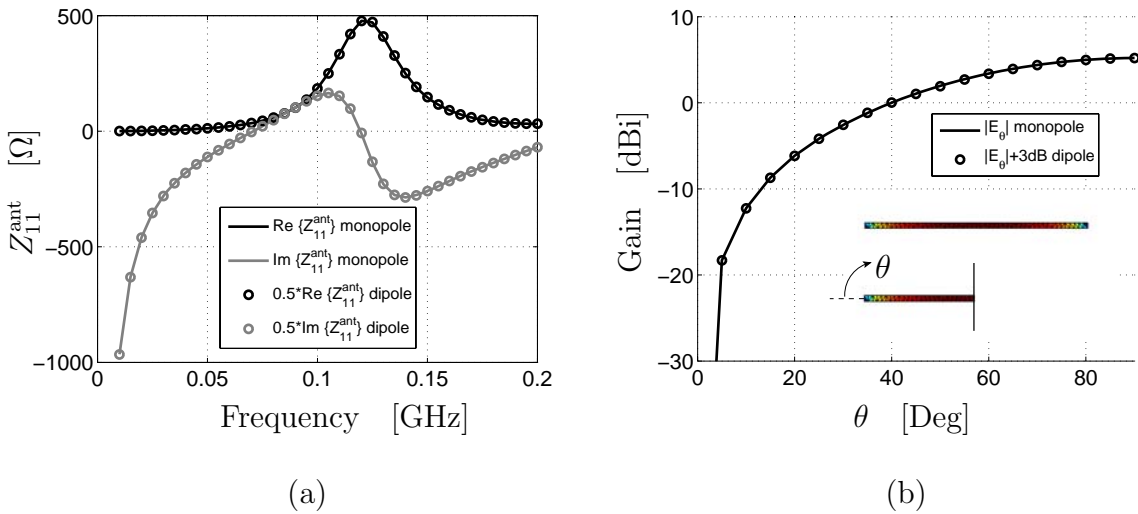
Figure 3.17: (a) Monopole and half of the dipole input impedance as a function of frequency. (b) Gain pattern of the $\lambda_0/4$ monopole antenna overlayed with the gain pattern of the $\lambda_0/2$ dipole antenna + 3 dB.

of 1 m, a strip width of 5 cm, and is electrically connected to the ground plane through a voltage source of zero-internal impedance, which is used to excite the element. The input impedance of the monopole antenna and half of the impedance of the corresponding dipole

antenna are plotted in Fig. 3.17(a) as a function of frequency. As expected, the agreement is excellent and demonstrates that the input impedance of the dipole antenna equals twice the input impedance of the monopole antenna. Furthermore, the respective gain patterns differ 3 dB in magnitude since the monopole is radiating all of its input power into the upper half space ($z > 0$).

3.6.4   Comparison with Commercially Available Tools

A comparison has been made with commercially available software tools in solving the impedance and radiation characteristics of a bow-tie antenna element. The geometrical parameters of the antenna element are depicted in Fig. 3.18. The antenna is placed above an infinite ground plane at $z = 0$ and excited by a voltage-gap generator in between the metallic fins.

Figure 3.18(b) shows the agreement between the antenna impedances as computed by the finite-element solver Ansoft HFSS, the Zeland moment method solver (IE3D), and the present moment method. The number of tetrahedra in HFSS is chosen adaptively and the surrounding air box with radiating boundary conditions has a separation distance to the structure of at least $\lambda_0/4$ at the lowest frequency. The adaptive mesh refinement terminates when the port solution has converged within 2% accuracy at the highest frequency. Although the computed impedance characteristics are similar, the maximum difference between the various curves turns out to be as large as $\sim 21\%$, which is not exceptionally large when different types of solvers are cross-validated for arbitrary antenna geometries using default discretizations [25]. In particular, this relative error may be larger near high-Q impedance resonances due to a minor frequency shift, which can be caused by the use of different feed models (wave ports, delta-gap sources, frill currents, etc.). Furthermore, numerical (round-off) errors are stronger pronounced at or near resonances.

The computed E-plane gain patterns are shown in Figs. 3.18(b) and (c) for 0.15 GHz and 0.24 GHz, respectively. The agreement between IE3D and the present moment method is visually indistinguishable. The HFSS solution differs slightly because of the different type of formulation used to compute the fields and currents.
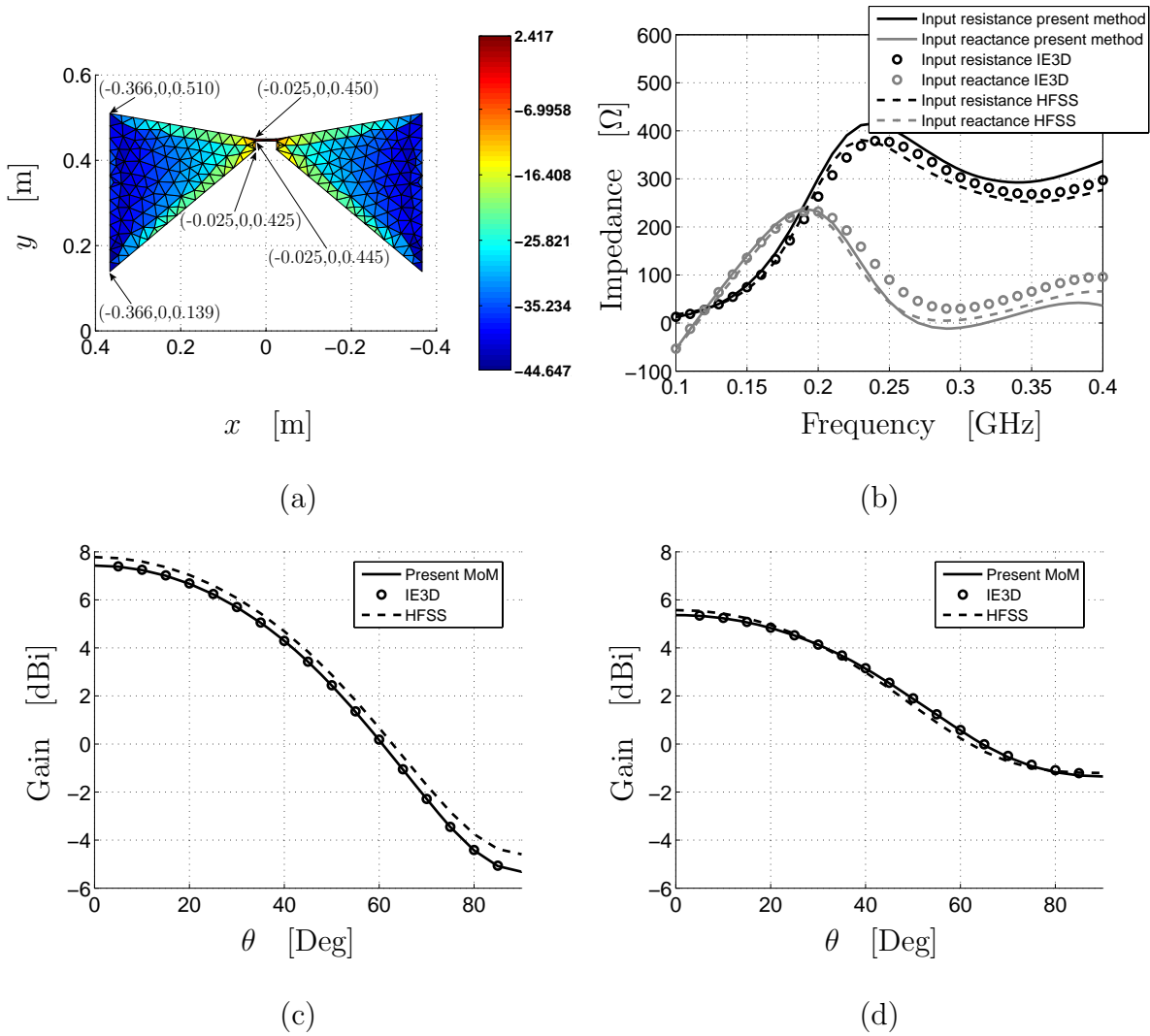
(a)

(b)

(c)

(d)

Figure 3.18: (a) Geometrical dimensions of the bow-tie element employing 555 RWG basis functions (mesh edge length ~ 3 cm). The magnitude of $\boldsymbol{J}_S$ is shown at 0.15 GHz. (b) The input impedance computed by HFSS, IE3D, and the present method. (c) and (d) The respective E-plane gain patterns at 0.15 and 0.24 GHz, respectively.

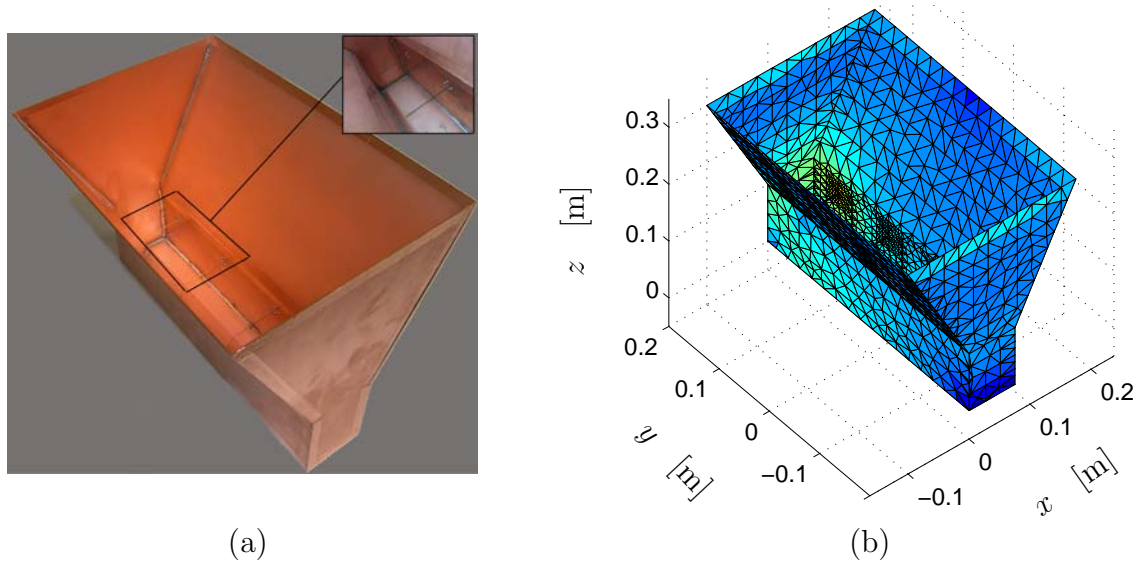### 3.6.5   Simulations and Measurements of a Reference Antenna

Figure 3.19: (a) Photograph of the 4-element monopole array, located inside a horn antenna. (b) Triangulation of the antenna structure and the magnitude of the computed surface current at 0.5 GHz when a corner monopole is excited.

A four-element monopole array has been designed, fabricated, and tested. The monopole array is located inside a horn antenna as shown in Fig. 3.19(a). This reference antenna has been used in combination with a low-noise receiver and a beamforming network to validate our system models and to perform studies on the antenna system noise temperature (*cf.* Chapter 5 and [85]). In the following, we only present the measured and simulated antenna four-port S-parameter matrix and the four embedded element gain patterns.

The reference plane for the S-parameters is positioned at the inputs of the SMA connectors, while the model utilizes voltage gaps at locations where the monopoles are connected to the horn structure. Therefore, a shift in reference plane must be accounted for to correctly compare measurements with simulations. For this purpose, the relatively short 50 Ω SMA connectors have been modeled as ideal lossless transmission lines, each having an effective length of 9 mm (in vacuum). This effective length roughly equals the physical length times a factor $\sqrt{2.1}$, since the Teflon substrate has a relative dielectric permittivity of $|\varepsilon_r| = 2.1$. The losses are characterized by the tangent delta which is as low as: $\tan(\delta) = \varepsilon_r''/\varepsilon_r' = 0.001$. The measured and simulated results are presented in Figs. 3.20–3.23.
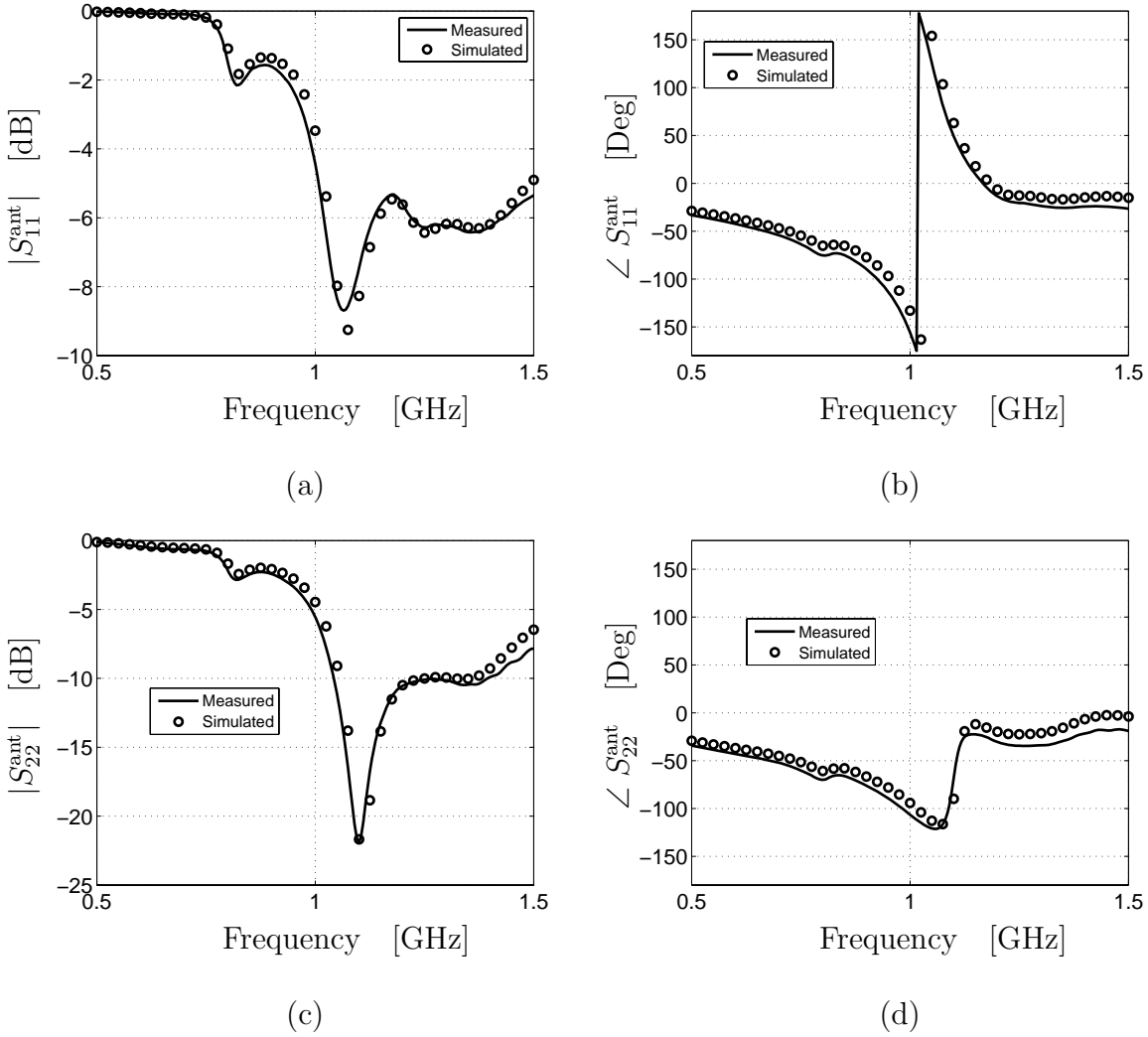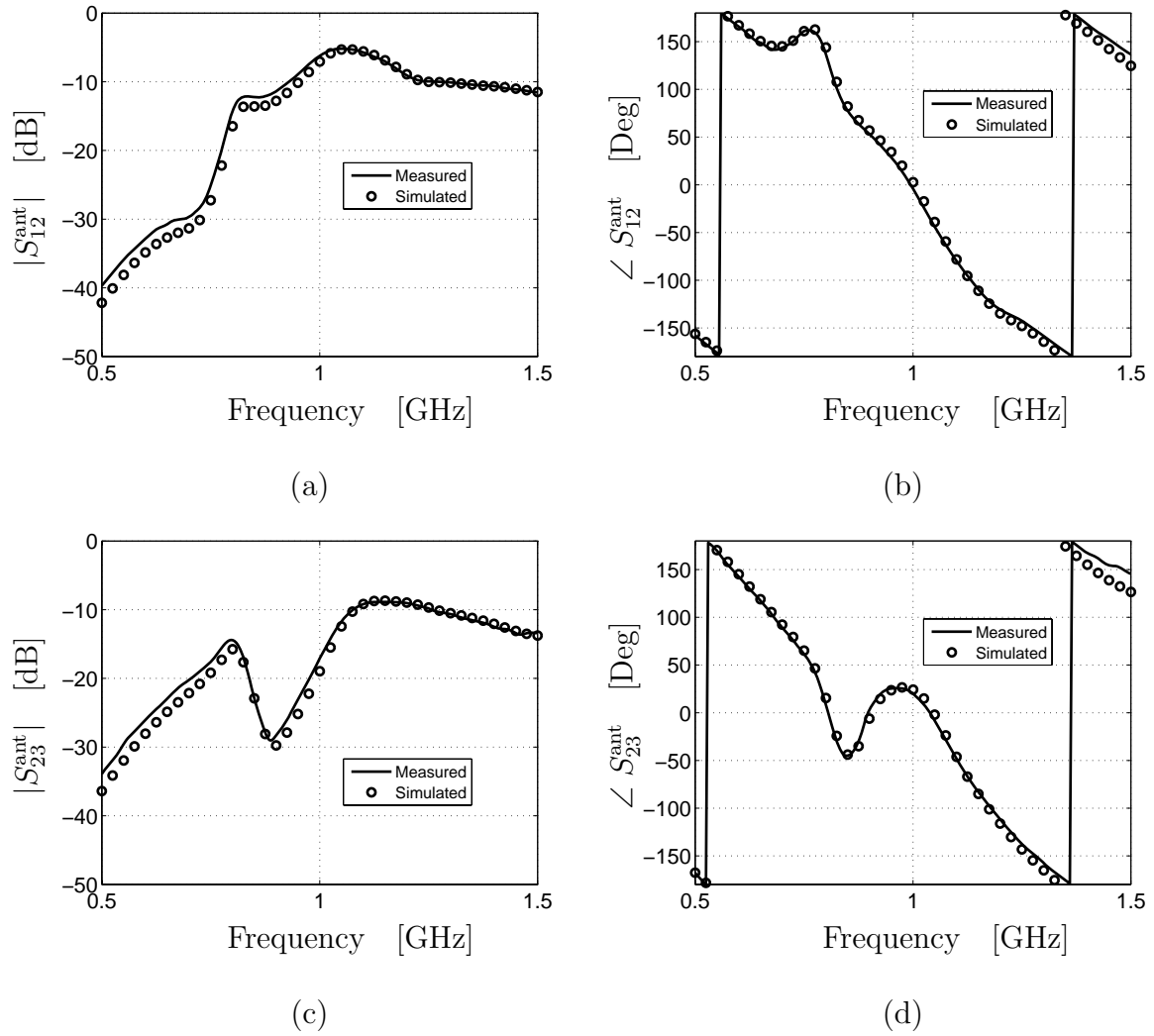
Figure 3.20: Measured and simulated 50 Ω S-parameters as a function of frequency: (a) Magnitude of S_{11}^{ant}; (b) Phase of S_{11}^{ant}; (c) Magnitude of S_{22}^{ant}, and; (d) Phase of S_{22}^{ant}.

A very good agreement between measurements and simulations is observed. The relative difference between the simulated and measured S parameters can be defined through the Frobenius norm (or Hilbert-Schmidt norm [86]) as

$$\Delta_\% = \frac{\|\mathbf{S}^{\mathrm{Meas}} - \mathbf{S}^{\mathrm{Sim}}\|_F}{\|\mathbf{S}^{\mathrm{Meas}}\|_F} = \frac{\sqrt{\sum_{m=1}^{4} \sum_{n=1}^{4} |S_{mn}^{\mathrm{Meas}} - S_{mn}^{\mathrm{Sim}}|^2}}{\sqrt{\sum_{m=1}^{4} \sum_{n=1}^{4} |S_{mn}^{\mathrm{Meas}}|^2}}. \tag{3.131}$$

The relative difference $\Delta_\%$ in measured and simulated S parameters for the 4×1 monopole

Figure 3.21: Measured and simulated 50 Ω S-parameters as a function of frequency: (a) Magnitude of S_{12}^{ant}; (b) Phase of S_{12}^{ant}; (c) Magnitude of S_{23}^{ant}, and; (d) Phase of S_{23}^{ant}.

antenna array has been plotted in Fig. 3.22. Not surprisingly (see previous section), this difference exhibits maxima near impedance resonances, that is, of about 24% at 1.0 GHz and 27% at 1.5 GHz (average difference is about 15%).

Generally, deviations can be attributed to measurement errors, fabrication tolerances (monopole length and strip width), model inaccuracies (infinitely thin metallic sheet assumption), and discretization errors arising in the moment method when approximating the actual current.
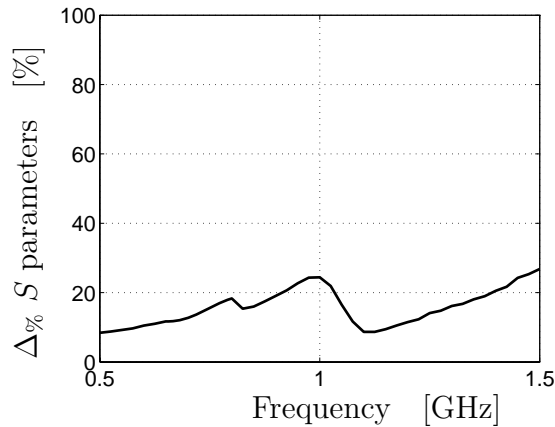
Figure 3.22: Relative difference between measured and simulated S parameters.

In addition to the impedance characteristics, the computed embedded element patterns in Fig. 3.23 (embedded = all antenna ports terminated, in this case by 50 Ω) are also in very good agreement with the measurements. These far-field patterns have been measured in an anechoic chamber using a planar near-field scanner, which has a limited scan range of about $\pm 70°$. As a result of this, and because the measurement equipment does not enable us to perform absolute gain measurements in an accurate manner, the gain patterns are normalized with respect to their maximum. The angle at which the maximum occurs may be different from $\theta = 0°$ as can be seen in Fig. 3.23(d), which explains the reduced normalized gain values in Fig. 3.23(c) for $\theta = 0°$.

3.7   Conclusions

Although closed-form expressions have been derived for both the Gram matrix elements and the excitation vector for plane-wave fields (for a RWG basis), a direct numerical scheme for the computation of the Gramm matrix elements has shown to be relatively inexpensive and sufficiently accurate. In practice, only three to four correctly computed significant digits are sufficient in the numerical solution of the pertaining integrals. In general, a robust compromise between accuracy and computational efficiency can be realized for a 7 point quadrature rule, but this is only required for the source triangle and if the separation distance between the source and observation triangle $\leq \lambda_0/2$ (empirically determined), otherwise a single point suffices.
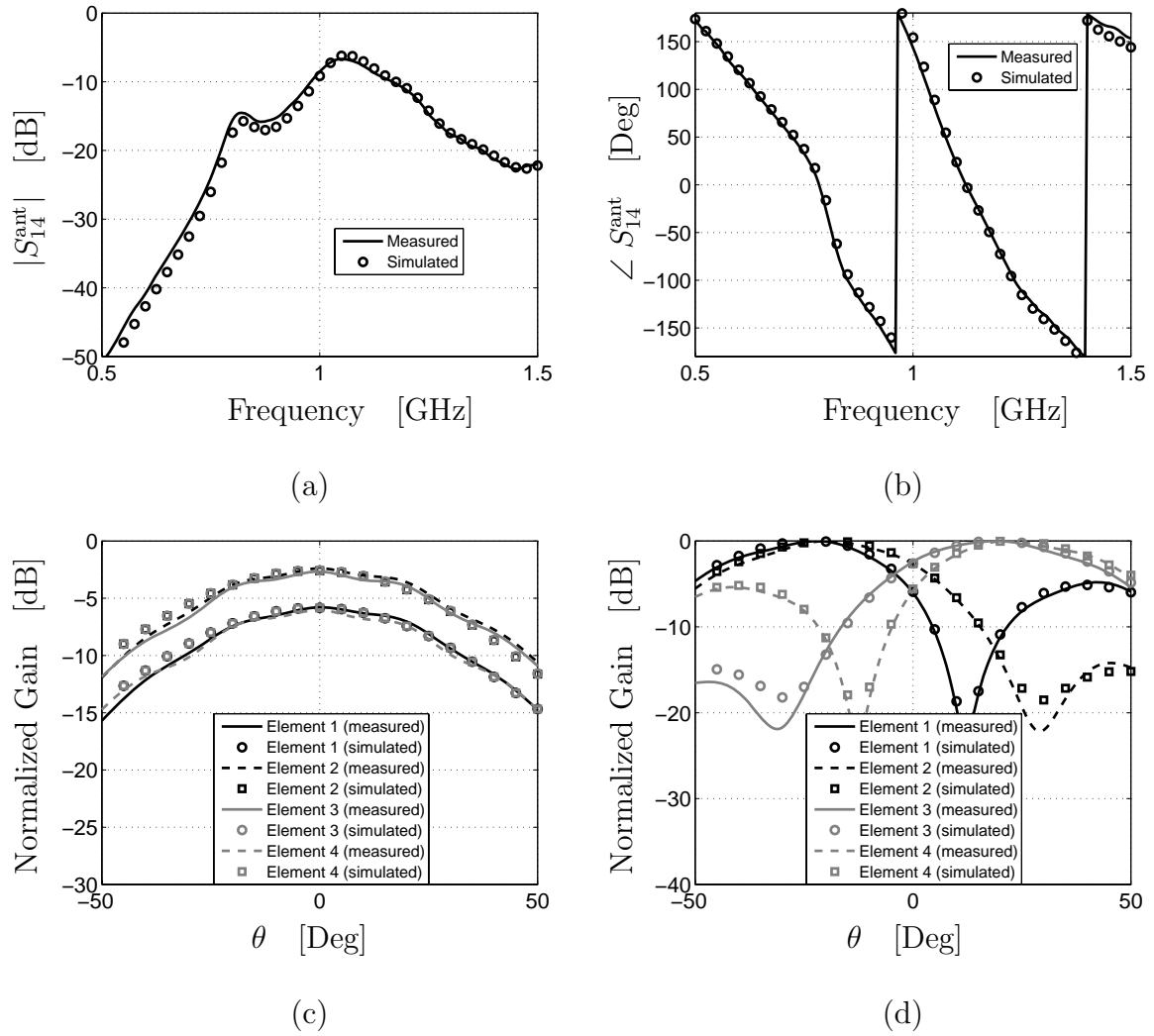
Figure 3.23: Measured and simulated 50 Ω S-parameters as a function of frequency: (a) Magnitude of S_{14}^{ant}; (b) Phase of S_{14}^{ant}. The measured and simulated normalized gain patterns of 4 elements at 1 GHz: (c) E-plane cuts, and; (d) H-plane cuts. The normalization is with respect to the maximum pattern gain.

It is sometimes advised to analytically integrate the singular terms in the potential integrals for the self patch and the nearest neighbors. However, the Singularity Subtraction Method (SSM) needs a careful implementation to avoid numerically unstable solutions for points outside of the source triangle, in particular near one of its edges or its edge extensions. Despite this drawback, the SSM turns out to be sufficiently adequate when solely applied to fully overlapping triangles.

The antenna admittance can be computed directly through dividing the applied source voltage by the locally induced port current. The so-determined "spot admittance" has shown to be identical to the one calculated from an integral formula, which is known to be second-order accurate. The results are identical, provided that the EFIE is discretized by Galerkin's method and tested by means of a symmetric product.

The delta-gap source may be incorrectly interpreted as a physical gap of infinitesimal width. An ideal voltage source, however, should not represent a capacitor, but a short circuit. The term "delta gap" may therefore be misleading, while the term "voltage gap" may be more appropriate. Furthermore, the literature is unclear when the voltage, current, and field relations are specified for a RWG voltage-gap source. In relation to this, a sign inconsistency was discovered in the stationary expression for the antenna input admittance as presented by Harrington [32, Eq. (6-12)]. This is an important observation because this expression is used as a reference formula in various numerical test cases, or in semi-analytical approaches.

Chapter 4

Efficiency Enhancement Technique for the Method of Moments

After a compendious literature review, the Characteristic Basis Method (CBFM) is selected and presented to efficiently compute the electromagnetic radiation and impedance characteristics of electrically-large dielectric-free antenna structures[1]. A post-windowing technique is developed for generating Characteristic Basis Functions (CBFs) for electrically interconnected antenna structures and the CBFM will be hybridized with the Adaptive Cross Approximation (ACA) technique to reduce the matrix construction time. Additionally, the quasi-Toeplitz structure of the reduced matrix is exploited and translation symmetry is used to rapidly compute the antenna element patterns. A perturbation approach and a multilevel CBFM technique are proposed for solving arrays of nested disjoint subarray problems. Finally, results are presented of a combined quasi-static and electrodynamic field model of a practical 8×7 dual-polarized array of Tapered Slot Antennas (TSAs).

---

[1]This chapter is based on a number of papers, including:

[87]: R. Maaskant, R. Mittra, and A. G. Tijhuis, "Fast analysis of large antenna arrays using the characteristic basis function method and the adaptive cross approximation algorithm," *IEEE Trans. Antennas Propag.*, vol. 56, no. 11, pp. 3440–3451, Nov. 2008.

[88]: R. Maaskant, R. Mittra, and A. G. Tijhuis, "Fast solution of multi-scale antenna problems for the square kilomtre array (SKA) radio telescope using the characteristic basis function method (CBFM)," *Applied Computational Electromagnetics Society (ACES) Journal*, vol. 24, no. 2, pp. 174–188, Apr. 2009.

[89]: R. Maaskant, M. V. Ivashina, O. Iupikov, E. A. Redkina, S. Kasturi, and D. H. Schaubert, "Analysis of Large Microstrip-Fed Tapered Slot Antenna Arrays by Combining Electrodynamic and Quasi-Static Field Models," *IEEE Trans. Antennas Propag.*, accepted for publication.

4.1   Introduction

The evolution of computational electromagnetics during the last decade has enabled us to analyze large real-world antenna and scattering problems that were beyond our reach only a few years ago. In recent years, a variety of novel and efficient computational methods have been introduced and combined. Herein, we provide only a concise overview of the literature that is closely related to the subject of the present thesis, i.e., large finite antenna arrays analyzed by using iterative-free integral equation techniques. Rather than solving a large matrix equation iteratively for each individual excitation, the proposed technique generates a relatively small matrix equation, which can be solved directly and efficiently for many different excitations (MRHS).

A variety of computational techniques have been developed that are based on the infinite-array approach with corrections that explicitly account for the edge behavior associated with finite arrays. These analyses are often based on the assumption that the edge behavior of an array is local, and almost independent of the array size. This is a valid assumption for very large arrays where the center elements behave as infinite-array elements. For instance, within the truncated Floquet-wave diffraction method an integral equation is solved for only the fringe current describing the difference between the finite-array current and the associated infinite array current [90]. The fringe current is expanded by using a relatively small set of basis functions, derived from a diffraction analysis of canonical structures, whose use requires the solution of only a moderately sized matrix equation. Other infinite-array-based techniques that relax the computational burden for a finite array analysis can be found in [91–94]. However; as these methods are based on the solution of infinite phased arrays, some of these may be limited in their application to certain types of excitation. In addition, for moderate-sized arrays, and for those that require a high degree of flexibility in terms of array lattice geometry and element shape, it is preferable to use alternative methods that are based on finite-size arrays.

To reduce the size of the matrix equation, one could employ subsectional basis functions of higher-order polynomials [95]; however, an even greater reduction in the number of unknowns can be achieved by employing macro basis/test functions. Moreover; since macro-domain functions can be constructed as fixed combinations of subsectional functions, these macro functions can conform to arbitrarily shaped geometries. An additional advantage of using these macro basis functions is that existing codes can be reused with only minor

modifications. These types of macro functions are sometimes referred to as aggregated basis functions, and have been applied to arrays of disconnected patch antennas in [96] and [97].

The expansion wave concept is also a method which reduces the number of unknowns without compromising the solution accuracy or geometrical flexibility of the low-level basis functions. It decomposes both the incident and scattered fields to and from an isolated array element in terms of only a few expansion functions [98]. This concept of reducing the matrix equation and decomposing the problem into smaller problems has been widely exploited in recently developed iterative-free methods for large-scale problems. For instance, the Characteristic Basis Function Method (CBFM) [99–103], which has been successfully applied to a large class of scattering and radiation problems, the Synthetic-Functions Approach (SFX) [104], [105], the Sub-Entire-Domain Basis Function Method (SED) [106], the eigencurrent approach [107], and a subdomain multilevel approach [108]. The objectives of these methods are similar, namely to reduce the matrix equation by employing (physics-based) macro basis and macro test functions for the electric and/or magnetic surface currents. The differences between these methods primarily arise from the way the macro functions are generated, and how the subdomains treat the flow of current between electrically interconnected subdomains. The savings realized in memory and computation time are significant for these approaches. In fact, the solution time (for direct solvers) scales as $\mathcal{O}(N^3)$, where N now becomes a relatively small number associated with the total number of macro functions. The proportionality constant, however, slightly increases because of the additional time that is required to generate these macro-basis functions.

In this thesis, we use the CBFM to solve antenna array problems, particularly, because this non-overlapping domain decomposition technique does not require additional basis functions at the subdomain interconnections and intrinsically employs excitation-dependent macro-domain basis functions.

The following novel enhancement techniques for the CBFM have been proposed and elaborated:

> *Numerical generation and post windowing of partially overlapping CBFs to model junction currents between subdomains (cf. Sections 4.3.2 and 4.4).*

We will focus in this chapter on arrays of Tapered Slot Antennas (TSAs) since their analysis constitutes a challenging numerical problem. Typically, the outer edges of the TSA fins

are (entirely) connected to the adjacent elements as a result of which the analysis of the entire array problem cannot be localized to the analysis of a single isolated TSA element. It is important to preserve the continuity of the surface current across TSA boundaries since discontinuities introduced by slots and gaps of sufficient size tend to radiate and may cause in-band anomalies which disrupt the impedance and radiation characteristics.

Special attention is devoted to the problem of efficient generation of a representative set of Characteristic Basis Functions (CBFs) on electrically small subarrays that can be used to synthesize the total surface current for the original problem consisting of many electrically interconnected array elements. For this purpose, a post-windowing technique is developed to shape the initially generated CBFs and to guarantee a piecewise continuous current flow at the interconnections. We minimize the computational cost by keeping the sizes of the subdomains that support the CBFs as small as possible, i.e., equal to the size of one antenna element plus a minor extension. Hence, we do choose the subdomains such that there exists a partial overlap between them and, as a result, between adjacent CBFs as well. This is an alternative method to [104], and does not require an independent set of "connection" basis functions to ensure the electrical connectivity between adjacent antenna elements. Hence, the present approach does not increase the total number of unknowns and enables us to solve larger problems, although the method in [104] may provide a better continuity of the current in those interconnection regions.

> *An array meshing method which exploits symmetry in connected antenna array problems (cf. Section 4.3.3).*

An array meshing method is proposed, which not only exploits the translation symmetry in arrays of electrically interconnected antennas, but also preserves the quasi-Toeplitz symmetry in the reduced moment matrix. In turn, this allows for a fast computation of antenna element patterns and mutual port impedances.

> *Fast construction of the reduced matrix using the ACA (cf. Sections 4.3.4 and 4.5).*

Although the CBFM reduces the number of unknowns, the construction time of the reduced matrix has not been shortened. This may not seem a problem as it scales as $\mathcal{O}(N^2)$, but N still represents here the total number of subsectional basis/testing functions making up the macro-basis functions. Typically, the number of subsectional basis/testing functions

is much larger than the number of macro functions, so that the fill-time of the reduced matrix governs the total execution time.

A number of hybrid methods have been proposed to reduce the matrix-fill time. For instance, in [109] the reaction integral between the macro basis and testing functions is computed using a suitable approximation. A generalization of this approach has led to the introduction of the Fast Multipole Method (FMM) for rapid computation of these reactions [110], [95]. Alternatively, the Adaptive Integral Method (AIM) has also been applied to compute these reduced matrix entries efficiently [111], [112]. In the present chapter we generate the reduced matrix in a time-efficient manner by hybridizing the CBFM with the Adaptive Cross Approximation (ACA) algorithm. The ACA algorithm was originally developed to exploit the low-rank properties of moment matrices representing reaction integrals between well-separated groups of low-level basis functions [113–115]; however, the algorithm is also suited for the CBFs since these are groups of aggregated low-level basis functions. The ACA algorithm is purely algebraic in nature, kernel independent and relatively easy to implement. Also, the algorithm does not require *a priori* knowledge of each impedance submatrix. As will be seen, it is an adaptive and on-the-fly rank-revealing block factorization of the rank-deficient submatrices.

Solution of large arrays of disjoint subarrays (cf. Section 4.6).

The problem of solving large arrays of nested disjoint subarrays is tackled through a perturbation approach. The results are shown for an antenna array comprised of 9 subarrays each of which consists of 64 TSAs. A multilevel CBFM is formulated as well, whose results will be published elsewhere.

Model and validation of a practical dual-polarized TSA array (cf. Section 4.7).

Quasi-static and electrodynamic field models are combined to compute the antenna impedance matrix of a practical 8×7 dual-polarized array of Tapered Slot Antennas (TSAs). The measurements and simulations are compared.

4.2   Entire-Domain Basis Function Approach

Consider the 7×1 singly-polarized TSA array in Fig. 4.1, where the domain $\mathcal{S}$ represents the entire conducting surface/support of the surface current $\boldsymbol{J}_S$. Our objective is to find
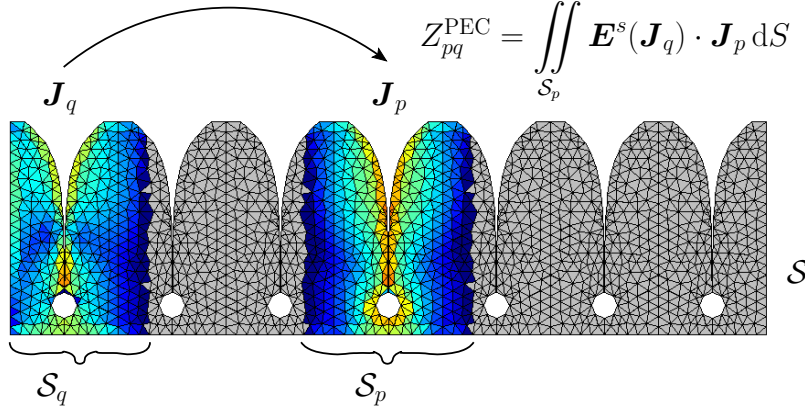

Figure 4.1: Computation of a matrix element Z_{pq}^{PEC}; a reaction between the (source) macro basis function $\boldsymbol{J}_q$ on the (observation) macro test function $\boldsymbol{J}_p$

a solution for $\boldsymbol{J}_S$, given a specific excitation situation. The current $\boldsymbol{J}_S$ can be determined by solving a boundary integral equation [EFIE (3.50)]:

$$-\boldsymbol{E}_{\tan}^i = \boldsymbol{E}_{\tan}^s(\boldsymbol{J}_S) - Z_S \boldsymbol{J}_S, \quad \text{for } \boldsymbol{r} \in \mathcal{S} \tag{4.1}$$

where $\boldsymbol{E}^i$ is the impressed incident electric field, Z_S is the surface impedance of the conducting sheet, and $\boldsymbol{E}^s(\boldsymbol{J}_S)$ denotes the radiated (or scattered) electric field generated by the impressed source current $\boldsymbol{J}_S$ which is supported by $\mathcal{S}$. For a harmonic time dependence $\exp(j\omega t)$, the radiated field $\boldsymbol{E}^s(\boldsymbol{J}_S)$ can be computed through the MPIE formulation [Eq. (3.52)] as:

$$\boldsymbol{E}^s(\boldsymbol{J}_S) = -j\omega\mu_0\boldsymbol{A} - \boldsymbol{\nabla}\Phi \tag{4.2a}$$

$$\boldsymbol{A}(\boldsymbol{r}) = \iint_{\mathcal{S}} G(\boldsymbol{r} - \boldsymbol{r}')\boldsymbol{J}_S(\boldsymbol{r}')\,\mathrm{d}S' \tag{4.2b}$$

$$\Phi(\boldsymbol{r}) = -\frac{1}{j\omega\varepsilon_0}\iint_{\mathcal{S}} G(\boldsymbol{r} - \boldsymbol{r}')\boldsymbol{\nabla}_t' \cdot \boldsymbol{J}_S(\boldsymbol{r}')\,\mathrm{d}S' \tag{4.2c}$$

$$G(\boldsymbol{r} - \boldsymbol{r}') = \frac{e^{-jk_0\|\boldsymbol{r}-\boldsymbol{r}'\|_2}}{4\pi\|\boldsymbol{r} - \boldsymbol{r}'\|_2}. \tag{4.2d}$$

Here, $\boldsymbol{A}$ is the magnetic vector potential, Φ is the electric scalar potential, G is the scalar free-space Green's function, $\boldsymbol{r}$ is an observation and $\boldsymbol{r}'$ is a source position on domain $\mathcal{S}$, and μ_0 and ε_0 are the permeability and permittivity of vacuum, respectively.

To solve (4.1) through a moment method approach, we subdivide the electrically large domain $\mathcal{S}$ into L smaller subdomains each of which supports a set of (physics-based) macro-domain basis functions. Typically, L is chosen to be equal to the number of antenna elements to optimally exploit translation symmetry (*cf.* Section 4.3.3). If the ith subdomain is denoted by $\mathcal{S}_i$, then

$$\mathcal{S} = \bigcup_{i=1}^{L} \mathcal{S}_i. \tag{4.3}$$

Since we propose an overlapping domain decomposition technique, $\mathcal{S}_p \cap \mathcal{S}_q \neq 0$, in general, for $p, q \in \{1, 2, \ldots, L\}$. However, in our approach, we require that $\mathcal{S}_p$ and $\mathcal{S}_q$ overlap only if the corresponding pair of antenna elements are electrically interconnected.

When an identical set of entire-domain basis and test functions (Galerkin's testing) is employed for the EFIE in (4.1), a small-size matrix equation is obtained that has the form

$$\mathbf{Z}\mathbf{I} = (\mathbf{Z}^{\mathrm{PEC}} - \mathbf{Z}^{\mathrm{IBC}})\mathbf{I} = \mathbf{V} \tag{4.4}$$

where the element Z_{pq}^{PEC} of the matrix $\mathbf{Z}^{\mathrm{PEC}}$ represents the reaction integral between the macro source current $\boldsymbol{J}_q$, supported by the qth subdomain $\mathcal{S}_q$, and the macro observation (test) current $\boldsymbol{J}_p$, supported by the pth subdomain $\mathcal{S}_p$, i.e. (see also Fig. 4.1),

$$Z_{pq}^{\mathrm{PEC}} = \langle \boldsymbol{E}^s(\boldsymbol{J}_q), \boldsymbol{J}_p \rangle = \iint_{\mathcal{S}_p} \boldsymbol{E}^s(\boldsymbol{J}_q) \cdot \boldsymbol{J}_p \, \mathrm{d}S. \tag{4.5}$$

The element Z_{pq}^{IBC} of the matrix $\mathbf{Z}^{\mathrm{IBC}}$ is computed as

$$Z_{pq}^{\mathrm{IBC}} = \langle \boldsymbol{J}_p, Z_S \boldsymbol{J}_q \rangle = \iint_{\mathcal{S}_p \cap \mathcal{S}_q} \boldsymbol{J}_p \cdot Z_S \boldsymbol{J}_q \, \mathrm{d}S \tag{4.6}$$

and the pth source term V_p is computed as

$$V_p = -\langle \boldsymbol{E}^i, \boldsymbol{J}_p \rangle = -\iint_{\mathcal{S}_p} \boldsymbol{E}^i(\boldsymbol{r}) \cdot \boldsymbol{J}_p \, \mathrm{d}S \tag{4.7}$$

In this chapter, we will consider PEC surfaces for which $Z_S = 0$, so that $\mathbf{Z}^{\mathrm{IBC}} = \mathbf{0}$. The conductor losses are examined only for relatively small antenna structures in Chapter 5. It will be demonstrated that the induced surface current resembles the PEC current when the conductor losses are small. This implies that, to first order, it suffices to solve for the PEC current first and then to estimate the total ohmic loss as

$$
P_{\mathrm{diss}} = \frac{1}{2}\mathfrak{Re}\left\{ \iint_{\mathcal{S}} \boldsymbol{J}_S^* \cdot Z_S \boldsymbol{J}_S \, \mathrm{d}S \right\} = \frac{1}{2}\mathfrak{Re}\left\{ (\mathbf{I}^{\mathrm{PEC}})^H \mathbf{Z}^{\mathrm{IBC}} \mathbf{I}^{\mathrm{PEC}} \right\} \tag{4.8}
$$

where the expansion $\boldsymbol{J}_S = \sum_{n=1}^{N} I_n^{\mathrm{PEC}} \boldsymbol{f}_n$ in terms of real-valued RWG basis functions $\{\boldsymbol{f}_n\}_{n=1}^{N}$ has been substituted in (4.8) for a known complex-valued expansion vector $\mathbf{I}^{\mathrm{PEC}}$.

4.3   The Characteristic Basis Function Method

4.3.1   Employing Characteristic Basis Functions (CBFs)

In CBFM, the macro functions are generated numerically (see Section 4.3.2), and are referred to as Characteristic Basis Functions (CBFs). The CBFs are formed by aggregating the low-level basis functions on that domain. We will employ the Rao-Wilton-Glisson basis [26], since it offers the flexibility of handling arbitrarily shaped geometries. Following the CBFM, we expand the CBF on the ith subdomain as

$$
\boldsymbol{J}_i(\boldsymbol{r}) = \sum_{m=1}^{N_i} I_m^i \boldsymbol{f}_m^i(\boldsymbol{r}) \tag{4.9}
$$

where $i = p$ for the observation CBF and $i = q$ for the source CBF. Furthermore, $\boldsymbol{f}_m^i$ represents the mth RWG on the ith subdomain, and I_m^i $(m = 1, 2, \ldots, N_i)$ are the N_i expansion coefficients for the CBF on the ith subdomain. Note that we use a local numbering scheme for the RWGs per subdomain and that some RWGs belong to more than one subdomain, since the subdomains may partially overlap. Substituting (4.9) in (4.5), and using the linearity of the operators in (4.2a) through (4.2d), yields

$$
Z_{pq}^{\mathrm{CBF}} = \sum_{m=1}^{N_p} \sum_{n=1}^{N_q} I_m^p \left[\iint_{\mathcal{S}_p} \boldsymbol{E}^s(\boldsymbol{f}_n^q) \cdot \boldsymbol{f}_m^p \, \mathrm{d}S \right] I_n^q = \mathbf{J}_p^T \, \mathbf{Z}_{pq}^{\mathrm{RWG}} \, \mathbf{J}_q \tag{4.10}
$$

where $\mathbf{J}_q = [I_1^q, I_2^q, \ldots, I_{N_q}^q]^T$, and $\mathbf{Z}_{pq}^{\mathrm{RWG}}$ is a $N_p \times N_q$ rectangular matrix block whose entries are the mutual reaction integrals involving the RWGs of domains p and q. Likewise, the voltage vector in (4.7) is then computed as

$$V_p^{\mathrm{CBF}} = -\sum_{m=1}^{N_p} I_m^p \left[\iint_{\mathcal{S}_p} \boldsymbol{E}^i \cdot \boldsymbol{f}_m^p \, \mathrm{d}S \right] = \mathbf{J}_p^T \mathbf{V}_p^{\mathrm{RWG}} \tag{4.11}$$

where $\mathbf{V}_p^{\mathrm{RWG}}$ is the voltage excitation vector for the RWGs on the pth domain.

So far, we have expanded the surface current using only one CBF per subdomain. However, for electrically large subdomains, a single CBF may not be adequate, and it becomes necessary to employ a sufficiently large and linearly independent set of CBFs per subdomain. As detailed in Section 4.3.2, there exist a number of ways of generating such a set of CBFs. To be more general, suppose that we need to employ K_p CBFs on the pth subdomain and K_q CBFs on the qth subdomain. Then, (4.10) would read $\mathbf{Z}_{pq}^{\mathrm{CBF}} = \mathbf{J}_p^T \mathbf{Z}_{pq}^{\mathrm{RWG}} \mathbf{J}_q$, where $\mathbf{Z}_{pq}^{\mathrm{RWG}}$ is a rectangular matrix block of size $K_p \times K_q$; $\mathbf{J}_p$ is a column augmented matrix of size $N_p \times K_p$; and $\mathbf{J}_q$ is of size $N_q \times K_q$. Furthermore, (4.11) would read $\mathbf{V}_p^{\mathrm{CBF}} = \mathbf{J}_p^T \mathbf{V}_p^{\mathrm{RWG}}$, where $\mathbf{V}_p^{\mathrm{CBF}}$ is of size $K_p \times 1$. As a result, the total reduced matrix equation $\mathbf{Z}^{\mathrm{CBF}} \mathbf{I}^{\mathrm{CBF}} = \mathbf{V}^{\mathrm{CBF}}$ has the following block structure

$$\begin{bmatrix} \mathbf{J}_1^T \mathbf{Z}_{11}^{\mathrm{RWG}} \mathbf{J}_1 & \mathbf{J}_1^T \mathbf{Z}_{12}^{\mathrm{RWG}} \mathbf{J}_2 & \cdots & \mathbf{J}_1^T \mathbf{Z}_{1L}^{\mathrm{RWG}} \mathbf{J}_L \\ \mathbf{J}_2^T \mathbf{Z}_{21}^{\mathrm{RWG}} \mathbf{J}_1 & \mathbf{J}_2^T \mathbf{Z}_{22}^{\mathrm{RWG}} \mathbf{J}_2 & \cdots & \mathbf{J}_2^T \mathbf{Z}_{2L}^{\mathrm{RWG}} \mathbf{J}_L \\ \vdots & \vdots & \ddots & \vdots \\ \mathbf{J}_L^T \mathbf{Z}_{L1}^{\mathrm{RWG}} \mathbf{J}_1 & \mathbf{J}_L^T \mathbf{Z}_{L2}^{\mathrm{RWG}} \mathbf{J}_2 & \cdots & \mathbf{J}_L^T \mathbf{Z}_{LL}^{\mathrm{RWG}} \mathbf{J}_L \end{bmatrix} \begin{bmatrix} \mathbf{I}_1^{\mathrm{CBF}} \\ \mathbf{I}_2^{\mathrm{CBF}} \\ \vdots \\ \mathbf{I}_L^{\mathrm{CBF}} \end{bmatrix} = \begin{bmatrix} \mathbf{V}_1^{\mathrm{CBF}} \\ \mathbf{V}_2^{\mathrm{CBF}} \\ \vdots \\ \mathbf{V}_L^{\mathrm{CBF}} \end{bmatrix} \tag{4.12}$$

where the total domain has been subdivided into L (overlapping) subdomains, each of which may support a distinct set of CBFs.

For problems of moderate size, the reduced matrix equation in (4.12) can be solved via a single LU-decomposition and one matrix-vector product per excitation. Hence, for each resulting $\mathbf{I}^{\mathrm{CBF}}$ the surface current can be re-expressed in terms of RWGs. This allows computing the desired antenna pattern and scattering parameters. However, when the degree of translation symmetry is large, as it is in arrays with antennas arranged on a uniformly spaced grid, it is preferable to use an alternative and more efficient approach for computing the total scattered/radiated field. In this method, we first compute the field of each individual CBF, multiply each field pattern by its corresponding CBF expansion coefficient, and then superimpose these individual patterns to obtain the total pattern.

Also, the antenna impedance matrix can be computed by using the reduced matrix and the expansion coefficients of the CBFs directly. This is explained in Section 4.3.6, where we present a stationary formula that has been used to compute the antenna admittance matrix.

4.3.2   Numerical Generation of Characteristic Basis Functions

For didactical reasons, we explain the generation of CBFs for an 1-D array of electrically interconnected TSAs. However, by using the same techniques, also 2-D arrays have been analyzed of which the results are described in the Sections 4.5–4.7. In [100], a novel technique has been proposed to generate CBFs for arrays of electrically interconnected antenna elements that are suitable as macro basis and macro test functions. As will be explained hereafter (Step IIIa), a specific version of this technique has been employed in the present chapter. For ease of understanding, and for comparing the results with those that were obtained in [100], the procedure for generating the CBFs will be briefly explained in four stages through an example of a 7×1 single-polarized array of TSAs (see Fig 4.2). More details are provided in the subsequent sections.

Step I: *Mesh generation*
To rapidly construct the mesh for the entire structure, only one array element is triangulated and replicated at various element positions throughout the array lattice by means of geometrical translations. The partitioning of RWGs is kept identical for each array element and the polarity of the RWGs that electrically interconnect the antenna elements is chosen consistently, and such that the entirely meshed array facilitates a one-to-one mapping of partially overlapping CBFs. This mapping of CBFs has been visualized in the transition from Step III to Step IV. More details are given in Section 4.3.3.

Step II *Generation of primary CBFs*
Subarrays are extracted from the entirely meshed array to generate the CBFs. The number of generating subarrays corresponds to the number of (uniquely) extended subdomains from which the mapping takes place. As illustrated in Step II, we distinguish three subarrays since we are not considering rotation symmetry, i.e., two corner elements and one central element along with their electrically interconnected adjacent element(s). Because our final objective is to compute both the overall antenna impedance matrix and all antenna element patterns, we consider the problem on transmit. For this reason, primary CBFs are also
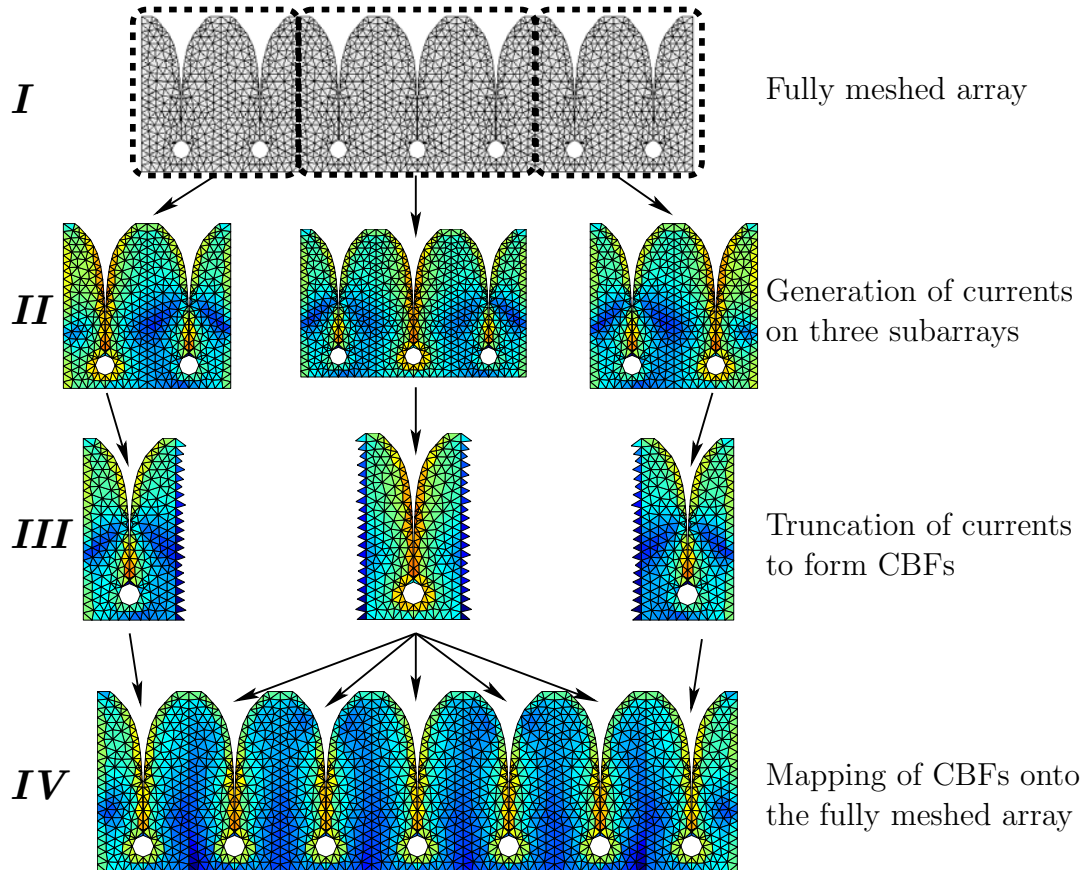
I   Fully meshed array

II   Generation of currents
                                                                                on three subarrays

III   Truncation of currents
                                                                                to form CBFs

IV   Mapping of CBFs onto
                                                                                the fully meshed array

Figure 4.2: Step I–Step III: A 7x1 TSA array decomposed into 3 subarrays for generating
the CBFs. Step IV: The synthesized surface current for broadside scan after solving the
reduced matrix equation.

generated on transmit to achieve an accurate representation of the current for any array
excitation. To generate the primary CBFs, each accessible port (pair of terminals) of the
three subarrays is excited sequentially. As a result, the number of primary generated CBFs
equals the number of accessible ports for each subarray. More specifically, suppose that
for one of the subarrays in Step II, the current $\boldsymbol{J}_{\text{sub}}$ on a subarray is expanded into the N
RWG basis functions $\{\boldsymbol{f}_1, \boldsymbol{f}_2, \ldots, \boldsymbol{f}_N\}$ as

$$\boldsymbol{J}_{\text{sub}}(\boldsymbol{r}) = \sum_{m=1}^{N} I_m \boldsymbol{f}_m(\boldsymbol{r}) \tag{4.13}$$

where $\{I_1, I_2, \ldots, I_N\}$ are the N corresponding RWG expansion coefficients; then, these
expansion coefficients are found by solving the corresponding matrix equation for the $N \times K$

column-augmented excitation matrix $\mathbf{V}_{\mathrm{sub}}$, i.e.,

$$\mathbf{J}_{\mathrm{sub}} = \mathbf{Z}_{\mathrm{sub}}^{-1}\mathbf{V}_{\mathrm{sub}} \tag{4.14}$$

where $\mathbf{Z}_{\mathrm{sub}}$ is the moment matrix of the RWGs supported by that subarray, and the K columns of matrix $\mathbf{J}_{\mathrm{sub}}$ represent the corresponding K expansion coefficient vectors of the CBFs that have been generated on that subarray (K equals the number of subarray ports). Hence, as a result of exciting the ports of the subarrays, 2 primary CBFs are generated on the outer two subarrays, while 3 CBFs are generated on the inner subarray.

We remark that, for large scattering problems, one is typically interested in the RCS, so that the scattered field of the entire structure has to be computed for a series of plane waves incident from various directions. Hence, when the CBFM is used to solve scattering problems, it is not uncommon to also let a plane-wave spectrum be incident on each extended subdomain in order to generate a set of representative CBFs for each of these subdomains. Although a plane-wave spectrum is an obvious choice to generate CBFs for scattering problems, it is demonstrated in Section 4.7 that this CBF generation method can also be applied to antenna problems, both on receive and transmit.

Step IIIa *Truncation and Post-Windowing of CBFs*
Although the CBFs suffer from truncation effects at the outer edges of each subarray (Step II, Fig. 4.2), these edge-singular currents can be eliminated by truncating the CBFs as illustrated in Step III.

Essentially, we apply a trapezoidal windowing function $\mathbf{\Lambda}$ to each of the sets of CBFs that were generated for each of the subarrays in Step II (Fig. 4.2) [100]. In particular, we will choose a trapezoidal window that approaches a pulse function. Upon using such a window, the support of each CBF reduces to the size of one antenna element only, but also incorporates possible "connection" RWGs (one-cell overlap). In fact, for each subarray, the final windowed set of CBFs $\mathbf{J}$ (Step III, Fig. 4.2) is computed as

$$\mathbf{J} = \mathbf{\Lambda}\mathbf{J}_{\mathrm{sub}} = \mathbf{\Lambda}\mathbf{Z}_{\mathrm{sub}}^{-1}\mathbf{V}_{\mathrm{sub}} \tag{4.15}$$

where the product with the $N \times N$ diagonal matrix $\mathbf{\Lambda}$ realizes that the RWG expansion coefficients, composing the set of CBFs $\mathbf{J}_{\mathrm{sub}}$, are post-multiplied/weigthed either by 0, 1/2, or 1, depending upon whether these RWGs are in the external, overlap, or internal region of the resulting truncated subdomain, respectively. Note that in Step III (Fig. 4.2), the "connection" RWGs in the overlap region are colored blue as a result of weighting these RWGs by 1/2, and that the zeros in $\mathbf{J}$ are discarded so as to truncate the support.

The advantage of the presently employed pulse-windowed CBFs is that the partially over-lapping CBFs in Step IV (Fig. 4.2) sum with a proper weight in the overlap region, since the corresponding partially overlapping pulse-windowing functions sum to unity (every-where). It was observed that the use of these pulse-windowed CBFs with reduced support and weighted edges leads to an improved accuracy of the surface current in the overlap regions as compared to the pulse-windowing function proposed earlier in [99]. The impact of choosing various other windowing functions on the accuracy is discussed in detail in Section 4.4.

Step IIIb *Reducing the number of CBFs by Means of a SVD*

Since each of the subdomains can support a number of self-overlapping CBFs; a well-conditioned reduced moment matrix can be constructed if the CBFs within each of these sets are linearly independent, and this is assured by the SVD operation which renders the CBFs orthogonal. Let the kth column of $\mathbf{J}_q$ be the expansion coefficient vector of the kth CBF on the qth subdomain. The matrix $\mathbf{J}_q$ is of size $N_q \times K_q$, where N_q and K_q denote the total number of RWGs and CBFs on the qth subdomain, respectively. This matrix is rank-deficient if the dimension of the column space spanned by the CBFs is less than the number of CBFs. It should be pointed out that this matrix can be ill-conditioned because of redundancy. The application of the Singular Value Decomposition (SVD) with a thresholding procedure on the singular values is a suitable tool for determining as well as controlling the effective rank of a matrix [116]. After performing the SVD, $\mathbf{J}_q$ is decomposed as

$$\mathbf{J}_q = \mathbf{U}\mathbf{D}\mathbf{Q}^H \tag{4.16}$$

where $\mathbf{U}$ is an $N_q \times K_q$ matrix with orthonormal columns [78, p. 27]; $\mathbf{Q}$ is a $K_q \times K_q$ unitary matrix; and, $\mathbf{D}$ is a $K_q \times K_q$ diagonal matrix of the form $\mathrm{diag}(\sigma_1, \sigma_2, \ldots, \sigma_{K_q})$. The nonnegative real-valued diagonal entries of $\mathbf{D}$ can be required to be ordered as $\sigma_1 \leq \sigma_2 \leq \ldots \leq \sigma_{K_q}$ and are the singular values of $\mathbf{J}_q$. The presence of singular values of zero, or near-zero, indicates that the matrix is singular or ill-conditioned. Therefore, to improve this condition number, a thresholding procedure is used on the normalized singular values

$$R_n = \frac{\sigma_n}{\sigma_{max}} \quad n = 1, 2, \ldots, K_q. \tag{4.17}$$

Each of these normalized quantities is compared to an appropriate threshold, and if this level is smaller than the threshold, then the corresponding singular value is set to zero. Suppose this happens for $n > N_\sigma$, then the first N_σ left singular vectors of $\mathbf{U}$ forms the orthonormal set of CBFs that are retained.

Step IIIc *Generation of Secondary CBFs*

The number of CBFs per subdomain can be enlarged to achieve a more accurate representation of the final surface current solution. For this purpose, the primary CBFs $\mathbf{J}_q$, which are supported by the qth subdomain and that were obtained in Step IIIb, are used as distant current sources to the subarrays shown in Step II (Fig. 4.2). Essentially, these distant CBFs mimic possible surface currents on neighboring array elements that are located within a certain electrical distance to each of these subarrays; and are used to re-induce surface currents on these subarrays. Following (4.14), the currents $\mathbf{J}_{\mathrm{sub}}$ on a subarray are computed as

$$\mathbf{J}_{\mathrm{sub}} = \mathbf{Z}_{\mathrm{sub}}^{-1}\mathbf{V}_{\mathrm{sub}} = \mathbf{Z}_{\mathrm{sub}}^{-1}\mathbf{Z}_{\mathrm{sub},q}\mathbf{J}_q \tag{4.18}$$

where $\mathbf{V}_{\mathrm{sub}} = \mathbf{Z}_{\mathrm{sub},q}\mathbf{J}_q$, and where $\mathbf{Z}_{\mathrm{sub},q}$ is the mutual moment matrix representing reactions between RWGs on the qth source domain, which supports a set of primary source CBFs $\mathbf{J}_q$, and the RWGs on the subarray under excitation. After accounting for all the distant source CBFs within a specified radius to the pertaining subarray, we truncate the supports of the resultant augmented set of CBFs $\mathbf{J}_{\mathrm{sub}}$ with the aid of (4.15), and append the so-generated secondary CBFs to the already existing set of primary CBFs $\mathbf{J}$. Finally, this relatively large combined set of primary and secondary CBFs is again orthonormalized and reduced by applying a SVD.

We point out that it often suffices to invoke the SVD procedure only once, namely, after generating both the primary and secondary CBFs. However, when a set of primary CBFs $\mathbf{J}_q$ contains redundant CBFs, a relatively large number of additional redundant secondary CBFs will be generated in view of (4.18), particularly for large radii. Hence, the combined set of primary and secondary CBFs may become unnecessarily large because of redundancy. A similar problem occurs for scattering problems whenever the CBFs are generated using a plane-wave spectrum [117]. Consequently, the SVD operation becomes more time-demanding than if we first reduce a small set of primary CBFs (typically less than 10), and follow this up with the reduction of a relatively small set of CBFs comprising of primaries and secondaries. Note that sets of primary CBFs are nearly identical to each other when the corresponding subarray possesses a large degree of symmetry, both in terms of the excitation and the geometry, as for instance in the case of subarrays that are extracted from dual-polarized arrays.

Obviously, the total number of initially generated secondary CBFs (columns of $\mathbf{J}_{\mathrm{sub}}$) depends upon the total number of distant subdomains q that are considered. One can increase

the specified radius to include more surrounding array elements/domains supporting primary CBFs. However, the SVD prevents us from adding secondary CBFs that are not sufficiently independent of the already existing set of CBFs. Hence, convergence of the solution depends upon the final solution accuracy that one requires and is controllable through the SVD threshold. Indirectly, the minimum radius for including the relevant number of secondary CBFs is thus dependent on the SVD threshold as well.

Step IV *Mapping of CBFs and solving for the current*
After retaining a relatively small set of CBFs for each truncated subdomain (Step III, Fig. 4.2), the CBFs are mapped onto the various subdomains throughout the entire array (Step IV, Fig. 4.2). Afterwards, a reduced matrix equation is constructed efficiently (see Section 4.3.4) and solved directly without resorting to iterative techniques. The resulting surface current for the 7×1 TSA array is shown in Fig. 4.2 for broadside scan when all elements are excited by a voltage source across the slotline section.

Regarding the generation of CBFs, it is instructive to consider how the CBFs differ from eigencurrents employed in the eigencurrent approach [107]. In CBFM, the induced surface current on each subarray is computed for a certain excitation vector $\mathbf{V}$ by solving the corresponding matrix equation for the unknown RWG expansion coefficient vector $\mathbf{I}$. The complex symmetric moment matrix $\mathbf{Z} = \mathbf{Z}^T$ is assumed to be nondefective and diagonalizable by its eigenvectors. Hence, an eigenvalue decomposition of $\mathbf{Z}$ exists and is herein expressed through the block factorization

$$\mathbf{Z} = \mathbf{U}\mathbf{D}\mathbf{U}^{-1} \tag{4.19}$$

where the nth diagonal entry ν_n of diagonal matrix $\mathbf{D}$ is the nth eigenvalue of $\mathbf{Z}$, and where the nth column $\mathbf{u}_n$ of $\mathbf{U}$ is the nth eigenvector of $\mathbf{Z}$. Hence, the unknown coefficient vector $\mathbf{I}$ can be expressed in terms of the eigenvectors $\{\mathbf{u}_n\}$, eigenvalues $\{\nu_n\}$, and excitation vector $\mathbf{V}$ as

$$\mathbf{I} = \sum_{n=1}^{N} \frac{1}{\nu_n} \left(\mathbf{u}_n \cdot \mathbf{V} \right) \mathbf{u}_n. \tag{4.20}$$

In the eigencurrent approach [107], the eigencurrents $\{\mathbf{u}_n\}$ of $\mathbf{Z}$ are used as macro-domain basis functions. Essentially, the set of eigencurrents forms a fingerprint of the physical structure and simultaneously forms a complete orthonormal basis for the currents that can exist on this structure. Accurate solutions have been obtained for arrays of disconnected

antenna elements, by using only an (incomplete) subset of $\{\mathbf{u}_n\}$. However, this reduced orthonormal basis does not include information about the port position of the antenna element or excitation field applied to the actual problem, and therefore may, in general, not lead to the most optimal/smallest basis. On the contrary, in CBFM, a representative excitation field $\mathbf{V}$ is applied to each subarray to generate CBFs, implying that we identify the left-hand-side of (4.20) as a basis. This can be advantageous, because when an antenna port of a subarray is excited, the induced surface current (and thus the CBF) naturally accounts for a possibly asymmetrical port position, and may therefore represent the final surface current quite well even when we employ only a limited number of the above macro-domain basis functions. However, one major drawback in generating macro basis functions in this manner is that these CBFs will generally not be mutually orthogonal. As a remedy, one would need to orthonormalize the CBFs, and retain only a minimal number of them as described in **Step IIIb** above.

Also, the eigencurrents are known to diagonalize the moment matrix, so that complete-ness of this basis is guaranteed. On the contrary, CBFs are generated through solving the moment matrix equation for various different excitations; this basis is generally not complete, even for an overdetermined set of CBFs. However, completeness is not required to effectively and accurately solve the actual problem, that is, the basis only needs to span a subspace of the entire solution space which is required to synthesize the range of physically possible currents. Consequently, the convergence of the solution accuracy as a function of the number of CBFs depends strongly on the way they have been generated.

4.3.3 Exploiting Translation Symmetry

Once each (extended) subdomain supports a set of CBFs, the reduced moment matrix in Eq. (4.12) can be constructed efficiently by exploiting the translation symmetry between CBFs. As an example, Fig. 4.3 graphically exemplifies that the reduced matrix block $\mathbf{Z}_{pq}^{\mathrm{CBF}}$ equals $\mathbf{Z}_{p+1;q+1}^{\mathrm{CBF}}$, because both blocks represent reactions between identical, though translated, set of CBFs.

It follows that,

$$\mathbf{Z}_{pq}^{\mathrm{CBF}} = \mathbf{J}_p^T \, \mathbf{Z}_{pq}^{\mathrm{RWG}} \mathbf{J}_q = \mathbf{Z}_{p+1;q+1}^{\mathrm{CBF}} \tag{4.21}$$

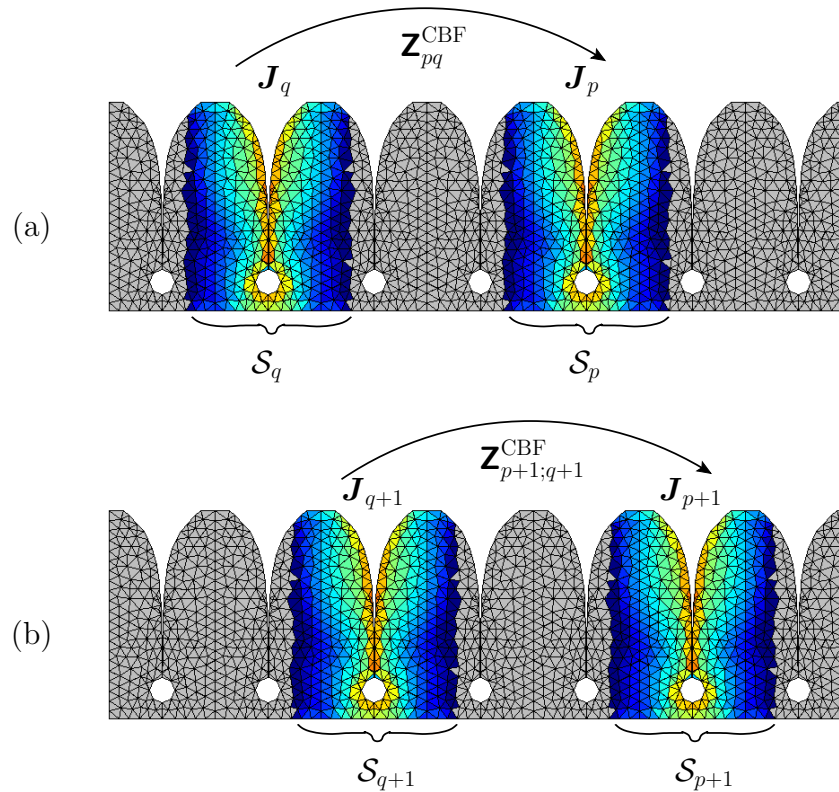provided that the extended subdomain $\mathcal{S}_q$ [Fig. 4.3(a)], that supports a set of source CBFs,

Figure 4.3: Construction of identical reduced matrix blocks $\mathbf{Z}_{pq}^{\mathrm{CBF}}$ and $\mathbf{Z}_{p+1;q+1}^{\mathrm{CBF}}$.

maps one-to-one onto the one-element translated subdomain $\mathcal{S}_{q+1}$ [Fig. 4.3(b)]. Similarly, the testing CBFs supported by the subdomain $\mathcal{S}_p$ have to map one-to-one onto the subdomain $\mathcal{S}_{p+1}$ for the same translation vector. This translation vector does include information on the mutual separation distance between identical sets of CBFs (2-norm of this vector), as well as on the mutual orientation (direction of this vector). To optimally exploit translation symmetry for connected antenna array problems, a consistent triangulation and partitioning of the RWGs of all subdomains (and thus array elements) is required as further clarified with the aid of Fig. 4.4.

Array Meshing Method

The entire array mesh can be efficiently constructed from a few elementary meshed array elements, called the base elements. The geometry of each base element is discretized by a number of polygonal facets of which the outlines are described by a set of boundary

nodes. Fig. 4.4 (Step I) shows a discretized TSA base element comprising of 3 polygonal surfaces (two tapered fins and one tiny port polygon across the slotline), where the polygonal boundary nodes are designated by (black) dots. Every polygonal facet is supplied by a non-uniform grid of internal nodes and subsequently triangulated (in a 2-D plane) using a Delaunay meshing routine [63, 118]. The internal grid is distributed such that the elementary triangles are very nearly equilateral (*cf.* Section 3.4.3). Subsequently, nodes and triangles are added along the boundaries to ensure that the triangulations will be consistent with those of the electrically interconnected adjacent elements when these base elements are placed in the array environment. Next, triangulated base elements are equipped with the RWGs. Step I (Fig. 4.4) shows a possible RWG polarity distribution, visualized by vectors that join the common edges of each pair of triangles to form an RWG.

Step II illustrates a one-to-one replication of the discretized base element at array element locations $r_1 \ldots r_7$. Note that, at this stage, the RWGs ensuring the electrical connection between array elements have not yet been defined. This is accomplished in Step III, where the triangles along a connection line are separately equipped with RWGs and subsequently mapped (recursively) onto the various corresponding connection lines that remain to be equipped with RWGs. For this purpose, we utilize the array symmetry as detailed in the next section. A pseudo Matlab code of the recursive-mapping algorithm is included in the appendix of [88]. Finally, a full meshing of the array geometry (Step IV) facilitates a one-to-one mapping of the CBFs, even though each supporting subdomain extends beyond the outer boundaries of an array element, as shown in Fig. 4.3.

Array Symmetry Extraction Method

For the full array geometry, the degree of translation symmetry between pairs of subdomains, each of which supports a set of CBFs, can be determined as explained below. Following the generation of the boundary nodes for the array in a manner shown in Fig. 4.4 of Step II, where we replicate the boundary nodes of the base antenna element(s) at their respective array positions, we can determine which array elements are electrically interconnected. Furthermore, when using multiple base elements, such as in the case of dual-polarized arrays, one can also keep track of the type of base element that is interconnected. Let the element interconnection and the corresponding base element type be stored in two separate matrices. Then, for our example, using only one type of base element (TSA
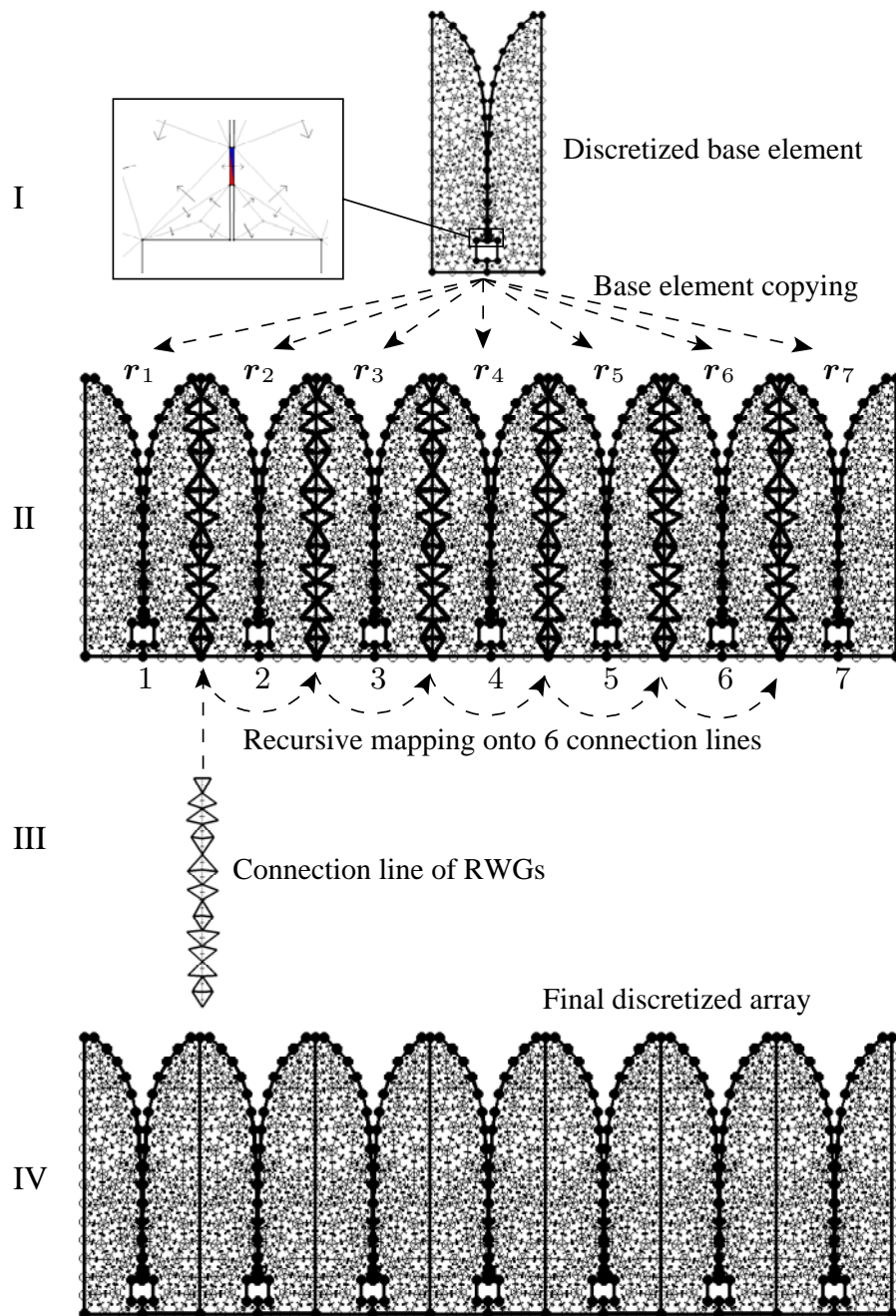
Figure 4.4: Efficient and consistent meshing of the antenna array structure to fully exploit translation symmetry.

element in Fig. 4.4, Step I), we have:

$$
\begin{pmatrix}
1 & 2 & 0 \\
2 & 1 & 3 \\
3 & 2 & 4 \\
4 & 3 & 5 \\
5 & 4 & 6 \\
6 & 5 & 7 \\
7 & 6 & 0
\end{pmatrix}
\quad \text{and} \quad
\begin{pmatrix}
1 & 1 & 0 \\
1 & 1 & 1 \\
1 & 1 & 1 \\
1 & 1 & 1 \\
1 & 1 & 1 \\
1 & 1 & 1 \\
1 & 1 & 0
\end{pmatrix}
\tag{4.22}
$$

where the first rows of the left- and right-hand matrices indicate that antenna element 1 is connected to antenna element 2, and that they are both base elements of type 1 (ignore the zero entries).

Also, for each array element, one can determine the relative positions of the electrically interconnected elements surrounding it. Upon comparing the groups of relative position vectors in conjunction with the corresponding base element types (rows of second matrix), one can readily determine which subdomains (and therefore corresponding set of CBFs) are identical. For our example, subdomains $\{2, 3, 4, 5, 6\}$; $\{1\}$; and $\{7\}$ form the 3 unique groups. We need to only generate one set of CBFs per unique subdomain, in this case for subdomains 1, 7 and 4, where subdomain 4 is chosen from the first group as the most central element. Elements 1, 7 and 4 are extracted from the fully meshed array, together with their neighboring array elements (within a specified radius), to form the resulting three subarrays that are used to generate the CBFs. After windowing these CBFs, the CBFs supported by subdomain 4 are mapped onto the subdomains 2, 3, 5, and 6.

After determining the unique subdomains (1, 4 and 7), from which the CBFs are mapped, we also compute the relative element array position vectors between all array elements and store these in matrix form. For our example, we have

$$
\begin{pmatrix}
\boldsymbol{r}_1 - \boldsymbol{r}_1 & 1 & 1 \\
\boldsymbol{r}_1 - \boldsymbol{r}_2 & 1 & 4 \\
\boldsymbol{r}_1 - \boldsymbol{r}_3 & 1 & 4 \\
\vdots & \vdots & \vdots \\
\boldsymbol{r}_7 - \boldsymbol{r}_5 & 7 & 4 \\
\boldsymbol{r}_7 - \boldsymbol{r}_6 & 7 & 4 \\
\boldsymbol{r}_7 - \boldsymbol{r}_7 & 7 & 7
\end{pmatrix}
\tag{4.23}
$$

where the first column holds the 49 relative array position vectors between element pairs, and the last two columns denote the corresponding two array elements that support the same set of CBFs from which they were initially mapped, namely either 1, 4 or 7. By comparing the rows, one can readily determine which element/subdomain pairs are identical in terms of the sets of CBFs supported by them (last two columns), as well as their mutual orientation and separation distance (first column). Upon selecting the unique rows, the minimal number of impedance matrix blocks that need to be filled can be determined (out of the 49 possible combinations). For convenience, we create a new matrix showing how the reduced matrix is built up from only a limited number of unique matrix blocks. For our example, the structure of the 7×7 matrix block is:

$$
\begin{array}{c}
\text{Subdomain\#} \\
1 \\
2 \\
3 \\
4 \\
5 \\
6 \\
7
\end{array}
\begin{array}{ccccccc}
\mathbf{1} & \mathbf{2} & \mathbf{3} & \mathbf{4} & \mathbf{5} & \mathbf{6} & \mathbf{7} \\
\left(\begin{array}{ccccccc}
1 & 2 & 3 & 4 & 5 & 6 & 7 \\
 & 8 & 9 & 10 & 11 & 12 & 13 \\
 & & 8 & 9 & 10 & 11 & 14 \\
 & & & 8 & 9 & 10 & 15 \\
 & & & & 8 & 9 & 16 \\
 & & & & & 8 & 17 \\
 & & & & & & 18
\end{array}\right)
\end{array}
\tag{4.24}
$$

where only 18 out of 49 non-redundant mutual impedance blocks have been identified, since we also exploited reciprocity (only the upper triangular part of the matrix is required). Note that, for this example, the matrix entry 11 denotes that the reactions between the CBFs supported by subdomains (antenna elements) 2 and 5 are identical to the reactions between the CBFs supported by subdomains 3 and 6, as we can verify from Fig. 4.4. In conclusion, symmetry can be exploited for arrays of electrically interconnected elements to reduce the complexity of the matrix-filling process. For the present example of a regular-spaced single-polarized antenna array (Fig. 4.4), the computational complexity becomes linear when the symmetry is exploited. Similarly, the pattern computations can be expedited as explained in Section 4.3.6.

4.3.4 Fast Reduced Matrix Generation Using ACA

As pointed out in Section 4.1, for direct methods the time it takes to solve the reduced matrix equation scales as $\mathcal{O}(N^3)$, where N is the total number of CBFs. This is a significant

timesaver when the number of CBFs is much smaller than the total number of RWGs used in the original matrix formulation. For these cases, however, the construction of the matrix in (4.12) dominates the total solution time as this scales with $\mathcal{O}(N^2)$, where N remains the total number of RWGs making-up the CBFs. In fact, Eq. (4.12) suggests that a full matrix block $\mathbf{Z}_{pq}^{\mathrm{RWG}}$ has to be built before its compressed version $\mathbf{J}_p^T \mathbf{Z}_{pq}^{\mathrm{RWG}} \mathbf{J}_q$ can be computed.

To decrease the time to construct the reduced matrix, we first exploit the translation symmetry of the antenna array by concluding that reactions between groups of CBFs are replicated elsewhere in the array. As a consequence, many blocks of the reduced matrix are identical and, hence, can be simply copied when the matrix is filled. We have seen that this also holds for arrays of electrically interconnected elements, where the block Toeplitz symmetry of the matrix is only slightly broken. In addition, we use reciprocity to fill only the upper triangular part of the matrix. Finally, and most importantly, each submatrix in (4.12) can be approximated as

$$\mathbf{Z}_{pq}^{\mathrm{CBF}} = \mathbf{J}_p^T \, \mathbf{Z}_{pq}^{\mathrm{RWG}} \mathbf{J}_q \approx \mathbf{J}_p^T \, \widetilde{\mathbf{Z}}_{pq}^{\mathrm{RWG}} \mathbf{J}_q \tag{4.25}$$

where $\widetilde{\mathbf{Z}}_{pq}^{\mathrm{RWG}}$ is a low-rank decomposition of $\mathbf{Z}_{pq}^{\mathrm{RWG}}$. It is worthwhile to note that in [111] each column of the matrix product $\mathbf{Z}_{pq}^{\mathrm{RWG}} \mathbf{J}_q$ is efficiently computed as an AIM matrix vector product, whereas, in the present approach, the matrix $\mathbf{Z}_{pq}^{\mathrm{RWG}}$ is approximated through a low-rank block factorization. Therefore, once $\widetilde{\mathbf{Z}}_{pq}^{\mathrm{RWG}}$ has been constructed, the product $\widetilde{\mathbf{Z}}_{pq}^{\mathrm{RWG}} \mathbf{J}_q$ is carried out efficiently and in a straightforward manner, for any arbitrary vector $\mathbf{J}_q$.

The degree of rank deficiency of $\mathbf{Z}_{pq}^{\mathrm{RWG}}$ depends on the electrical distance that separates the observation and source groups p and q, as well as their sizes and mutual orientation. The effective rank decreases for an increasingly larger separation distance. For well-separated groups of RWGs, the electric field at the observation group p produced by any source RWG can be expressed as a linear combination of the fields produced by only a few of these source RWGs (source sampling). Likewise, the electric field tested at the observation group p produced by any source RWG can be expressed as a linear combination of the fields tested by only a few of these observation RWGs (field sampling). Hence, a cross-approximation technique can be used to adaptively construct the subsets of relevant source and observation RWGs.

In this work, we use the Adaptive Cross Approximation (ACA) algorithm [113–115], which is an adaptive and on-the-fly rank-revealing block factorization of the rank-deficient sub-

matrices. The ACA algorithm is purely algebraic in nature and can be used irrespectively of the kernel of the integral equation, basis functions or type of integral equation formulation. This makes the ACA algorithm attractive for handling problems involving arbitrary geometries. The ACA algorithm can be regarded as a rank-revealing column-pivoted LU-decomposition of the approximate matrix, and therefore inherits the advantages of many other algebraic block factorization methods. In addition, the ACA algorithm only requires partial knowledge of the original matrix and belongs to a large group of fast integral equation algebraic methods (see [114], and references therein). It has been shown that for low-frequency EMC problems of moderate electrical size both the memory and CPU time requirements for the ACA algorithm scale as $N^{4/3} \log N$ [114].

The ACA algorithm approximates $\widetilde{\mathbf{Z}}_{pq}^{\mathrm{RWG}}$ through the following block factorization

$$\widetilde{\mathbf{Z}}_{pq}^{\mathrm{RWG}} = \mathbf{U}_p^{N_p \times \mathrm{rk}} \mathbf{V}_q^{\mathrm{rk} \times N_q} = \sum_{i=1}^{\mathrm{rk}} \mathbf{u}_i^{N_p \times 1} \mathbf{v}_i^{1 \times N_q} \tag{4.26}$$

where rk is a short-hand notation for $\mathrm{rk}(\widetilde{\mathbf{Z}}_{pq}^{\mathrm{RWG}})$, which denotes the effective rank of the matrix $\widetilde{\mathbf{Z}}_{pq}^{\mathrm{RWG}}$. Further, $\mathbf{U}_p^{N_p \times \mathrm{rk}}$ is a column-augmented matrix of size $N_p \times \mathrm{rk}$ and $\mathbf{V}_q^{\mathrm{rk} \times N_q}$ is a row-augmented matrix of size $\mathrm{rk} \times N_q$. The ith column vector of $\mathbf{U}$ and the ith row vector of $\mathbf{V}$ are denoted by $\mathbf{u}_i$ and $\mathbf{v}_i$, respectively. Clearly, instead of storing the full matrix $\widetilde{\mathbf{Z}}_{pq}^{\mathrm{RWG}}$ of size $N_p \times N_q$, the algorithm requires the storage of only $(N_p + N_q) \times \mathrm{rk}$ matrix entries. Also, the CPU time scales as $\mathcal{O}\left(\mathrm{rk}^2 (N_p + N_q)\right)$. The ACA algorithm should not be used when subdomains overlap fully ($p = q$), or partially. This is because, for these cases, the submatrices are diagonally dominant and, hence, seldom rank-deficient. For these cases, the computational overhead of the ACA algorithm becomes too high, so that a direct matrix-fill approach suffices. This will be demonstrated in Section 4.5 via a numerical example.

Finally, upon combining (4.25) and (4.26), the matrix $\mathbf{Z}_{pq}^{\mathrm{CBF}}$ is efficiently computed as

$$\mathbf{Z}_{pq}^{\mathrm{CBF}} \approx \mathbf{J}_p^T \mathbf{U}_p \mathbf{V}_q \mathbf{J}_q. \tag{4.27}$$

4.3.5 Construction of $\mathbf{U}_p$ and $\mathbf{V}_q$

The ACA algorithm constructs the rectangular matrices $\mathbf{U}_p$ and $\mathbf{V}_q$ by successively selecting rows and columns of the original matrix $\mathbf{Z}_{pq}^{\mathrm{RWG}}$ (source and field sampling). When

constructing $\mathbf{U}_p$ and $\mathbf{V}_q$, and thus $\widetilde{\mathbf{Z}}_{pq}^{\mathrm{RWG}}$, we also construct an approximate error matrix, given by $\|\widetilde{\mathbf{R}}\|_F = \|\mathbf{Z}_{pq}^{\mathrm{RWG}} - \widetilde{\mathbf{Z}}_{pq}^{\mathrm{RWG}}\|_F$, where $\|.\|_F$ denotes the Frobenius norm, which is defined as the square root of the sum of the absolute squares of its matrix elements [86]. Furthermore, each time a new row or column of $\mathbf{Z}_{pq}^{\mathrm{RWG}}$ is selected, the corresponding error vector (row or column) is computed. This is done by subtracting the actual row or column vector from the corresponding row or column vector of the approximate matrix that has been constructed in the previous iteration. The row to be selected next corresponds to the index where the largest entry of the last computed error column is located. Likewise, the column to be selected next corresponds to the index where the largest entry of the last computed error row is located. After terminating the iterative process, the columns of $\mathbf{U}_p$ are the successively computed error columns, whereas the rows of $\mathbf{V}_q$ are the successively computed error rows. Furthermore, each row vector in $\mathbf{V}_q$ is normalized by the maximum element of the last computed error column.

If the coupling matrix $\mathbf{Z}_{pq}^{\mathrm{RWG}}$ is of size $M \times N$, convergence of the ACA is guaranteed after $\min(M,N)$ iterations, since all the rows and columns of $\mathbf{Z}_{pq}^{\mathrm{RWG}}$ have then been selected/computed and are thus reconstructed exactly [114]. The ACA does not exploit the oscillatory nature of the kernel in integral equations, and may therefore not be as efficient as multipole approaches. However, for many practical applications, with moderate electrical sizes, it is found that the ACA algorithm outperforms the Fast Multipole Method (FMM), particularly with multiple right-hand-side excitations [114]. For any case, to gain an appreciable speed advantage relative to a direct matrix fill method, the ACA algorithm should be terminated ahead, e.g. after rk iterations with rk $\ll \min(M,N)$, or when

$$\|\mathbf{R}\|_F \leq \kappa \|\mathbf{Z}_{pq}^{\mathrm{RWG}}\|_F \tag{4.28}$$

for a given tolerance κ. Because the number of iterations depends on the chosen tolerance κ, it readily determines the effective rank rk of $\mathbf{Z}_{pq}^{\mathrm{RWG}}$. Since $\mathbf{Z}_{pq}^{\mathrm{RWG}}$ is only partially known, the norm of error matrix $\mathbf{R}$ is estimated after the kth iteration as

$$\|\mathbf{R}^{(k)}\|_F \approx \|\mathbf{u}_k\|_F \|\mathbf{v}_k\|_F. \tag{4.29}$$

Also,

$$\|\mathbf{Z}_{pq}^{\mathrm{RWG},(k)}\|_F^2 \approx \|\widetilde{\mathbf{Z}}_{pq}^{\mathrm{RWG},(k)}\|_F^2 = \|\mathbf{U}_p^{(k)}\mathbf{V}_q^{(k)}\|_F^2$$
$$= \|\widetilde{\mathbf{Z}}^{\mathrm{RWG},(k-1)}\|_F^2 + 2\sum_{j=1}^{k-1} |\mathbf{u}_j^T\mathbf{u}_k| \cdot |\mathbf{v}_j\mathbf{v}_k^T| + \|\mathbf{u}_k\|_F^2 \|\mathbf{v}_k\|_F^2 \tag{4.30}$$

where the last expression is written in terms of a recursive formula. The algorithm approximates the original matrix by requiring only *partial* knowledge of the original matrix.

Finally, we will list a code implementation of the ACA algorithm. Let the original matrix $\mathbf{Z}$ be of size $M \times N$. In addition, let $\mathbf{I}^{\text{row}} = [I_1^{\text{row}}, I_2^{\text{row}}, \ldots, I_{\text{rk}}^{\text{row}}]$ and $\mathbf{I}^{\text{col}} = [I_1^{\text{col}}, I_2^{\text{col}}, \ldots, I_{\text{rk}}^{\text{col}}]$ be the arrays containing orderly selected row and column indices of $\mathbf{Z}$. $\mathbf{u}_k$ is the kth column of matrix $\mathbf{U}$ and $\mathbf{v}_k$ is the kth row of matrix $\mathbf{V}$. In Matlab's notation, $\mathbf{R}(I_1^{\text{row}}, :)$ indicates the I_1^{row}th row of matrix $\mathbf{R}$. $\widetilde{\mathbf{Z}}^{(k)}$ is the matrix $\widetilde{\mathbf{Z}}$ at the kth iteration. Then, in pseudo-Matlab code, the algorithm is summarized as follows [114]:

Initialization ($k = 1$):

1. Initialize the 1st row index $I_1^{\text{row}} = 1$ and set $\widetilde{\mathbf{Z}} = \mathbf{0}$.

2. Initialize the 1st row of the approximate error matrix: $\widetilde{\mathbf{R}}(I_1^{\text{row}}, :) = \mathbf{Z}(I_1^{\text{row}}, :)$.

3. Find the 1st column index $I_1^{\text{col}} : |\widetilde{\mathbf{R}}(I_1^{\text{row}}, I_1^{\text{col}})| = \max_j(|\widetilde{\mathbf{R}}(I_1^{\text{row}}, j)|)$.

4. $\mathbf{v}_1 = \widetilde{\mathbf{R}}(I_1^{\text{row}}, :) / \widetilde{\mathbf{R}}(I_1^{\text{row}}, I_1^{\text{col}})$.

5. Initialize the 1st column of the approximate error matrix: $\widetilde{\mathbf{R}}(:, I_1^{\text{col}}) = \mathbf{Z}(:, I_1^{\text{col}})$.

6. $\mathbf{u}_1 = \widetilde{\mathbf{R}}(:, I_1^{\text{col}})$.

7. $\left\|\widetilde{\mathbf{Z}}^{(1)}\right\|_F^2 = \|\mathbf{u}_1\|_F^2 \|\mathbf{v}_1\|_F^2$.

8. Find the 2nd row index $I_2^{\text{row}} : |\widetilde{\mathbf{R}}(I_2^{\text{row}}, I_1^{\text{col}})| = \max_i (|\widetilde{\mathbf{R}}(i, I_1^{\text{col}})|), i \neq I_1^{\text{row}}$.

kth iteration:

1. Update the I_k^{row}th row of $\widetilde{\mathbf{R}}$: $\widetilde{\mathbf{R}}(I_k^{\text{row}}, :) = \mathbf{Z}(I_k^{\text{row}}, :) - \sum_{l=1}^{k-1} (\mathbf{u}_l)_{I_k^{\text{row}}} \mathbf{v}_l$.

2. Find the kth column index $I_k^{\text{col}} : |\widetilde{\mathbf{R}}(I_k^{\text{row}}, I_k^{\text{col}})| = \max_j(|\widetilde{\mathbf{R}}(I_k^{\text{row}}, j)|), j \neq I_1^{\text{col}}, \ldots, I_{k-1}^{\text{col}}$.

3. $\mathbf{v}_k = \widetilde{\mathbf{R}}(I_k^{\text{row}}, :) / \widetilde{\mathbf{R}}(I_k^{\text{row}}, I_k^{\text{col}})$.

4. Update the I_k^{col}th column of $\widetilde{\mathbf{R}}$: $\widetilde{\mathbf{R}}(:, I_k^{\text{col}}) = \mathbf{Z}(:, I_k^{\text{col}}) - \sum_{l=1}^{k-1} (\mathbf{v}_l)_{I_k^{\text{col}}} \mathbf{u}_l$.

5. $\mathbf{u}_k = \widetilde{\mathbf{R}}(:, I_k^{\text{col}})$.

6. $\|\widetilde{\mathbf{Z}}^{(k)}\|_F^2 = \|\widetilde{\mathbf{Z}}^{(k-1)}\|_F^2 + 2\sum\limits_{j=1}^{k-1}|\mathbf{u}_j^T\mathbf{u}_k||\mathbf{v}_j^T\mathbf{v}_k| + \|\mathbf{u}_k\|_F^2\|\mathbf{v}_k\|_F^2.$

7. Check convergence, if $\|\mathbf{u}_k\|_F\|\mathbf{v}_k\|_F \leq \epsilon\|\widetilde{\mathbf{Z}}^{(k)}\|_F$, end iteration.

8. Find the next row index $I_{k+1}^{\mathrm{row}}: |\widetilde{\mathbf{R}}(I_{k+1}^{\mathrm{row}}, I_k^{\mathrm{col}})| = \max_i(|\widetilde{\mathbf{R}}(i, I_k^{\mathrm{col}})|), i \neq I_1^{\mathrm{row}}, \ldots, I_k^{\mathrm{row}}.$

4.3.6   Computation of Antenna Impedances and Patterns

Computation of the Antenna Admittance Matrix

The mutual impedance Z_{ab}^{ant} between two accessible ports a and b can be computed in terms of a reaction integral, and is of a variational form [30, pp. 348–349]. Suppose $\boldsymbol{J}_S^a$ is the entire surface current as a result of exciting terminal a with a voltage source of amplitude V_a, while all other terminals are short-circuited. Likewise, $\boldsymbol{J}_S^b$ is a result of exciting terminal b with V_b, while all other terminals are short-circuited. A stationary formula for the mutual antenna admittance Y_{ab}^{ant} is given by [see also Eq. (3.123)]

$$Y_{ab}^{\mathrm{ant}} = \frac{-1}{V_aV_b}\iint\limits_{\mathcal{S}_a}\boldsymbol{E}^s(\boldsymbol{J}_S^b)\cdot\boldsymbol{J}_S^a\,\mathrm{d}S. \tag{4.31}$$

By expanding the entire surface current for excitation i $(i = a, b)$ in terms of K CBFs, we can write

$$\boldsymbol{J}_S^i(\boldsymbol{r}) = \sum\limits_{k_i=1}^{K}I_{k_i}^{\mathrm{CBF}}\boldsymbol{J}_{k_i}^{\mathrm{CBF}}(\boldsymbol{r}). \tag{4.32}$$

Next, we substitute (4.32) in (4.31) and set $V_a = V_b = 1$ to obtain

$$Y_{ab}^{\mathrm{ant}} = -\sum\limits_{k_a=1}^{K}\sum\limits_{k_b=1}^{K}I_{k_a}^{\mathrm{CBF}}\left[\iint\limits_{\mathcal{S}_a}\boldsymbol{E}^s(\boldsymbol{J}_{k_b}^{\mathrm{CBF}})\cdot\boldsymbol{J}_{k_a}^{\mathrm{CBF}}\,\mathrm{d}S\right]I_{k_b}^{\mathrm{CBF}} \tag{4.33}$$

where we have used the linearity of the operators in (4.2). Equation (4.33) can be compactly rewritten as

$$Y_{ab}^{\mathrm{ant}} = -\left(\mathbf{I}_a^{\mathrm{CBF}}\right)^T\left(\mathbf{Z}^{\mathrm{CBF}}\right)^T\mathbf{I}_b^{\mathrm{CBF}} \tag{4.34}$$

which shows that each entry of the antenna admittance matrix can be expressed in terms of the reduced matrix $\mathbf{Z}^{\mathrm{CBF}}$ and the expansion coefficients for the CBFs $\mathbf{I}_i^{\mathrm{CBF}}$. In order to

obtain the antenna impedance matrix we simply invert the admittance matrix. Alternatively, we could have directly used a stationary formula for the input impedance. However, in most MoM formulations the surface currents are induced when elements are excited by voltage sources, while all other terminals are short-circuited so that the admittance matrix is obtained naturally, without additional manipulations.

Computation of the Antenna Element Patterns

Symmetry can be used to efficiently compute the array (element) far-field pattern function $\{\boldsymbol{E}^{\text{far,tot}}, \boldsymbol{H}^{\text{far,tot}}\}$ by expanding these fields in terms of M known CBF far-field patterns $\{\boldsymbol{E}^{\text{far,CBF}}, \boldsymbol{H}^{\text{far,CBF}}\}$ as follows (see also [88, 110]):

$$\{\boldsymbol{E}^{\text{far,tot}}(\theta,\phi), \boldsymbol{H}^{\text{far,tot}}(\theta,\phi)\} = \sum_{m=1}^{M} I_m^{\text{CBF}}\{\boldsymbol{E}^{\text{far,CBF}}(\theta,\phi), \boldsymbol{H}^{\text{far,CBF}}(\theta,\phi)\} \tag{4.35}$$

where I_m^{CBF} is the mth expansion coefficient for the mth CBF current. The coefficient vector I^{CBF} is computed via the CBFM for a certain array excitation. Because many of the subdomains support the same set of CBFs, the respective CBF patterns are identical as well, apart from a phase correction due to their translated position. For instance, we can write

$$\{\boldsymbol{E}_p^{\text{far,CBF}}, \boldsymbol{H}_p^{\text{far,CBF}}\} = \{\boldsymbol{E}_q^{\text{far,CBF}}, \boldsymbol{H}_q^{\text{far,CBF}}\}e^{-jk_0(\boldsymbol{r}_{pq}\cdot\hat{\boldsymbol{r}}(\theta,\phi))} \tag{4.36}$$

where the pth CBF pattern is derived from the qth one by accounting for the translation vector $\boldsymbol{r}_{pq}$. The unit vector $\hat{\boldsymbol{r}}(\theta,\phi)$ denotes the direction of observation. Note that, for our example (Fig. 4.4), we need to explicitly compute the CBF patterns for the sets of CBFs supported only by the subdomains 1, 4 and 7. The remaining CBF patterns are obtained simply via translation.

4.4   On the Choice of the Post-Windowing Function

In this section, we examine the accuracy of the computed impedance and radiation characteristics for various types of trapezoidal taper functions experimentally, i.e., relative to

a direct MoM solution[2]. The specific pulse-windowing function that has been presented in Section 4.3.2 (**_Step IIIa_**), which realizes a single RWG overlap between CBFs, belongs also to this general class of trapezoidal taper functions.

It is essential that the superimposed CBFs be free of discontinuities at the interfaces between the antenna elements to preserve the continuity of the surface current across these junctions. One way to achieve this is to employ connection/bridge functions, which locally compensate for the spurious surface charges that would arise in the absence of these functions [104]. However, this approach introduces an additional set of unknowns in the matrix equation, which is undesirable. Furthermore, the matrix condition number generally increases if macro-domain basis functions are mixed with subsectional basis functions. Instead, in the present approach, all subdomains are extended beyond their original boundaries, ensuring that the CBFs so generated overlap with those residing in the adjacent subdomains. Although the time needed to generate the CBFs slightly increases, the construction time and number of unknowns in the final reduced matrix equation will be much smaller, and this, in turn, enables us to solve electrically large problems.

As discussed in Section 4.3.2, we suppress and truncate the singular currents by using a suitable windowing function Λ for each of the CBFs. Several envelopes for the trapezoidal tapers have been examined, including the rooftop and pulse-type windowing functions. We will first examine the accuracy of the windowing technique for a 3×1 TSA array in case only primary CBFs are generated. Afterwards, the same set of primary CBFs are also used to synthesize the surface current on a larger 7×1 TSA array. In both cases, the coupling coefficients are computed by using a direct MoM approach and CBFM, respectively, and for the sake of comparison, the degree of agreement between the above coefficients is used as a measure for the computational accuracy of CBFM.

4.4.1   A 3×1 Tapered Slot Antenna Array

The CBFM is applied to the 3×1 TSA array of Fig. 4.5(a). To generate the primary CBFs, we extract three subarrays from this array, comprising of elements 1–2, 1–2–3 and 2–3.

---

[2]This section is based on:

[100]: <u>R. Maaskant</u>, R. Mittra and A. G. Tijhuis, "Application of trapezoidal-shaped characteristic basis functions to arrays of electrically interconnected antenna elements," *Proc. Int. Conf. on Electromagn. in Adv. Applicat. (ICEAA)*, Torino, Sep. 2007, pp. 567–571.

However, we consider only two of them since subarrays 1–2 and 2–3 have mirror symmetry. After generating the CBFs for the subarrays, four different post-windowing functions, ranging from pulse function to rooftop, are considered, and are depicted in Fig. 4.5(b). The continuous trapezoidal taper function Λ, which determines the post multiplication
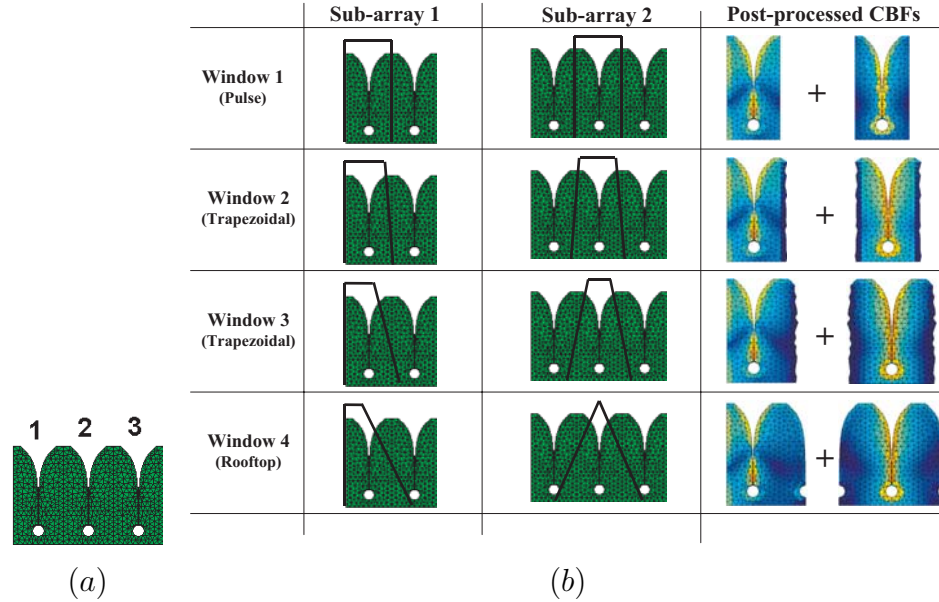

(a) (b)

Figure 4.5: (a) A 3-element TSA array. (b) The two subarrays that have been extracted from the 3×1 array. Four types of windowing functions have been considered, ranging from the pulse (without overlap) to the rooftop window. The first CBF after windowing is shown on the right for each windowing function and subarray.

factors for the RWG expansion coefficients, is specified as

$$\Lambda(d_{\min}, d_t) = \begin{cases} 1 & d_{\min} > \frac{d_t}{2} \text{ and } \boldsymbol{r} \in \mathcal{S}_\Lambda \\ \frac{1}{2} - \frac{d_{\min}}{d_t} & -\frac{d_t}{2} \leq d_{\min} \leq \frac{d_t}{2} \\ 0 & \text{otherwise.} \end{cases} \quad (4.37)$$

where $d_{\min}$ is the projection distance from the common-edge center of a RWG basis function, to the nearest edge that connects the antenna element(s) under consideration, and d_t is the width of the linear taper. If $d_{\min} = 0$, a point on the connecting edge is considered for

which the weighting function $\Lambda = 1/2$. The weighting function $\Lambda = 0$ for points outside the support $\mathcal{S}_\Lambda$ of the trapezoidal taper function, and $\Lambda = 1$ for interior points, but outside the support of the linear taper. For the windowing functions 2–4 in Fig. 4.5(b), we have chosen d_t to be 33%, 67%, and 100% of the antenna element width, respectively. If $d_t = 0$, the pulse taper is obtained that realizes a single basis-function overlap as described in Section 4.3.2. However, for the sake of illustration, we will choose the pulse window in this subsection not to overlap (no electrical connection).

An examination of the coupling coefficients in Fig. 4.6(a) and (b) indicate that the solution accuracy is lowest for the pulse-type windowing functions (no overlap), which is expected because such a choice introduces a discontinuity at the interface between the two elements. Although the total number of unknowns is only 2+3+2=7, excellent agreement is observed for all applied trapezoidal windows, because they: (i) provide overlap between the CBFs; and, (ii) do not taper the CBFs at the antenna terminals.

(a) (b)
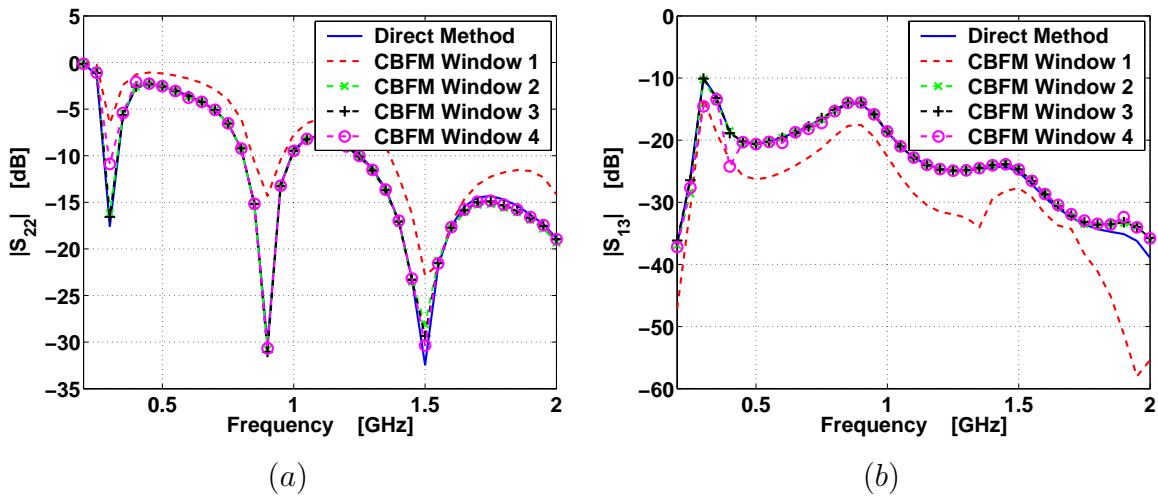
Figure 4.6: The computed S-parameters are shown for the four different windowing functions: (a) Coupling coefficient S_{22}^{ant} and, (b) Coupling coefficient S_{13}^{ant}. The direct MoM solution is designated by a solid line.
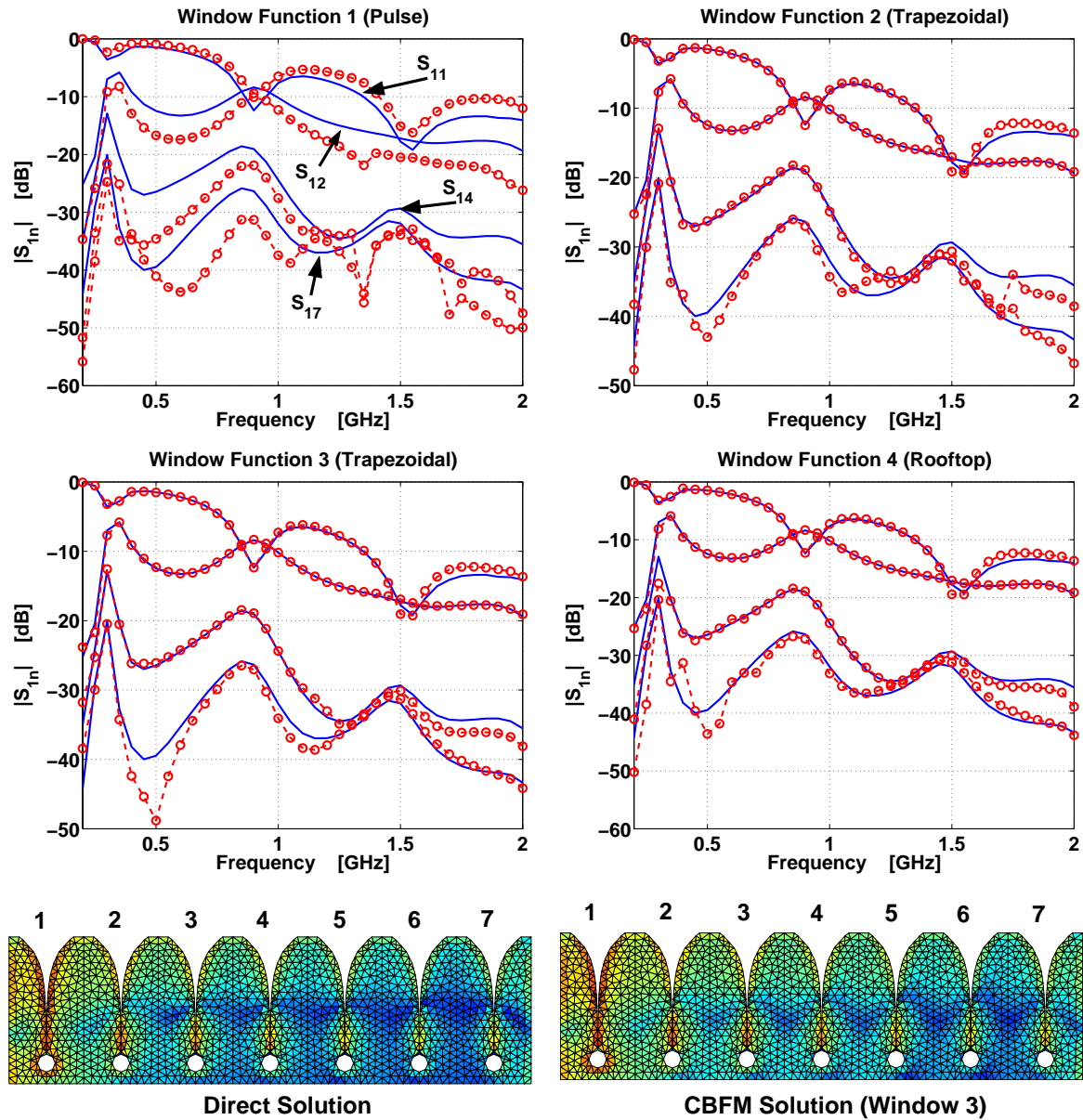
Figure 4.7: Coupling coefficients S_{11}^{ant}, S_{12}^{ant}, S_{14}^{ant} and S_{17}^{ant} for various frequencies computed with a direct MoM approach (solid lines) and CBFM (dashed lines). Each graph corresponds to a certain windowing function that has been applied to the CBFs, ranging from the pulse function to the rooftop function. The antenna element numbering and current distribution @ 900 MHz is shown for both the direct MoM approach and CBFM (window 3), for the case that the corner element is excited and the other terminals are short-circuited.

4.4.2   A 7×1 TSA Array

Since the generating subarrays of an $N \times 1$-element array are identical to that of a 3×1-element array, the previously generated CBFs are reused to synthesize the surface current, and to subsequently compute the full S-parameter matrix of the 7×1 TSA array. Fig. 4.7 shows a comparison of the coupling coefficients, derived by using MoM and CBFM, respectively, for each of the four windowing functions. As expected, the choice that attains the lowest accuracy is the pulse window, while all remaining windowing functions yield accurate results for the mutual coupling down to -30 dB level, despite the fact that the total number of unknowns (CBFs) is only 19, which is orders of magnitude less than the original 4557 unknowns (RWGs) needed in the direct MoM formulation.
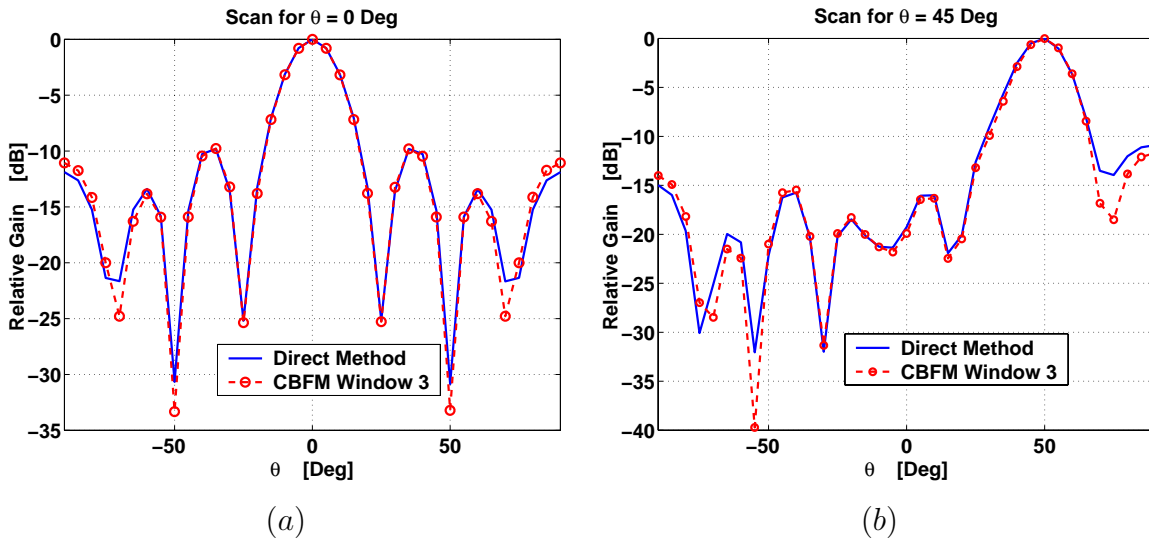
Figure 4.8: Relative gain pattern for two E-plane scans: (a) 0 degrees (broadside scan), and (b) 45 degrees. The solid line corresponds to the pattern (@ 900 MHz) computed by the direct MoM, while the dotted curve refers to the CBFM solution (window 3).

For completeness, also the surface current distribution (@ 900 MHz) is shown in Fig. 4.7 (bottom, left) for the direct MoM approach, where the corner element is excited by a voltage source and all other terminals are short-circuited. As can be seen in Fig. 4.7 (bottom, right), the approximated surface current distribution is visually indistinguishable (for CBFM window 3). Moreover, with reference to the radiation patterns computed by the direct MoM, the approximated patterns for both the 0 and 45 degree scans are also

well predicted (see Fig. 4.8).

This leads to the conclusion that, as soon as an overlap is provided between CBFs, all trapezoidal taper functions yield accurate results. Henceforth, we will therefore employ the pulse function to minimize the support of the CBFs, but will retain a single cell overlap as proposed in Section 4.3.2.

4.5   Results on Hybridizing CBFM and ACA

The numerical accuracy and efficiency of the CBFM combined with the ACA will be assessed in this section [87]. Unless specified differently, a threshold of 10^{-2} is used for the SVD procedure in CBFM, and the threshold used in ACA.

4.5.1   Accuracy of CBFM for a 7×1 TSA Array

The accuracy of CBFM will be discussed for an 1-D single-polarized array of electrically interconnected TSA elements. For the sake of validation, we compare the CBFM solution to a direct MoM solution employing only RWG basis functions. This means that we essentially consider the consequences of reducing the number of MoM basis functions with the CBFM. The CBFs are generated as described in Sec. 4.3.2, where the radius for generating the secondary CBFs has been chosen equal to the width of two elements, and has been specified independent of the frequency. After the SVD procedure, only 3 CBFs are retained for the outer two corner elements and 5 CBFs for the inner elements (@ 900 MHz). Fig. 4.9 shows the computed results for a 7×1 array of TSAs.

One visually observes a very good agreement between the CBFM and direct solution for both the radiation and impedance characteristics. These results show that the electrical interconnection between TSA elements is treated accurately, even though small differences are noticeable in the error surface current distribution $\boldsymbol{J}_S^{\text{Error}}$ [Fig. 4.9(d)]. However, $\|\boldsymbol{J}_S^{\text{Error}}\|_2$ is at least 30 dB lower than the largest magnitude observed in $\|\boldsymbol{J}_S^{\text{MoM}}\|_2$, which is found to be ~ 12 dBA/m. The current is a smoothly varying function across the common edge connecting both the element under excitation (#1) and its direct adjacent element (#2), whereas the current continuity degrades across common edges for elements farther
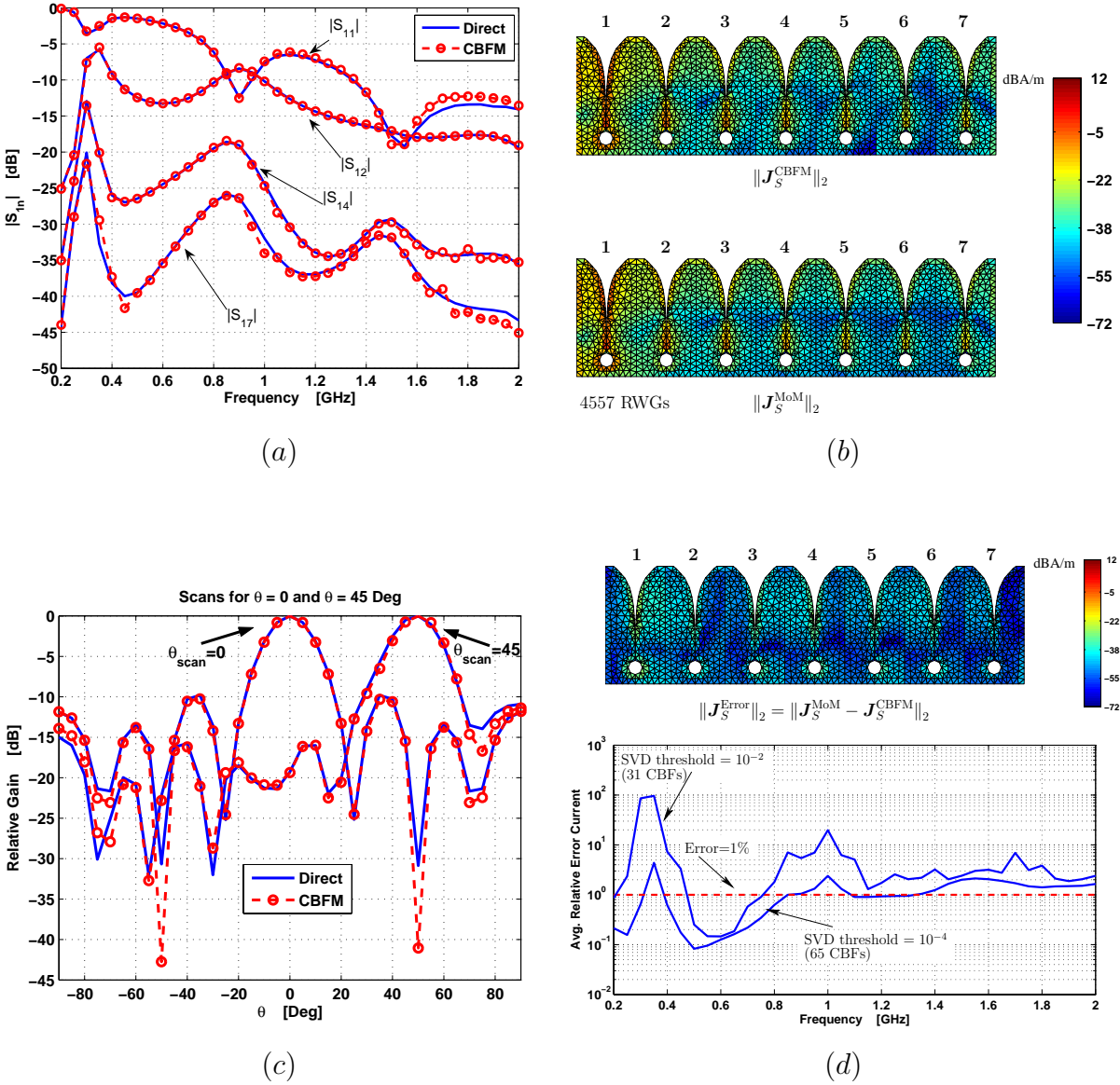
(a)

(b)

(c)

(d)

Figure 4.9: (a) Scattering parameters S_{1n}^{ant}, for $n = 1, 2, 4, 7$ over frequency for a 150 Ω port termination, computed by a direct approach (solid blue line) and CBFM (dashed red line with circles). (b) Magnitude of the normalized surface current distribution in [dBA/m] and port/element numbering for the direct solution and CBFM solution when element 1 is excited by a voltage source and all other terminals are short-circuited (@ 900 MHz). The difference between both current distributions is shown in (d) (top). Fig. (c) shows the relative total gain patterns for two E-plane scans: 0 degrees (broadside scan); and 45 degrees (150 Ω port termination). The solid blue line corresponds to the pattern (@ 900 MHz) computed by a direct MoM approach and the pattern in red (dashed with circles) refers to the CBFM solution. The average error between the RWG expansion coefficients over frequency is shown in (d) (bottom).

out. This can be understood by realizing that CBFs have been generated to accurately represent the current on the excited element as well as on those elements that are directly adjacent (see generation of CBFs in Section 4.3.2). The all-excited array case in Fig. 4.2 (Step IV) demonstrates therefore a better continuity of the current across all the common edges. To reduce the error for the one-element excitation case, more CBFs need to be generated to represent the rapidly varying current on the TSA elements farther out, at the cost of sacrificing the total execution time.

Fig. 4.9(d) (bottom) illustrates the average error of the RWG expansion coefficients as a result of comparing the CBFM solution to a direct MoM solution. This error is plotted as a function of frequency and refers to the case that corner element 1 is excited by a voltage source while all others are short-circuited; it is defined as

$$
\text{Rel. Error} = \frac{\sqrt{\sum_{n=1}^{N} \left| I_n^{\text{RWG,MoM}} - I_n^{\text{RWG,CBFM}} \right|^2}}{\sqrt{\sum_{n=1}^{N} \left| I_n^{\text{RWG,MoM}} \right|^2}} \times 100\%. \tag{4.38}
$$

Note that this situation does not correspond to the match-terminated case of which the results are shown in Fig. 4.9(a) and (c). On average, the relative error is less than 5% but may become larger as it tends to oscillate in accordance with the resonant behavior of the surface current. Obviously, near such a resonance, a small shift in frequency may result in a large relative error of the surface current. Resonances appear at almost constant intervals and weaken in strength as the array becomes electrically large, resulting in a relative error that levels out below 5%. For completeness, we also plot the reduced error curve when the SVD threshold is lowered to 10^{-4}. A close inspection of the corresponding current distribution reveals that the current improves globally, which also mitigates the problem of discontinuous behavior of the current across the common edges (although not shown).

4.5.2   Error and Fill-Time of the ACA Algorithm

Based on the previous array example, the memory requirements and CPU time of the ACA approach are examined in detail for a number of subdomain pairs having a certain mutual orientation and separation distance.
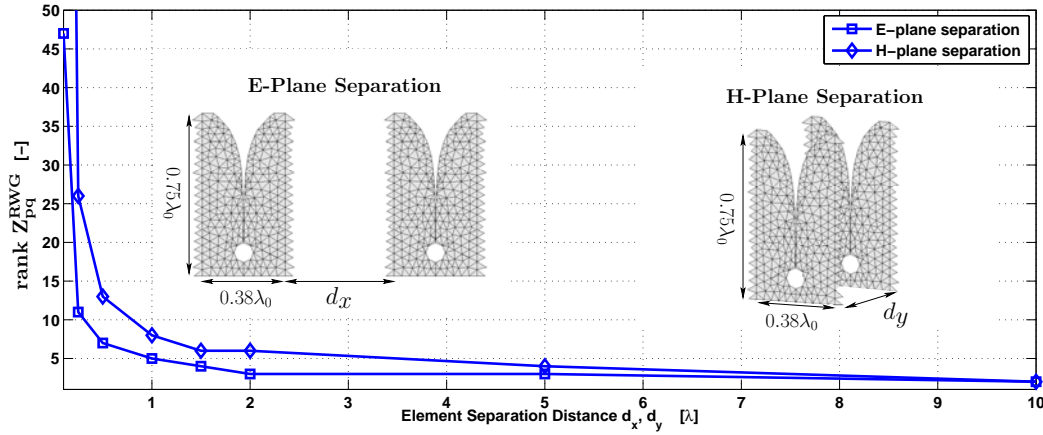
Figure 4.10: Effective rank of coupling matrix $\mathbf{Z}_{pq}^{\mathrm{RWG}}$, where the matrix entries are the mutual reactions between two separated groups of RWGs, and where each group corresponds to one TSA element. The matrix $\mathbf{Z}_{pq}^{\mathrm{RWG}}$ is of size 675×675 and the rank is computed using a full SVD (threshold on the normalized singular values is 10^{-2}) for various E-plane and H-plane separation distances.

Fig. 4.10 illustrates the effective rank distribution of a coupling matrix $\mathbf{Z}_{pq}^{\mathrm{RWG}}$, where the matrix entries are the mutual reactions between two separated groups of RWGs. The two groups of RWGs represent two TSA elements that are either separated in the E- or H-plane, for different separation distances d_x and d_y, respectively. The effective rank is computed by means of a full SVD with a threshold on the normalized singular values of 10^{-2}. The size of the matrix $\mathbf{Z}_{pq}^{\mathrm{RWG}}$ is 675×675. It is observed that, as the element separation distance becomes less than a wavelength, the effective rank of $\mathbf{Z}_{pq}^{\mathrm{RWG}}$ increases rapidly and is approximately proportional to $1/\sqrt{d_x}$ for E-plane separations, and to $1/d_y$ for H-plane separations. This indicates that a rank-revealing algorithm, such as the ACA, can be computationally more effective than a straightforward matrix fill, even for electrically small separation distances. Finally, we mention that, for a fixed frequency and separation distance, the (maximum) effective rank is only weakly dependent upon the mesh density [114].

The time to construct matrix $\widetilde{\mathbf{Z}}_{pq}^{\mathrm{RWG}}$ using ACA, relative to the time to construct matrix $\mathbf{Z}_{pq}^{\mathrm{RWG}}$ using a straightforward approach, has been plotted in Fig. 4.11 as a function of the ACA threshold level and for a number of E-plane and H-plane element separation

distances. The relative block fill time has been defined as

$$\text{Rel. BlockFillTime} = \frac{\text{Time to build } \widetilde{\mathbf{Z}}_{pq}^{\text{RWG}}}{\text{Time to build } \mathbf{Z}_{pq}^{\text{RWG}}} \times 100\%. \tag{4.39}$$

Also, the relative error between the block factored matrix $\widetilde{\mathbf{Z}}_{pq}^{\text{RWG}}$ and the actual matrix $\mathbf{Z}_{pq}^{\text{RWG}}$ has been illustrated in Fig. 4.11. The relative matrix error has been defined as

$$\text{Rel. Error} = \frac{\|\mathbf{Z}_{pq}^{\text{RWG}} - \widetilde{\mathbf{Z}}_{pq}^{\text{RWG}}\|_F}{\|\mathbf{Z}_{pq}^{\text{RWG}}\|_F} \times 100\%. \tag{4.40}$$

As expected, Figs. 4.11(a) and (b) show that the time to construct the approximant $\widetilde{\mathbf{Z}}_{pq}^{\text{RWG}}$ inevitably exceeds the time to construct the actual matrix $\mathbf{Z}_{pq}^{\text{RWG}}$ if the threshold level for the ACA is set (too) high, or if the element separation distance becomes (too) small. Typically, an ACA threshold of 10^{-2} is used so that the relative error is expected to be in the order of a few percent or less. Remarkably enough, for this ACA threshold, the ACA is computationally more effective than a straightforward approach down to an E-plane separation of $0.1\lambda_0$. The corresponding rank of the matrix is then 47 (see Fig. 4.10). In case of H-plane separations, the elements are facing each other and, consequently, the separation distance has to be at least $0.2\lambda_0$. The relative error of the approximated matrix is plotted in Fig. 4.11(c) and (d) and decreases uniformly for increasingly larger ACA threshold levels as the algorithm successively reduces the rank of $\mathbf{Z}_{pq}^{\text{RWG}}$. The successive rank reduction has been proven in [113] for matrices generated by asymptotically smooth functions and is mainly determined by the polynomial interpolation method that is used by the ACA algorithm. However, despite the fact that our matrices are generated by oscillatory kernels, the ACA algorithm is found to be very robust for all the antenna problems that we have studied, and the error resembles the typical error distributions of Fig. 4.11(c) and (d).

The ACA algorithm only stops constructing an approximant of a matrix block if the error of that approximated matrix is below a certain specified threshold. Hence, the error of the approximation is therefore equal for all the matrix blocks that have been constructed using ACA, irrespective of the fact whether subdomains are large, small, closely separated, well separated, or even overlapping. The penalty, however, is that for closely separated domains, or for domains that largely differ in size, the ACA algorithm becomes inefficient, because of the large number of iterations required to construct an almost full-rank matrix block to meet a certain error threshold level.
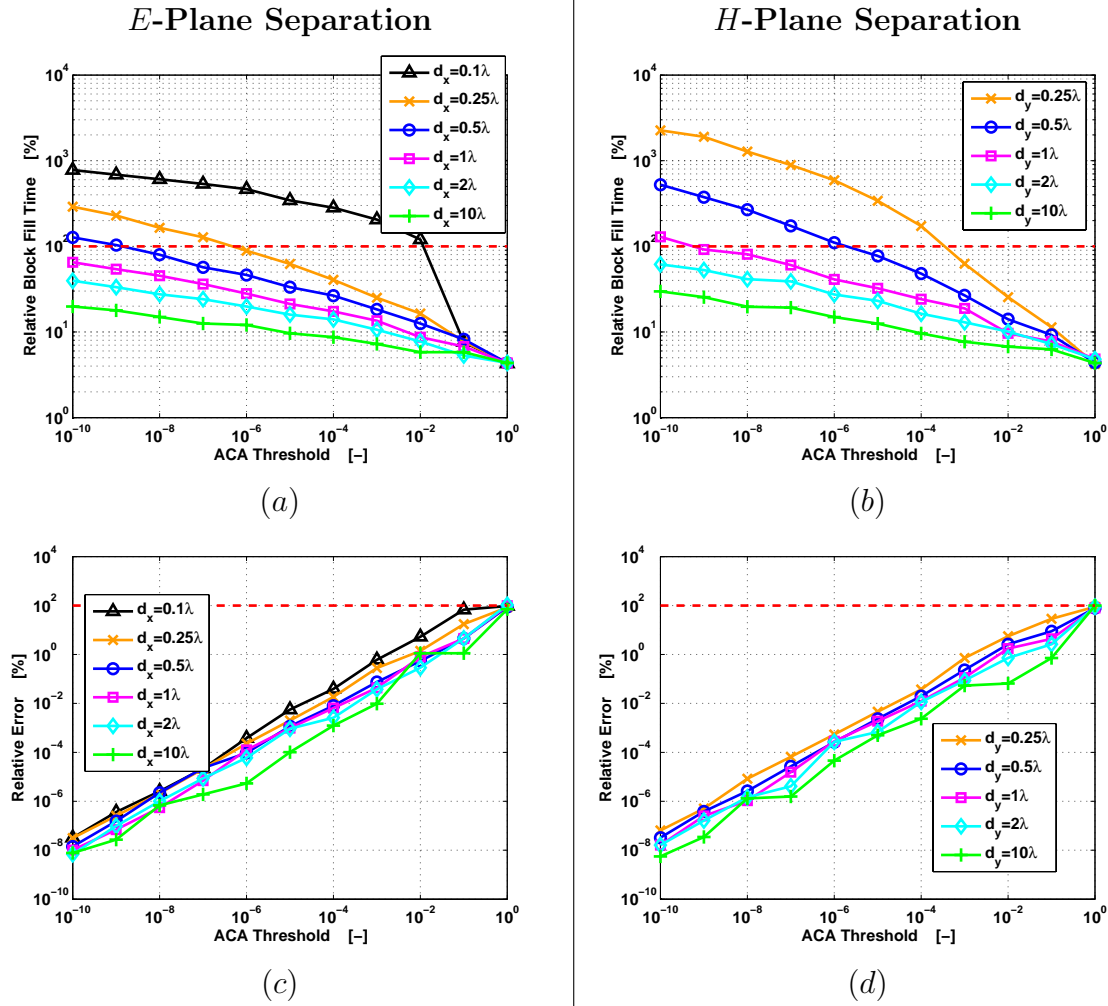
Figure 4.11: ACA block fill time of matrix $\widetilde{\mathbf{Z}}_{pq}^{\mathrm{RWG}}$ relative to the time to fill $\mathbf{Z}_{pq}^{\mathrm{RWG}}$ in a straightforward manner, as a function of the ACA threshold level κ, for various (a) E-plane TSA element separations, and (b) H-plane TSA element separations. Matrix $\mathbf{Z}_{pq}^{\mathrm{RWG}}$ is of size 675×675 of which the rank distributions are shown in Fig. 4.10. The relative error between $\widetilde{\mathbf{Z}}_{pq}^{\mathrm{RWG}}$ and $\mathbf{Z}_{pq}^{\mathrm{RWG}}$ as a function of the ACA threshold level is plotted, for various (c) E-plane TSA element separations, and (d) H-plane TSA element separations.

4.5.3 Compression of the ACA Algorithm

Fig. 4.12 illustrates the total storage requirement of the blocks $\mathbf{U}_p$ and $\mathbf{V}_q$, relative to a full storage of $\mathbf{Z}_{pq}^{\mathrm{RWG}}$ as a function of both the E- and H-plane element separation distances.

Here, the relative RAM usage is defined as

$$\text{Rel. RAM} = \frac{\text{Total number of entries } \mathbf{U}_p;\ \mathbf{V}_q}{\text{Total number of entries } \mathbf{Z}_{pq}^{\text{RWG}}} \times 100\%. \tag{4.41}$$
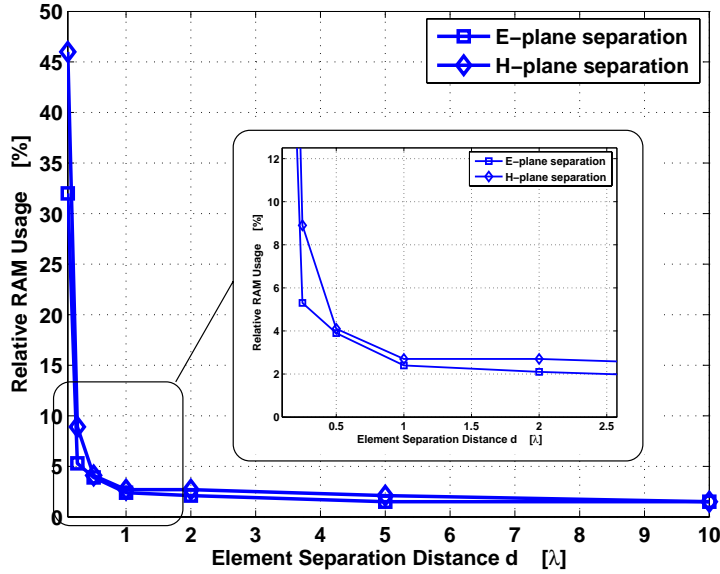
	$0.1\lambda_0$	$0.25\lambda_0$	$0.5\lambda_0$	$1\lambda_0$	$2\lambda_0$	$5\lambda_0$	$10\lambda_0$
E-plane, rank rk	107	18	13	8	7	5	5
H-plane, rank rk	156	30	14	9	9	7	5

Figure 4.12: Total RAM usage of $\mathbf{U}_p$ and $\mathbf{V}_q$, relative to the RAM required to store $\mathbf{Z}_{pq}^{\text{RWG}}$, for various E- and H-plane element separation distances. ACA threshold $\kappa = 10^{-2}$. The corresponding number of iterations rk, which also equals the effective rank, is shown in the table (full rank is 675).

Typically, the ACA algorithm requires the storage of less than 5% of the full matrix block when the separation distance becomes larger than $0.2\lambda_0$. Moreover, also the matrix product $\mathbf{J}_p^T\,\mathbf{U}_p\mathbf{V}_q\mathbf{J}_q$ will be evaluated in a numerically efficient manner. To analyze the computational complexity of this product, let us assume two identical domains, each of them supporting N RWGs, and an effective matrix rank rk as a result of a certain group separation distance and frequency. Then, if we employ K CBFs per group, the computational complexity of the multiplications in (4.27) scales as $\mathcal{O}(KN[2\text{rk} + K])$. On the other hand, a straightforward matrix fill method requires a computational complexity of

$\mathcal{O}(KN[N + K])$, which is an order larger in N (usually $N \gg K$) if rk $\ll N$. The rank rk, as computed by the ACA algorithm, is also shown in Fig. 4.12 for the various separation distances in both the E- and H-planes. Comparing this rank distribution to the distribution shown in Fig. 4.10 obtained by using a full SVD approach, we conclude that, in a sense, the ACA algorithm can be regarded as a "poor man's SVD" for determining the effective rank of a matrix.

4.5.4   Computational Complexity for 1-D and 2-D Arrays

Next, we consider the computational complexity of both CBFM and CBFM+ACA for analyzing large arrays of electrically interconnected TSA elements. The total CPU time required to compute the antenna impedance matrix of 1-D single-polarized arrays, ranging from 10 up to 400 TSA elements, is specified in Table 4.1. The total CPU time includes the time to generate primary and secondary CBFs, to perform the SVD, to construct and solve the reduced matrix equation, either with or without the ACA algorithm, and to compute the antenna impedance matrix.

Table 4.1: Total CPU time required to compute the port impedance matrix of various 1-D single-polarized TSA arrays (@ 900 MHz).

No. TSAs	CBFM [sec.]	CBFM+ ACA [sec.]	No. $\mathbf{Z}_{pq}^{\mathrm{RWG}}$	No. RWGs	No. CBFs
10×1	264	206	29	6519	46
20×1	353	207	59	13059	96
40×1	549	223	119	26139	196
80×1	937	262	239	52299	396
160×1	1779	607	479	104619	796
320×1	3400	1053	959	209259	1596
400×1	4108	1344	1199	261579	1996

As the degree of translation symmetry is large for 1-D arrays, the total number of matrix blocks $\mathbf{Z}_{pq}^{\mathrm{RWG}}$ that need to be constructed remains relatively low. In fact, for a 400 element TSA array, 400×400 blocks need to be constructed but this quantity is reduced to only 1199 (0.7%) by exploiting reciprocity and translation symmetry. Moreover, this number

scales as $\mathcal{O}(N)$, where N is the total number of TSA elements. Hence, for relatively small arrays, a large portion of the time is devoted to the generation of CBFs, which implies that the speed advantage of the ACA algorithm becomes more apparent for very large arrays, or for arrays that exhibit little translation symmetry. Due to the fine geometrical features of a TSA element, as well as the utilized method to generate CBFs (primaries+secondaries), the reduction factor of unknowns is quite significant (~ 135).

In order to reduce the degree of translation symmetry, 2-D arrays of single-polarized TSA elements are considered. In effect, we increase the number of distinct separation distances and mutual orientations between pairs of CBFs. The element spacing in both the E- and H-plane are chosen equal to the width of a single TSA element. The results are shown in Table 4.2 for various array sizes, ranging from a 4×4 up to a 20×20 element array configuration.

Table 4.2: Total CPU time required to compute the port impedance matrix of various 2-D single-polarized TSA arrays (@ 900 MHz).

No. TSAs	CBFM [sec.]	CBFM+ ACA [sec.]	No. $\mathbf{Z}_{pq}^{\mathrm{RWG}}$	No. RWGs	No. CBFs
4×4	457	341	54	10380	112
6×6	743	393	150	23418	264
8×8	1160	445	294	41688	480
10×10	1738	537	486	65190	760
12×12	2500	684	726	93924	1104
14×14	3476	934	1014	127890	1512
16×16	4666	1280	1350	167088	1984
18×18	6136	1787	1734	211518	2520
20×20	8022	2527	2166	261180	3120

Since more secondary CBFs are generated for a 2-D array configuration, the reduction factor for the total number of unknowns for 2-D arrays is slightly less than for the 1-D array case (95 versus 135). Also, for 2-D arrays, the number of $\mathbf{Z}_{pq}^{\mathrm{RWG}}$ matrix blocks that need to be constructed is increasing more rapidly, so that the computational advantage of the ACA algorithm becomes more pronounced.

For ease of comparison of the computational cost of CBFM to the combined CBFM–ACA approach, the results of Tables 4.1–4.2 have been graphically illustrated in Fig. 4.13. As
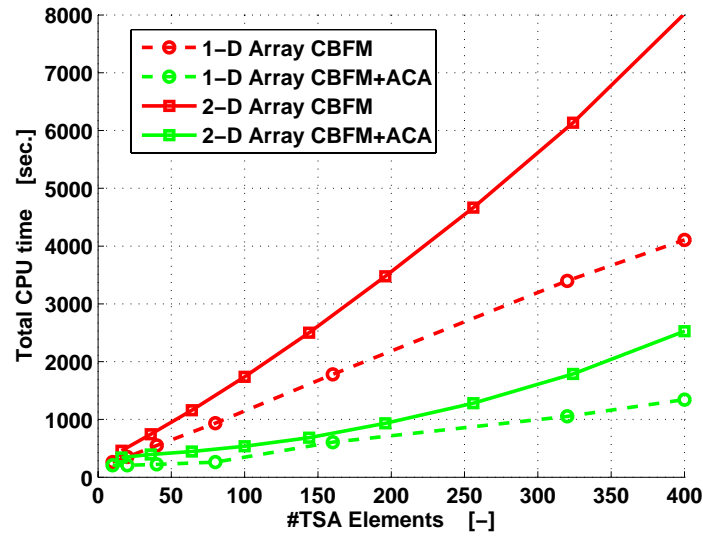
Figure 4.13: Total CPU time as a function of the total number of TSA elements for 1-D and 2-D array configurations of various sizes.
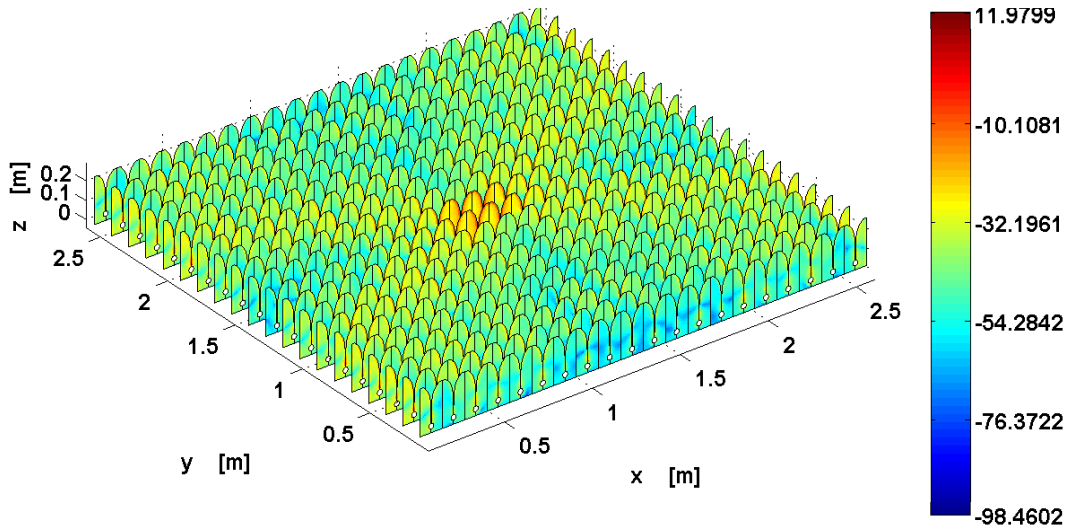

Figure 4.14: Surface current distribution of a 20×20 TSA array (Magnitude in [dBA/m] @ 900 MHz). The four center elements are equally excited by voltage generators (1 V) while the others are short-circuited.

expected, the CPU time scales linearly for 1-D arrays, whereas the order of complexity increases (slightly) when 2-D arrays are analyzed. For the array configurations and sizes that we have studied it is concluded that a combined CBFM–ACA approach approximately

halves the total execution time with respect to a straightforward CBFM approach.

Fig. 4.14 illustrates the corresponding coupling effect and magnitude of the surface current distribution (logarithmic scale) of a 20×20 TSA array when the four center elements are excited while the other ports are short-circuited.

4.6 Analysis of Large Arrays of Subarrays

A rigorous full-wave analysis of phased arrays, each of them surrounded by a number of other disjoint actively phased-steered arrays, becomes computationally prohibitive for a large number of electrically large subarrays. Despite the fact that the computational complexity of solving the matrix equation can be reduced by a large factor by employing a relatively small number of CBFs, the numerical analysis of a much larger array of subarrays will inevitably pose a computational burden, along with an increase in the number of unknowns beyond a certain point. Conventional infinite-array approaches may be accurate and fast for an extremely large array of subarrays. However, the subarrays have to be electrically small and positioned over a uniform (possibly skewed) rectangular lattice.

4.6.1 A Perturbation Approach

In this method, the CBFM is used to construct a reduced moment matrix for only one of the subarrays, and the matrix entries are modified to account for the mutual coupling by using the characterization of the actively phase-steered surrounding subarrays. Towards this end, we enforce the final surface current solution to be identical on every subarray, apart from a phase difference depending on the scan angle and position vector of a subarray, whereas, within each subarray, surface currents may differ per element.

Although the subarrays support identical currents (apart from a phase shift), the present method differs from the array factor method where the current on each subarray is taken equal to the isolated subarray current, or the current induced on an actively steered sub-array embedded in an infinite array of subarrays. In fact, it is proposed to employ a quasi infinite array approach, where only a finite number of subarrays are taken into account, but where the current on each subarray is assumed to be identical (apart from a phase

shift).

Computing the fields in a given region of a periodic structure, while assuming that they are identical in other regions is a perturbation approach, has also been proposed by Skrivervik and Mosig [92, 119]. The first publication exposes a spectral-domain approach, the latter shows a spatial-domain approach. In its implementation, the latter is closer to the approach considered in this section; the main difference is that in the Skrivervik and Mosig papers, the region referred to above is one (microstrip) antenna, while it here corresponds to a subarray.

Basically, the CBFM is used at antenna element level, whereas an infinite-array approach is used at subarray level. The concept of combining infinite-array approaches with macro-domain basis-functions has been examined before in similar methods, e.g., in [90] and [91].

The use of an infinite-array assumption at the subarray level obviates the need to solve for all the subarrays at once, and reduces the total solve time significantly. Obviously, such an approximate method is exact for infinite arrays of mutually coupled subarrays, as well as for finite arrays of non-coupled subarrays (isolated subarrays), or for mutually coupled subarrays where the end effects of bordering subarrays do not disrupt the impedance characteristics of the subarray under study. Hence, for a finite and all-excited array, the active mutual coupling (or active mutual scan impedance) between the subarrays is one of the primary factors that determines the approximation error of the proposed method. Generally, the accuracy of the approximate method depends upon the scan angle, number of surrounding subarrays, the electrical distance between the subarrays, the electrical size of a subarray, and the type of the antenna element.

Let us refer to Fig. 4.15, in which we depict the scheme for computing the scan impedance matrix of the six antenna elements that comprise the central subarray. Basically, the scan impedance matrix is obtained by adding the phase-shifted coupling impedance matrices of the surrounding subarrays to the array impedance matrix of the central subarray.

As we impose the condition that the final surface currents among the various subarrays be identical, except for a phase shift, we are led to conclude that the corresponding CBF expansion coefficients have to be equal, though phase-shifted as well. Fig. 4.15(a) illustrates how the (active) reduced matrix block $\mathbf{Z}_{pq}^{\mathrm{CBF}}$ is computed by testing the electric field, which is generated not only by the source CBF $\mathbf{J}_q$, but also by the respective phase-

shifted neighboring source CBFs $\mathbf{J}_q e^{j\varphi}$ and $\mathbf{J}_q e^{-j\varphi}$ (coupling terms), where the phase shift φ depends on both the scan direction $\hat{\boldsymbol{r}}(\theta, \phi)$ and the relative position of the subarray w.r.t. the central subarray.
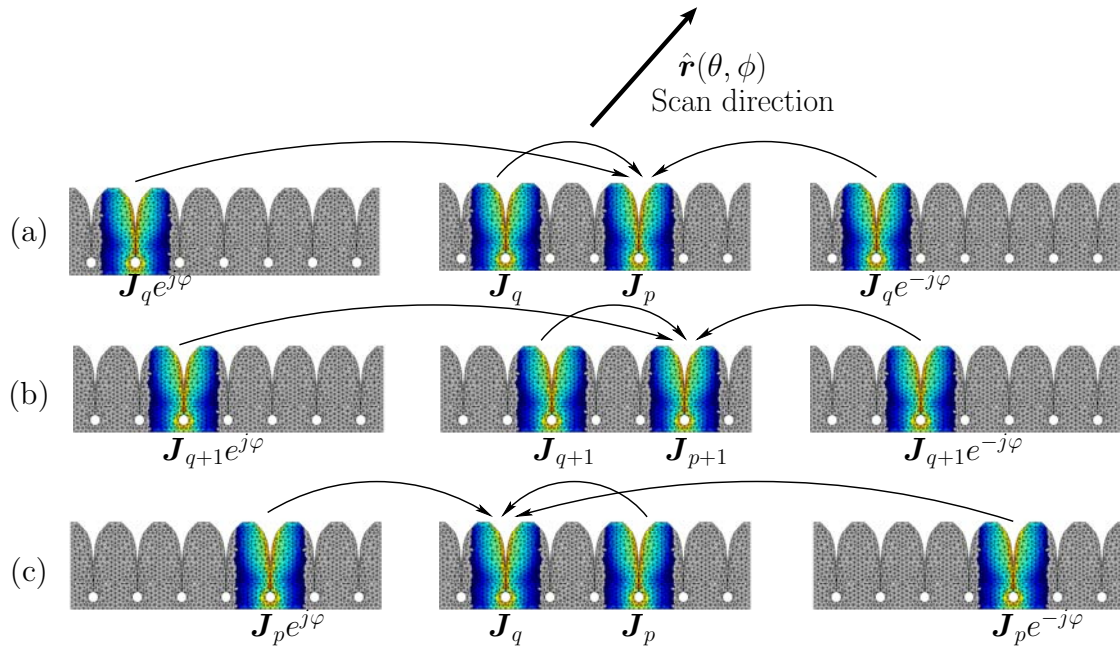

Figure 4.15: Reduced matrix construction for the central subarray while accounting for the coupling with the actively phase-steered surrounding subarrays.

In the process of computing all the mutual reactions, the translation symmetry can again be exploited for fast construction of the $\mathbf{Z}^{\mathrm{CBF}}$. This can be observed by comparing Fig. 4.15(a) to Fig. 4.15(b) [*cf.* Fig. 4.3], where an identical though one-element translated reaction between the CBFs is visualized.

Finally, for an off-broadside scan direction, one can easily verify that the active reduced matrix block $\mathbf{Z}_{pq}^{\mathrm{CBF}} \neq \left(\mathbf{Z}_{qp}^{\mathrm{CBF}}\right)^{T}$. This is depicted in Fig. 4.15(c), where the source and test domains on the central subarray have been interchanged with respect to the domains shown in Fig. 4.15(b). Consequently, the final active reduced matrix $\mathbf{Z}^{\mathrm{CBF}}$ will not be symmetric; therefore, both the upper- and lower-triangular part of the matrix must be at least partially computed.

Numerical Results

The numerical accuracy and efficiency of the modified CBFM approach, relative to a direct CBFM approach, will be evaluated in this section for an array of disjoint subarrays of TSA elements.

The anomalous antenna impedance effects, associated with the (resonant) gaps/slots between disjoint subarray tiles, have been reported in [120, 121] and will therefore not be discussed in this thesis. These gaps may need to be introduced for servicing purposes, so that, e.g., individual subarrays can be installed and/or removed as modular units. Furthermore, the transport and manufacturability of relatively small units may be advantageous.

A threshold of 10^{-2} is used both for the SVD procedure in CBFM, and the threshold used in the Adaptive Cross Approximation Algorithm. These parameter settings are chosen to be equal for both the direct and modified CBFM approaches, and we will exploit the translation symmetry for all the cases that are studied, which enables us to make relative comparisons.

9 Subarrays Composed of 64 TSA Elements Each

Fig. 4.16 illustrates an array of 9 TSA subarrays (3×3) for which a total of 375,192 RWG basis functions have been employed. We compute the antenna impedance matrix of the 576 TSA elements by using a direct CBFM approach, and then proceed to derive the scan reflection coefficient for each TSA element (150 Ω source-reference impedance). These scan reflection coefficients are taken as references for further comparison. It should be noted that the scan impedances (or scan reflection coefficients) are not only of interest for the characterization of transmit antennas, but can also be used to evaluate noise coupling in receive antennas (see e.g. [122, 123], and Chapter 5).

Let the scan reflection coefficient of the nth antenna element be denoted as Γ_n^{scan}, and let the total number of the central subarray elements be N_{sub}. Then, within the central subarray, the average relative error between the actual and approximated scan reflection
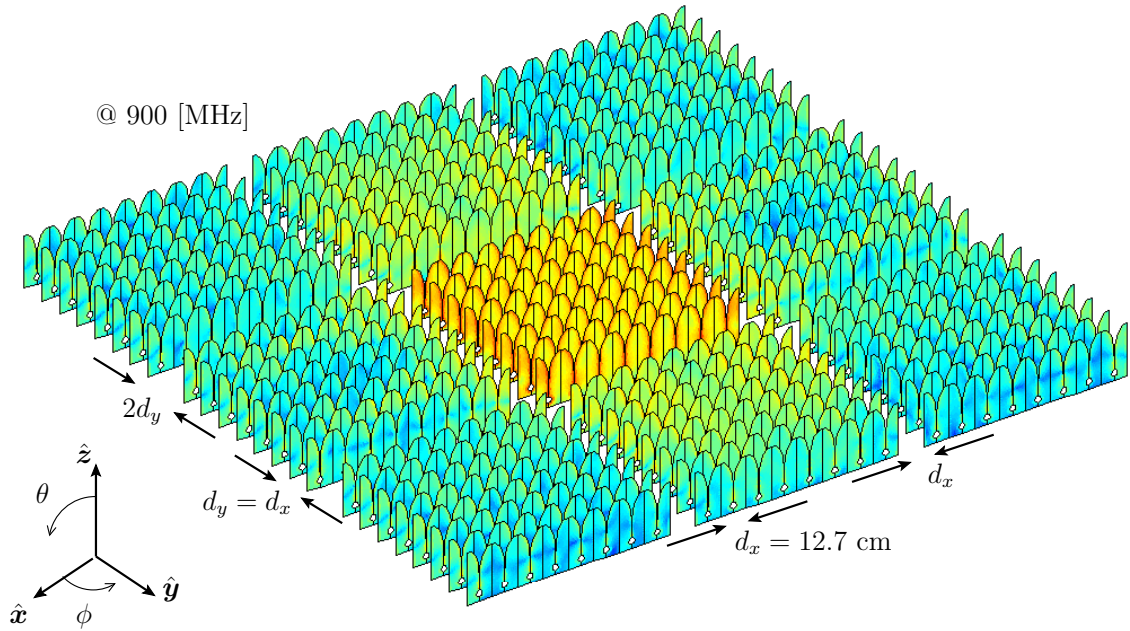
Figure 4.16: Array of 9 subarrays (3×3), each of them composed of 64 TSA elements (8×8). To illustrate coupling effects, the active antennas within the central tile are excited by a voltage-gap generator placed over the slot of each TSA element. The central tile scans to broadside (end-fire direction), whereas the TSAs of the surrounding tiles are short-circuited. The magnitude of the surface current distribution is shown (logarithmic scale) as computed by a direct CBFM approach.

coefficients can be defined as

$$\text{Rel. Error} = \frac{\sum\limits_{n=1}^{N_{\text{sub}}} |\Gamma_n^{\text{scan,ref}}(\theta_0, \phi_0) - \Gamma_n^{\text{scan,approx}}(\theta_0, \phi_0)|^2}{\sum\limits_{n=1}^{N_{\text{sub}}} |\Gamma_n^{\text{scan,ref}}(\theta_0, \phi_0)|^2} \times 100\% \qquad (4.42)$$

where θ_0 and ϕ_0 designates the scan direction. For the sake of comparison, the error in the scan reflection coefficients has been computed for a single isolated subarray, as well as for a single subarray where we account for the coupling effects with the neighboring subarrays. Fig. 4.17(a) and (c) show the scan reflection coefficient of the central element of the central subarray, obtained by using the direct CBFM (reference solution). The same figures also plot the results obtained by using both the single isolated subarray configuration and the subarray configuration with coupling. The corresponding average relative errors for the two scan directions have been plotted in Fig. 4.17(b) and (d) as a function of the frequency for the reference case; the isolated array case; and, for the approximate method as proposed

(a)

(b)

(c)

(d)
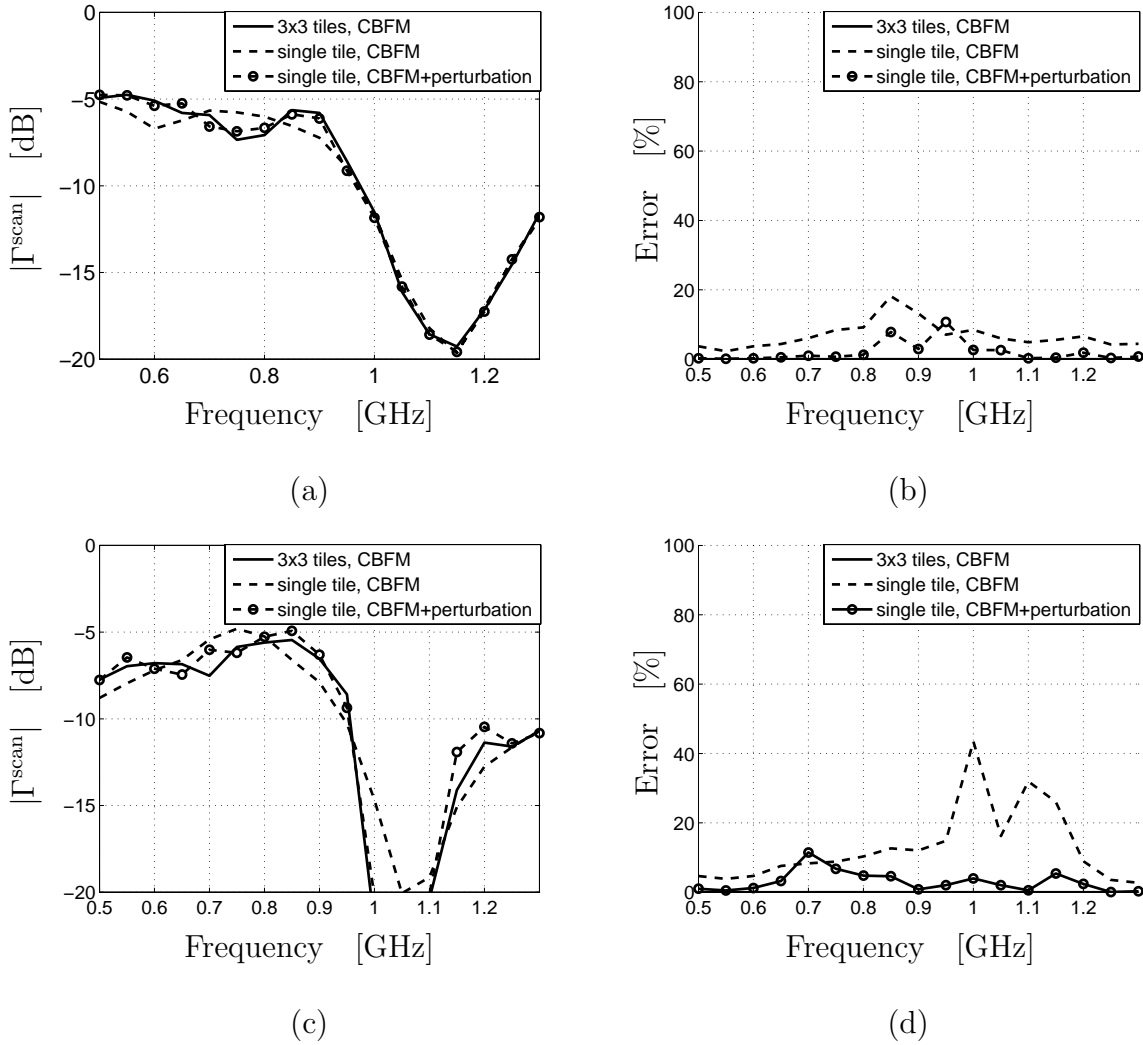
@ 900 MHz ($\theta_0 = 0$)	#RWGs	#CBFs	#MoM Blocks	#MoM Blocks (Symmetry)	Time to build MoM Blocks	Total Exec. Time
3×3 Tiles	375192	4320	331776	8394	144 min 29 s	209 min 25 s
1 Isolated Tile	41688	464	4096	294	3 min 54 s	11 min 45 s
1 Tile + Coupl.	41688	480	4096	294	8 min 42 s	16 min 48 s

Figure 4.17: (a) Scan reflection coefficient of the central element of the central subarray for broadside scan ($\theta = 0°, \phi = 0°$); (b) Average relative error of all the scan reflection coefficients of the central tile/subarray, for broadside scan; (c) Scan reflection coefficient of the central element of the central subarray for a 22.5 Deg E-plane scan ($\theta = 22.5°, \phi = 0°$); (d) Average relative error of all the scan reflection coefficients of the central tile/subarray, for a 22.5 Deg E-plane scan.

in this section.

As compared to the single isolated subarray case, the accuracy of the scan reflection co-efficients is higher for the one-tile array with coupling, particularly for off-broadside scan directions. Obviously, a relatively good accuracy can be obtained for a solve time that is comparable to the time required to solve a single isolated subarray problem (~ 17 min versus ~ 12 min). The larger solve time is due to the overhead required to construct the reduced matrix while accounting for the coupling terms with neighboring subarrays. Despite this overhead, the overall solve time is about 12 times shorter than the total time required when we use the CBFM approach.

4.6.2   The Multilevel CBFM

As demonstrated in the previous section, the mutual interaction between disjoint subarrays (tiles) of TSAs is much weaker than the self-interaction of a subarray. This property has been exploited using a perturbation approach, where the mutual coupling between a central tile and a number of surrounding phase-steered tiles has been accounted for by assuming periodicity in the currents on the various antenna tiles. This procedure is particularly attractive if one is only interested in the active scan impedances of the antenna elements within a subarray. However, alternative methods should be used if the antenna patterns and/or (passive) antenna impedance matrix of the entire array, or a subarray, have to be determined.

A suitable choice is the multilevel CBFM (ML-CBFM), which naturally extends the range of applicability of the conventional monolevel CBFM; it enables one to solve larger problems in the same amount of time and for an equal memory usage [124]. It is conjectured that the solutions for the currents on the array of M disjoint subarrays can be accurately synthesized by those found on a single isolated subarray[3]. For instance, one could apply a two-level CBFM to the array of 9 subarrays as shown in Fig. 4.16. More generally, if a single isolated subarray consists of N antenna elements, we first excite the N elements sequentially and compute the associated subarray currents using a monolevel CBFM approach (level 1). Afterwards, these so obtained/generated solutions are used as a set of primary CBFs to synthesize the current distribution on each of the M disjoint subarrays (level 2). At the

---

[3]The results have been reported in a journal paper which is currently under review.

highest level, we therefore have to solve for only $M \times N$ unknown CBF expansion coefficients (per excitation), as opposed to the $M \times K$ CBFs that would be required for a monolevel CBFM (with $K \gg N$), where K is the total number of CBFs needed to synthesize the current on a single subarray (level 1).

To generalize this concept, let a CBF $\boldsymbol{J}_q^{[i]}$ at the level i on the qth subdomain be expanded into $K_q^{[i-1]}$ CBFs at the lower level $i-1$, i.e.,

$$\boldsymbol{J}_q^{[i]} = \sum_{n=1}^{K_q^{[i-1]}} I_{n,q}^{[i-1]} \boldsymbol{J}_q^{[i-1]} \tag{4.43}$$

where $\{I_{n,q}^{[i-1]}\}$ are the $K_q^{[i-1]}$ expansion coefficients for the CBFs on the qth subdomain at the lower level $i-1$. Then, if $Z_{pq}^{[i]}$ denotes an element of the reduced moment matrix at level i for the mutual reaction between a source and observation (test) CBF on the subdomains p and q, respectively, $Z_{pq}^{[i]}$ is computed in accordance with (4.10) as

$$Z_{pq}^{[i]} = \sum_{m=1}^{K_p^{[i-1]}} \sum_{n=1}^{K_q^{[i-1]}} I_{m,p}^{[i-1]} \left[\iint_{\mathcal{S}_p} \boldsymbol{E}^s(\boldsymbol{J}_{n,q}^{[i-1]}) \cdot \boldsymbol{J}_{m,p}^{[i-1]} \, \mathrm{d}S \right] I_{n,q}^{[i-1]} = \left(\mathbf{J}_p^{[i-1]} \right)^T \mathbf{Z}_{pq}^{[i-1]} \mathbf{J}_q^{[i-1]} \tag{4.44}$$

where the vector $\mathbf{J}_q^{[i-1]} = [I_{1,q}^{[i-1]}, I_{2,q}^{[i-1]}, \dots, I_{K_q^{[i-1]},q}^{K_q^{[i-1]}}]^T$ holds the $K_q^{[i-1]}$ expansion coefficients for the CBFs on the qth subdomain at the lower level $i-1$. Similarly, the elements of $\mathbf{Z}_{pq}^{[i-1]}$ can be expressed into the CBFs at the lower level $i-2$, etc.; this presents a recursive scheme through which the reduced moment matrix at the highest level can be computed. At the lowest level, $i=0$, we do not employ CBFs but RWGs.

Likewise, an element of the voltage vector $\mathbf{V}^{[i]}$ at the ith level for the pth subdomain is computed in accordance with (4.7) as

$$V_p^{[i]} = -\sum_{m=1}^{K_p^{[i-1]}} I_{m,p}^{[i-1]} \left[\iint_{\mathcal{S}_p} \boldsymbol{E}^i \cdot \boldsymbol{J}_{m,p}^{[i-1]} \, \mathrm{d}S \right] = \left(\mathbf{J}_p^{[i-1]} \right)^T \mathbf{V}_p^{[i-1]} \tag{4.45}$$

where $\mathbf{V}_p^{[i-1]}$ is the voltage excitation vector for the CBFs on the pth subdomain at the lower level $i-1$. Yet again, at the lowest level of this recursion, $i=0$, the voltage excitation vector of the RWGs is taken.

It is to be noted that a set of CBFs need to be generated at each level, and this requires additional operations in comparison with a monolevel CBFM. In conclusion, even though

the number of unknowns may be significantly reduced, the speed advantage becomes only apparent for electrically large problems [124].

4.7   A Practical 8×7 Dual-Polarized TSA array

Tapered slot antennas are traditionally etched on high-performance dielectrics, particularly because dielectrically loaded TSA arrays demonstrate an increased operational impedance bandwidth [125], and offer a direct means to feed the antenna elements as well. However, the dielectric-free TSA arrays are low loss and may represent a more cost-effective technology to manufacture large phased-array antennas, which is of great interest to the development of the next generation radio telescope: the Square Kilometer Array (SKA) [11, 126].

Figure 4.18: Dual-polarized array of aluminum TSA elements (*cf.* ref. [23]), which is subjected to a reduced-order modeling approach.

In [23], the design of a dual-polarized TSA array has been described where a dielectric substrate is employed, but only locally, and solely for the purpose of feeding each TSA element (see also Fig. 4.18). The radiating tapered slots are composed of relatively thick aluminum fins in order to realize a slotline capacitance which closely resembles the capacitance of an equivalent slotline sheet that is printed on a dielectric substrate. Furthermore, the relatively thick metals improve the self-supportiveness of the structure. In the present section we aim to develop a reduced-order model for these types of microstrip-fed TSA

arrays.

Because the strongly coupled wideband antenna elements are composed of both dielectrics and metals, an accurate full-wave analysis of such TSA arrays represents an even larger challenge [24, 127–129]. The computational burden of the entire problem can often be relaxed by decomposing it into smaller subproblems that each can be solved relatively easily, and can afterwards be combined into a single aggregated model to obtain its full solution. By decomposing the problem into subproblems, not only the elementary physics of the problem gets revealed, but also the opportunity is offered to perform global optimizations in a time-efficient manner, namely, by first solving for a local subproblem and then accounting for the interactions with its environment, rather than recomputing the entire problem in full detail during each optimization cycle.

In [130], a decomposition technique has been proposed to model the scan impedance of an infinite array of stripline-fed TSAs. To model these bilateral structures, a moment-method formulation was proposed based upon the periodic Green's function for currents located inside and on a protruding dielectric slab. The scan impedance was calculated on the stripline feed crossing the slotline section, and therefore included both the reactance of the radial stripline stub, and the stripline-to-slotline transition. The reactance of the stub was independently modeled between two infinite ground planes using the same full-wave formulation. Afterwards, the stub reactance was de-embedded to retain a scan impedance representing only the antenna element and stripline-to-slotline transition. It was concluded that the radial stub can be optimized independently, and be seen as an individual reactance in series with the de-embedded scan impedance representing only the antenna and stripline-to-slotline transition.

A further decomposition into microwave circuit models has been proposed in [131]. Therein, the microstrip-to-slotline transition is modeled by Knorr's equivalent circuit [132] (an ideal transformer), whereas the microstrip stub and feed lines, and even the slotline cavity of the antenna, have all been modeled by ideal transmission lines. Following this, it has been demonstrated in [133] that both the microstrip feed and antenna slot cavity of a single bunny-ear antenna can then be optimized to realize a desired impedance bandwidth. However, in [130], it has been stated that, for arrays of TSAs, both the tapered slot and the slotline cavity exhibit a significant interaction with the neighboring elements. As a result, a quantitative analysis of wideband phased arrays was not found to work for such a detailed antenna-feed decomposition.

In the following sections, it is explained how the feed model can be modified in order to analyze (large) arrays of TSAs in a quantitative manner. The distinction with other papers is that both the strongly coupled tapered slots and the slotline cavities are now represented by electrodynamic field models, whereas the microstrip lines and stubs, including their microstrip-to-slotline transitions, are represented by quasi-static field models. The antenna array can be analyzed as a dielectric-free structure if the effect of the dielectric substrate on its radiation characteristics is negligible, which is particularly true if the dielectric: (i) is employed only locally; (ii) is effectively thin compared to the TSA fins, and; (iii) has a low relative dielectric permittivity. We will consider only one specific realization for which mainly the first two requirements are satisfied.

The dielectric-free antenna array is analyzed with the aid of the moment method in which we employ an adequate number of numerically generated entire-domain basis functions on each of the metallic TSA elements and then account for the mutual reaction between them through the CBFM. The direct interaction between antenna feed boards is neglected as the coupling is assumed to occur only via antenna elements.

Validation of the impedance characteristics of the combined quasi-static and electrodynamic field models has been carried out via measurements for several practically realized TSA arrays. The results demonstrate a very good agreement over a large scan range, as well as over a wide frequency band.

4.7.1 Geometrical Dimensions of the Reference TSA

Fig. 4.19(a) illustrates the geometrical dimensions of the reference TSA element that has been examined. The element geometry has been adopted from [23], where the design of an infinite dual-polarized phased array of such elements has been described and analyzed with the aid of periodic boundary conditions.

The magnitude and phase of S_{11}^{ant} of a single array element, both measured and simulated, are shown in Figs. 4.19(b) and 4.19(c), respectively. The agreement between the measured and simulated (HFSS) impedance characteristics of a single TSA element (mounted on an infinitely large PEC ground plane) is sufficiently good and will, henceforth, be used in the development and validation of the combined model for both the microstrip feed and the antenna structure.
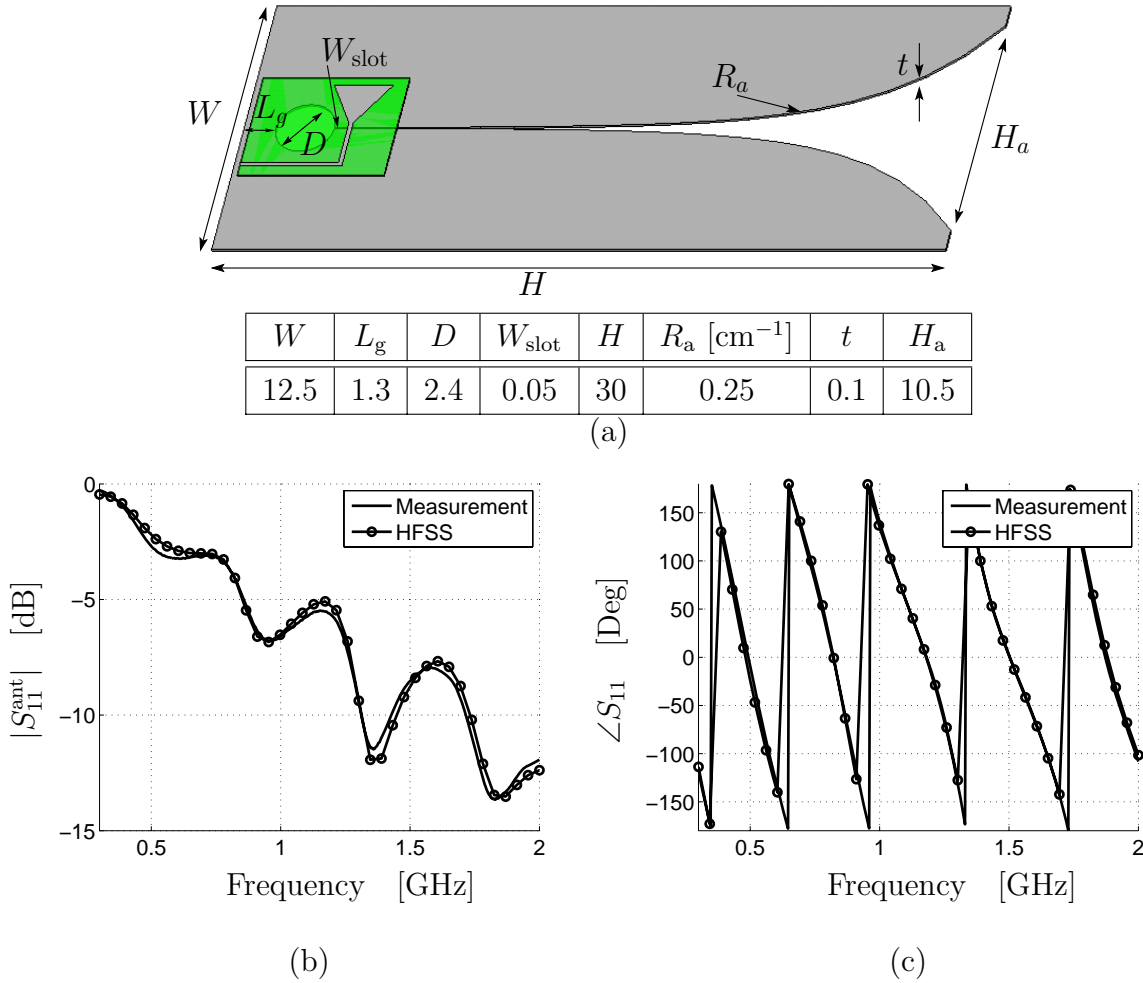
Figure 4.19: (a) Geometrical dimensions of the reference TSA element in cm. The magnitude and phase of S_{11}^{ant}, both measured and simulated, are shown in figures (b) and (c), respectively.

4.7.2   Reduced Order Model of a Single Microstrip-fed TSA

We will utilize the measurements or simulations of a single TSA element to extract the model parameters of the microstrip feed. First, the TSA element is excited by a voltage-gap generator across the slotline section in the absence of the microstrip feed. The currents inside the actual antenna conductor of finite thickness are effectively represented by average surface currents supported by infinitely thin metallic sheets. It is crucial that the actual thickness of the conductors is modeled accurately in order to obtain the correct fields inside the slot region, and thereby the correct gap impedance. Therefore; the edges of the current

sheets have been right-angled folded as illustrated in Fig. 4.20.
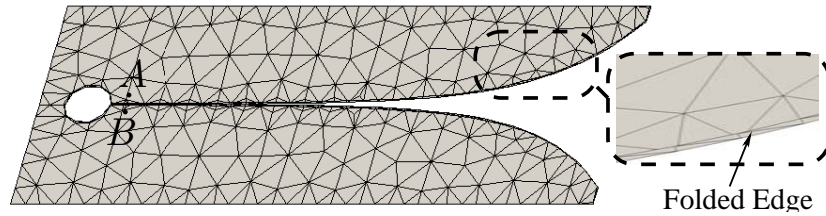
Figure 4.20: Triangular meshed TSA element with folded edges to simulate a finite thickness of the metal, and delta-gap excitation between A and B.

Following Chapter 3, the current sheets are supplied with a triangular mesh (see Fig. 4.20) and an adequate number of subsectional Rao-Wilton-Glisson (RWG, [26]) basis/testing functions is employed. The surface current is subsequently synthesized by discretizing an Electric Field Integral Equation (EFIE) with the aid of the moment method (Galerkin's testing scheme), after which the resulting system of linear equations is solved for the unknown RWG expansion coefficients.

After computing the antenna impedance between terminals A–B (see Fig. 4.20), the microstrip feed is modeled as schematically shown in Fig. 4.21.
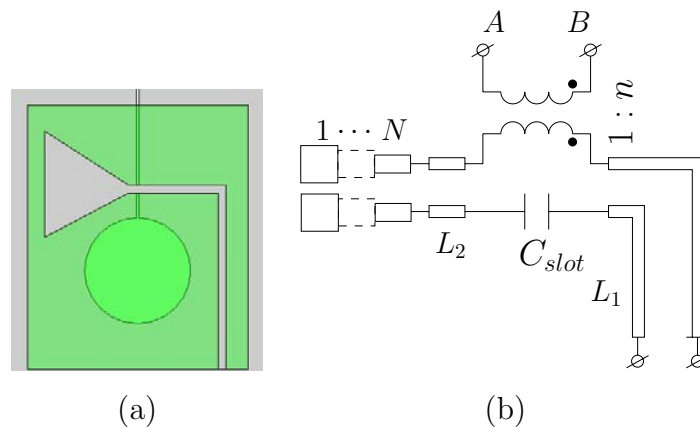
Figure 4.21: (a) A microstrip feed on a localized substrate carrier, and; (b) an equivalent circuit representation of this feed. Preliminary results have been reported for a 3×1 TSA array in [134].

Fig. 4.21(b) illustrates a modified representation of Knorr's equivalent circuit [132] in which

the microstrip-to-slotline transition is modeled as an ideal transformer with a (non-integer) turns ratio $n = V_{\text{sec}}/V_{\text{prim}}$, where V_{prim} and V_{sec} are the microstrip and slotline voltages across the primary and secondary windings, respectively. A capacitor has been added in series with the microstrip line because the ground conductor of the microstrip line is interrupted by the slotline. We therefore have placed this capacitor in the ground conductor of the transformer [*cf.* the actual situation in Fig. 4.21(a)]. This capacitor becomes a required element when wide slots and low-permittivity substrates are considered. However, in the present case the slot is relatively narrow and composed of two relatively thick metals, so that the capacitor becomes virtually short-circuited and therefore a non-required circuit element.

As described in [135], the impedance of wide-band circular stubs can be accurately modeled by a cascaded series of transmission lines with varying strip widths, although this method neglects the stub radiation, parasitic effects at junctions, and the fringing field effect at the stub end. Because the latter effects are small, also the impedance of the triangular stub of Fig. 4.21(a) could be accurately modeled with this technique. For this purpose, the design equations of [136, pp. 87–92] for each of the microstrip sections were used, and the stub impedance was evaluated for a series of cascaded sections with the help of the CAESAR circuit simulation software (see Chapter 5 and Appendix F).

The impedance of the triangular stub has also been computed with the aid of a full-wave method (HFSS) and subsequently compared to the presently modeled stub impedance; the results are shown in Fig. 4.22. The phase accuracy of the reflection coefficient is even reasonable for a single microstrip section, but readily improves by adding a few more sections. The magnitude of the reflection coefficient of the stub only is not shown since $|S_{11}| > -0.05$ dB for both models over the entire frequency band. The reflection coefficient of the entire microstrip feed section, when placed above a PEC ground plane (transformer short circuited), has both been measured and simulated. The agreement for the magnitude in Fig. 4.22(c), and phase in Fig. 4.22(d) is very good, even outside the operational frequency range from 0.5–1.5 GHz. Because the microwave network is non-radiative, the dissipation losses are only due to the ohmic losses in the conductor and the dielectric material. For the computations, we have used that $\tan(\delta) = 0.0027$ and $\sigma_{\text{cond}} = 5.8 \times 10^7 \ \Omega^{-1}\text{m}^{-1}$. The corresponding frequency-dependent attenuation coefficients α_{diel} and α_{cond}, for a passively matched terminated microstrip line, range from $0.01 - 0.1$ Np/m and $0.03 - 0.1$ Np/m, respectively. As a result, it is observed in Fig. 5(c) that $|S_{11}| > -0.2$ dB for a standing-wave current along the microstrip feed.

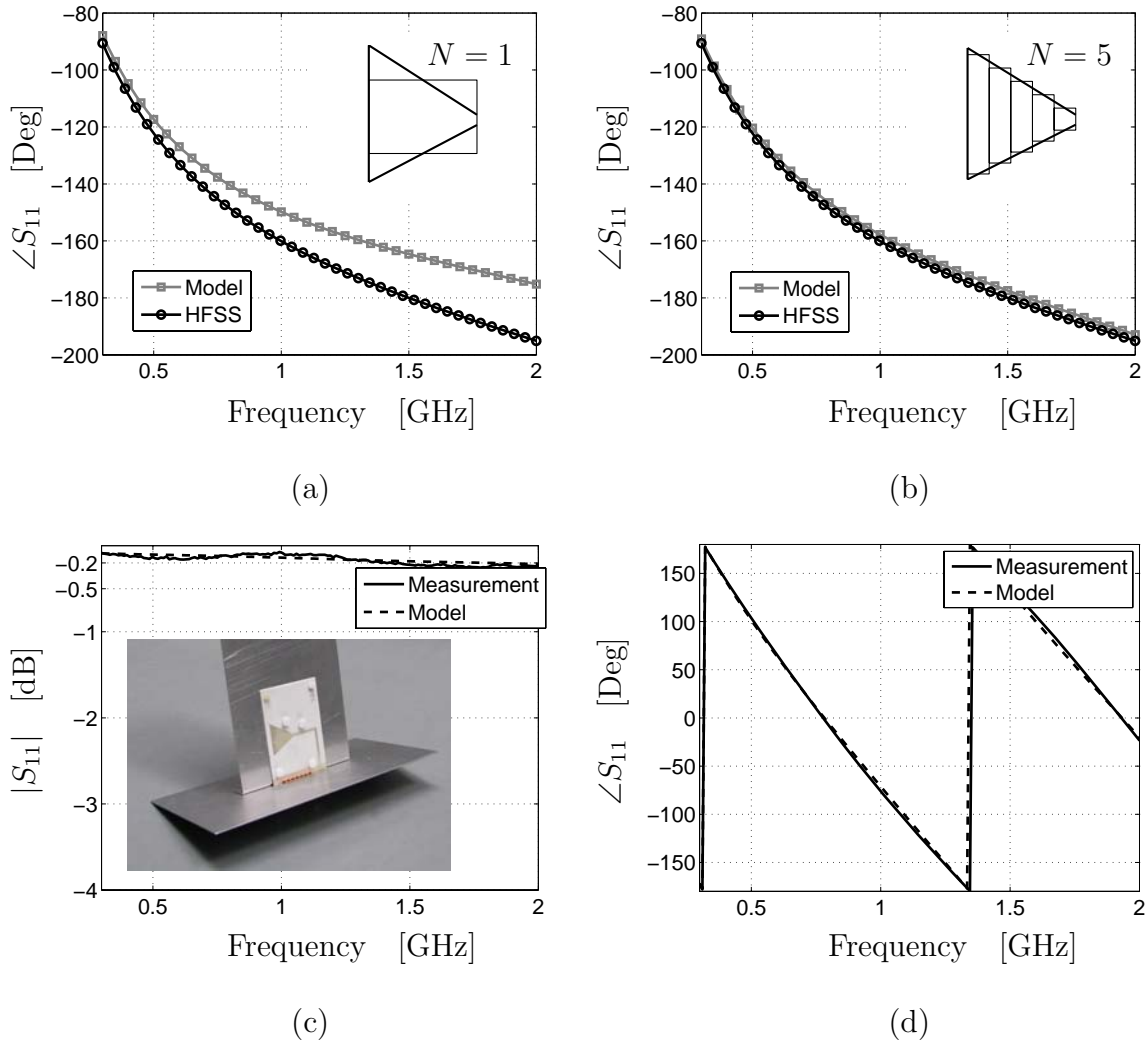Figure 4.22: The modeled and simulated (HFSS) phase of S_{11} of the (a) triangular stub ($Z_0^{\text{ref}} = 50\Omega$) using (a) $N = 1$ section; (b) $N = 5$ sections. (c), (d) The measured magnitude and phase of the reflection coefficient of the microstrip-feed section (transformer short circuited).

Since the physical dimensions of the microstrip feed as well as the electrical properties of the substrate carrier are known ($\varepsilon_r = 3.38$, $d_{\text{sub}} = 0.8$ mm, $w_{\text{strip}} = 1.8$ mm), most of the model parameters of the equivalent circuit [Fig. 4.21(b)] can readily be determined, and are listed in Table 4.3.

The length L_1 of the transmission line includes the equivalent connector length. The parameter n has been determined by a least-squares fit of the port impedance of the cascaded

Table 4.3: Model parameters of the circuit shown in Fig. 4.21

N	L_1	L_2	Z_0^{ref}	n	C_{slot}
5	67.8 mm	2.2 mm	50 Ω	0.95	–

model (antenna+feed) onto the reference impedance shown in Figs. 4.19(b) and 4.19(c). Although n is generally a complex-valued quantity, it is herein taken real-valued since the capacitor accounts for a possible reactive part. Moreover, the conservation of power between the primary and secondary windings is then automatically satisfied. We remark that n and C_{slot} need to be determined only once because they solely depend upon the geometry of the microstrip-to-slotline transition, which is often not altered during a design optimization, as opposed to the geometry of the triangular stub, circular cavity, exponential taper, width and height of the TSA element.

Figs. 4.23(a) and 4.23(b) illustrate that the overall return loss of the cascaded antenna in combination with the feed circuit is in good agreement with the reference full-wave solution (HFSS). Figs. 4.23(c) and 4.23(d) depict the magnitude of S_{11}^{ant} when the circular cavity size D and the height H of the TSA element are varied. As expected, the accuracy remains satisfactory (i.e. $\leq 20\%$ error) when the TSA element geometry is altered, while the feed geometry and its model parameters are kept fixed. This confirms that n is almost invariant to these geometrical changes. The S_{11}^{ant} of the antenna element in the absence of the feed circuit is also shown for these cases, and illustrates that the effect of the feed circuit on the return loss is rather significant.

4.7.3 Analysis of Large TSA Arrays

It is important to demonstrate that the non-radiative feed model, which has been developed for a single TSA element, can directly be applied to analyze the impedance characteristics of large arrays of mutually coupled TSAs. In the following subsections, we present some specific results of the CBFM for a 4×4 singly-polarized and an 8×7 doubly-polarized TSA array.

For antenna problems, it is customary to generate and employ primary and secondary CBFs [87]. However, we will illustrate that, from an accuracy point of view, one can
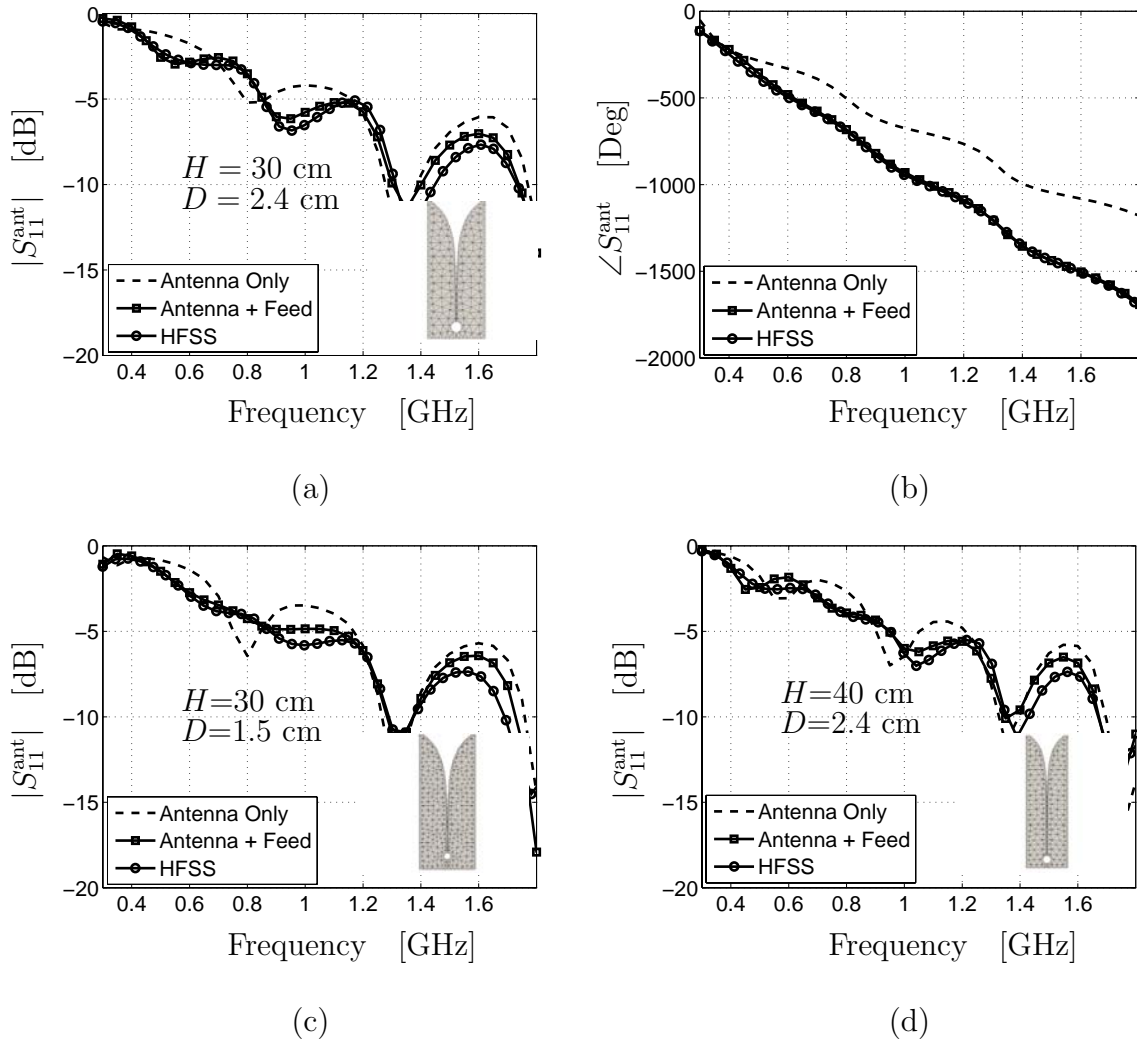
(a)

(b)

(c)

(d)

Figure 4.23: Modeled and full-wave simulation results (HFSS) of S_{11}^{ant} of a single TSA element ($Z_0^{\text{ref}} = 50\Omega$). The magnitude (a) and phase (b) of S_{11}^{ant} for the reference geometry. (c); (d) The magnitude $|S_{11}^{\text{ant}}|$ for two different element geometries but for identical feed models.

obviate the generation of secondary CBFs and, equally well, let a spectrum of incident plane waves (PWS) be incident on a smaller subarray. These additional CBFs are needed to accurately synthesize the coupling effects, and are appended to the already existing set of primary CBFs (after applying a trapezoidal post-windowing procedure, see Section 4.4 and [100]). For this purpose, a PWS is used for the two orthogonal θ and ϕ polarizations with an angular step size of 20° (typical value) in both the θ and ϕ directions, where the θ range is limited to the upper hemisphere in case an infinite ground plane is present.

To achieve high solution accuracy for the complicated problem of a dual-polarized array of interconnected TSAs (which basically form tapered waveguides), the threshold of the singular value decomposition (SVD), which is used to orthonormalize and to truncate the number of numerically generated CBFs, has been set to 10^{-4}. The threshold of the Adaptive Cross Approximation (ACA) algorithm, which is used for the fast construction of off-diagonal (reduced) moment matrix blocks, has been set to 10^{-3} [87]. These threshold values have been determined empirically and yield a relative difference between the measured and simulated antenna impedance matrix elements of about 20%.

The HFSS v10 computations have been performed on a slightly more powerful Linux desktop PC which has 8 GB of RAM and 2 dual core AMD processors.

Results for a 4×4 Singly-Polarized TSA Array

To be able to validate the measured antenna impedances by commercial solvers, a relatively small 4×4 singly-polarized TSA array has been fabricated as shown in Fig. 4.24(a).

Although the problem requires only 9848 RWG basis functions, it cannot be handled by a plain MoM solver because of memory overflow errors above ~ 7000 RWGs. When CBFM is used instead, it is worth realizing that the computational overhead of CBFM is relatively large for small arrays, since the total execution time (for this case ~ 1 hour per frequency point) is governed by the time to generate CBFs and to construct a reduced matrix. The details on CBFM will therefore only be discussed for the larger 8×7 dual-polarized TSA array for which it outperforms any direct moment method solver, hypothetically.

From the measured antenna S-parameters, we have computed the active scan reflection coefficient Γ_{act}^n for the nth antenna element as

$$\Gamma_{\text{act}}^n = \frac{1}{a_n} \sum_{m=1}^{N} S_{nm}^{\text{ant}} a_m \tag{4.46}$$

where a_p for $p \in \{m, n\}$ is the complex valued transmission line mode amplitude of the excitation wave incident on the pth antenna port with $p \in \{1, 2, \ldots, N\}$.

Figs. 4.24(b)–(d) depict the active scan reflection coefficients of one of the four center elements for different phased-array excitation schemes. A good agreement is observed
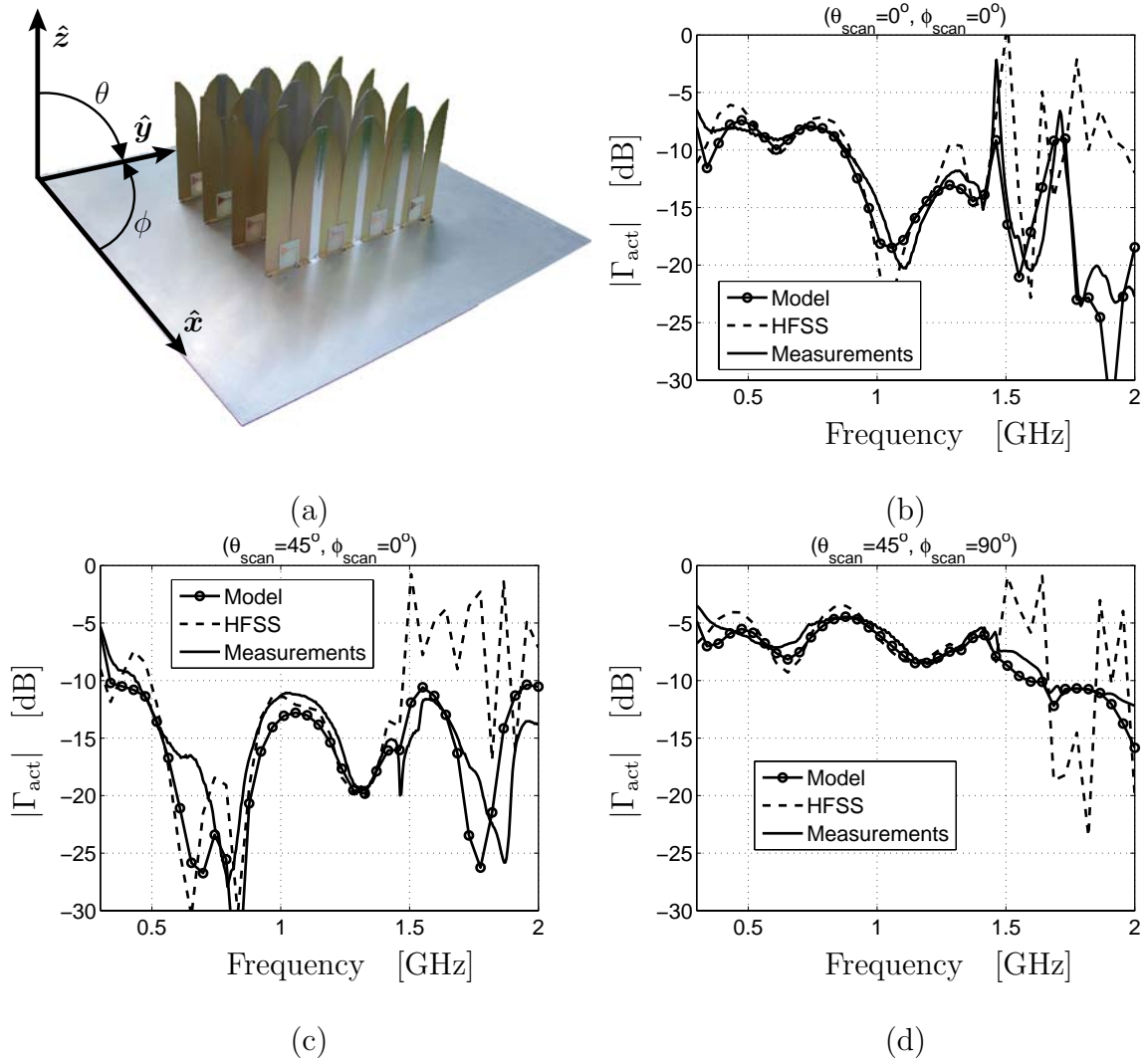
(a)

(b)

(c)

(d)

Figure 4.24: (a) A 4×4 singly-polarized microstrip-fed TSA array mounted on a finite ground plane. The magnitude of the measured, simulated (HFSS), and modeled active scan reflection coefficients are shown for: (b) $\theta = 0°$, $\phi = 0°$; (c) $\theta = 45°$, $\phi = 0°$ (H-plane scan), and; (d) $\theta = 45°$, $\phi = 90°$ (E-plane scan).

between the measured and modeled magnitudes of the active reflection coefficients for various scan angles and as a function of frequency. The results that have been computed by the finite-element solver HFSS are also in good agreement, i.e., up to ~ 1.5 GHz. The high-frequency results ($\gtrsim 1.5$ GHz) have been computed with reduced accuracy because of memory constraints. More specifically, to assure that the size of the radiation box is $\lambda_0/4$ away from element edges at 0.5 GHz, the solution frequency for convergence (used

for adaptive mesh refinement in HFSS) had to be set to 1.0 GHz (the center frequency). Finally, it is worth mentioning that the onset of grating lobes above 1.2 GHz occurs in conjunction with high-Q impedance resonances which are difficult to predict accurately with limited computational resources.

Results for an 8×7 Doubly Polarized TSA Array

The impedance matrix of the 112-port TSA array of Fig. 4.18 has been evaluated with the above proposed model and compared to measurements. The problem requires 79450 RWG basis functions, which is a number of unknowns that would significantly increase whenever the dielectric microstrip feed becomes part of the EM model, and such a problem is beyond the reach of (most) commercial solvers.

The first step in solving this problem is to construct the entire array mesh. We mesh only two base elements (a co- and cross-polarized antenna element) and the bottom edge of each base element is connected along the diagonal of a square ground plane. Note that, when such a base element is replicated at the various element positions throughout the lattice, a finite dual-polarized array is formed over a finite ground plane.

After the construction of the entire array mesh, a minimum number of unique supports[4] is identified throughout the array lattice each of which holds a distinct set of CBFs. Any other support function (associated to an array element), inherits one of these unique sets of CBFs through translation. In the end, all the array elements support a set of (mutually overlapping) CBFs. The total number of identifiable unique sets of CBFs depends on the regularity of the meshed antenna array geometry and is independent of the array size [88]. For the present problem we generate 18 sets of CBFs by extracting 18 subarrays from the fully meshed array. That is, for each polarization, we extract 4 corner element, 4 edge elements, and an inner element along with their direct electrically interconnected adjacent elements. Next, currents are induced on these 18 subarrays by exciting each of the array elements sequentially as well as by applying a PWS, after which the supports of these currents are reduced to the size of a single element plus a minor extension [100]. The 18 sets of CBFs generated in this manner are subsequently mapped onto the array mesh through translation. Finally, each of the 112 antenna elements supports a set of

---

[4]In the present overlapping domain-decomposition technique, a CBF support is comprised of the mesh of one antenna element including a minor extension over the electrically interconnected adjacent elements.

CBFs which partially overlaps with the CBFs supported on the electrically interconnected adjacent elements, and this preserves the continuity of the current in the final solution. By using a 20 degrees angular step size of the PWS, and a SVD threshold of 10^{-4}, about 31 CBFs are generated for each of the 112 antenna elements (@ 1.0 GHz).

The above meshing strategy has been detailed in [88] and allows for a fast construction of the (reduced) moment matrix since we can exploit the block-Toeplitz symmetry of this matrix. This is possible since a large degree of translation symmetry exists between group pairs of RWGs (or CBFs) throughout the array lattice. Because of this symmetry, only 5166 unique moment matrix blocks out of the $112 \times 112 = 12544$ need to be constructed to compute the reaction integrals between CBFs (reciprocity not exploited).

The reduced matrix equation is solved through Gaussian elimination for 112 excitation vectors (112 element excitations). The total execution time, which also includes the meshing and post-processing time of the currents, impedances, far-field patterns, and the solve time of the microwave network, is shown in Table 4.4. The magnitude of the measured

Table 4.4: Total execution time (@ 1.0 GHz, for 79450 RWGs).

CBF generation for 18 distinct supports in the array	1 h 51 min
Construction of the reduced matrix equation	0 h 50 min
Computation of CBF far-field patterns	0 h 45 min
Total number of CBFs	3506
Solve time reduced matrix equation (3506×3506)	36 sec
Total execution time	3 h 36 min

and simulated active scan reflection coefficient Γ_{act} for a center element as a function of frequency is shown in Figs. 4.25(a)–(c). For completeness, the HFSS results for a periodic unit-cell analysis of an infinite-by-infinite TSA array have been overlayed with the finite-array results. Even though the array size is only $5\lambda_0 \times 5\lambda_0$ at 1.5 GHz, the active impedance characteristics are comparable for a broadside scan down to 0.8 GHz. Deviations are mainly caused by edge-truncation effects, which increase at low frequencies and large scan angles. Three scan angles have been considered: broadside scan ($\theta = 0^o, \phi = 0^o$), a 45 degree E-plane scan ($\theta = 45^o, \phi = 180^o$), and a 45 degree H-plane scan ($\theta = 45^o, \phi = 90^o$). Only the x-oriented TSAs are excited, while the cross-polarized elements are passively terminated by 50 Ohm loads at the microstrip feed ends. Even though the proposed antenna-feed decomposition approach is rather crude, the agreement between measurements and simulations
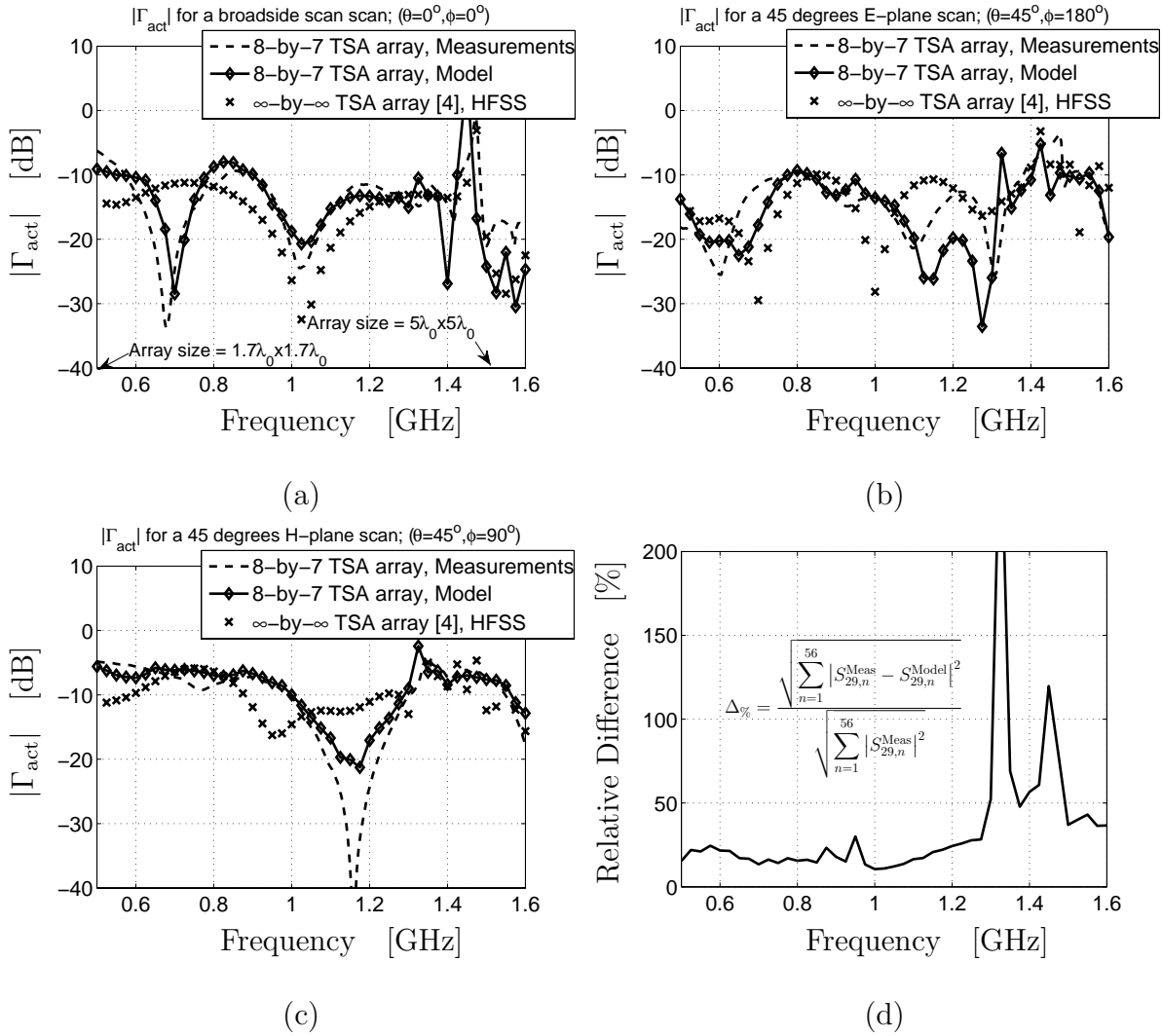
(a)

(b)

(c)

(d)

Figure 4.25: (a)–(c) Magnitude of the measured and simulated active scan reflection coefficient Γ_{act} as a function of frequency and for various scan directions. The HFFS results are for an $\infty \times \infty$ TSA array [23]. (d) The relative difference of the measured and simulated coupling between the center element and all other equally polarized elements as a function of frequency.

is found to be remarkably good. In fact, up to the first resonance frequency, at around 1.45 GHz (broadside scan), the relative difference between the measured and modeled mutual coupling coefficients between the center element (#29) and all other equally polarized elements, is about 20%. This result has been plotted in Fig. 4.25(d). The resonance seems well-predicted in Fig. 4.25(a); however, it is obvious that the relative difference as defined in Fig. 4.25(d) can become large (> 100%) due to a minor frequency shift.
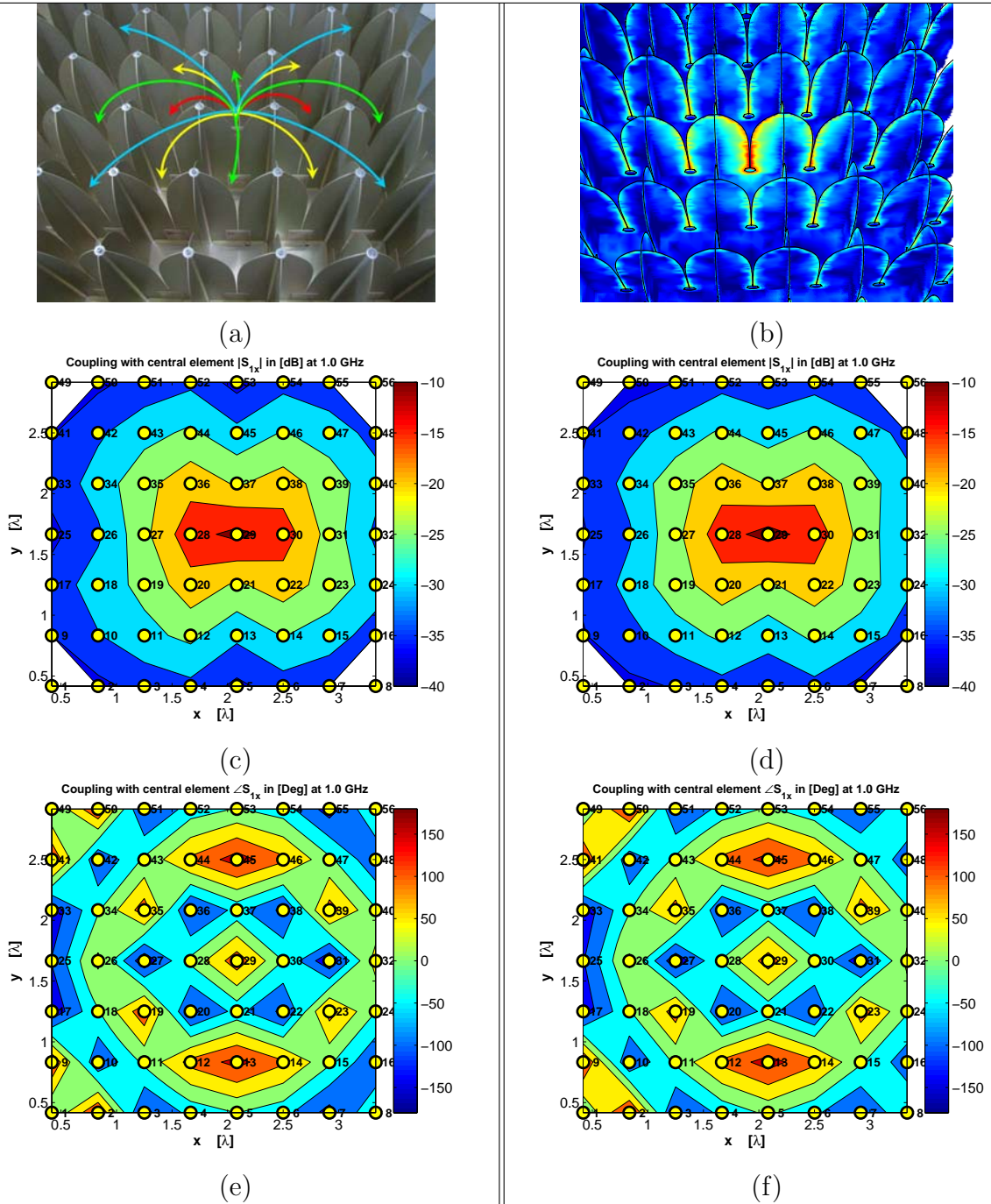
Measured Mutual Coupling | Modeled Mutual Coupling

(a)

(b)

(c)

(d)

(e)

(f)

Figure 4.26: Results for the measured and simulated mutual couplings $S_{29,x}^{\mathrm{ant}}$ for $x = 1, \ldots, 56$, between the central element $x = 29$ and all other equally polarized elements, for 1.0 GHz. (a) Top view of the array. (b) Magnitude of the current when element 29 is excited (logarithmic scale, 60 dB dynamic range). (c) The measured $|S_{29,x}^{\mathrm{ant}}|$ in [dB]. (d) The simulated $|S_{29,x}^{\mathrm{ant}}|$ in [dB]. (e) The measured $\angle S_{29,x}^{\mathrm{ant}}$ in [Deg] (f) The simulated $\angle S_{29,x}^{\mathrm{ant}}$ in [Deg].

Fig. 4.26 visualizes the measured and simulated magnitudes and phases of the coupling coefficients between the center element (#29) and all other equally polarized elements (@ 1.0 GHz). It is observed from the contour plots in Fig. 4.26(c) and (d) that the E-plane coupling is stronger than the H-plane coupling, but this depends on the frequency and the reference impedance (element termination). The latter conclusion can also be drawn from the magnitude of the current distribution shown in Fig. 4.26(b). Both the magnitude and phase distributions are well predicted, that is, the relative difference according to Fig. 4.25(d) is $\sim 10\%$ @ 1.0 GHz. A similar agreement is obtained at other frequencies, except near or above 1.3 GHz, where element impedances are disrupted by resonant array effects which are difficult to predict accurately (the $\lambda_0/2$ element separation distance is at 1.2 GHz). In this respect, it is also worth mentioning that the microstrip feed boards have
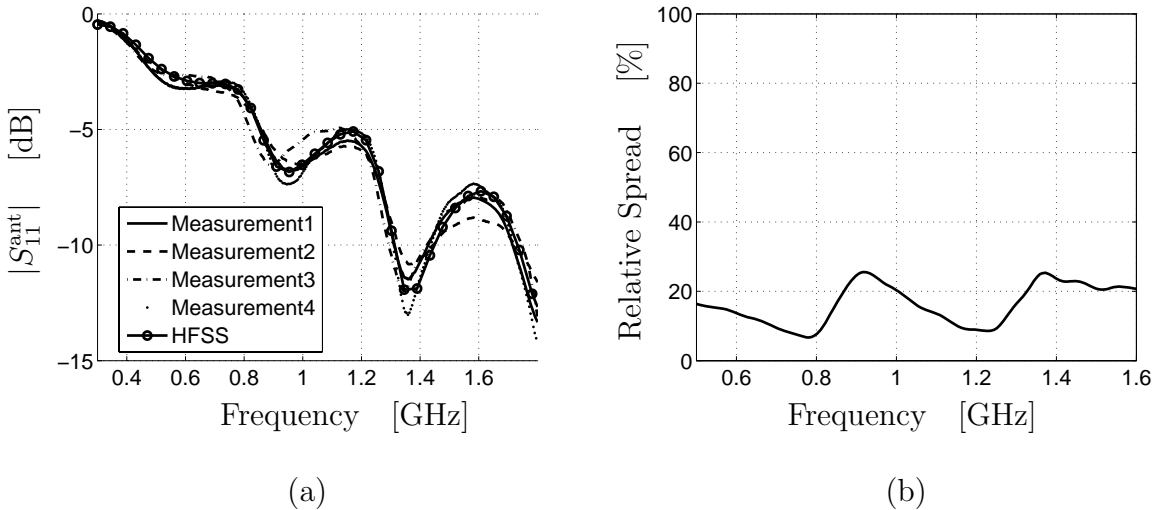

Figure 4.27: (a) Measured S_{11}^{ant} values of four isolated TSA elements. (b) Relative spread in measured S_{11}^{ant} values.

been glued on the elements by hand, and that, due to this, the relative spread (standard deviation of S_{11}^{ant} divided by its mean value) in measured impedances between four isolated elements can be as large as 25% in the frequency band of operation [*cf.* Fig. 4.27(a)]. This variation is partly caused by a misalignment of the feed, and/or a small air gap between the microstrip feed board and the aluminum antenna. Measurements with a Time Domain Reflectometer revealed that, for each [μm] air gap, the characteristic impedance of the microstrip line increases by 72 mΩ. The maximum in relative spread in Fig. 4.27(b) occurs at 900 MHz, and this is also observed in Fig. 4.25(d). It is likely that an increase in the relative difference between the modeled and simulated coupling coefficients in Fig. 4.25(d)

is partly due fabrication tolerances. Mechanically more robust solutions to firmly clamp the feed are currently being examined [137].

Even though element #29 is not an exact center element, one expects symmetry in the computed coupling coefficients along the y-direction. The coupling coefficients are derived from the moment matrix solution, but from the reaction concept and reciprocity theorem, we know that symmetry is preserved in the moment matrix whenever Galerkin's method is combined with a symmetric product for testing the integral equation. However, in our implementation, the moment matrix is only symmetric up to a limited number of computed digits because the source and test integrals are evaluated using unequal quadrature rules. The degree of asymmetry depends on the mutual orientation between pairs of RWGs and the order of the Gaussian quadrature rule that is employed to compute their reaction integrals (i.e. the moment matrix entries). If desired, the degree of symmetry can be improved by choosing equal quadrature rules or by increasing their orders at the cost of a reduced matrix-fill time. Reciprocity can be exploited beyond a certain point and would save approximately a factor of two in total fill time.

4.7.4 Simulated Far-Field Patterns and Orthogonality of a Co- and Cross-Polarized Array Beam

The computed embedded-element patterns are illustrated in Fig. 4.28. These are the patterns that arise if one element is excited while the other elements are passively-matched terminated using 50 Ohm loads at the microstrip feed ends. Not surprisingly, the far-field
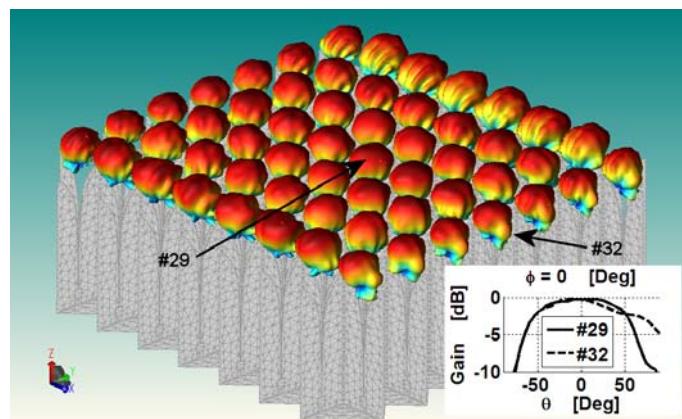

Figure 4.28: Embedded-element power-patterns at 1.0 GHz (linear scale).

patterns of the edge and corner elements exhibit many ripples and, although not shown, were found to be frequency-dependent as well. Furthermore, as a result of the coupling effects, it can be observed that the power patterns of the center elements are "smoother" and more symmetrical than the patterns of the boundary elements.

In radio astronomy, it is of primary importance to recover the intensity and/or polarization information of the incident electromagnetic field. The Stokes parameters $\{I, Q, U, V\}$ are commonly used to define the polarization state of a partially polarized field. In a fixed $\{\hat{\boldsymbol{x}}, \hat{\boldsymbol{y}}\}$ basis, the Stokes parameters are defined as [3, p. 4-8]

$$I = |E_x^{\text{inc}}|^2 + |E_y^{\text{inc}}|^2 \qquad\qquad Q = |E_x^{\text{inc}}|^2 - |E_y^{\text{inc}}|^2 \qquad (4.47)$$

$$U = 2\Re\{E_x^{\text{inc}}(E_y^{\text{inc}})^*\} \qquad\qquad V = 2\Im\{E_x^{\text{inc}}(E_y^{\text{inc}})^*\}. \qquad (4.48)$$

To measure these Stokes parameters, we can let the 112 TSA element array operate in phased-array mode and separately combine the output signals of the x- and y-oriented elements into a co- and cross-polarized beam, respectively. Even though the pertaining array elements are geometrically orthogonal to each other, it is essential that also the realized co- and cross-polarized beams are sufficiently orthogonal over a large scan volume and frequency band in order to effectively recover the Stokes parameters of the incident field [138].

Let the vectors

$$\boldsymbol{e}^{\text{co}}(\theta_0, \phi_0) = e_\theta^{\text{co}}\hat{\boldsymbol{\theta}} + e_\phi^{\text{co}}\hat{\boldsymbol{\phi}} \qquad (4.49\text{a})$$

$$\boldsymbol{e}^{\text{cross}}(\theta_0, \phi_0) = e_\theta^{\text{cross}}\hat{\boldsymbol{\theta}} + e_\phi^{\text{cross}}\hat{\boldsymbol{\phi}} \qquad (4.49\text{b})$$

denote the complex-valued electric far-field vectors of the co- and cross-polarized beam patterns in the direction (θ_0, ϕ_0) of the source. These vectors are normalized such that $V_x = \boldsymbol{e}^{\text{co}} \cdot \boldsymbol{E}^i$ and $V_y = \boldsymbol{e}^{\text{cross}} \cdot \boldsymbol{E}^i$ are the received output voltages corresponding to the x- and y-oriented elements, respectively. Clearly, the set $\{\boldsymbol{e}^{\text{co}}, \boldsymbol{e}^{\text{cross}}\}$ forms a basis along which the incident field $\boldsymbol{E}^i$ is decomposed. The beam orthogonality in the (θ_0, ϕ_0) direction is conveniently measured through the normalized cross-correlation term

$$\rho_{\text{cor}} = \frac{\langle \boldsymbol{e}^{\text{co}}, \boldsymbol{e}^{\text{cross}} \rangle}{\sqrt{\langle \boldsymbol{e}^{\text{co}}, \boldsymbol{e}^{\text{co}} \rangle \langle \boldsymbol{e}^{\text{cross}}, \boldsymbol{e}^{\text{cross}} \rangle}} \qquad (4.50)$$

where $\langle \boldsymbol{a}, \boldsymbol{b} \rangle = \boldsymbol{a}^* \cdot \boldsymbol{b} = \boldsymbol{a}^H \boldsymbol{b}$ represents the Hermitian inner product. We point out that, if $\rho_{\text{cor}}(\theta_0, \phi_0) = 0$, the beams are orthogonal in the (θ_0, ϕ_0) direction and the Stokes parameters can, potentially, be measured with high precision, provided that a possible

rotation of this orthogonal basis with respect to a given reference frame (usually of the source) is known and can be corrected for in the post-processing of the data (calibration). On the contrary, if $|\rho_{\mathrm{cor}}(\theta_0, \phi_0)| \approx 1$, the Stokes parameters are recovered with low precision. One could orthonormalize this basis by adapting the beamformer weights, but this is likely to result in a loss of sensitivity as well.

The beam orthogonality $10 \log(|\rho_{\mathrm{cor}}|)$ of the 112 TSA element array has been analyzed over a large scan volume (@ 1.0 GHz). The results are shown in Fig. 4.29. As expected, the
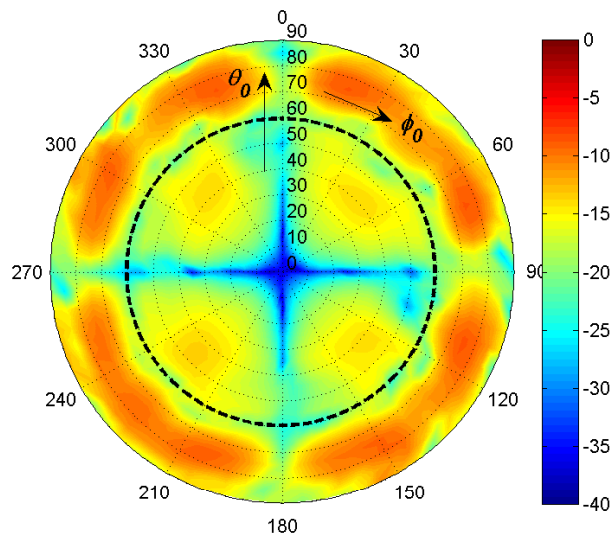

Figure 4.29: Correlation (here used as the measure of orthogonality) between a co- and cross-polarized beam in the scan direction (θ_0, ϕ_0), for $0 \le \theta_0 \le 90^o$ and $0 \le \phi_0 \le 360^o$. The scale is logarithmic.

orthogonality is best in the principal planes, i.e., in the E and H planes, but ρ_{cor} reduces in the D planes down to -14 dB for $0 \le \theta_0 \le 60^o$. The level of orthogonality that is required depends on the kind of observation and the operation of the system as a whole; it is therefore considered to be a system specification, even though the beam orthogonality as presented in Fig. 4.29 is rather intrinsic to the antenna type, excitation scheme, and the chosen array configuration. Also, it should be clear that the co and cross polarization of a single TSA element is not very important; it is the combination of the patterns generated by a x- and y-oriented antenna which determines the capabilities of the instrument to perform an adequate polarization discrimination.

4.8   Conclusions

The junction current between electrically interconnection subdomains is modeled by partially overlapping CBFs, rather than by an independent set of connection/bridge functions across the common interface between subdomains, since this would affect the total execution time and/or reduce the maximum size of the problem that can be handled. Furthermore, a mixture of macro-domain and subsectional basis functions may increase the matrix condition number.

A novel method has been developed to generate the CBFs; they are first generated on an extended subdomain constituting the interconnected adjacent antenna elements. The current distributions are then truncated by reducing their support, which eliminates undesired edge-singular currents. Finally, the CBFs are reshaped using a (trapezoidal) post-windowing technique and such that, when superimposed, the resulting synthesized surface current is continuous across the boundary interfaces between adjacent subdomains. When the CBFs are generated in this manner, it suffices to retain only a one-cell overlap between adjacent groups. This scheme allows one to compute the surface current and the mutual coupling between antennas down to -30 dB level (for a typical 10^{-2} threshold level on the singular values of the matrix containing the CBFs).

An array meshing method has been developed for an overlapping Domain Decomposition Technique (DDT) to optimally exploit the quasi-Toeplitz symmetry of the reduced moment matrix. Although an overlapping DDT saves unknowns (no junction basis functions required), the degree of translation symmetry is reduced as one can identify multiple supports with distinct sets of CBFs. A consistent triangulation and partitioning of the RWGs of all subdomains (and thus array elements) is required, so that a fully meshed array geometry facilitates a one-to-one mapping of CBFs, each of which can extend beyond the outer boundaries of an array element. For an equally-spaced singly-polarized antenna array, the computational complexity was found to scale linearly when the symmetry is exploited. For a 400 element TSA array, 400×400 MoM blocks need to be constructed, but the number of blocks is reduced to only 1199 (0.7%) by exploiting reciprocity and translation symmetry. The reduction factor reduces from ~ 135 down to ~ 95 for 2-D arrays of electrically interconnected singly-polarized TSAs.

It has been shown that each entry of the antenna admittance matrix can directly be

expressed in terms of the reduced matrix and the expansion coefficients for the CBFs. The pattern computations can be expedited by exploiting the property that many of the subdomains support the same set of CBFs, so that the respective CBF patterns are identical as well, apart from a phase shift due to their translated position.

The fill time of the reduced matrix has been shortened by hybridizing CBFM with the Adaptive Cross Approximation (ACA) algorithm. The iteratively robust ACA algorithm approximates a rank-deficient (off-diagonal) submatrix by requiring only *partial* knowledge of the original submatrix. The ACA does not exploit the oscillatory nature of the kernel in integral equations and may therefore not be as efficient as e.g. multipole approaches. However, it is kernel independent and purely algebraic. Results indicate that, when the element separation distance for singly-polarized TSA arrays becomes less than a wavelength, the effective rank of the MoM coupling matrix increases rapidly and is approximately proportional to $1/\sqrt{d_x}$ for E-plane separations, and to $1/d_y$ for H-plane separations. The ACA (for a typical threshold of 10^{-2}) is computationally more effective than a straightforward matrix-fill approach down to an element separation of $0.1\lambda_0$ and $0.2\lambda_0$ in the E- and H-plane, respectively. The ACA algorithm requires the storage of less than 5% of the full matrix block when the separation distance becomes larger than $0.2\lambda_0$. For arrays up to 20×20 TSAs, it is concluded that a combined CBFM–ACA approach approximately halves the total execution time compared to a straightforward CBFM approach.

To solve arrays of disjoint subarray problems, the CBFM has been used to construct a reduced moment matrix for only one of the subarrays, and the matrix entries are modified to account for the mutual coupling with the actively phase-steered surrounding subarrays. This perturbation approach exploits the periodicity of the phase-steered subarrays by enforcing an identical current distribution on every subarray, with a phase factor depending on the scan angle and position vector of a subarray; it yields the scan impedances of the antennas of a central subarray, which can be used to evaluate the noise-coupling effects in receive antennas. This approximation is accurate for infinite arrays of mutually coupled subarrays, as well as for finite arrays of non-coupled subarrays (isolated subarrays), or for mutually coupled subarrays where the end effects of bordering subarrays do not disrupt the impedance characteristics of the subarray under study. Generally, the accuracy of the approximate method depends upon the scan angle, number of surrounding subarrays, the electrical distance between the subarrays, the electrical size of a subarray, the type of the antenna element, and whether the array is at resonance (strong coupling). It has been shown that the accuracy of the scan reflection coefficients is higher for a broadside scan

direction for which the end effects are relatively insignificant. The solve time of ~ 17 min. is comparable to the ~ 12 min. required to solve a single isolated subarray problem (9 tiles of 8×8 TSAs each), which is about 12 times faster than a direct CBFM approach.

Previously, the state of the art was that a quantitative analysis of wideband TSA arrays was not feasible for a detailed antenna-feed decompositions with associated models. However, we have presented a reduced-order model where the strongly coupled tapered slots and the slotline cavities are represented by electrodynamic field models, whereas the microstrip lines and stubs, including their microstrip-to-slotline transitions, are represented by quasi-static field models. The antenna array can be analyzed as a dielectric-free structure if the effect of the dielectric substrate on its radiation characteristics is negligible. The direct interaction between antenna feed boards is neglected as the coupling is assumed to occur only via antenna elements. Even though the analyzed array has a size of only $5\lambda_0 \times 5\lambda_0$ at 1.5 GHz, the active infinite-array impedance characteristics are comparable for a broadside scan down to 0.8 GHz. Deviations are mainly caused by edge-truncation effects, which have an increasing influence for lower frequencies and larger scan angles. The relative difference between the measured and modeled mutual coupling coefficients is about 20%.

A formula for the beam orthogonality/correlation ρ_{cor} has been proposed to indicate how accurate a radio interferometer can measure the polarization characteristics of the incident field. The co and cross polarization of the transmitted field vector by a single-polarized array is not very important; it is the combination of the patterns generated by an x- and y-oriented antenna which determines the capabilities of the instrument to perform an adequate polarization discrimination. For a practical 8×7 doubly-polarized array, it has been shown that ρ_{cor} can be as large as -14 dB for a D-plane scan ($0 \leq \theta_0 \leq 60^o$), which is still much lower than if we would consider the co and cross polarization level of the field vector transmitted by e.g. the x-oriented TSAs only.

Chapter 5

Receiver System Modeling

A numerical and semi-analytical method is developed in this chapter to model the receiver sensitivity of antenna arrays at system level[1]. The antenna array, low-noise amplifiers, weighting devices, and arbitrary beamforming networks are characterized by S parameters to model the interaction and propagation of signal and noise wave amplitudes between interconnected microwave components. Internal noise and signal generators are represented, at port level, by a noise-wave correlation matrix and a signal-wave vector, respectively. The antenna's external noise is generated by the cosmic microwave background radiation, and internal noise by ohmic conductor losses. External signal sources are modeled as deterministic plane-wave fields. Emphasis is on the noise that emanates from the amplifier inputs and re-enters the system coherently through the mutually coupled antennas (noise coupling). Simplified analytical system models are developed which are validated through the combined electromagnetic-microwave simulation software.

---

[1]This chapter is based on a number of papers; the most important are:

[139]: R. Maaskant, E. E. M. Woestenburg, and M. J. Arts, "A generalized method of modeling the sensitivity of array antennas at system level," in *Proc. 34th European Microwave Conference*, Amsterdam, Oct. 2004, pp. 1541-1544.

[85]: R. Maaskant and B. Yang, "A combined electromagnetic and microwave antenna system simulator for radio astronomy," in *Proc. European Conference on Antennas and Propag. (EuCAP)*, Nice, France, Nov. 2006, pp. 1-4.

[122]: R. Maaskant and B. Woestenburg, "Applying the active antenna impedance to achieve noise match in receiving array antennas," in *Proc. IEEE AP-S International Symposium*, Honulollu, Hawaii, Jun. 2007, pp. 5889-5892.

[37]: R. Maaskant, D. J. Bekers, M. J. Arts, W. A. van Cappellen, and M. V. Ivashina, "Evaluation of the radiation efficiency and the noise temperature of low-loss antennas," *IEEE Antennas Wireless Propag. Lett.*, vol. 8, pp. 1536-1225, Jan. 2009.

[140]: M. V. Ivashina, R. Maaskant, and B. Woestenburg, "Equivalent system representation to model the beam sensitivity of receiving antenna arrays," *IEEE Antennas Wireless Propag. Lett.*, vol. 7, pp. 733-737, Jan. 2008.

5.1 Organization of the Chapter

Throughout this chapter, we will assume that the various RF components of an antenna array receiving system are interconnected via single-mode transmission lines. The total field along each transmission line is the sum of a forward and backward traveling wave (transmission-line mode). The interactions between the modal wave amplitudes at the ports of a device are described by scattering parameters, or S parameters. Section 5.2 describes how a scattering matrix relates the incident modal voltage amplitudes to the scattered ones, both for deterministic and stochastic signals. The transmission lines are assumed to have zero length, or are modeled as separate S-parameter matrices otherwise. Accordingly, the "incident/scattered modal voltage amplitudes" are simply called "incident/scattered waves", as in most microwave books.

Section 5.3 describes how the signal and noise waves propagate through a receiver system in case it is modeled as a cascaded series of S-parameter matrices. For this purpose, the correlation between noise-wave amplitudes is accounted for by the elements of a noise-wave correlation matrix, and the antenna array on receive is represented by a Thévenin network (*cf.* Section 2.5) whose internal voltage generators (open-circuit voltages) are transformed to signal-wave generators as this is in accordance with the S-parameter description. The noise-wave characterization of active and passive receiver components is explained in Section 5.4; this includes the antenna array in conjunction with an external nonuniform brightness temperature distribution of the sky. Numerical results for a practical noise measurement setup are described in Section 5.4.5.

The noise coupling phenomenon is explained in Section 5.5, where it is shown that minimum receiver noise can be achieved by noise matching each of the receiver channels to the active scan impedance of the corresponding antenna element. Accordingly, Section 5.6 describes how mutually coupled receiver channels can be "noise decoupled" and be represented by an equivalent single-channel receiver. Formulas for the receiver sensitivity are derived and expressed in terms of the coupling, mismatch, and radiation efficiency, after which the single-channel receiver model is validated by numerical results. Since the radiation efficiency plays a major role in the formula for the system sensitivity, it must be determined accurately and is therefore considered separately in Section 5.7. Various examples demonstrate that the numerically computed radiation efficiency does not exceed 100% for low-loss antennas, as opposed to a number of commercially available software tools.

5.2   Signal and Noise Wave Representation

Because we consider weak signals, it is assumed that the nonlinear network components can be linearized, which allows us to work in the frequency domain and to use an S-parameter matrix formulation. Consider the equivalent representation of a noisy two port in Fig. 5.1; it is modeled as a noiseless two port in conjunction with the two external noise-wave sources c_1 and c_2. Likewise, the internal signal generators are represented by the external signal-wave amplitudes g_1 and g_2. In the presence of signal and/or noise sources, incident
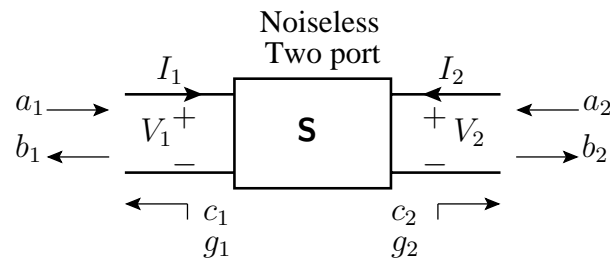

Figure 5.1: Signal and noise-wave representation for a two port.

and reflected waves with complex-valued amplitudes $\{a_n\}$ and $\{b_n\}$, for $n \in \{1,2\}$, start propagating; these complex-valued power wave amplitudes (or power waves for short) are defined in [141] as

$$a_n = \frac{V_n + Z_{0n}^{\text{ref}} I_n}{2\sqrt{\Re\mathfrak{e}\{Z_{0n}^{\text{ref}}\}}} \qquad \text{and} \qquad b_n = \frac{V_n - \left(Z_{0n}^{\text{ref}}\right)^* I_n}{2\sqrt{\Re\mathfrak{e}\{Z_{0n}^{\text{ref}}\}}} \qquad (\text{for } \Re\mathfrak{e}\{Z_{0n}^{\text{ref}}\} > 0) \quad (5.1)$$

where V_n and I_n denote the voltage and current amplitude at the nth port, respectively (the arrows in Fig. 5.1 define the positive direction), and where Z_{0n}^{ref} denotes the corresponding complex-valued normalization impedance for this port. The asterisk denotes the complex conjugate. The associated inverse relations are [141]

$$V_n = \frac{\left(Z_{0n}^{\text{ref}}\right)^* a_n + Z_{0n}^{\text{ref}} b_n}{\sqrt{\Re\mathfrak{e}\{Z_{0n}^{\text{ref}}\}}} \qquad \text{and} \qquad I_n = \frac{a_n - b_n}{\sqrt{\Re\mathfrak{e}\{Z_{0n}^{\text{ref}}\}}}. \qquad (5.2)$$

By stacking the power waves in the respective column vectors $\mathbf{a} = [a_1, a_2]^T$ and $\mathbf{b} = [b_1, b_2]^T$, and by introducing the signal- and noise-wave vectors $\mathbf{g} = [g_1, g_2]^T$ and $\mathbf{c} = [c_1, c_2]^T$, respectively, the signal- and noise-wave amplitudes at the terminals of a linear two-port

device are related via the scattering matrix $\mathbf{S}$ as: $\mathbf{b} = \mathbf{S}\mathbf{a} + \mathbf{g} + \mathbf{c}$, that is,

$$\begin{pmatrix} b_1 \\ b_2 \end{pmatrix} = \begin{pmatrix} S_{11} & S_{12} \\ S_{21} & S_{22} \end{pmatrix} \begin{pmatrix} a_1 \\ a_2 \end{pmatrix} + \begin{pmatrix} g_1 \\ g_2 \end{pmatrix} + \begin{pmatrix} c_1 \\ c_2 \end{pmatrix} \tag{5.3}$$

where the noise-wave vector $\mathbf{c}$ has been temporarily treated as a deterministic signal, and where $\mathbf{a}$ is the incoming, $\mathbf{b}$ is the outgoing, and $\mathbf{g}$ is the signal-wave vector.

With the aid of the above definitions, the total accepted (input) power P_{acc} by an N-port device is conveniently computed from the incident and scattered waves as

$$P_{\mathrm{acc}} = \sum_{n=1}^{N} \mathfrak{Re}\{V_n I_n^*\} = \mathfrak{Re}\{\mathbf{I}^H \mathbf{V}\} = \sum_{n=1}^{N} \left(|a_n|^2 - |b_n|^2\right) = \mathbf{a}^H \mathbf{a} - \mathbf{b}^H \mathbf{b} \tag{5.4}$$

where the amplitudes are assumed to be RMS values. The matrix $\mathbf{S}$ depends on the chosen normalization impedances $\{Z_{0n}^{\mathrm{ref}}\}$. Choosing a new set of normalization impedances $\left\{\left(Z_{0n}^{\mathrm{ref}}\right)'\right\}$, leads to the renormalized scattering matrix $\mathbf{S}'$, according to [142, p. 22]

$$\mathbf{S}' = \mathbf{Q}^{-1}(\mathbf{S} - \mathbf{U}^H)(\mathbf{I} - \mathbf{U}\mathbf{S})^{-1}\mathbf{Q}^H \tag{5.5}$$

where $\mathbf{U}$ is a diagonal matrix with the nth element u_n on the diagonal equal to

$$u_n = \frac{\left(Z_{0n}^{\mathrm{ref}}\right)' - Z_{0n}^{\mathrm{ref}}}{\left(Z_{0n}^{\mathrm{ref}}\right)' + \left(Z_{0n}^{\mathrm{ref}}\right)^*}. \tag{5.6}$$

Furthermore, the nth diagonal element q_n of the diagonal matrix $\mathbf{Q}$ is given by

$$q_n = \frac{1 - u_n^*}{|1 - u_n|} \sqrt{|1 - u_n u_n^*|}. \tag{5.7}$$

As opposed to the deterministic signal-wave vector $\mathbf{g}$, the elements of the noise-wave vector $\mathbf{c}$ are stochastic and may be mutually correlated. Henceforth, we shall assume that the statistical noise sources are (wide-sense) stationary random processes which exhibit ergodicity. For such processes, the Wiener-Khintchine theorem states that the self- and cross-power spectral densities are defined as the Fourier transform of their auto- and cross-correlation functions [143]. Furthermore, the statistical properties can be deduced from a single, though sufficiently long sample (realization) of the process, and ensemble averages may be replaced by time averages. The latter is an advantageous property since the practical implementation of time averages is straightforward.

We consider the temporal noise voltages $v_1(t)$ and $v_2(t)$, and compute the cross-correlation function between these ergodic processes as [144, 145]

$$R_{v_1 v_2}(\tau) = \mathbb{E}\left\{v_1(t)v_2(t+\tau)\right\} = \lim_{T\to\infty} \frac{1}{T}\int_0^T v_1(t)v_2(t+\tau)\,\mathrm{d}t = \overline{v_1(t)v_2(t+\tau)} \qquad (5.8)$$

where $\mathbb{E}\{\cdot\}$ denotes the statistical expectation, and the overbar the time average. Next, let us record the stochastic voltages $v_1(t)$ and $v_2(t)$ for the time interval $0 \leq t \leq T$ and continue these samples periodically. The corresponding Fourier series representations are

$$v_1(t) = \sum_{n=-\infty}^{\infty} a_n e^{j\omega_n t} \qquad \text{and} \qquad v_2(t) = \sum_{n=-\infty}^{\infty} b_n e^{j\omega_n t} \qquad (5.9)$$

where $\omega_n = 2\pi n/T$, and where the complex-valued amplitudes $\{a_n, b_n\}$ are given by

$$a_n = \frac{1}{T}\int_0^T v_1(t)e^{-j\omega_n t}\,\mathrm{d}t \qquad \text{and} \qquad b_n = \frac{1}{T}\int_0^T v_2(t)e^{-j\omega_n t}\,\mathrm{d}t. \qquad (5.10)$$

In the limiting case, for $T \to \infty$, the statistical expectation $\mathbb{E}\{a_n b_n^*\}$ of the mutual power $a_n b_n^*$ defines the cross-power spectral-density function $S_{v_1 v_2}$ according to [146, p. 12]

$$S_{v_1 v_2}(\omega) = \lim_{T\to\infty} T\overline{a_n b_n^*} \quad [\mathrm{W/Hz}]. \qquad (5.11)$$

By substituting (5.10) in (5.11), introducing new integration variables, and adopting different integration limits, the Wiener-Khintchine theorem is derived as [146, pp. 169–170]:

$$S_{v_1 v_2}(\omega) = \lim_{T\to\infty} T\overline{a_n b_n^*} = \int_{-\infty}^{\infty} \overline{v_1(t)v_2(t+\tau)}e^{j\omega\tau}\,\mathrm{d}\tau \qquad (5.12)$$

where $S_{v_1 v_2}$ is the Fourier transform of the cross-correlation function $R_{v_1 v_2}$ in (5.8). A similar derivation of the Wiener-Khintchine theorem is given in [145, pp. 406–409]. From (5.11), it is observed that, within a narrow frequency bandwidth $\Delta\omega$ centered around ω_0, one can write $S_{v_1 v_2}(\omega_0) = \overline{a_n b_n^*}/\Delta\omega$.

The noise waves c_1 and c_2 that emanate from the two port in Fig. 5.1 are fully characterized in terms of their spectral noise wave powers $\overline{|c_1|^2}$ and $\overline{|c_2|^2}$ [W/Hz], respectively, together with their mutual correlations $\overline{c_1 c_2^*} = \overline{c_2 c_1^*}$, which are complex-valued in order to contain the phase information. The mutual and self terms can be physically measured by a complex correlator [147], and are conveniently represented in terms of a spectral noise-wave

correlation matrix $\mathbf{C}$ [143], that is, for a general N port device,

$$\mathbf{C} = \overline{\mathbf{c}\mathbf{c}^H} = \begin{pmatrix} \overline{|c_1|^2} & \overline{c_1 c_2^*} & \cdots & \overline{c_1 c_N^*} \\ \overline{c_2 c_1^*} & \overline{|c_2|^2} & \cdots & \overline{c_2 c_N^*} \\ \vdots & \vdots & \ddots & \vdots \\ \overline{c_N c_1^*} & \overline{c_N c_2^*} & \cdots & \overline{|c_N|^2} \end{pmatrix} \tag{5.13}$$

where the superscript H denotes the Hermitian complex conjugate for vectors and matrices and $\mathbf{c} = [c_1, c_2, \ldots, c_N]^T$. The matrix $\mathbf{C}$ is a Hermitian matrix.

5.3 An Antenna Receiver Model at RF System Level

The various RF system blocks in an antenna array receiving system will be characterized in terms of scattering and noise-wave correlation matrices. A typical receiving system modeled by S-matrices is shown in Fig. 5.2. The N-port antenna array is described by an S-matrix, called $\mathbf{S}^{\text{ant}}$. This matrix can be obtained from measurements, simulations or analytical models. The scattering matrix depends on the antenna array geometry, a certain characteristic impedance, and the frequency under consideration. The Low Noise Amplifiers (LNAs) are described by a $2N$-port scattering matrix, called $\mathbf{S}^{\text{LNA}}$. The output signals of the LNAs are fed to a beamformer network, described by $\mathbf{S}^{\text{BF}}$. The beamformer network combines the output signals of the LNAs to create M beams at the final output. The amplitudes of the waves that flow to and from the RF system blocks are denoted by $\mathbf{a}$ and $\mathbf{b}$ vector waves, respectively.

The objective is to obtain a general expression for the signal-to-noise ratio of the antenna system in its entirety, i.e., to compute the noise and signal power of an element of the output vector $\mathbf{b}$ to measure the sensitivity of a certain beam. To this end, we will first perform a noise analysis, and subsequently a signal analysis.

5.3.1 Noise Wave Propagation in the Receiving System

For the system as shown in Fig. 5.2, we assume that only the antenna array and LNAs are noisy. Typically, the noise that is generated after the first stage of amplification will contribute only moderately to the total output noise power whenever the amplifier gains
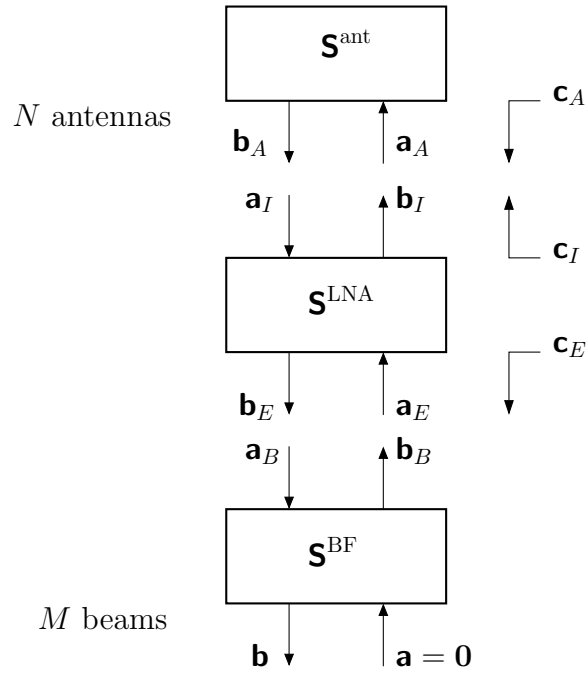
Figure 5.2: An antenna array receiving system described by S-matrices.

are sufficiently high. The second-stage noise contribution will therefore not be taken into consideration.

If the N-port antenna array is lossy, or the antenna array is receiving noise, a noise wave vector $\mathbf{c}_A$ is generated and is added to the reflected output signal $\mathbf{S}^{\mathrm{ant}}\mathbf{a}_A$ of the antenna. The linear relation between $\mathbf{a}_A$, $\mathbf{b}_A$ and $\mathbf{S}^{\mathrm{ant}}$ and the noise wave vector $\mathbf{c}_A$ is given by

$$\mathbf{b}_A = \mathbf{S}^{\mathrm{ant}}\mathbf{a}_A + \mathbf{c}_A. \tag{5.14}$$

We assume a small-signal model around the operating point for the individual LNAs, so that we can work with linear equations. Although not required, we also assume that the direct coupling between the LNAs is negligible, while the LNAs may still be different from each other. We introduce noise waves that emanate from the input and output of the LNAs and their spectral voltage amplitudes are contained in the vectors $\mathbf{c}_I$ and $\mathbf{c}_E$, respectively. Then, we write

$$\left(\begin{array}{c} \mathbf{b}_I \\ \mathbf{b}_E \end{array} \right) = \left(\begin{array}{cc} \mathbf{S}_{11}^{\mathrm{LNA}} & \mathbf{S}_{12}^{\mathrm{LNA}} \\ \mathbf{S}_{21}^{\mathrm{LNA}} & \mathbf{S}_{22}^{\mathrm{LNA}} \end{array} \right) \left(\begin{array}{c} \mathbf{a}_I \\ \mathbf{a}_E \end{array} \right) + \left(\begin{array}{c} \mathbf{c}_I \\ \mathbf{c}_E \end{array} \right) \tag{5.15}$$

where the amplitude vectors (complex quantities) are related via the $N \times N$ diagonal matrices $\mathbf{S}_{11}^{\mathrm{LNA}}$, $\mathbf{S}_{12}^{\mathrm{LNA}}$, $\mathbf{S}_{21}^{\mathrm{LNA}}$ and $\mathbf{S}_{22}^{\mathrm{LNA}}$. Obviously, the elements of the noise wave vectors

$\mathbf{c}_A$, $\mathbf{c}_E$, and $\mathbf{c}_I$ are mutually correlated. Later on, these correlations will be expressed in terms of the noise wave correlation matrix $\mathbf{C}$.

Next, we describe the electrical connections between the LNAs and N antenna outputs by[2]

$$\mathbf{a}_I = \mathbf{b}_A \qquad \text{and} \qquad \mathbf{a}_A = \mathbf{b}_I. \qquad (5.16)$$

Finally, every LNA output signal is complex weighted before the final addition is carried out to yield a single beamformer output. We assume that the beamformer is able to create M beams, hence, we define

$$\begin{pmatrix} \mathbf{b}_B \\ \mathbf{b} \end{pmatrix} = \begin{pmatrix} \mathbf{S}_{11}^{\mathrm{BF}} & \mathbf{S}_{12}^{\mathrm{BF}} \\ \mathbf{S}_{21}^{\mathrm{BF}} & \mathbf{S}_{22}^{\mathrm{BF}} \end{pmatrix} \begin{pmatrix} \mathbf{a}_B \\ \mathbf{a} \end{pmatrix}, \qquad (5.17)$$

where $\mathbf{S}_{11}^{\mathrm{BF}}$ is a $N \times N$ diagonal matrix, which contains the complex reflection coefficients at the input of the beamformer if no coupling between the inputs exists. $\mathbf{S}_{12}^{\mathrm{BF}}$ is a $M \times N$ matrix, holding the complex transmission coefficients from output to input. $\mathbf{S}_{21}^{\mathrm{BF}}$ is a $N \times M$ matrix; each row of the matrix holds a complex steering vector (phased arrays) or weighting vector (focal plane arrays) to create a particular beam. $\mathbf{S}_{22}^{\mathrm{BF}}$ is a $M \times M$ diagonal matrix, holding the complex reflection coefficients at the output of the beamformer if no coupling between the outputs exists. In conclusion, we observe that $\mathbf{S}^{\mathrm{BF}}$ is a $(N + M) \times (N + M)$ matrix.

The connections between the LNAs and the beamformer are expressed in terms of the following relations

$$\mathbf{a}_B = \mathbf{b}_E \qquad \text{and} \qquad \mathbf{a}_E = \mathbf{b}_B. \qquad (5.18)$$

In summary, we developed the following linear set of equations:

$$\mathbf{b}_A = \mathbf{S}^{\mathrm{ant}} \mathbf{a}_A + \mathbf{c}_A \qquad (5.19\mathrm{a})$$
$$\mathbf{b}_I = \mathbf{S}_{11}^{\mathrm{LNA}} \mathbf{a}_I + \mathbf{S}_{12}^{\mathrm{LNA}} \mathbf{a}_E + \mathbf{c}_I \qquad (5.19\mathrm{b})$$
$$\mathbf{b}_E = \mathbf{S}_{21}^{\mathrm{LNA}} \mathbf{a}_I + \mathbf{S}_{22}^{\mathrm{LNA}} \mathbf{a}_E + \mathbf{c}_E \qquad (5.19\mathrm{c})$$
$$\mathbf{a}_I = \mathbf{b}_A \qquad (5.19\mathrm{d})$$
$$\mathbf{a}_A = \mathbf{b}_I \qquad (5.19\mathrm{e})$$

$$\mathbf{b}_B = \mathbf{S}_{11}^{\mathrm{BF}} \mathbf{a}_B + \mathbf{S}_{12}^{\mathrm{BF}} \mathbf{a} \qquad (5.19\mathrm{f})$$
$$\mathbf{b} = \mathbf{S}_{21}^{\mathrm{BF}} \mathbf{a}_B + \mathbf{S}_{22}^{\mathrm{BF}} \mathbf{a} \qquad (5.19\mathrm{g})$$
$$\mathbf{a}_B = \mathbf{b}_E \qquad (5.19\mathrm{h})$$
$$\mathbf{a}_E = \mathbf{b}_B. \qquad (5.19\mathrm{i})$$

---

[2]One should use [142, Eq. (3.65)] for imperfect connections, i.e., for unequal reference impedances.

In order to compute the total noise-wave vector at the final output of the system, as a consequence of the noise sources $\mathbf{c}_A$, $\mathbf{c}_I$ and $\mathbf{c}_E$, we first express the output signal $\mathbf{b}_E$ as a function of $\mathbf{c}_A$, $\mathbf{c}_I$, and $\mathbf{c}_E$. From (5.19d), (5.19e) and (5.19a), it follows that

$$\mathbf{a}_I = \mathbf{S}^{\text{ant}}\mathbf{b}_I + \mathbf{c}_A. \tag{5.20}$$

Upon combining (5.20) and (5.19b), and by isolating $\mathbf{b}_I$, we find that

$$\mathbf{b}_I = \left(\mathbf{I} - \mathbf{S}_{11}^{\text{LNA}}\mathbf{S}^{\text{ant}}\right)^{-1}\left(\mathbf{S}_{11}^{\text{LNA}}\mathbf{c}_A + \mathbf{c}_I + \mathbf{S}_{12}^{\text{LNA}}\mathbf{a}_E\right) \tag{5.21}$$

where $\mathbf{I}$ is the identity matrix. Now, it is possible to write $\mathbf{b}_E$ as a function of $\mathbf{c}_A$, $\mathbf{c}_I$ and $\mathbf{c}_E$. To achieve this, we substitute (5.21) in (5.20) and (5.19c), so that the total noise coupling vector at the output of the LNAs is given by

$$\begin{aligned}
\mathbf{b}_E &= \mathbf{S}_{21}^{\text{LNA}}\mathbf{S}^{\text{ant}}\mathbf{b}_I + \mathbf{c}_E + \mathbf{S}_{22}^{\text{LNA}}\mathbf{a}_E + \mathbf{S}_{21}^{\text{LNA}}\mathbf{c}_A \\
&= \mathbf{c}_E + \mathbf{S}_{21}^{\text{LNA}}\mathbf{S}^{\text{ant}}\left(\mathbf{I} - \mathbf{S}_{11}^{\text{LNA}}\mathbf{S}^{\text{ant}}\right)^{-1}\mathbf{c}_I \\
&\quad + \mathbf{S}_{21}^{\text{LNA}}\left(\mathbf{I} + \mathbf{S}^{\text{ant}}\left(\mathbf{I} - \mathbf{S}_{11}^{\text{LNA}}\mathbf{S}^{\text{ant}}\right)^{-1}\mathbf{S}_{11}^{\text{LNA}}\right)\mathbf{c}_A \\
&\quad + \left(\mathbf{S}_{22}^{\text{LNA}} + \mathbf{S}_{21}^{\text{LNA}}\mathbf{S}^{\text{ant}}\left(\mathbf{I} - \mathbf{S}_{11}^{\text{LNA}}\mathbf{S}^{\text{ant}}\right)^{-1}\mathbf{S}_{12}^{\text{LNA}}\right)\mathbf{a}_E.
\end{aligned} \tag{5.22}$$

The physical interpretation of Eq. (5.22) is as follows. Suppose that the LNAs are matched at the output ($\mathbf{a}_E = \mathbf{0}$) and that the LNAs are identical ($\mathbf{S}_{11}^{\text{LNA}} = S_{11}^{\text{LNA}}\mathbf{I}$). We then find that

$$\mathbf{b}_E = \mathbf{c}_E + S_{21}^{\text{LNA}}\mathbf{c}_A + S_{21}^{\text{LNA}}\mathbf{S}^{\text{ant}}\left(\mathbf{I} - S_{11}^{\text{LNA}}\mathbf{S}^{\text{ant}}\right)^{-1}\left(\mathbf{c}_I + S_{11}^{\text{LNA}}\mathbf{c}_A\right) \tag{5.23}$$

where $S_{21}^{\text{LNA}}\mathbf{S}^{\text{ant}}\left(\mathbf{I} - S_{11}^{\text{LNA}}\mathbf{S}^{\text{ant}}\right)^{-1}\mathbf{c}_I$ is the noise contribution at the LNA outputs; this term describes how the noise waves that emanate from the LNA inputs re-enter the system through the mutually coupled antenna elements. Note that this simplified result has also been reported by other authors [148]. With the aid of the geometric series expansion (Neumann expansion) $(1 - x)^{-1} = \sum_{n=0}^{\infty} x^n$ (for $|x| < 1$), one can write that

$$\begin{aligned}
S_{21}^{\text{LNA}}\mathbf{S}^{\text{ant}}\left(\mathbf{I} - S_{11}^{\text{LNA}}\mathbf{S}^{\text{ant}}\right)^{-1}\mathbf{c}_I &= S_{21}^{\text{LNA}}\mathbf{S}^{\text{ant}}\sum_{n=0}^{\infty}\left(S_{11}^{\text{LNA}}\mathbf{S}^{\text{ant}}\right)^n\mathbf{c}_I \\
&= S_{21}^{\text{LNA}}\mathbf{S}^{\text{ant}}\mathbf{c}_I + S_{21}^{\text{LNA}}\mathbf{S}^{\text{ant}}S_{11}^{\text{LNA}}\mathbf{S}^{\text{ant}}\mathbf{c}_I + \dots
\end{aligned} \tag{5.24}$$

which converges if $\left(S_{11}^{\text{LNA}}\mathbf{S}^{\text{ant}}\right)^{\infty} = \mathbf{0}$, or, equivalently, if the magnitudes of all the eigenvalues of $S_{11}^{\text{LNA}}\mathbf{S}^{\text{ant}}$ are smaller than unity. The first-order term represents the noise wave $\mathbf{c}_I$ that reflects from the antenna and is then amplified by $S_{21}^{\text{LNA}}\mathbf{S}^{\text{ant}}$ (see also Fig. 5.2), whereas

the second contribution represents the noise reflected wave from the antenna which, in turn, reflects at the LNA inputs and antenna after which it is amplified by the amplifiers, etc. The vector quantity $S_{21}^{\text{LNA}}\mathbf{c}_A$ in (5.23) is the output noise due to a direct transfer of the antenna noise, while $S_{21}^{\text{LNA}}\mathbf{S}^{\text{ant}}\left(\mathbf{I} - S_{11}^{\text{LNA}}\mathbf{S}^{\text{ant}}\right)^{-1}S_{11}^{\text{LNA}}\mathbf{c}_A$ describes the propagation of the antenna noise waves to the output via the mutual coupling between antenna elements and reflection at the LNA inputs.

We can express (5.22) in a short-hand form, i.e.

$$\mathbf{b}_E = \mathbf{c}_E + \mathbf{A}\mathbf{c}_I + \mathbf{B}\mathbf{c}_A + \mathbf{C}\mathbf{a}_E \tag{5.25}$$

in which the transfer matrices are given as

$$\mathbf{A} = \mathbf{S}_{21}^{\text{LNA}}\mathbf{S}^{\text{ant}}\left(\mathbf{I} - \mathbf{S}_{11}^{\text{LNA}}\mathbf{S}^{\text{ant}}\right)^{-1} \tag{5.26}$$

$$\mathbf{B} = \mathbf{S}_{21}^{\text{LNA}}\left(\mathbf{I} + \mathbf{S}^{\text{ant}}\left(\mathbf{I} - \mathbf{S}_{11}^{\text{LNA}}\mathbf{S}^{\text{ant}}\right)^{-1}\mathbf{S}_{11}^{\text{LNA}}\right) \tag{5.27}$$

$$\mathbf{C} = \mathbf{S}_{22}^{\text{LNA}} + \mathbf{S}_{21}^{\text{LNA}}\mathbf{S}^{\text{ant}}\left(\mathbf{I} - \mathbf{S}_{11}^{\text{LNA}}\mathbf{S}^{\text{ant}}\right)^{-1}\mathbf{S}_{12}^{\text{LNA}} = \mathbf{S}_{22}^{\text{LNA}} + \mathbf{A}\mathbf{S}_{12}^{\text{LNA}}. \tag{5.28}$$

From (5.19i), (5.19f) and (5.19h), it follows that

$$\mathbf{a}_E = \mathbf{b}_B = \mathbf{S}_{11}^{\text{BF}}\mathbf{a}_B + \mathbf{S}_{12}^{\text{BF}}\mathbf{a} = \mathbf{S}_{11}^{\text{BF}}\mathbf{b}_E + \mathbf{S}_{12}^{\text{BF}}\mathbf{a} \tag{5.29}$$

so that, together with (5.25),

$$\mathbf{b}_E = \left(\mathbf{I} - \mathbf{C}\mathbf{S}_{11}^{\text{BF}}\right)^{-1}\left(\mathbf{c}_E + \mathbf{A}\mathbf{c}_I + \mathbf{B}\mathbf{c}_A + \mathbf{C}\mathbf{S}_{12}^{\text{BF}}\mathbf{a}\right). \tag{5.30}$$

As a result, the total output noise vector $\mathbf{b}$ for M beams is obtained after substitution of (5.30) and (5.19h) in (5.19g), i.e.,

$$\mathbf{b} = \mathbf{S}_{22}^{\text{BF}}\mathbf{a} + \mathbf{S}_{21}^{\text{BF}}\left(\mathbf{I} - \mathbf{C}\mathbf{S}_{11}^{\text{BF}}\right)^{-1}\left(\mathbf{c}_E + \mathbf{A}\mathbf{c}_I + \mathbf{B}\mathbf{c}_A + \mathbf{C}\mathbf{S}_{12}^{\text{BF}}\mathbf{a}\right). \tag{5.31}$$

5.3.2 The Output Noise Powers and Their Correlations

We expressed the M-element output-wave vector $\mathbf{b} = [b_1, b_2, \ldots, b_M]^T$ in terms of the noise sources $\mathbf{c}_A$, $\mathbf{c}_I$, and $\mathbf{c}_E$. For a real-valued characteristic impedance Z_0^{ref}, the relationship between $\mathbf{b}$ and the corresponding transmission-line wave voltages contained in $\mathbf{V}$ follows from (5.2), i.e.,

$$\mathbf{b} = \frac{\mathbf{V}}{\sqrt{Z_0^{\text{ref}}}} - \mathbf{a} = \left.\frac{\mathbf{V}^-}{\sqrt{Z_0^{\text{ref}}}}\right|_{\mathbf{a}=\mathbf{0}} \tag{5.32}$$

where $\mathbf{V} = \mathbf{V}^-$ is the complex-valued spectral RMS amplitude $[\mathrm{VHz}^{-1/2}]$ of the reflected voltage wave in case the beamformer output is reflectionless. Accordingly, for stochastic waves amplitudes, and with reference to Eq. (5.13), it follows that the total spectral noise powers at the beamformer output can be arranged in an $M \times M$ noise-wave correlation matrix $\mathbf{C}^o$, i.e.,

$$\mathbf{C}^o = \overline{\mathbf{b}\,\mathbf{b}^H} = \begin{pmatrix} \overline{|b_1|^2} & \overline{b_1 b_2^*} & \cdots & \overline{b_1 b_M^*} \\ \overline{b_2 b_1^*} & \overline{|b_2|^2} & \cdots & \overline{b_2 b_M^*} \\ \vdots & \vdots & \ddots & \vdots \\ \overline{b_M b_1^*} & \overline{b_M b_2^*} & \cdots & \overline{|b_M|^2} \end{pmatrix}. \tag{5.33}$$

The diagonal of $\mathbf{C}^o$ contains the output noise powers for each of the beams, while the off-diagonal terms indicate their mutual correlations. The matrix $\mathbf{C}^o$ can be expressed in terms of the self- and mutual-correlation matrices concerning the noise waves $\mathbf{c}_A$, $\mathbf{c}_I$ and $\mathbf{c}_E$. The relationship between $\mathbf{b}$ and these noise waves is given by Eq. (5.31) through a transfer matrix $\mathbf{T}$, i.e., for $\mathbf{a} = \mathbf{0}$ we have

$$\mathbf{b} = \mathbf{Tc} \tag{5.34}$$

with

$$\mathbf{T} = \mathbf{S}_{21}^{\mathrm{BF}} \left(\mathbf{I} - \mathbf{C}\mathbf{S}_{11}^{\mathrm{BF}}\right)^{-1} [\mathbf{I} \,|\, \mathbf{A} \,|\, \mathbf{B}] \qquad \text{and} \qquad \mathbf{c} = [\mathbf{c}_E^T \,|\, \mathbf{c}_I^T \,|\, \mathbf{c}_A^T]^T, \tag{5.35}$$

where $|$ denotes matrix augmentation (column-wise concatenation).

The transfer matrix $\mathbf{T}$ represents a chain of scattering matrices and describes how the noise waves $\mathbf{c}$ propagate through the beamforming network towards the beamformer output $\mathbf{b}$. Equation (5.34) can be substituted in (5.33) to obtain the noise-wave correlation matrix $\mathbf{C}^o$, i.e.,

$$\mathbf{C}^o = \overline{\mathbf{b}\,\mathbf{b}^H} = \overline{\mathbf{Tc}\,(\mathbf{Tc})^H} = \mathbf{T}\overline{\mathbf{c}\,\mathbf{c}^H}\mathbf{T}^H \tag{5.36}$$

where the last equality is proven in [143]. The term $\overline{\mathbf{c}\,\mathbf{c}^H}$ is the correlation matrix of the antenna noise waves $\mathbf{c}$. If this matrix is denoted by $\mathbf{C}$, Eq. (5.36) is rewritten as

$$\mathbf{C}^o = \mathbf{TCT}^H \tag{5.37}$$

which shows that the noise-wave correlation matrix $\mathbf{C}$ is transformed to the correlation matrix $\mathbf{C}^o$ by using the transfer matrix $\mathbf{T}$. Thus, the total spectral noise power at every

beamformer output, i.e., $\overline{|b_1|^2}$, $\overline{|b_2|^2}$, ..., $\overline{|b_M|^2}$ is written in terms of the noise-wave powers $\overline{|c_1|^2}$, $\overline{|c_2|^2}$, ..., $\overline{|c_N|^2}$ and the correlations between the relevant noise-wave amplitudes.

The next step is to express the elements of the noise-wave correlation matrix $\mathbf{C}$ in terms of the sources that produce these noise waves. To this end, we need to further specify/model the LNAs and the antenna array in terms of their internal noise sources; this will be detailed in Section 5.4, where e.g. the antenna noise-wave vector $\mathbf{c}_A$ is expressed in terms of a nonuniform equivalent noise-temperature distribution of the sky.

5.3.3 Determination of the Total Signal Output Powers

We expressed the total noise at M outputs of a receiving system in terms of noise sources that emanate from the antenna ports and LNAs. Besides these stochastic signals, deterministic signals can be considered. For instance, if a plane wave is incident on the antenna array with a deterministic amplitude and phase defined at a certain reference point in space, the total signal output power after beamforming can be computed and, hence, a signal-to-noise ratio can be determined.

The output signal-wave vector at the antenna ports, which arises due to this incident plane wave, will be denoted by $\mathbf{g}$ (as in Fig. 5.1 for internal signal generators). This signal wave propagates towards the M beamformer outputs in a similar way as the antenna noise-wave vector $\mathbf{c}_A$ is doing. Therefore, we define that $\mathbf{c}_A = \mathbf{g}$ and $\mathbf{c}_I = \mathbf{c}_E = 0$. Then, we simply make use of Eq. (5.31), so that the output wave vector $\mathbf{b}$ is given by

$$\mathbf{b} = \mathbf{S}_{22}^{\mathrm{BF}}\mathbf{a} + \mathbf{S}_{21}^{\mathrm{BF}}\left(\mathbf{I} - \mathbf{CS}_{11}^{\mathrm{BF}}\right)^{-1}\left(\mathbf{Bg} + \mathbf{CS}_{12}^{\mathrm{BF}}\mathbf{a}\right). \qquad (5.38)$$

The antenna array signal $\mathbf{g}$ is determined by the antenna properties and is a quantity that can be measured by terminating the array elements with the characteristic impedance. Alternatively, it is possible to find a relationship between the antenna-array signal $\mathbf{g}$ and the open-port voltage vector $\mathbf{V}^{\mathrm{oc}}$. Open-port voltages are convenient, because relationships exist that relate the open-port voltages to the electromagnetic field that is illuminating the array (*cf.* Section 2.5). The relationship between $\mathbf{g}$ and $\mathbf{V}^{\mathrm{oc}}$ can be derived from Fig. 5.3, where the antenna is characterized by an impedance matrix $\mathbf{Z}^{\mathrm{ant}}$.

With the aid of Kirchhoff's voltage law, it is observed that

$$\mathbf{V}^{\mathrm{oc}} = \mathbf{V} + \mathbf{Z}^{\mathrm{ant}}\mathbf{I}_A. \qquad (5.39)$$
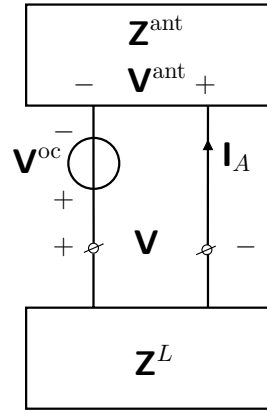
Figure 5.3: A circuit representation of a loaded receiving antenna array.

For real-valued and equal normalization impedances, it follows from (5.2) that $\mathbf{I}_A = (\mathbf{a}_I - \mathbf{b}_I)/\sqrt{Z_0^{\mathrm{ref}}}$ and $\mathbf{V} = \sqrt{Z_0^{\mathrm{ref}}}\,(\mathbf{a}_I + \mathbf{b}_I)$, so that

$$\mathbf{V}^{\mathrm{oc}} = \sqrt{Z_0^{\mathrm{ref}}}\,(\mathbf{a}_I + \mathbf{b}_I) + \mathbf{Z}^{\mathrm{ant}}\frac{1}{\sqrt{Z_0^{\mathrm{ref}}}}\,(\mathbf{a}_I - \mathbf{b}_I) \tag{5.40}$$

which in turn allows us to isolate $\mathbf{a}_I$. This yields

$$\mathbf{a}_I = \left(\mathbf{Z}^{\mathrm{ant}} + \mathbf{Z}_0^{\mathrm{ref}}\right)^{-1}\left(\mathbf{Z}^{\mathrm{ant}} - \mathbf{Z}_0^{\mathrm{ref}}\right)\mathbf{b}_I + \left(\mathbf{Z}^{\mathrm{ant}} + \mathbf{Z}_0^{\mathrm{ref}}\right)^{-1}\sqrt{\mathbf{Z}_0^{\mathrm{ref}}}\,\mathbf{V}^{\mathrm{oc}} \tag{5.41a}$$

$$= \mathbf{S}^{\mathrm{ant}}\mathbf{b}_I + \mathbf{g} \tag{5.41b}$$

where $\mathbf{Z}_0^{\mathrm{ref}} = Z_0^{\mathrm{ref}}\mathbf{I}$ is a diagonal matrix, holding the characteristic impedances of the antenna-output transmission lines. Furthermore, because $\mathbf{a}_I = \mathbf{b}_A$ and $\mathbf{b}_I = \mathbf{a}_A$ [*cf.* Eqs. (5.19d) and (5.19e)], we can rewrite (5.41b) as $\mathbf{b}_A = \mathbf{S}^{\mathrm{ant}}\mathbf{a}_A + \mathbf{g}$, so that,

$$\mathbf{g} = \left(\mathbf{Z}^{\mathrm{ant}} + \mathbf{Z}_0^{\mathrm{ref}}\right)^{-1}\sqrt{\mathbf{Z}_0^{\mathrm{ref}}}\mathbf{V}^{\mathrm{oc}}. \tag{5.42}$$

This demonstrates that the signal-wave vector $\mathbf{g}$ is related to the open-port voltages $\mathbf{V}^{\mathrm{oc}}$ as given by Eq. (5.42). As one can see, the antenna signal $\mathbf{g}$ is simply added to the reflected signal from the antenna and is independent on the load $\mathbf{Z}_L$; $\mathbf{g}$ is "driving" the beamformer.

In conclusion, once the field incident on the antenna array is known, the open-port voltages can be determined through EM-simulations after which the antenna array signal $\mathbf{g}$ can be computed from Eq. (5.42). Alternatively, it is possible to obtain the open-port voltages via the element patterns of the array antennas by using relationships obtained by reciprocity analysis as described in Section 2.5.

5.4   Noise Wave Characterization of the Receiver Components

Noise-wave correlation matrices for active and passive devices can be expressed in terms of their internal sources, or be re-expressed in terms of more commonly used noise parameters; most of these relations have been published in the literature and will be summarized here for completeness.

5.4.1   The Antenna Array Receive Voltages due to External Noise Sources

A Partially Polarized Galactic Source Distribution

Thus far, only monochromatic plane-wave fields have been considered, each of which has a deterministic amplitude and state of polarization. In particular, we considered in Section 2.5 the completely polarized plane wave $\boldsymbol{E}^i(\boldsymbol{r}) = \boldsymbol{E}_0 e^{j(\boldsymbol{k}_0 \cdot \boldsymbol{r})}$ to be incident on the antenna array from the direction $\hat{\boldsymbol{r}}_i$. Then, the mth open-circuit port voltage on receive is determined through the projection [*cf.* Eq. (2.54)]

$$V_m^{\text{oc}} = (j\omega\mu_0)^{-1}\boldsymbol{E}_0 \cdot \boldsymbol{e}_m^T(\hat{\boldsymbol{r}}_i) \tag{5.43}$$

where $\boldsymbol{E}_0$ defines the state of polarization of the incident electric field at the origin of the coordinate system, and $\boldsymbol{e}_m^T = 4\pi \exp{(jk_0)}\boldsymbol{E}_m^T$ is the mth normalized element far-field pattern on transmit with the distance r taken equal to unity in the far-field expression. This pattern arises if the mth element is excited by a current source of unit amplitude, while all other elements are open-circuited.

In radio astronomy, however, one observes distributed sources of a certain spatial extent. In the following, we let $\boldsymbol{E}_0(\theta, \phi)\,\mathrm{d}\Omega$ be the total amplitude polarization vector[3] from sources which subtend a solid angle $\mathrm{d}\Omega$ at the antenna in the direction defined by θ and ϕ. Thence, the mth open-circuit port voltage on receive is computed as [80, p. 115]

$$V_m^{\text{oc}} = \frac{1}{j\omega\mu_0} \iint\limits_{\mathcal{S}_\infty} \boldsymbol{E}_0(\Omega) \cdot \boldsymbol{e}_m^T(\Omega)\,\mathrm{d}\Omega \tag{5.44}$$

---

[3]Note that the unit of $\boldsymbol{E}_0$ has changed to Volt per meter per steradian.

where Ω is a short-hand notation for the (θ, ϕ) direction. Next, the mutual product $V_m^{\mathrm{oc}} (V_n^{\mathrm{oc}})^*$ is taken between the open-circuit output voltage of antennas m and n, i.e.,

$$V_m^{\mathrm{oc}} (V_n^{\mathrm{oc}})^* = \frac{1}{\omega^2 \mu_0^2} \iint_{\mathcal{S}_\infty} \iint_{\mathcal{S}_\infty} \left[\boldsymbol{E}_0(\Omega_1) \cdot \boldsymbol{e}_m^T(\Omega_1) \right] \left[\boldsymbol{E}_0(\Omega_2) \cdot \boldsymbol{e}_m^T(\Omega_2) \right]^* \mathrm{d}\Omega_1 \, \mathrm{d}\Omega_2. \quad (5.45)$$

The field vectors can be expressed in terms of spherical coordinates as $\boldsymbol{E}_0(\Omega) = E_\theta(\Omega)\hat{\boldsymbol{\theta}} + E_\phi(\Omega)\hat{\boldsymbol{\phi}}$ and $\boldsymbol{e}^T(\Omega) = e_\theta(\Omega)\hat{\boldsymbol{\theta}} + g_\phi(\Omega)\hat{\boldsymbol{\phi}}$, where $\hat{\boldsymbol{\theta}}$ and $\hat{\boldsymbol{\phi}}$ are the unit vectors of the spherical coordinate system. Then, Eq. (5.45) is written as

$$V_m^{\mathrm{oc}} (V_n^{\mathrm{oc}})^* = \frac{1}{\omega^2 \mu_0^2} \iint_{\mathcal{S}_\infty} \iint_{\mathcal{S}_\infty} \left[E_\theta(\Omega_1)e_{m,\theta}(\Omega_1) + E_\phi(\Omega_1)e_{m,\phi}(\Omega_1) \right]$$
$$\left[E_\theta^*(\Omega_2)e_{n,\theta}^*(\Omega_2) + E_\phi^*(\Omega_2)e_{n,\phi}^*(\Omega_2) \right] \mathrm{d}\Omega_1 \, \mathrm{d}\Omega_2. \quad (5.46)$$

Eq. (5.46) holds for completely polarized waves, whereas, in general, partially polarized waves are emitted by cosmic sources within a narrow frequency band. The exact polarization state $\boldsymbol{E}_0$ can only be determined in a statistical sense. As in Section 5.2, we are interested in the quantity $\mathbb{E}\left\{V_m^{\mathrm{oc}} (V_n^{\mathrm{oc}})^*\right\} = \overline{V_m^{\mathrm{oc}} (V_n^{\mathrm{oc}})^*}$ within a narrow frequency sub-band, where $\mathbb{E}\{\cdot\}$ denotes the statistical expectation, and the overbar time average. Applying this time averaging on (5.46), and interchanging the order of time averaging and integration over Ω_1 and Ω_2, changes (5.46) into

$$\overline{V_m^{\mathrm{oc}} (V_n^{\mathrm{oc}})^*} = \frac{1}{\omega^2 \mu_0^2} \iint_{\mathcal{S}_\infty} \iint_{\mathcal{S}_\infty} \mathrm{tr}\left\{ \boldsymbol{\Gamma}^{(1)} \boldsymbol{\Gamma}^{(2)} \right\} \mathrm{d}\Omega_1 \, \mathrm{d}\Omega_2 \quad (5.47)$$

where the $\mathrm{tr}\{\cdot\}$ operator takes the trace of the resultant matrix multiplication (sum of diagonal terms), and where the polarization coherence matrix $\boldsymbol{\Gamma}^{(1)}$ of the incident field is given as [80, p. 115]

$$\boldsymbol{\Gamma}^{(1)}(\Omega_1, \Omega_2) = \begin{pmatrix} \overline{E_\theta(\Omega_1) E_\theta^*(\Omega_2)} & \overline{E_\theta(\Omega_1) E_\phi^*(\Omega_2)} \\ \overline{E_\phi(\Omega_1) E_\theta^*(\Omega_2)} & \overline{E_\phi(\Omega_1) E_\phi^*(\Omega_2)} \end{pmatrix} \quad (5.48)$$

and the mutual coherence matrix $\boldsymbol{\Gamma}^{(2)}$ of the antenna pair as

$$\boldsymbol{\Gamma}^{(2)}(\Omega_1, \Omega_2) = \begin{pmatrix} e_{m,\theta}(\Omega_1)e_{n,\theta}^*(\Omega_2) & e_{m,\theta}(\Omega_1)e_{n,\phi}^*(\Omega_2) \\ e_{m,\phi}(\Omega_1)e_{n,\theta}^*(\Omega_2) & e_{m,\phi}(\Omega_1)e_{n,\phi}^*(\Omega_2) \end{pmatrix}. \quad (5.49)$$

In most cases of practical interest there is no correlation between the radiation incident from the two directions Ω_1 and Ω_2, except when $\Omega_1 = \Omega_2 = \Omega$. Under these conditions, the mutual coherence matrix $\boldsymbol{\Gamma}^{(1)}$ reduces to the coherence matrix $\boldsymbol{J}^{(1)}$. Substituting

$\mathbf{\Gamma}^{(1)}(\Omega_1, \Omega_2) = \mathbf{J}^{(1)}(\Omega)\delta(\Omega_1 - \Omega_2)$ in (5.47), and making use of the sifting property of the delta distribution function, yields [80, p. 116]

$$\overline{V_m^{\mathrm{oc}}\,(V_n^{\mathrm{oc}})^*} = \frac{1}{\omega^2\mu_0^2} \iint\limits_{\mathcal{S}_\infty} \mathrm{tr}\left\{\mathbf{J}^{(1)}\mathbf{J}^{(2)}\right\}\,\mathrm{d}\Omega \tag{5.50}$$

where the coherence matrix of the incident electric field $\boldsymbol{E}_0$ is given as

$$\mathbf{J}^{(1)}(\Omega) = \begin{pmatrix} \overline{|E_\theta(\Omega)|^2} & \overline{E_\theta(\Omega)E_\phi^*(\Omega)} \\ \overline{E_\phi(\Omega)E_\theta^*(\Omega)} & \overline{|E_\phi(\Omega)|^2} \end{pmatrix} \tag{5.51}$$

and, due to the sifting property, the mutual coherence matrix of the antenna reduces to

$$\mathbf{J}^{(2)}(\Omega) = \begin{pmatrix} e_{m,\theta}(\Omega)e_{n,\theta}^*(\Omega) & e_{m,\theta}(\Omega)e_{n,\phi}^*(\Omega) \\ e_{m,\phi}(\Omega)e_{n,\theta}^*(\Omega) & e_{m,\phi}(\Omega)e_{n,\phi}^*(\Omega) \end{pmatrix}. \tag{5.52}$$

In the above analysis we assumed that the averaging is performed over an infinitely long period of time. In practice, however, the integration time is limited and the accuracy of the measurement is inversely proportional to the square root of the integration time [3, p. 3-44].

Once the polarization characteristics of the incident field are known, Eq. (5.50) can be used to construct the voltage correlation matrix

$$\mathbf{V} = \overline{\mathbf{V}^{\mathrm{oc}}\,(\mathbf{V}^{\mathrm{oc}})^H} = \begin{pmatrix} \overline{|V_1^{\mathrm{oc}}|^2} & \overline{V_1^{\mathrm{oc}}\,(V_2^{\mathrm{oc}})^*} & \cdots & \overline{V_1\,(V_M^{\mathrm{oc}})^*} \\ \overline{V_2\,(V_1^{\mathrm{oc}})^*} & \overline{|V_2^{\mathrm{oc}}|^2} & \cdots & \overline{V_2^{\mathrm{oc}}\,(V_M^{\mathrm{oc}})^*} \\ \vdots & \vdots & \ddots & \vdots \\ \overline{V_M^{\mathrm{oc}}\,(V_1^{\mathrm{oc}})^*} & \overline{V_M^{\mathrm{oc}}\,(V_2^{\mathrm{oc}})^*} & \cdots & \overline{|V_M^{\mathrm{oc}}|^2} \end{pmatrix} \tag{5.53}$$

where $\mathbf{V}^{\mathrm{oc}} = [V_1^{\mathrm{oc}}, \ldots, V_M^{\mathrm{oc}}]^T$ is the vector holding the complex-valued voltage amplitudes on receive.

In practical surveys, one measures $\mathbf{V}$ (usually at the output of an amplifying circuit), with the intention to recover the polarization information of the incident field (inverse problem). Consider an x- and y-oriented element with corresponding far-field patterns $\boldsymbol{e}^{\mathrm{co}}(\Omega)$ and $\boldsymbol{e}^{\mathrm{cross}}(\Omega)$, respectively. Then, for a deterministic polarization vector $\boldsymbol{E}_0$ of the incident field, the deterministic receive voltage vector $\mathbf{V}^{\mathrm{oc}} = [V_x^{\mathrm{oc}}, V_y^{\mathrm{oc}}]^T$ can be computed through a matrix-vector product as $\mathbf{V}^{\mathrm{oc}} = \mathbf{J}_0\boldsymbol{E}_0$, where $\mathbf{J}_0 = (j\omega\mu_0)^{-1}[\boldsymbol{e}^{\mathrm{co}}(\Omega)\,|\,\boldsymbol{e}^{\mathrm{cross}}(\Omega)]^T$ is the column-augmented E-Jones matrix of the mutual orthogonally-oriented antenna

pair [149]. With the above definitions, the 2×2 voltage-correlation matrix $\mathbf{V}$ can be determined directly, i.e.,

$$\mathbf{V} = \overline{\mathbf{V}^{\mathrm{oc}} \, (\mathbf{V}^{\mathrm{oc}})^H} = \iint\limits_{\mathcal{S}_\infty} \mathbf{J}_0 \mathbf{J}^{(2)} \mathbf{J}_0^H \, \mathrm{d}\Omega \tag{5.54}$$

where we used that

$$\overline{\mathbf{V}^{\mathrm{oc}} \, (\mathbf{V}^{\mathrm{oc}})^H} = \overline{\mathbf{J}_0 \boldsymbol{E}_0 \, (\mathbf{J}_0 \boldsymbol{E}_0)^H} = \mathbf{J}_0 \overline{\boldsymbol{E}_0 \boldsymbol{E}_0^H} \mathbf{J}_0^H = \mathbf{J}_0 \mathbf{J}^{(2)} \mathbf{J}_0^H. \tag{5.55}$$

In beamformed arrays, there are many x- and y-oriented elements, which can be combined into the two beams $\boldsymbol{e}^{\mathrm{co}}(\Omega, \Omega_0)$ and $\boldsymbol{e}^{\mathrm{cross}}(\Omega, \Omega_0)$, respectively. Here, Ω_0 denotes the scan direction of the beams. For large arrays, the beam width is small, so that the integral in (5.54) does not need to be carried out over the entire galactic plane. To first order, one therefore has that $\mathbf{V}(\Omega_0) = \mathbf{J}_0(\Omega_0)\mathbf{J}^{(2)}(\Omega_0)\mathbf{J}_0^H(\Omega_0)$ for a certain scan angle Ω_0. In order to recover the polarization information of the source, i.e., $\mathbf{J}^{(2)}(\Omega_0)$, it is crucial to know the beam patterns of the array, i.e., the E-Jones matrix $\mathbf{J}_0(\Omega_0)$. Basis functions for the patterns are employed to model the matrix $\mathbf{J}_0(\Omega_0)$, whose unknown parameters are determined by measuring a number of known sources. Once the model parameters are determined (calibration), the models are used to predict the beam behavior in other directions, and because $\mathbf{V}(\Omega_0)$ is measured, while $\mathbf{J}_0(\Omega_0)$ is modeled, the polarization information $\mathbf{J}^{(2)}(\Omega_0)$ can be recovered through inversion, provided that the condition number of $\mathbf{J}_0 = (j\omega\mu_0)^{-1}[\boldsymbol{e}^{\mathrm{co}}(\Omega) \,|\, \boldsymbol{e}^{\mathrm{cross}}(\Omega)]^T$ is sufficiently small. To measure the degree of independency of the columns of $\mathbf{J}_0$, we introduced a cross-correlation term in (4.50) to quantify the beam orthogonality between $\boldsymbol{e}^{\mathrm{co}}$ and $\boldsymbol{e}^{\mathrm{cross}}$.

A Non-Uniform Brightness Temperature Distribution

We will consider randomly polarized waves, for which there is zero correlation between the electrical field components θ and ϕ of the incident field. Then, the coherence matrix, Eq. (5.51), of the incident radiation (noise field), reduces to

$$\mathbf{J}^{(1)}(\Omega) = \begin{pmatrix} \overline{|E_\theta(\Omega)|^2} & 0 \\ 0 & \overline{|E_\phi(\Omega)|^2} \end{pmatrix}. \tag{5.56}$$

Consequently, Eq. (5.50) simplifies to

$$\overline{V_m^{\mathrm{oc}} \, (V_n^{\mathrm{oc}})^*} = \frac{1}{\omega^2 \mu_0^2} \iint\limits_{\mathcal{S}_\infty} \left\{ \overline{|E_\theta(\Omega)|^2} e_{m,\theta}(\Omega) e_{n,\theta}^*(\Omega) + \overline{|E_\phi(\Omega)|^2} e_{m,\phi}(\Omega) e_{n,\phi}^*(\Omega) \right\} \mathrm{d}\Omega. \tag{5.57}$$

Because we are dealing with randomly polarized incident fields, the power is equally distributed in both polarizations, so that $\overline{|E_\theta(\Omega)|^2} = \overline{|E_\phi(\Omega)|^2} = P(\Omega)/2$, where $P(\Omega)$ is the total expected incident noise power coming from the direction Ω. Accordingly, (5.57) is written as

$$
\begin{aligned}
\overline{V_m^{\mathrm{oc}} (V_n^{\mathrm{oc}})^*} &= \frac{1}{2\omega^2\mu_0^2} \iint_{\mathcal{S}_\infty} P(\Omega) \left[e_{m,\theta}(\Omega)e_{n,\theta}^*(\Omega) + e_{m,\phi}(\Omega)e_{n,\phi}^*(\Omega) \right] \, \mathrm{d}\Omega \\
&= \frac{1}{2\omega^2\mu_0^2} \iint_{\mathcal{S}_\infty} P(\Omega) \left[\boldsymbol{e}_m(\Omega) \cdot \boldsymbol{e}_n^*(\Omega) \right] \, \mathrm{d}\Omega
\end{aligned}
\tag{5.58}
$$

which is a similar equation as presented in [150], although not derived therein.

Next, we seek an expression for $P(\Omega)$. To this end, the incident noise power is related to the spatial noise-temperature distribution of the sky. The power per unit area and per unit solid angle, which is incident on the element within a solid angle $\mathrm{d}\Omega$, is given by $\mathbb{E}\left\{\boldsymbol{E}_0 \cdot \boldsymbol{E}_0^*\right\}/2Z_0$ in watts per square meter per steradian, where Z_0 is the free-space impedance. This incident power has a spectral width $\mathrm{d}f$. The incident power per unit area and per unit solid angle in a unit frequency interval is called the brightness B of the noise source in the sky [80, p. 117]. Hence,

$$
B(\theta, \phi) \, \mathrm{d}f = \frac{\mathbb{E}\left\{\boldsymbol{E}_0 \cdot \boldsymbol{E}_0^*\right\}}{2Z_0}.
\tag{5.59}
$$

The randomly polarized space waves are assumed to be radiated by a black body (cosmic background radiation). The intensity of the black-body radiation is described over frequency by Plancks' law. However, at microwave frequencies, the Rayleigh-Jeans approximation of Plancks' law can be used which, for a single-sided spectrum, reads (*cf.* [3, p. 3-40], or [151, p. 4.14])

$$
B(\theta, \phi) = \frac{2k_B f^2}{c_0^2} T_{\mathrm{sky}}(\theta, \phi) \quad [\mathrm{W/m^2} \text{ per steradian and per Hertz}]
\tag{5.60}
$$

where $k_B = 1.380 \times 10^{-23}$ J/K (Boltzmann's constant), c_0 is the speed of light, f the frequency and T_{sky} the equivalent noise temperature of the sky. An expression for T_{sky} can be found in [152]. Combining (5.59) and (5.60), yields

$$
\mathbb{E}\left\{\boldsymbol{E}_0 \cdot \boldsymbol{E}_0^*\right\} = P(\theta, \phi) = 4k_B T_{\mathrm{sky}}(\theta, \phi) Z_0 \frac{f^2}{c_0^2} \, \mathrm{d}f.
\tag{5.61}
$$

The substitution of (5.61) in (5.58) gives us the antenna open-port voltage-correlation

elements, i.e.,

$$
\begin{aligned}
\overline{V_m^{\mathrm{oc}}\,(V_n^{\mathrm{oc}})^*} &= \frac{2k_B Z_0 f^2\,\mathrm{d}f}{\omega^2 \mu_0^2 c_0^2} \iint\limits_{\mathcal{S}_\infty} T_{\mathrm{sky}}(\theta,\phi)\left[\boldsymbol{e}_m(\theta,\phi)\cdot \boldsymbol{e}_n^*(\theta,\phi)\right]\sin\theta\,\mathrm{d}\theta\,\mathrm{d}\phi \\
&= \frac{k_B\,\mathrm{d}f}{2\pi^2 Z_0} \iint\limits_{\mathcal{S}_\infty} T_{\mathrm{sky}}(\theta,\phi)\left[\boldsymbol{e}_m(\theta,\phi)\cdot \boldsymbol{e}_n^*(\theta,\phi)\right]\sin\theta\,\mathrm{d}\theta\,\mathrm{d}\phi.
\end{aligned}
\tag{5.62}
$$

From (5.62), the elements of the voltage correlation matrix $\mathbf{V}$ in (5.53) can be readily computed. The above voltage-correlation matrix for an antenna array is a function of the element patterns and the spatial temperature distribution of the sky. To transform this correlation matrix to the antenna noise wave correlation matrix $\mathbf{C}^A$, the following transformation is used:

$$
\mathbf{C}^A = \mathbf{L}\mathbf{V}\mathbf{L}^H
\tag{5.63}
$$

where [*cf.* Eq. (5.42)]

$$
\mathbf{L} = \sqrt{Z_0^{\mathrm{ref}}}\left(\mathbf{Z}^{\mathrm{ant}} + Z_0^{\mathrm{ref}}\mathbf{I}\right)^{-1}
\tag{5.64}
$$

and where $\mathbf{Z}^{\mathrm{ant}}$ is the impedance matrix of the antenna and Z_0^{ref} is a real-valued normalization constant. Eqs. (5.62)–(5.64) define the antenna-noise wave correlation matrix $\mathbf{C}^A$, which is needed for determining the overall noise-wave correlation matrix of the receiving system.

5.4.2 Active Components

For active two-port devices, it is possible to express the entries of the noise-wave correlation matrix in terms of the more commonly used noise parameters: the minimum noise temperature $T_{\min}$, the optimum noise reflection coefficient Γ_{opt}, and the equivalent noise resistance R_n (see e.g. [153]). Then,

$$
\overline{|c_1|^2} = kT_{\min}(|s_{11}|^2 - 1) + \frac{kT|1 - s_{11}\Gamma_{\mathrm{opt}}|^2}{|1 + \Gamma_{\mathrm{opt}}|^2},
\tag{5.65a}
$$

$$
\overline{|c_2|^2} = |s_{21}|^2\left(kT_{\min} + \frac{kT|\Gamma_{\mathrm{opt}}|^2}{|1 + \Gamma_{\mathrm{opt}}|^2}\right),
\tag{5.65b}
$$

$$
\overline{c_1 c_2^*} = \frac{-s_{21}^*\Gamma_{\mathrm{opt}}^* kT}{|1 + \Gamma_{\mathrm{opt}}|^2} + \frac{s_{11}}{s_{21}}\overline{|c_2|^2},
\tag{5.65c}
$$

where kT is the normalized temperature-energy given by

$$kT = \frac{4k_B T_0 R_n}{Z_0^{\text{ref}}}. \tag{5.66}$$

The normalization impedance is denoted by Z_0^{ref}, k_B is Boltzmann's constant and T_0 (290 K) is the reference temperature.

5.4.3   Passive Components

The spectral noise-wave correlation matrix for passive linear microwave devices, having a uniform temperature T_a, is computed by Bosma's theorem as [154]

$$\mathbf{C} = k_B T_a \left[\mathbf{I} - \mathbf{S}\mathbf{S}^H \right], \tag{5.67}$$

where $\mathbf{S}$ is the scattering matrix of the passive device and $\mathbf{I}$ is the identity matrix.

5.4.4   Linear Connection Matrix Theory

Once the scattering and noise-wave correlation matrices are defined for all microwave components, and when the incident source field is specified, the overall receiver sensitivity can be computed with the aid of the analytical formulas that have been developed in Section 5.3 (based on [139]). Alternatively, one could utilize the connection matrix theory as described in [142], which is a numerical approach. Then, the scattering matrix $\mathbf{S}$ of the total circuit is partitioned into submatrices associated with the internal and external ports, i.e.,

$$\begin{pmatrix} \mathbf{b}_e \\ \mathbf{b}_i \end{pmatrix} = \begin{pmatrix} \mathbf{S}_{ee} & \mathbf{S}_{ei} \\ \mathbf{S}_{ie} & \mathbf{S}_{ii} \end{pmatrix} \begin{pmatrix} \mathbf{a}_e \\ \mathbf{a}_i \end{pmatrix} + \begin{pmatrix} \mathbf{c}_e \\ \mathbf{c}_i \end{pmatrix}, \tag{5.68}$$

where $\mathbf{b}_e$ and $\mathbf{b}_i$ are the external and internal outgoing circuit waves, and $\mathbf{c}_e$ and $\mathbf{c}_i$ are the external and internal noise (or signal) waves, respectively. The connections of pairs of internal ports are imposed by $\mathbf{b}_i = \mathbf{\Gamma}_i \mathbf{a}_i$, where $\mathbf{\Gamma}_i$ is the connection matrix. It can be shown that, when the receiver outputs are terminated characteristically ($\mathbf{a}_e = \mathbf{0}$), the overall outgoing wave vector $\mathbf{b}_e$ can be computed as

$$\mathbf{b}_e = \left[\mathbf{I} | \mathbf{S}_{ei} (\mathbf{\Gamma}_i - \mathbf{S}_{ii})^{-1} \right] \begin{pmatrix} \mathbf{c}_e \\ \mathbf{c}_i \end{pmatrix} = \mathbf{T} \begin{pmatrix} \mathbf{c}_e \\ \mathbf{c}_i \end{pmatrix}, \tag{5.69}$$

where $[\mathbf{A}|\mathbf{B}]$ denotes a compound matrix, which is formed by augmenting the columns of $\mathbf{A}$ by the columns of $\mathbf{B}$, and where the transfer matrix $\mathbf{T} = [\mathbf{I}|\mathbf{S}_{ei}(\mathbf{\Gamma}_i - \mathbf{S}_{ii})^{-1}]$. The overall noise-wave correlation matrix $\mathbf{C}^o = \mathbf{b}_e\mathbf{b}_e^H$ is then computed as

$$\mathbf{C}^o = \mathbf{T} \left(\begin{array}{cc} \overline{\mathbf{c}_e\mathbf{c}_e^H} & \overline{\mathbf{c}_e\mathbf{c}_i^H} \\ \overline{\mathbf{c}_i\mathbf{c}_e^H} & \overline{\mathbf{c}_i\mathbf{c}_i^H} \end{array} \right) \mathbf{T}^H = \mathbf{T}\mathbf{C}\mathbf{T}^H, \tag{5.70}$$

where $\mathbf{C}$ is the block partitioned noise-wave correlation matrix containing the noise-wave correlation matrices of each of the microwave devices. The receiver sensitivity S_m/N_m at output m is then computed from (5.69) and (5.70), i.e.,

$$\frac{S_m}{N_m} = \frac{|b_{e,m}|^2}{C_{mm}^{\mathrm{net}}}. \tag{5.71}$$

5.4.5   Numerical Results for a Practical Noise Measurement

A 4×1 monopole array has been designed and fabricated as shown in Fig. 5.4 (see also Section 3.6.5). The beamforming network consists of two LNAs, two dummy loaded antenna elements, coaxial cables, a Wilkinson power combiner, an additional amplifier and a tunable band-pass filter. The scattering and noise-wave correlation matrices of all these microwave devices have been obtained through measurements and/or simulations [155]. In addition to the modeled antenna characteristics in Section 3.6.5, the modeled noise and scatter parameters of the LNAs are also in very good agreement as reported in [155]. The receiver system was measured above a reflector surface to shield RFI sources and a tunable band-pass filter was used to limit the bandwidth of the received frequency spectrum. Despite these measures, RFI sources were observed appearing in the band of the cell phones that operate from 876–960 MHz. A noisy "hot" sky was simulated by placing an absorber with a noise temperature of 280 K (ambient temperature was 7 ^{o}C) at the antenna aperture with minimal impact on the antenna impedance characteristics. Clearly, the RFI sources were suppressed while the absolute noise-power level at the receiver output increased as correctly predicted by the simulations in a quantitative manner.
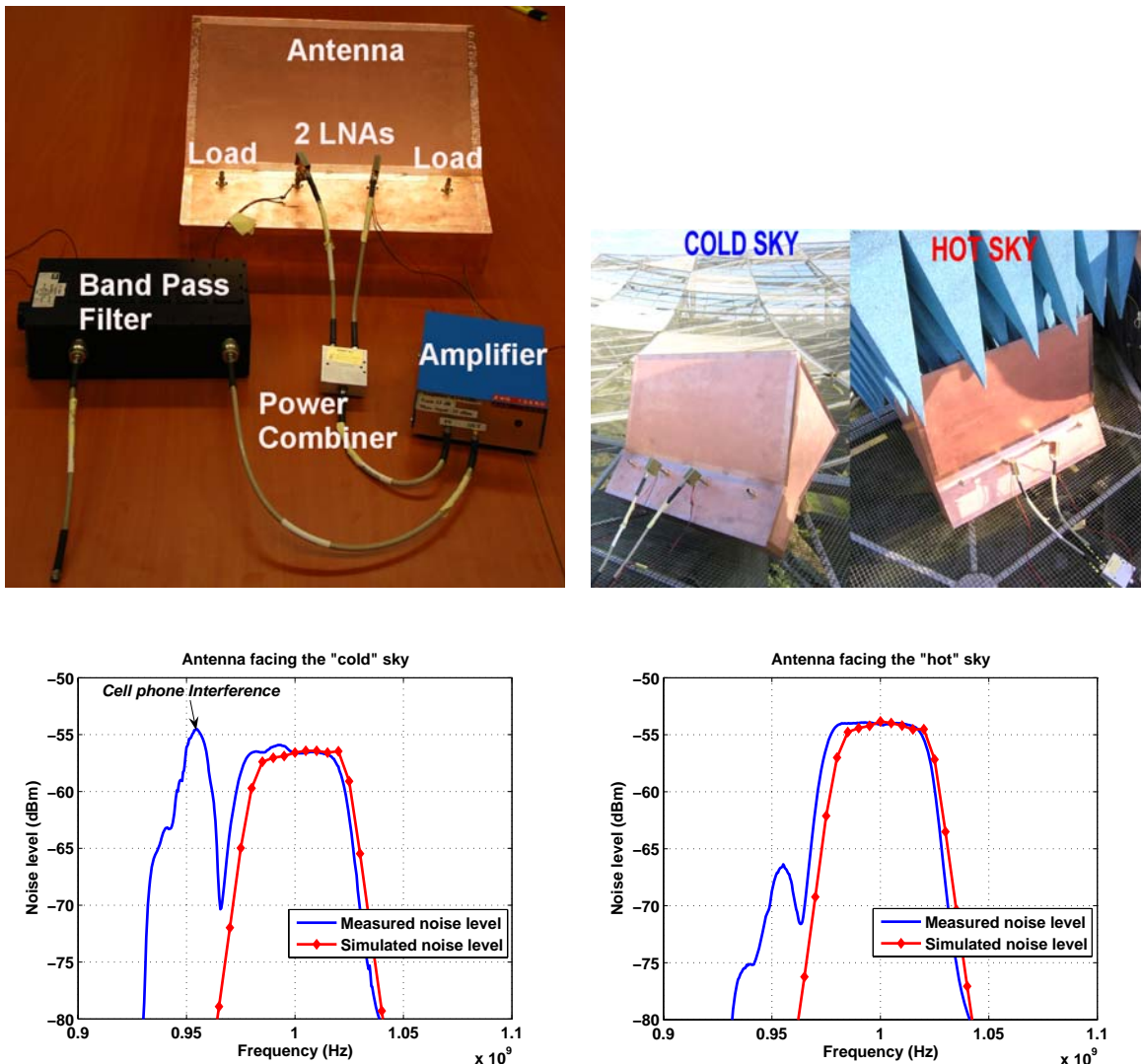
Figure 5.4: The scatter and noise properties of all microwave devices have been character-
ized by measurements and simulations [155]. The measured output noise power levels for
the "hot" and "cold" sky agree well with the predicted output power levels.

5.5   Role of the Scan Impedance in Noise Coupling

In this section it is demonstrated that the active instead of the passive antenna reflection
coefficient is the key parameter in realizing low-noise receiver designs. This is an important
statement, which has currently been brought into practice by designing dedicated low-noise
receivers for radio astronomical applications [18]. From our experience, this noise match

condition is not yet commonly known among a large scientific audience. In fact, at a first glance, one might aim to noise-match the Low Noise Amplifiers (LNAs) to the passive antenna input impedance. As we know for conventional single-chain antenna receivers, consisting of only one antenna element and one LNA, this noise-match condition will lead to the lowest receiver noise temperature. However, as will be shown, higher receiver sensitivity for array systems can be reached by noise matching the LNA to the active scan impedance of the corresponding array element. This will be demonstrated for two cases. First, an idealized and abstract example is used to visualize the underlying phenomena and to gain basic insight. Second, numerical results are discussed for a two-element dipole array to confirm the validity of this concept.

5.5.1 Idealized Phased Array Receiver Model

Fig. 5.5(a) illustrates a schematic of an idealized two-element phased array receiver.
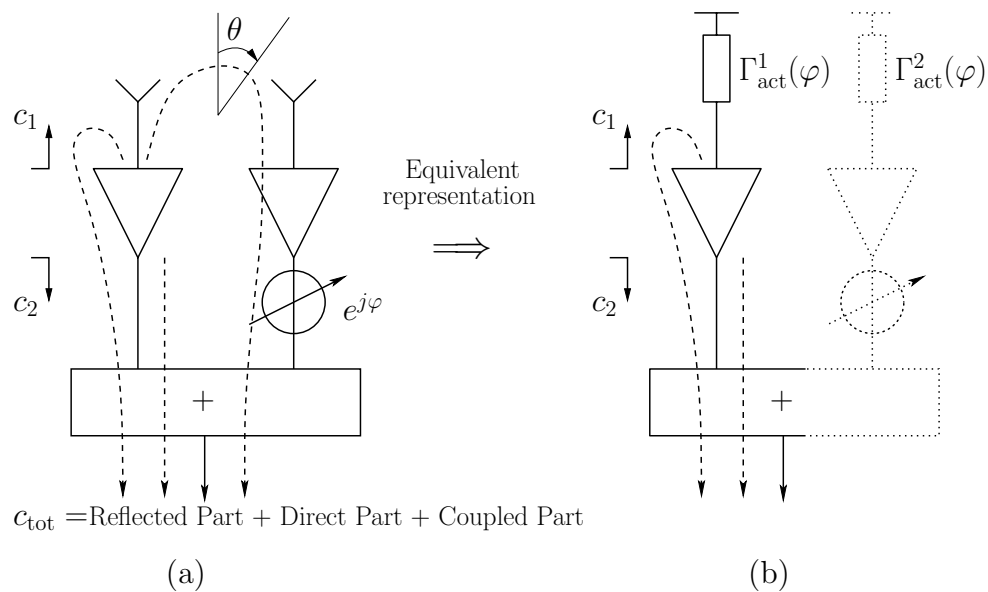
Figure 5.5: (a) Propagation paths of noise waves c_1 and c_2 that emanate from the input and output of the LNA, respectively. (b) Equivalent representation for the noise-wave propagation involving active reflection coefficients of antenna elements.

The receiver system in Fig. (5.5)(a) is considered to be noise-free except for the LNAs.

The beam is electronically steered by adjusting the phase φ. For the sake of simplicity, we consider the noise contribution of only one LNA, since no correlation exists between the noisy LNAs. Further, we assume that $S_{11}^{\text{LNA}} = 0$ and that the LNAs are identical. Otherwise, if $S_{11}^{\text{LNA}} \neq 0$, the (complex) reference impedance has to be adjusted such that S_{11}^{LNA} becomes 0. The same reference impedance is used for all S-matrices. The correlated noise waves that emanate from the input and output of the LNA are denoted by c_1 and c_2, respectively [153]. Fig. (5.5)(a) illustrates that, in case of an ideal combiner, the total outgoing noise wave c_{tot} is a superposition of three noise-wave contributions, i.e.,

$$
\begin{aligned}
c_{\text{tot}} &= \text{Direct Part} + \text{Reflected Part} + \text{Coupled Part} \\
&= c_2 + c_1 S_{11}^{\text{ant}} S_{21}^{\text{LNA}} + c_1 S_{21}^{\text{ant}} S_{21}^{\text{LNA}} e^{j\varphi} \\
&= c_2 + c_1 S_{21}^{\text{LNA}} \left(S_{11}^{\text{ant}} + S_{21}^{\text{ant}} e^{j\varphi} \right) \\
&= c_2 + c_1 S_{21}^{\text{LNA}} \Gamma_{\text{act}}^1(\varphi),
\end{aligned}
\tag{5.72}
$$

where we used that $\Gamma_{\text{act}}^1(\varphi) = S_{11}^{\text{ant}} + S_{21}^{\text{ant}} e^{j\varphi}$, i.e., the active reflection coefficient of the first antenna element. A similar expression can be derived for the second receiver channel where, $\Gamma_{\text{act}}^2(\varphi) = S_{22}^{\text{ant}} + S_{12}^{\text{ant}} e^{-j\varphi}$.

The result of (5.72) can be interpreted as having an equivalent array representation that is shown in Fig. 5.5(b) consisting of two "decoupled" receiver channels. Essentially, the full antenna S-parameter matrix is replaced by a diagonal matrix where the entries on the diagonal are given by the active reflection coefficients of the individual array elements. For this system, the total receiver temperature is minimized if the noise contribution for each receiver channel is minimized. The noise-match condition for a single receiver channel is straightforward as shown in Fig. (5.6).

$$
T_{\text{LNA}} = T_{\text{min}} + \frac{4 T_0 R_n}{Z_0} \frac{|\Gamma_s - \Gamma_{\text{opt}}|^2}{|1 + \Gamma_{\text{opt}}|^2 (1 - |\Gamma_s|^2)}
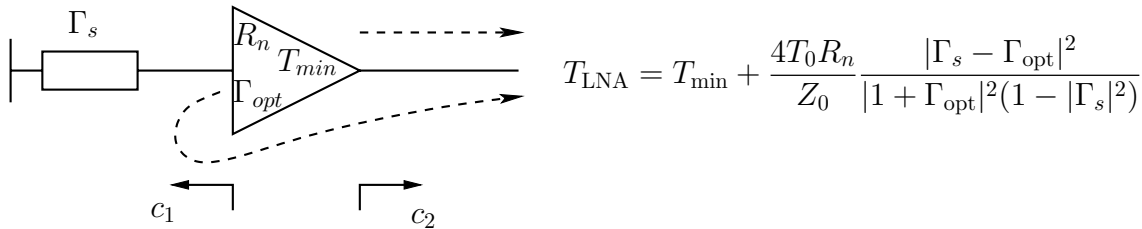$$

Figure 5.6: Equivalent noise temperature of LNA, given a source reflection coefficient.

One can noise match the LNA to the source impedance by requiring that the noise parameter Γ_{opt} of the LNA equals the source reflection coefficient Γ_s, so that $T_{\text{LNA}} = T_{\text{min}}$. This

leads to the conclusion that, for the single receiver channel of Fig. 5.5(b), noise match for the first channel is achieved if $\Gamma_{\mathrm{opt}}^1 = \Gamma_s^1 = \Gamma_{\mathrm{act}}^1(\varphi)$. This condition is also valid for the second channel, even though $\Gamma_{\mathrm{act}}^1(\varphi) \neq \Gamma_{\mathrm{act}}^2(\varphi)$ if $\varphi \neq 0$.

5.5.2 Numerical Results for a Two-Element Array

To demonstrate the validity of this noise matching condition, the numerical tool has been used, which is outlined in the previous sections and based on the Method of Moments (MoM) for modeling antenna structures, combined with scattering matrices and noise-wave correlation matrices for modeling microwave circuits [85]. The two-element dipole array of Fig 5.5(a) is the subject of investigation with electrical antenna dimensions as shown in Table 5.1.

Table 5.1: Electrical Antenna Dimensions and computed S-parameters for 50 Ω.

Parameter	Value
Dipole length	$0.45\lambda_0$
Dipole width	$0.015\lambda_0$
Dipole to gndplane spacing	$0.225\lambda_0$
Element separation distance	$0.465\lambda_0$
Groundplane size	$3\lambda_0 \times 3\lambda_0$

$\rightarrow$

Parameter	Value
S_{11}^{ant}	0.166 - 0.123j
S_{12}^{ant}	0.272 + 0.219j
S_{21}^{ant}	0.272 + 0.219j
S_{22}^{ant}	0.166 - 0.123j

The following parameters are assumed to be identical for both LNAs: $s_{11}^{\mathrm{LNA}} = s_{12}^{\mathrm{LNA}} = s_{22}^{\mathrm{LNA}} = 0$, $s_{21}^{\mathrm{LNA}} = 10$, $T_{\mathrm{min}} = 100$ K and $R_n/Z_0^{\mathrm{ref}} = 0.5$. Next, we satisfy the noise-matching condition by setting $\Gamma_{\mathrm{opt}}^1 = \Gamma_{\mathrm{act}}^1(\varphi)$ and $\Gamma_{\mathrm{opt}}^2 = \Gamma_{\mathrm{act}}^2(\varphi)$ to minimize the receiver noise temperature T_{rec}. As $\Gamma_{\mathrm{act}}^{1,2}$ changes as a function of φ, noise match can be realized for only one value of φ, thus for one particular scan angle. Also, if $\Gamma_{\mathrm{act}}^1 \neq \Gamma_{\mathrm{act}}^2$ two different LNAs have to be used with different $\Gamma_{\mathrm{opt}}^{1,2}$. Fig. 5.7a visualizes the change of Γ_{act}^1 and Γ_{act}^2 over scan angle. It is observed that Γ_{act}^1 and Γ_{act}^2 are different and describe a circle in the Smith chart for which the return loss value is the exact center.

Next, four scan directions are considered for which we aim to achieve noise match, i.e., at $\theta = \theta_0$ for $\theta_0 = 0^0, 30^0, 60^0$ and 90^0. To this end, 4 sets of LNAs are used with different
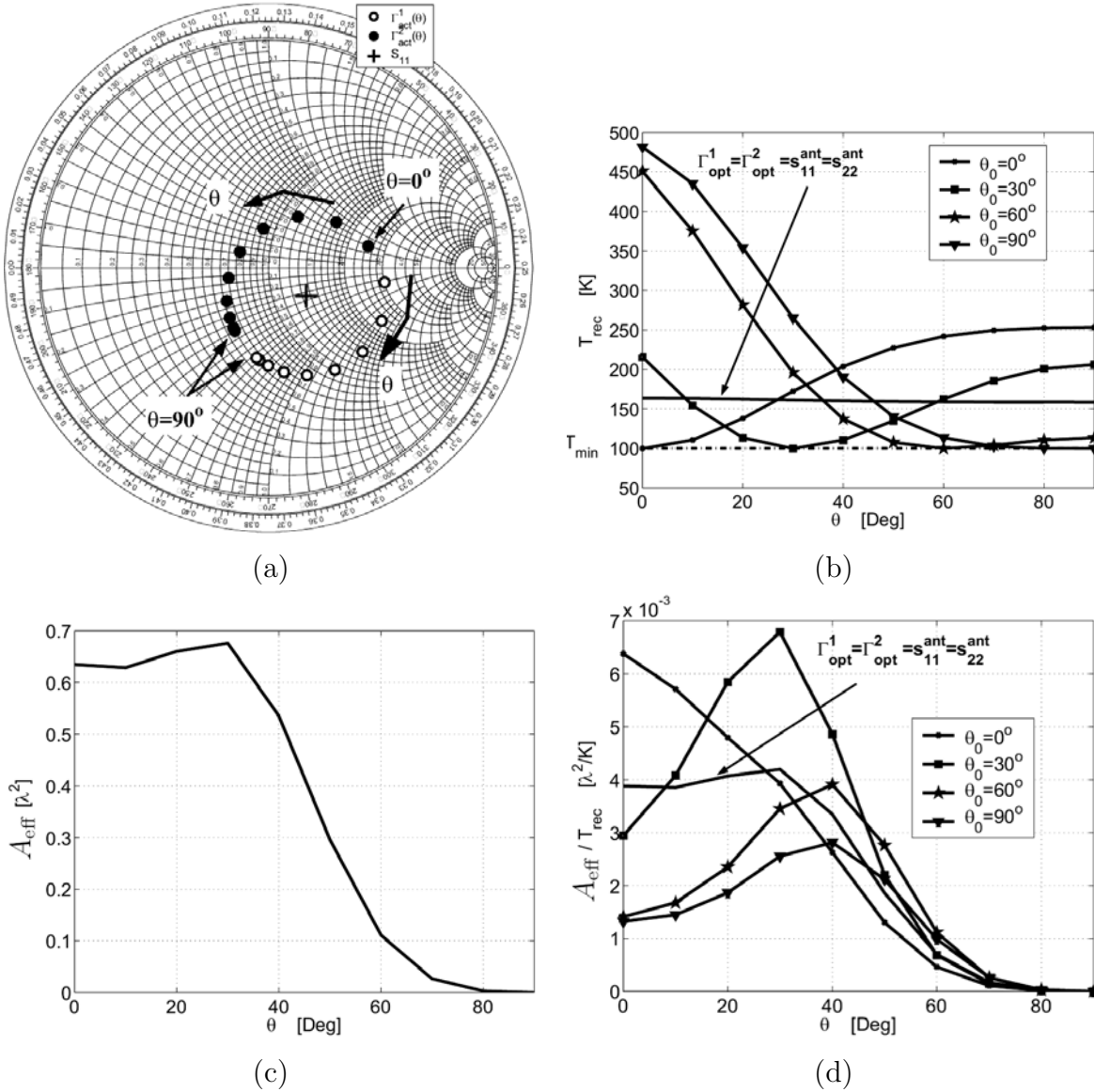
(a)

(b)

(c)

(d)

Figure 5.7: (a) The active and passive antenna impedances normalized to 50 Ω and visualized in a Smith chart. (b) The receiver noise temperature as a function of scan angle θ, optimized for four values of θ_0. (c) The effective area A_{eff} as a function of scan angle θ. (d) The receiver sensitivity as a function of scan angle θ, with noise matching for four values of θ_0.

Γ_{opt} values. For each case, Fig. 5.7(b) shows how the receiver input noise temperature varies over scan angle. As can be seen, the system noise temperature is minimized ($T_{\text{rec}} = T_{\text{min}} = 100$ K) for the scan direction at which noise match is achieved. The effective area A_{eff} is shown in Fig. 5.7(c) and does not depend on the noise properties of the LNAs (reference plane is at the input of the receiver system). The receiver sensitivity, defined by the ratio between the effective area and the receiver noise temperature, is shown in Fig. 5.7(d). As demonstrated, if noise match is achieved for a particular scan angle, the receiver sensitivity is highest for that particular scan angle. To observe this, consider a vertical cut in Fig. 5.7(d) for the optimized scan angle and note that the ensemble maximum is reached, even though the overall maximum sensitivity may occur at a different scan angle. Obviously, this noise match condition does not guarantee that the receiver sensitivity is always lower for other scan angles. In fact, this depends on the behavior of the effective area $A_{\text{eff}}(\theta)$ as a function of the scan angle.

It is also observed that a reasonably high sensitivity over a large scan volume is achieved by noise matching to the passive antenna reflection coefficient S_{11}^{ant}, S_{22}^{ant}, whereas a higher sensitivity can be reached for a slightly smaller scan volume if we noise match each LNA to the active reflection coefficient of the corresponding antenna element. For this particular example, and depending on the design requirements, we could choose to noise match for $\theta = 30^0$ in order to obtain a large receiver sensitivity over a large scan volume.

5.6   An Equivalent Single-Channel Receiver Modeling Approach

The "noise decoupling" of receiver channels, which has been described in the previous section for a two-element receiving system, can be generalized and be used to simplify the sensitivity analysis of array receiver systems comprised of N strongly coupled antenna elements. This "noise-decoupling technique" allows us to represent an antenna array receiver by an equivalent single-channel receiver model and to develop expressions for the beam sensitivity of the receiver. In the present approach, we focus on Focal Plane Array (FPA) receiving systems and account for the strong effects of noise coupling that such systems may exhibit. We remark that noise-coupling effects have been accounted for previously in various different antenna models [46, 148, 156]. However, we employ the recently intro-

duced coupling efficiency [157, 158] and factorize it to separately account for the losses due to dissipation and impedance mismatch effects of the equivalent antenna.

Essentially, the coupling efficiency is expressed as a product of the standard IEEE definitions termed: the "radiation efficiency"; and "impedance mismatch factor" [159]. These definitions are commonly applied to single-port antennas, whereas we will evaluate these definitions for the array case with a specific beam excitation. The "impedance mismatch factor" is herein called "mismatch efficiency" since it will be used in a chain of subefficiencies whose product is the total efficiency.

Furthermore, we combine the above mentioned efficiencies with the noise temperature models of multi-channel receiving systems that were proposed in [160] and extended in [161, 162] (and Section 5.5) for phased-array receivers with noise coupling effects. In addition, we will recall the standard definitions for the aperture efficiency and spillover noise temperature so as to complement the set of developed model parameters in the expression for the sensitivity.

It will be demonstrated that the results obtained by the pertaining model are consistent with the results computed by the CAESAR software (see Appendix F and [85, 163]), which is a tool that can be used to compute the receiver noise and sensitivity of a complex array system in a direct numerical manner. This numerical analysis is based on a signal-noise wave covariance approach and the connection matrix theory as explained in Section 5.4. Both methods can be used to analyze and design antenna receiving systems, albeit that the full numerical approach is more general, while the semi-analytical approach may provide a deeper insight.

5.6.1   An S-parameter model of a typical FPA receiving system

We consider a typical FPA case (Fig. 5.8), where a group of array elements is used to provide the desired illumination of the reflector, and where the remaining array elements are resistively terminated by loads at ambient temperature T_{amb}. Furthermore, the beamformer is comprised of (i) identical Low Noise Amplifiers (LNAs) that generate noise from their in- and outputs and (ii) complex weight devices (vector modulators) in combination with a power combiner that are both assumed to be free of noise sources and reflections. The receiver output in Fig. 5.8 is located at reference plane $\Sigma = 2$; this single output port
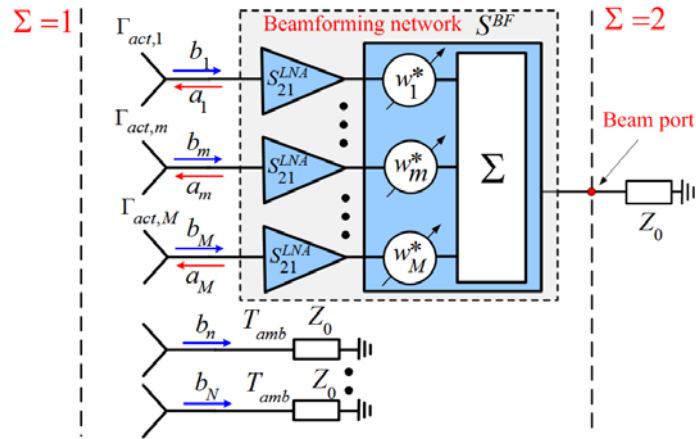
Figure 5.8: A block diagram of a typical focal plane array receiving system with N array elements, among which M elements are connected to LNAs and used in the beamforming; while $(N - M)$ elements are characteristically terminated.

is referred to as the "beam port". Both the effective area A_{eff} and the system noise temperature T_{sys} can be determined at this beam port. We will use the term "refer to" to designate the reference plane at which A_{eff} and T_{sys} pertain to. One can refer these quantities to another reference plane, say to the fictitious port in the sky at $\Sigma = 1$, by dividing A_{eff} and T_{sys} by the system available gain $G_{\text{sys}}^{\text{av}}$, i.e., the available gain between reference plane $\Sigma = 1$ and $\Sigma = 2$.

The outgoing/reflected waves $\mathbf{b} = [b_1, b_2, \cdots, b_N]^T$ from the antenna array in Fig. 5.8 are related to the incident waves $\mathbf{a} = [a_1, a_2, \cdots, a_N]^T$ via the scattering matrix $\mathbf{S}^{\text{ant}}$ of the antenna array, i.e., $\mathbf{b} = \mathbf{S}^{\text{ant}}\mathbf{a}$. We will distinguish between the incident and reflected waves for the M actively and $(N - M)$ passively terminated ports, respectively, and set

$$\mathbf{a} = [\mathbf{a}_{\text{act}}, \mathbf{a}_{\text{pas}}]^T \qquad \text{and} \qquad \mathbf{b} = [\mathbf{b}_{\text{act}}, \mathbf{b}_{\text{pas}}]^T \tag{5.73}$$

and perform the following matrix decomposition on $\mathbf{S}^{\text{ant}}$:

$$\begin{pmatrix} \mathbf{b}_{\text{act}} \\ \mathbf{b}_{\text{pas}} \end{pmatrix} = \begin{pmatrix} \mathbf{S}_{\text{act,act}}^{\text{ant}} & \mathbf{S}_{\text{act,pas}}^{\text{ant}} \\ \mathbf{S}_{\text{pas,act}}^{\text{ant}} & \mathbf{S}_{\text{pas,pas}}^{\text{ant}} \end{pmatrix} \begin{pmatrix} \mathbf{a}_{\text{act}} \\ \mathbf{a}_{\text{pas}} \end{pmatrix}. \tag{5.74}$$

Next, we set $\mathbf{a}_{\text{pas}} = 0$, since the corresponding antenna ports are assumed to be characteristically terminated, so that

$$\mathbf{b}_{\text{act}} = \mathbf{S}_{\text{act,act}}^{\text{ant}}\mathbf{a}_{\text{act}}, \qquad \text{and} \qquad \mathbf{b}_{\text{pas}} = \mathbf{S}_{\text{pas,act}}^{\text{ant}}\mathbf{a}_{\text{act}}. \tag{5.75}$$

Likewise, we block partition the beamformer S-parameter matrix $\mathbf{S}^{\mathrm{BF}}$ as

$$\mathbf{S}^{\mathrm{BF}} = \begin{pmatrix} \mathbf{S}_{11}^{\mathrm{BF}} & \mathbf{S}_{12}^{\mathrm{BF}} \\ \mathbf{S}_{21}^{\mathrm{BF}} & \mathbf{S}_{22}^{\mathrm{BF}} \end{pmatrix} \tag{5.76}$$

where we distinguished between the M input ports on the left-hand side of the beamforming network (side 1), and possibly multiple output beam ports on the right-hand side (side 2). However, we will restrict ourselves to a single output beam port and set $\mathbf{S}_{22}^{\mathrm{BF}} = 0$ (1×1 matrix, scalar). Furthermore, we assume no isolation and beamformer reflection losses, so that $\mathbf{S}_{12}^{\mathrm{BF}}$ and $\mathbf{S}_{11}^{\mathrm{BF}}$ are zero matrices of sizes $M \times 1$ and $M \times M$, respectively. The latter requirement is not a severe restriction for practical systems where commercial LNAs and loads are employed that are based on standard reference impedances, but we emphasize that the present model does entail several assumptions.

Let the complex weight coefficients of the beamforming network on receive be defined by the row vector

$$\mathbf{w}^H = [w_1^*, w_2^*, \cdots, w_M^*] \tag{5.77}$$

where the superscript H denotes the hermitian conjugate, and $*$ the complex conjugate.

Then, when assuming an ideal beamformer, we can define the transmission factors by a matrix of size $1 \times M$ as

$$\mathbf{S}_{21}^{\mathrm{BF}} = \frac{1}{\sqrt{M}} S_{21}^{\mathrm{LNA}} \mathbf{w}^H. \tag{5.78}$$

In the following two sections we apply Eqs. (5.75), (5.77), and (5.78), and demonstrate how the FPA model shown in Fig. 5.8 can be reduced to a single-port antenna followed by a two-port LNA as illustrated in Fig. 5.9. For this purpose, expressions will be derived for the equivalent model parameters η_{coup} (coupling efficiency), η_{mis} (mismatch efficiency), η_{rad} (radiation efficiency), $G_{\mathrm{Eq}}^{\mathrm{power}}$ (equivalent power gain), and $T_{\mathrm{Eq}}^{\mathrm{LNA}}$ (equivalent amplifier noise temperature).

The beamformer transmission coefficients on receive in (5.78) are applied as the excitation coefficients of the array on transmit to realize the same radiation pattern as the receiving pattern. Hence, the excitation vector $\mathbf{a}_{\mathrm{act}}$ assumes the value:

$$\mathbf{a}_{\mathrm{act}} = \left(\mathbf{S}_{21}^{\mathrm{BF}} \right)^T \Big|_{\mathbf{a}_{\mathrm{pas}}=\mathbf{0}} \tag{5.79}$$

so that the mth vector element is given by

$$a_{\text{act},m} = \frac{1}{\sqrt{M}} S_{21}^{\text{LNA}} w_m^*. \tag{5.80}$$

Note that $\mathbf{S}_{21}^{\text{BF}}$ represents a row vector on receive, whereas the excitation vector $\mathbf{a}_{\text{act}}$ is a column vector on transmit.

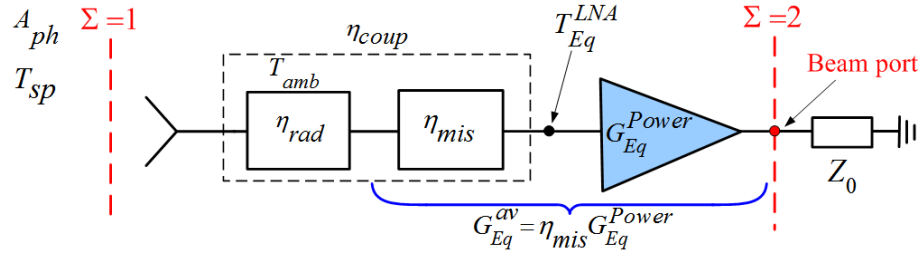## 5.6.2 Representing the FPA by an equivalent antenna element

Figure 5.9: An equivalent single-channel receiver model of the (focal plane) array system shown in Fig. 5.8.

The element pattern of the equivalent single-port antenna will be the same as the realized beam of the array when the excitation coefficients are chosen according to (5.80). Upon exciting the array in this specific manner, one can readily quantify the dissipation losses in the resistively terminated ports on transmit. The total dissipative loss is accounted for by the radiation efficiency of the equivalent antenna (Fig. 5.9). With reference to Fig. 5.9, and by using (5.75) and (5.80), we obtain:

- ***The radiation efficiency*** of the equivalent antenna as

$$\eta_{\text{rad}} = 1 - \frac{P_{\text{diss}}}{P_{\text{acc}}} \approx 1 - \frac{\mathbf{b}_{\text{pas}}^H \mathbf{b}_{\text{pas}}}{\mathbf{a}_{\text{act}}^H \mathbf{a}_{\text{act}} - \mathbf{b}_{\text{act}}^H \mathbf{b}_{\text{act}}} =$$
$$\frac{\mathbf{W}^H \left(\mathbf{I} - \left[\left(\mathbf{S}_{\text{act,act}}^{\text{ant}} \right)^H \mathbf{S}_{\text{act,act}}^{\text{ant}} + \left(\mathbf{S}_{\text{pas,act}}^{\text{ant}} \right)^H \mathbf{S}_{\text{pas,act}}^{\text{ant}} \right] \right) \mathbf{W}}{\mathbf{W}^H \left(\mathbf{I} - \left(\mathbf{S}_{\text{act,act}}^{\text{ant}} \right)^H \mathbf{S}_{\text{act,act}}^{\text{ant}} \right) \mathbf{W}} \tag{5.81}$$

where $\mathbf{W} = \mathbf{w}^*$, and where P_{acc} is the total accepted power by the array. The approximation in (5.81) indicates that we only account for the power absorption P_{load} in passively

terminated ports, whereas in general, one could define that $P_{\mathrm{diss}} = P_{\mathrm{load}} + P_{\mathrm{diel}} + P_{\mathrm{cond}}$, so that the dielectric and conductor losses are also included. The presently proposed model will then still apply, provided that the losses are associated with the same physical temperature, which is typically chosen to be the ambient temperature.

Next, we introduce the mismatch efficiency of the equivalent antenna which accounts for reflection losses at the actively used ports of the array.

- **The mismatch efficiency** (or impedance mismatch factor) of the equivalent antenna is defined as

$$\eta_{\mathrm{mis}} = 1 - \frac{P_{\mathrm{refl}}}{P_{\mathrm{inc}}} = 1 - \frac{\mathbf{b}_{\mathrm{act}}^{H}\mathbf{b}_{\mathrm{act}}}{\mathbf{a}_{\mathrm{act}}^{H}\mathbf{a}_{\mathrm{act}}} = \frac{\mathbf{W}^{H}\left[\mathbf{I} - \left(\mathbf{S}_{\mathrm{act,act}}^{\mathrm{ant}}\right)^{H}\mathbf{S}_{\mathrm{act,act}}^{\mathrm{ant}}\right]\mathbf{W}}{\mathbf{W}^{H}\mathbf{W}}. \qquad (5.82)$$

The product of the former two efficiencies equals the recently introduced coupling efficiency [157, 164], which is considered to be a fundamental parameter of (transmitting) antenna arrays and is used here to quantify the total lost signal power of the equivalent antenna. Fig. 5.8 shows that the mismatch efficiency reduces both the transmitted signal and noise powers, which seems to imply that the beam sensitivity (see Section 5.6.4) is independent of the mismatch efficiency. However, it does influence the noise mismatch between the receiver and antenna array as well, so that the beam sensitivity is still dependent on the mismatch efficiency, albeit indirectly through the active reflection coefficients of the antenna elements as discussed in the next section.

- **The coupling efficiency** is defined as

$$\eta_{\mathrm{coup}} = 1 - \frac{P_{\mathrm{coup}}}{P_{\mathrm{inc}}} = 1 - \frac{\mathbf{b}_{\mathrm{act}}^{H}\mathbf{b}_{\mathrm{act}} + \mathbf{b}_{\mathrm{pas}}^{H}\mathbf{b}_{\mathrm{pas}}}{\mathbf{a}_{\mathrm{act}}^{H}\mathbf{a}_{\mathrm{act}}} =$$
$$\frac{\mathbf{W}^{H}\left(\mathbf{I} - \left[\left(\mathbf{S}_{\mathrm{act,act}}^{\mathrm{ant}}\right)^{H}\mathbf{S}_{\mathrm{act,act}}^{\mathrm{ant}} + \left(\mathbf{S}_{\mathrm{pas,act}}^{\mathrm{ant}}\right)^{H}\mathbf{S}_{\mathrm{pas,act}}\right]\right)\mathbf{W}}{\mathbf{W}^{H}\mathbf{W}}. \qquad (5.83)$$

Finally, one can readily verify that $\eta_{\mathrm{coup}} = \eta_{\mathrm{mis}}\eta_{\mathrm{rad}}$.

The above mentioned efficiencies are the model parameters of the equivalent single-port antenna shown in Fig. 5.8 and depend on the weights of the beamforming network. Note that, in case the loads are replaced by LNAs followed by zero weights, the absorption loss

in the passively terminated elements effectively moves from the radiation efficiency to the mismatch efficiency, where $\mathbf{b}_{\mathrm{act}}$ is then replaced by $\mathbf{b}$.

5.6.3 Representing the beamforming network by an equivalent amplifier

In order to represent the beamforming network by an equivalent amplifier, we first compute the total noise temperature due to the LNAs, $T_{\mathrm{out}}^{\mathrm{LNA}}$, at the output beam port ($\Sigma = 2$ in Fig. 5.8). For this purpose, we consider the receiver system representation shown in Fig. 5.10. In this representation, each receiver channel is noise decoupled from the other channels by replacing the full antenna S-matrix by a diagonal matrix where the entries on the diagonal represent the active reflection coefficients of the corresponding array elements (*cf.* [122, 161], and Fig. 5.5). This is permitted when the antenna S-matrix is symmetric, and when the beamformer is ideal and free of reflections at its inputs.
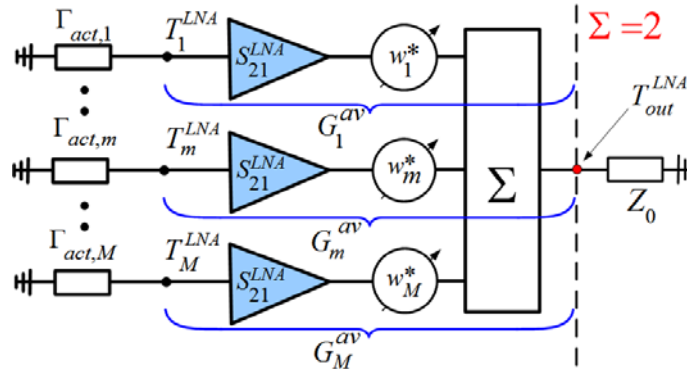
Figure 5.10: A noise decoupled system representation used to evaluate $T_{\mathrm{out}}^{\mathrm{LNA}}$.

The active reflection coefficient $\Gamma_{\mathrm{act},m}$ of the mth antenna element is defined as

$$\Gamma_{\mathrm{act},m} = \frac{b_{\mathrm{act},m}}{a_{\mathrm{act},m}} = \frac{1}{W_m} \sum_{n=1}^{M} S_{m,n}^{\mathrm{ant}} W_n \tag{5.84}$$

where (5.75), (5.78), (5.79) and $\mathbf{W} = \mathbf{w}^*$ have been substituted.

It is convenient to work with the representation in Fig. 5.10, since $T_{\mathrm{out}}^{\mathrm{LNA}}$ can now directly

be computed as the weighted sum of uncorrelated noise contributions:

$$T_{\text{out}}^{\text{LNA}} = \sum_{m=1}^{M} G_m^{\text{av}} T_m^{\text{LNA}} \tag{5.85}$$

where the noise temperature T_m^{LNA} of the mth channel is referred to the input of the mth LNA and is weighted by its available channel gain G_m^{av}. In view of Fig. 5.10, G_m^{av} is defined from the output of the mth antenna element – thus includes the antenna-LNA mismatch – to the output of the beamformer:

$$G_m^{\text{av}} = \left(\frac{1}{M} \left| S_{21}^{\text{LNA}} \right|^2 |w_m|^2 \right) \left(1 - |\Gamma_{\text{act},m}|^2 \right) \tag{5.86}$$

where the first term on the right-hand side represents the power transmission coefficient of the mth element/channel of $\mathbf{S}_{21}^{\text{BF}}$ in (5.78). The second term quantifies the power loss due to reflection and coupling effects at the port of the mth element. Herein, the gain definition in [160] for decoupled receiver channels has been extended to account for noise coupling effects through the use of Γ_{act} [161].

The noise temperature contributions of individual LNAs in (5.85) for each beamforming channel can be computed by using a well-known formula for noisy two ports, which for the case of the array receivers, as described in Section 5.6.1 (with noise coupling), assumes the form [161, 162]:

$$T_m^{\text{LNA}} = T_{\text{min}} + \frac{4R_n T_o}{Z_o} \frac{|\Gamma_{\text{act},m} - \Gamma_{\text{opt}}|^2}{|1 + \Gamma_{\text{opt}}|^2 (1 - |\Gamma_{\text{act},m}|^2)} \tag{5.87}$$

where $\{T_{\text{min}}, R_n, \Gamma_{\text{opt}}\}$ are the noise parameters of a two port, and $\Gamma_{\text{act},m}$ represents the active source-reflection coefficient seen from the input of the LNA of the mth receiver channel (see Fig. 5.10). The second term on the right-hand side of (5.87) measures the increase in the LNA noise temperature due to noise coupling effects, since it involves the active source-reflection coefficient.

Next, we determine the effective noise temperature $T_{\text{Eq}}^{\text{LNA}}$ of the equivalent amplifier in Fig. 5.9 and therefore divide $T_{\text{out}}^{\text{LNA}}$ at the output beam port ($\Sigma=2$) by $G_{\text{Eq}}^{\text{power}}$ to refer it to the desired reference plane. We point out that, commonly, $T_{\text{out}}^{\text{LNA}}$ is divided by the available gain $G_{\text{Eq}}^{\text{av}}$ of the equivalent amplifier rather than by $G_{\text{Eq}}^{\text{power}}$. Then, the LNA noise temperature would be referenced in front of the mismatch efficiency block in Fig. 5.9, since $G_{\text{Eq}}^{\text{av}} = \eta_{\text{mis}} G_{\text{Eq}}^{\text{power}}$. However, as we aim to express the final receiver sensitivity in terms of the coupling efficiency, we will combine the radiation with the mismatch efficiency, thus

separating η_{mis} from $G_{\mathrm{Eq}}^{\mathrm{av}}$, and then work with the remaining power gain $G_{\mathrm{Eq}}^{\mathrm{power}}$ instead (see Fig. 5.9). We remark that, regardless of the choice of reference point for the equivalent LNA noise temperature, the final expression for the beam sensitivity will be the same. Herein, we define

- **The effective noise temperature**:

$$T_{\mathrm{Eq}}^{\mathrm{LNA}} = T_{\mathrm{out}}^{\mathrm{LNA}}/G_{\mathrm{Eq}}^{\mathrm{power}} \tag{5.88}$$

where $G_{\mathrm{Eq}}^{\mathrm{power}}$ is defined as the ratio of the beamformer output power $P_{\mathrm{out}}^{\mathrm{BF}}$ at the beam port (see Fig. 5.8) to the input power $P_{\mathrm{in},m}^{\mathrm{BF}}$ of a single beamformer channel when all M receiver inputs are excited by uncorrelated sources of equal power [160]. Therefore, $G_{\mathrm{Eq}}^{\mathrm{power}}$ is termed

- **The uncorrelated power gain**:

$$G_{\mathrm{Eq}}^{\mathrm{power}} = \frac{P_{\mathrm{out}}^{\mathrm{BF}}}{P_{\mathrm{in},m}^{\mathrm{BF}}} = \frac{1}{M} \left| S_{21}^{\mathrm{LNA}} \right|^2 \mathbf{w}^H \mathbf{w} \tag{5.89}$$

where we have used (5.78).

5.6.4 The beam sensitivity

The beam sensitivity $A_{\mathrm{eff}}/T_{\mathrm{sys}}$ of the equivalent receiving system can be derived by using the system model in Fig. 5.9 with the model parameters that were described in the previous two sections ($\eta_{\mathrm{mis}}, \eta_{\mathrm{rad}}, \eta_{\mathrm{coup}}, G_{\mathrm{Eq}}^{\mathrm{power}}$ and $T_{\mathrm{Eq}}^{\mathrm{LNA}}$), as well as the aperture efficiency η_{ap} and the spillover noise temperature $T_{\mathrm{sp}} = (1 - \eta_{\mathrm{sp}})T_{\mathrm{ground}}$. Parameters η_{ap} and T_{sp} are determined by the shape of the equivalent antenna pattern and the subtended angle of the reflector, and can be calculated from standard formulas. Alternatively, one can use the definitions from [165] that were specifically derived for receiving arrays.

The sensitivity at the output beam port (plane $\Sigma = 2$ in Fig. 5.9) is defined in terms of the spectral output SNR as

$$\frac{A_{\mathrm{eff}}}{T_{\mathrm{sys}}} = \frac{S_{\mathrm{out}}/S_{\mathrm{flux}}}{N_{\mathrm{out}}/k_B} \tag{5.90}$$

where A_{eff} is the effective area of the equivalent antenna, T_{sys} is the total system noise temperature, S_{out} is the signal power at the output beam port, S_{flux} the power flux density of the incident field (assuming perfect polarization match), N_{out} is the output noise power, and k_B is Boltzmann's constant.

Since we have already derived the model parameters for the single-channel receiver in Fig. 5.9, we may readily evaluate (5.90) and express the sensitivity at the output beam port as

$$\frac{A_{\text{eff}}}{T_{\text{sys}}} = \frac{A_{\text{ph}}\eta_{\text{ap}}\eta_{\text{rad}}G_{\text{Eq}}^{\text{av}}}{T_{\text{sp}}\eta_{\text{rad}}G_{\text{Eq}}^{\text{av}} + (1 - \eta_{\text{rad}})T_{\text{amb}}G_{\text{Eq}}^{\text{av}} + T_{\text{out}}^{\text{LNA}}}, \qquad (5.91)$$

where A_{ph} is the physical aperture area of the (reflector) antenna (at the reference plane $\Sigma = 1$), which is reduced by both the aperture efficiency η_{ap} and radiation efficiency η_{rad}, and then amplified by the available gain $G_{\text{Eq}}^{\text{av}}$ of the equivalent amplifier (see Fig. 5.9, where $G_{\text{Eq}}^{\text{av}} = \eta_{\text{mis}}G_{\text{Eq}}^{\text{power}}$). The spillover temperature T_{sp} is also defined at the reference plane $\Sigma = 1$ and is affected by the same factor. Note that this factor represents the available gain $G_{\text{sys}}^{\text{av}}$ of the entire receiver system:

$$G_{\text{sys}}^{\text{av}} = \eta_{\text{rad}}G_{\text{Eq}}^{\text{av}} = \eta_{\text{rad}}\eta_{\text{mis}}G_{\text{Eq}}^{\text{power}} = \eta_{\text{coup}}G_{\text{Eq}}^{\text{power}}. \qquad (5.92)$$

The noise temperature T_{ant} of the equivalent antenna at ambient temperature T_{amb} is defined as $T_{\text{ant}} = (1 - \eta_{\text{rad}})T_{\text{amb}}$, which is amplified by $G_{\text{Eq}}^{\text{av}}$ and added to the LNA output noise temperature $T_{\text{out}}^{\text{LNA}}$.

Substituting (5.88) in (5.91), and using (5.92), yields

$$\frac{A_{\text{eff}}}{T_{\text{sys}}} = \frac{A_{\text{ph}}\eta_{\text{ap}}\eta_{\text{coup}}}{T_{\text{sp}}\eta_{\text{coup}} + (1 - \eta_{\text{rad}})\eta_{\text{mis}}T_{\text{amb}} + T_{\text{Eq}}^{\text{LNA}}}. \qquad (5.93)$$

For the design and modeling, it is often convenient to reference the sensitivity to the plane $\Sigma = 1$. This can be done by dividing both the numerator and denominator of (5.93) by the system available gain $G_{\text{sys}}^{\text{av}} = \eta_{\text{coup}}G_{\text{Eq}}^{\text{power}}$. Hence, the sensitivity at plane $\Sigma = 1$ takes the following form:

$$\frac{A_{\text{eff}}}{T_{\text{sys}}} = \frac{A_{\text{ph}}\eta_{\text{ap}}}{T_{\text{sp}} + \left(\dfrac{1 - \eta_{\text{rad}}}{\eta_{\text{rad}}}\right)T_{\text{amb}} + \left(\dfrac{1}{\eta_{\text{coup}}}\right)T_{\text{Eq}}^{\text{LNA}}}. \qquad (5.94)$$

The system noise temperature consists of three main contributions: (i) the spillover noise, (ii) the noise due to the dissipation losses of the equivalent antenna and (iii) the noise due

to LNAs which depends on the noise properties of LNAs and active reflection coefficients seen at the ports of the antenna array. The latter contribution is inversely proportional to the coupling efficiency of the equivalent antenna.

At this point, we recall that $T_{\mathrm{Eq}}^{\mathrm{LNA}}$ and η_{coup} both depend on the weights, therefore, one may not conclude that the coupling efficiency is generally the dominating factor in the term $T_{\mathrm{Eq}}^{\mathrm{LNA}}/\eta_{\mathrm{coup}}$, or that η_{coup} has to be maximized for optimum sensitivity. However, when η_{coup} becomes very small, as in case of arrays of strongly coupled elements operating at low frequencies, it will dominate and may severely reduce the receiver sensitivity.

5.6.5 Numerical Validation

Next, the consistency of the proposed model is validated through a numerical example of a 4-element dipole FPA receiver system as illustrated in Fig. 5.11(a). The outer two parasitic antenna elements generate thermal noise that re-enters the system as a result of the mutual coupling between the antenna elements. These loads also dissipate power and therefore reduce the radiation efficiency. The amplifiers are identical and their noise and scattering parameters are as indicated in Fig. 5.11(a).

The efficiencies η_{mis}, η_{rad}, and η_{coup} have been separately calculated and visualized in Fig. 5.11(b) as a function of the magnitude of w, while $\arg(w) = 0$. The corresponding change in the system noise temperature has been computed for $T_{\mathrm{sp}} = 0$ [see Fig. 5.11(c)], so that one basically computes the receiver noise temperature T_{rec}. Note that the results are referred to the input of the receiver ($\Sigma = 1$). With reference to (5.94), the thermal noise due to the loads $T_{\mathrm{load}} = T_{\mathrm{amb}}(1 - \eta_{\mathrm{rad}})/\eta_{\mathrm{rad}}$ and the noise contribution due to LNAs $T_{\mathrm{LNA}} = T_{\mathrm{Eq}}^{\mathrm{LNA}}/\eta_{\mathrm{coup}}$ have been plotted in Fig. 5.11(c) as well.

By analyzing Fig. 5.11(c), one can see that, for this specific example, the total receiver noise is dominated by the thermal noise that is generated by the loads when $|w| < -7.8\mathrm{dB}$, whereas the noise of the LNAs begins to dominate for larger $|w|$. We remark that this cross-over point is independent of the choice of the reference planes. Furthermore, one observes that, when the active elements are equally excited on transmit ($w = 1$), the power absorption in the loads is minimized due to destructive mutual coupling interference effects at the passively terminated ports. Hence, η_{rad} is maximized. Likewise, on receive, the noise contribution due to the loads $(1/\eta_{\mathrm{rad}} - 1)T_{\mathrm{amb}}$ is minimized when η_{rad} is maximized
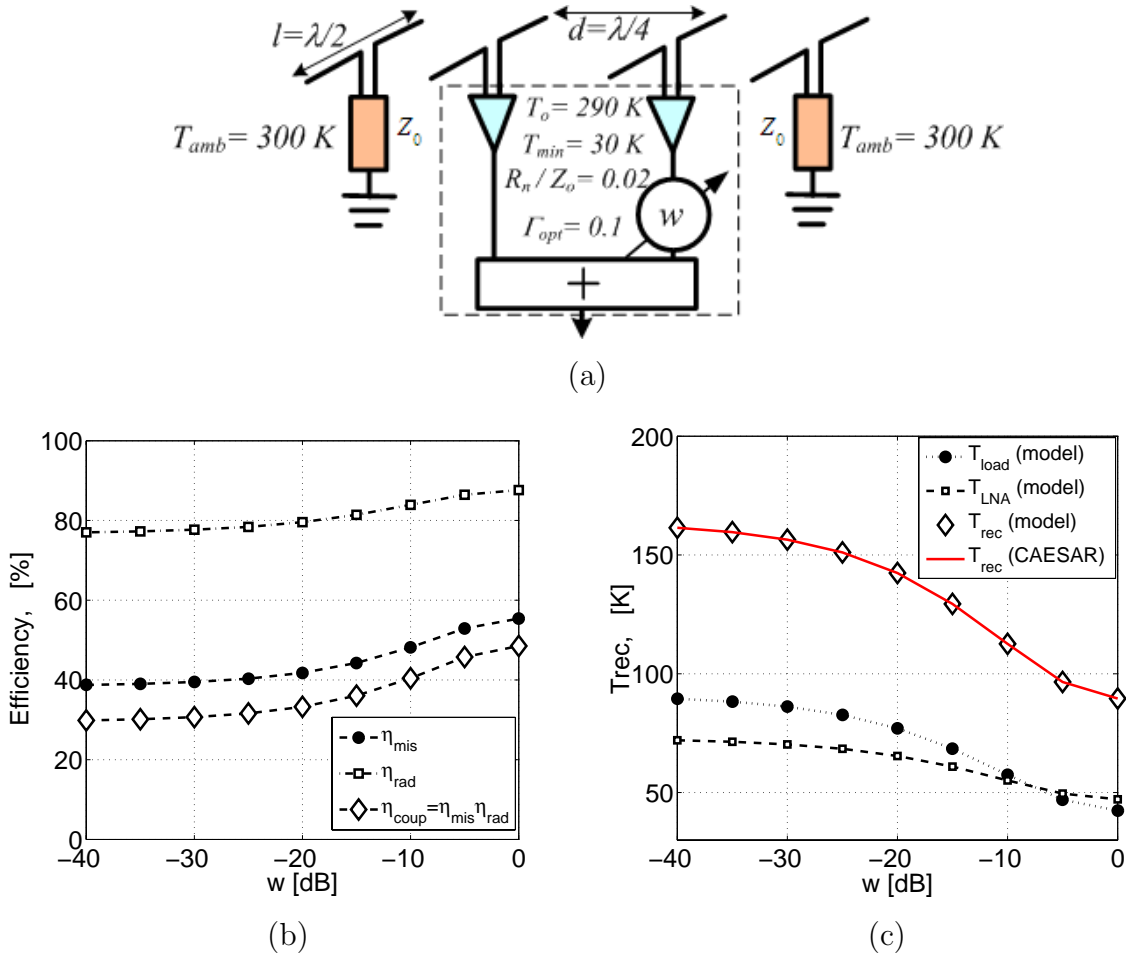
(a)

(b)

(c)

Figure 5.11: (a) A 4-element dipole (focal plane) array receiving system; (b) Efficiencies η_{mis}, η_{rad}, and η_{coup} of the equivalent single-port antenna shown in Fig. 5.9; (c) The noise temperature contributions T_{load} and T_{LNA} as computed by the proposed model, and the total receiver noise temperature in comparison with the result computed with CAESAR.

for $w = 1$ as a result of destructive noise coupling interference effects.

Finally, it has been demonstrated in Fig. 5.11(c) that the system noise temperature that was computed with the aid of the proposed model is consistent with the one computed by the CAESAR software (see Appendix F and [85], i.e., the results are identical up to machine precision.

5.7 Radiation Efficiency and Noise Temperature of Low-Loss Antennas

Thus far, we did not consider the power dissipation losses in antenna conductors, but we solely considered the losses that are caused by the resistively loaded parasitic antenna-array elements. For radio astronomical applications, however, the total loss and the associated noise temperature of non-cooled antenna systems is strictly specified. For example, in [20], the target system temperature is set to 50 K, of which 7–10 K is the maximum allowed contribution due to the antenna, including the connection loss with a low noise amplifier at the feedpoint. To achieve such low noise temperatures, antennas with only metal conductors are an obvious choice, since additional dielectric material may increase the loss (*cf.* the TSA design in Section 4.7). In the absence of other noise sources, T_{sys} of the receiving antenna is related to the radiation efficiency η_{rad} by [see also (5.94)]

$$T_{\mathrm{sys}} = T_{\mathrm{amb}} \left(\frac{1 - \eta_{\mathrm{rad}}}{\eta_{\mathrm{rad}}} \right) \tag{5.95}$$

where T_{amb} is the ambient temperature of the antenna, and where η_{rad} is defined by

$$\eta_{\mathrm{rad}} = \frac{P_{\mathrm{rad}}}{P_{\mathrm{acc}}}. \tag{5.96}$$

Here P_{acc} is the total accepted input power by the antenna and P_{rad} is the total radiated power. It is readily seen that, if η_{rad} reduces to 98 %, T_{sys} increases by 6 K at $T_{\mathrm{amb}} = 300$ K and, hence, this significant increase should be determined accurately.

Efficiency measurements for low-loss antennas can be carried out with for example Wheeler cap, radiometric, directivity/gain, or calorimetric methods [166]. However, the accuracies of these methods are of the order of a few percent [167], which is not sufficient in our case. Alternatively, one can resort to numerical simulations, but they suffer from accuracy problems. Fig. 5.12 shows η_{rad} of a single TSA as specified in Fig. 4.19, computed by the finite-element-method (FEM) solver Ansoft HFSS (v. 11.1.3), the Method-of-Moments (MoM) solver Ansoft Designer (v. 4.0.0), and the finite-difference time-domain (FDTD) solver CST MWS (v. 2008.04) for perfect (PEC) and good electric conductors. In HFSS, two different settings are employed: the standard adaptive mesh and a fixed maximum mesh. The surface mesh in Designer and the global mesh in CST are both adaptively generated. For all meshes, the mesh density is the highest near the tapered slot with sizes as low as 2 mm. In the HFSS results, η_{rad} highly exceeds 100%, where the fixed mesh size
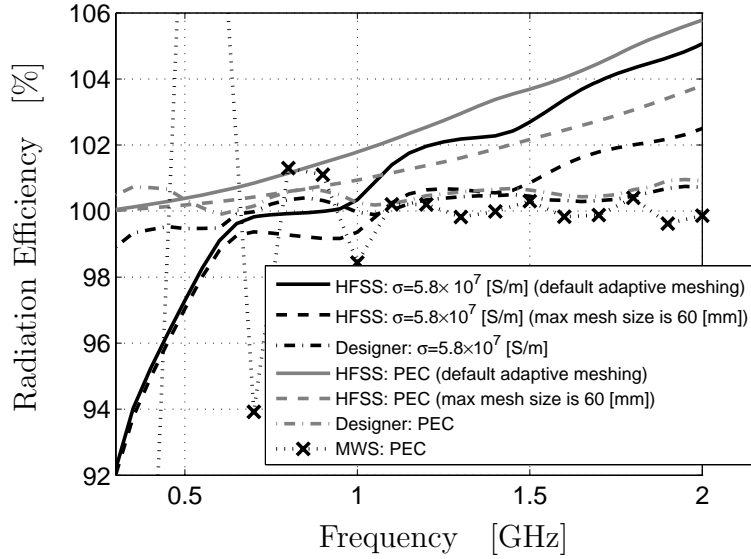
Figure 5.12: η_{rad} of a TSA computed by HFSS, Designer, and MWS. Settings: HFSS: airbox $500 \times 700 \times 800$ mm^3, adaptive meshing with maximum 20 passes at 2 GHz, 53966 tetrahedra for setting maximum mesh size 60 mm (maximum tetrahedra size $\lambda_0/5$ at 1 GHz). Designer: adaptive meshing at 2 GHz (maximum 10 passes, 25% refinement per pass, maximum $\Delta S = 0.05$, minimum mesh angle 5 Deg, edge length factor 12). MWS: adaptive hexahedral mesh (FPBA) with 2371008 mesh cells, at least 30 lines per λ_0, mesh step ≥ 0.25 mm, refine factor 6, boundary condition open (space added of at least 15 mesh lines or $\lambda_0/5$).

provides the best result. The Designer results seem better, but η_{rad} varies between 100.0% and 100.7% for a PEC and between 99.4% and 100.4% for a good conductor. The MWS result for a PEC is particularly unreliable below 0.8 GHz. The results of all three solvers are not sufficient for an accurate computation of T_{sys}.

As noted in [168] numerical sampling (of the far field) and integration (of the Poynting vector) are still required for a majority of antenna radiation problems despite efforts to find alternatives, e.g., [110, 168]. Sampling and integration may lead to a high computational cost and substantial (integration) errors, in particular for large arrays with rapidly varying far fields. In this work, we evaluate η_{rad} and T_{sys} of arrays of low-loss loops and of a low-loss TSA by computing the dissipated power P_{diss} from a MoM solution. Such an approach is implemented in some commercial and non-commercial MoM solvers and is similar to the computation of the complex power, see [32, p. 90], [79, pp. 95–98]. We first

summarize the approach for computing P_{diss} and utilize the concept of surface impedance to describe metal losses. Next, we show that η_{rad} cannot become larger than 100%, independent of numerical errors. Finally, we discuss numerical results for η_{rad} and T_{sys}, and we compare these results with results obtained by numerical integration and by the MoM solver FEKO 5.4 (v. 4.0.117480). We comment on computation times, mesh issues, and efficiency computations by the MoM solvers Designer and Zeland's IE3D (v. 12.1)[4].

5.8 Considerations on the Radiation Efficiency

Instead of computing η_{rad} by (5.96), one can directly compute the dissipated power P_{diss}, and subsequently employ

$$\eta_{\mathrm{rad}} = 1 - \frac{P_{\mathrm{diss}}}{P_{\mathrm{acc}}} \tag{5.97}$$

where P_{diss} satisfies $P_{\mathrm{rad}} = P_{\mathrm{acc}} - P_{\mathrm{diss}}$. To ease the explanations that follow, we will first summarize the steps to calculate P_{acc} and P_{diss}. For a multiport antenna array, $P_{\mathrm{acc}} = \Re\mathfrak{e}\{(\mathbf{I}^{\mathrm{ant}})^H \mathbf{V}^{\mathrm{ant}}\}/2$ where H indicates the Hermitian transpose, and $\mathbf{V}^{\mathrm{ant}}$ and $\mathbf{I}^{\mathrm{ant}}$ are column vectors of voltage and current amplitudes at the ports. Modeling the antenna as an infinitely thin impedance sheet with associated surface impedance Z_S, surface current $\boldsymbol{J}_S$, and boundary condition $\boldsymbol{E}_{\mathrm{tan}} = Z_S \boldsymbol{J}_S$, we compute P_{diss} by

$$P_{\mathrm{diss}} = \frac{1}{2}\Re\mathfrak{e}\left\{ \int_{\mathcal{S}} \boldsymbol{J}_S^* \cdot Z_S \boldsymbol{J}_S \, \mathrm{d}S \right\}. \tag{5.98}$$

Note that Z_S may depend on the position vector $\boldsymbol{r}$. In a MoM setting, we expand $\boldsymbol{J}_S$ into the N basis functions $\{\boldsymbol{f}_n\}_{n=1}^N$, with $\boldsymbol{f}_n$ non-zero on the support $\mathcal{S}_n \subset \mathcal{S}$, and employ the expansion coefficient vector $\mathbf{I}^{\mathrm{MoM}}$. Substituting this expansion in (5.98), yields

$$P_{\mathrm{diss}} = \frac{1}{2}\Re\mathfrak{e}\left\{ \left(\mathbf{I}^{\mathrm{MoM}}\right)^H \mathbf{Z}^{\mathrm{IBC}} \mathbf{I}^{\mathrm{MoM}} \right\} \tag{5.99}$$

where the matrix elements of $\mathbf{Z}^{\mathrm{IBC}}$ are given by

$$Z_{mn}^{\mathrm{IBC}} = \int_{\mathcal{S}_m \cap \mathcal{S}_n} \boldsymbol{f}_m^* \cdot Z_S \boldsymbol{f}_n \, \mathrm{d}S = \langle \boldsymbol{f}_m, Z_S \boldsymbol{f}_n \rangle \tag{5.100}$$

---

[4]In [25], an extensive assessment of software tools (MoM, FEM, FDTD) for antenna design is described, although the losses are only discussed shortly in Section 6.3.

where $\langle \cdot, \cdot \rangle$ denotes the classical inner product on $\mathcal{S}$. For constant Z_S, Z^{IBC} equals a constant times the Gram matrix of the basis functions. Then, (5.99) resembles the complex-power expressions in [32, p. 90] and [79, (4.15)].

Henceforth, we will employ real-valued basis functions, so that the complex inner product in (5.100) can be replaced by a symmetric product; this is in accordance with the EFIE discretization scheme outlined in Chapter 3. The more general case of employing a complex inner product is discussed in detail in [37]. Note that, if a symmetric product is used in conjunction with a Galerkin's scheme for testing the EFIE, Eq. (5.100) becomes identical to Eq. (3.76) when employing RWG basis functions.

From Chapter 3, we recall that $\mathbf{I}^{\mathrm{MoM}}$ is computed from the EFIE: $\boldsymbol{E}^s_{\mathrm{tan}}(\boldsymbol{J}_S) - Z_S \boldsymbol{J}_S = -\boldsymbol{E}^i_{\mathrm{tan}}$ on $\mathcal{S}$, of which the discretized form reads

$$(\mathbf{Z}^{\mathrm{PEC}} - \mathbf{Z}^{\mathrm{IBC}})\mathbf{I}^{\mathrm{MoM}} = \mathbf{V}^{\mathrm{MoM}} \tag{5.101}$$

where $V_m^{\mathrm{MoM}} = -\langle \boldsymbol{f}_m, \boldsymbol{E}^i \rangle$ and $Z_{mn}^{\mathrm{PEC}} = \langle \boldsymbol{f}_m, \boldsymbol{E}^s(\boldsymbol{f}_n) \rangle$. Thus, $\mathbf{Z}^{\mathrm{IBC}}$ and $\mathbf{I}^{\mathrm{MoM}}$ are available in a MoM and P_{diss} can be computed by the two matrix-vector multiplications in (5.99).

Given the relatively low numerical effort, the question arises whether we avoid computed radiation efficiencies larger than 100%. We can rewrite (5.99) as

$$\begin{aligned} P_{\mathrm{diss}} &= \frac{1}{4} \left[\left(\mathbf{I}^{\mathrm{MoM}}\right)^H \mathbf{Z}^{\mathrm{IBC}}\mathbf{I}^{\mathrm{MoM}} + \left(\left(\mathbf{I}^{\mathrm{MoM}}\right)^H \mathbf{Z}^{\mathrm{IBC}}\mathbf{I}^{\mathrm{MoM}}\right)^H \right] \\ &= \frac{1}{4} \left[\left(\mathbf{I}^{\mathrm{MoM}}\right)^H \mathbf{Z}^{\mathrm{IBC}}\mathbf{I}^{\mathrm{MoM}} + \left(\mathbf{I}^{\mathrm{MoM}}\right)^H \left(\mathbf{Z}^{\mathrm{IBC}}\right)^H \mathbf{I}^{\mathrm{MoM}} \right] \\ &= \frac{1}{4} \left(\mathbf{I}^{\mathrm{MoM}}\right)^H \left[\mathbf{Z}^{\mathrm{IBC}} + \left(\mathbf{Z}^{\mathrm{IBC}}\right)^H \right] \mathbf{I}^{\mathrm{MoM}} \tag{5.102} \\ &= \frac{1}{2} \left(\mathbf{I}^{\mathrm{MoM}}\right)^H \mathfrak{Re}\left\{\mathbf{Z}^{\mathrm{IBC}}\right\} \mathbf{I}^{\mathrm{MoM}} \tag{5.103} \end{aligned}$$

where we used that $\mathbf{Z}^{\mathrm{IBC}} = (\mathbf{Z}^{\mathrm{IBC}})^T$ for passive reciprocal systems. Note that (5.103) equals [32, Eq. (10-8)] for the power dissipated in linear N-port networks. The matrix $\mathbf{A} = \mathbf{Z}^{\mathrm{IBC}} + \left(\mathbf{Z}^{\mathrm{IBC}}\right)^H$ in (5.102) is Hermitian, because $\mathbf{A}\mathbf{A}^H = \mathbf{A}^H \mathbf{A}$. Hence, $\mathfrak{Re}\left\{\mathbf{Z}^{\mathrm{IBC}}\right\}$ is a positive semidefinite matrix, so that $P_{\mathrm{diss}} = 1/2 \left(\mathbf{I}^{\mathrm{MoM}}\right)^H \mathfrak{Re}\left\{\mathbf{Z}^{\mathrm{IBC}}\right\} \mathbf{I}^{\mathrm{MoM}} \geq 0$ for all complex vectors $\mathbf{I}^{\mathrm{MoM}}$.

When, for a symmetric product, we apply the basic properties $\langle \boldsymbol{a}, \boldsymbol{b} \rangle = \langle \boldsymbol{b}, \boldsymbol{a} \rangle$ and $\langle \boldsymbol{a}, \alpha\boldsymbol{b} \rangle = \langle \alpha\boldsymbol{a}, \boldsymbol{b} \rangle$, we find that $(\mathbf{Z}^{\mathrm{IBC}})_{mn}^H = \langle \boldsymbol{f}_n, Z_S \boldsymbol{f}_m \rangle^* = \langle \boldsymbol{f}_m^*, Z_S^* \boldsymbol{f}_n^* \rangle = \langle \boldsymbol{f}_m, Z_S^* \boldsymbol{f}_n \rangle$. Then,

$$\left(\mathbf{Z}^{\mathrm{IBC}} + (\mathbf{Z}^{\mathrm{IBC}})^H\right)_{mn} = 2\langle \sqrt{\mathfrak{Re}\left\{Z_S\right\}}\boldsymbol{f}_m, \sqrt{\mathfrak{Re}\left\{Z_S\right\}}\boldsymbol{f}_n \rangle. \tag{5.104}$$

Thus, the Hermitian matrix $\mathbf{G} = (\mathbf{Z}^{\mathrm{IBC}} + (\mathbf{Z}^{\mathrm{IBC}})^H)/2$ is the Gram matrix of the functions $\sqrt{\mathfrak{Re}\{Z_S\}}\boldsymbol{f}_n$, $n = 1, \ldots, N$. Computing the inner products in (5.104) by a quadrature rule with points $\boldsymbol{r}_p$, $p = 1, \ldots, P$, and weights w_p, $\mathbf{G}$ is numerically speaking the Gram matrix of the vectors $(\sqrt{w_1 \mathfrak{Re}\{Z_S(\boldsymbol{r}_1)\}}\boldsymbol{f}_n(\boldsymbol{r}_1), \ldots, \sqrt{w_P \mathfrak{Re}\{Z_S(\boldsymbol{r}_P)\}}\boldsymbol{f}_n(\boldsymbol{r}_P))$. Consequently, $\mathbf{G}$ is numerically positive and, hence, $P_{\mathrm{diss}} \geq 0$. Since $P_{\mathrm{acc}} \geq 0$, we conclude from (5.97) that $\eta_{\mathrm{rad}} \leq 100\%$ numerically. From this point of view, given the Designer results in Fig. 5.12, i.e., η_{rad} larger than 100%, support the idea that Designer v. 4.0.0 does not compute η_{rad} from (5.97) and (5.99). Moreover, IE3D does not employ this computation either and clips η_{rad} to 100% in case it encounters $\eta_{\mathrm{rad}} > 100\%$.

To compute P_{diss} from (5.99) and (5.101), we need to take two additional steps compared to the EFIE for a PEC, i.e., to specify Z_S, and to compute Z^{IBC}. For good conducting and electrically thin sheets with thickness $d \ll \lambda_0$ and $\sigma \gg \omega\varepsilon_0|\varepsilon_r|$, one can use the surface impedance formula (3.44) for Z_S and, accordingly, the matrix Z^{IBC} is computed by numerical integration. In case Z_S is piecewise constant on the triangles of a mesh with RWG functions, we obtain the exact value of the mnth component by numerically integrating the function $\boldsymbol{f}_m \cdot \boldsymbol{f}_n$ by a Gaussian quadrature with three points in the triangle. Alternatively, we can use an analytical expression, Eq. (3.76).

We will briefly recall the necessary expressions from Section 3.2.2 and 3.2.3, and provide a concise literature overview as an alternative source for the derivations in Chapter 3, which are based on Makarov's approach. In [169, Sec. 4.8], the surface impedance of a plane conductor excited from one side is derived by field analysis [169, (4-113)],

$$Z_S^{\mathrm{single}}(d) = \frac{1 - j}{\sigma\delta \tan((1 - j)d/\delta)}. \tag{5.105}$$

The expression for a sheet excited from both sides is derived in [170, p. 15] by equivalent-circuit analysis and equals $Z_S^{\mathrm{single}}(d/2)$. If the sheet is modeled as infinitely thin, the surface impedance is composed of two impedances $Z_S^{\mathrm{single}}(d/2)$ from the lower and upper side that are in parallel. Consequently, $Z_S = Z^{\mathrm{single}}(d/2)/2$. The same expression follows from the field-based surface-impedance derivation in [43, Sec. 7.1] for a thin dielectric sheet by setting the wavenumber β equal to $(1 - j)/\delta$ and by replacing $j\omega(\varepsilon - \varepsilon_{\mathrm{diel}})$ in the relation for the current by σ. The derivation in [171, App. II] for the metal case is analogous to the one for the thin dielectric sheet. The expansions of Z_S for $d/\delta \ll 1$ and $d/\delta \gg 1$ are

[*cf.* Eqs. (3.45) and (3.47)]

$$Z_S = \frac{1}{\sigma d} \left\{ 1 + \frac{jd^2}{6\delta^2} + \mathcal{O}((d/\delta)^4) \right\} \tag{5.106}$$

$$Z_S = \frac{1+j}{2\delta\sigma} \left\{ 1 + 2e^{-(1+j)d/\delta} + \mathcal{O}(e^{-2d/\delta}) \right\}. \tag{5.107}$$

The zero-order terms are the low and high frequency approximations of Z_S, whose relative errors are less than 0.5% for $d/\delta \leq 0.17$ and $d/\delta \geq 6$.

5.8.1   Numerical Results

First we consider planar rectangular arrays of $X \times X$ loops in free space ($X = 1, 2, 4, 8, 16$). Each loop is a thin strip ($d = 0.035$ mm), whose width b is much smaller than λ_0, while the spacing D and the loop radius a are of the same order as λ_0. The currents and the fields in the EFIE (vector-potential formulation) are width averaged [79, Sec. 2.3.3]. The basis functions in the MoM are six cosine and two sine functions with radial frequencies $0, 1, \ldots, 5$ and $1, 2$, whose Gram matrix is diagonal with diagonal component 2π for the constant function and π otherwise. Each loop is excited by a delta gap of 1 V located at the position $\varphi = \pi$ [79, Ch. 4].

For specific parameter values, Table 5.2 shows η_{rad} computed by (5.97) and (5.99), and by (5.96) through numerical integration of the Poynting vector by a composite Simpson rule on $M_\theta \times M_\phi$ points ($0 \leq \theta \leq \pi$, $-\pi \leq \phi \leq \pi$). Moreover, P_{rad} computed as $P_{\mathrm{acc}} - P_{\mathrm{diss}}$ is shown.

Because of an increasing number of far-field lobes for an increasing number of loops, η_{rad} is erroneously computed by (5.96) for the larger array sizes (4×4 and larger) and a relatively low number of integration points (21×41). For larger numbers of points η_{rad} obtained by (5.96) is closer to the result obtained by (5.97), but even for 81×161 points, η_{rad} is almost 101% for the array of 16×16 loops.

Evaluating P_{rad} for the 16×16 array we compute the electric far field in 81×161 points. This matrix of points is much smaller than the moment matrix of the 16×16 array, i.e., 2048×2048, used in the evaluation of (5.99). Despite that, the evaluation of η_{rad} through (5.97) and (5.99) takes less than 0.02 s for all array sizes, while the evaluation through (5.96) with numerical integration takes up to 138 s for the 16×16 array with

Table 5.2: η_{rad} computed by (5.96) with numerical integration (composite Simpson rule on $M_\theta \times M_\phi$ points), and by (5.97), (5.99) for planar rectangular arrays of $X \times X$ loops with $a = \lambda_0/6$, $b/a = 0.06$, $D/a = 3$, $\sigma = 3 \times 10^7$ $\Omega^{-1}\mathrm{m}^{-1}$ ($X = 1, 2, 4, 8, 16$).

	η_{rad} [%] from (5.96)			η_{rad} [%]	P_{rad}
Loops	21×41	41×81	81×161	from (5.97)	[mW]
1	99.7	99.7	99.7	99.8	3.47
2×2	99.8	99.8	99.8	99.8	9.35
4×4	101.1	99.8	99.8	99.8	34.0
8×8	90.5	100.9	99.8	99.8	130
16×16	30.0	90.1	100.9	99.8	504

81×161 integration points (Matlab 7.02 implementation on a HP PC with Windows XP Prof. 2002 (SP3), Intel Core (TM)2 Duo CPU, E6550 @2.33 GHz, 1.95 GB RAM). This difference is explained by the relatively large evaluation time of the far field. Having computed the current coefficients $\mathbf{I}^{\mathrm{MoM}}$, the far field of each loop is expressed as a sum of Bessel functions [79, App. C]. Both such an analytical approximation and a numerical computation of the far field of each element are costly compared to the matrix-vector products in (5.99).

Next, we consider the TSA as specified in Fig. 4.19 with height 30 cm, width 12.5 cm, slot opening (at the top) 10.5 cm, and tapering opening rate 0.25 cm^{-1}. The TSA is excited by a voltage source across the slotline gap at 0.5–2 GHz. In the test cases we specify the thickness d or bound it from below; d is bounded from above by $d/\lambda_0 \ll 1$, where $\lambda_0 \geq 15$ cm.

Figure 5.13 shows η_{rad} for 0.5, 1, and 2 GHz as a function of σ, where we employ the approximation $Z_S = (1 + j)/2\sigma\delta$. For Z_S errors of less than 0.5%, the curves apply to thicknesses d that satisfy $d/\delta \geq 6$. Note that $\delta = 1.59 \times \{10^{-1}, 10^{-2}, 10^{-3}\}$ mm for $\sigma = 10^4, 10^6, 10^8$ $\Omega^{-1}\mathrm{m}^{-1}$ at 1 GHz and, hence, $Z_S = (1 + j) \times \{0.31, 0.031, 0.0031\}$ Ω with a relative error of less than 0.5% for $d \geq 9.6 \times \{10^{-1}, 10^{-2}, 10^{-3}\}$ mm. For increasing σ, η_{rad} in Fig. 5.13 is approaching 100%. Although the (normalized) magnitudes of the surface currents at 1 GHz for $\sigma = 10^4, 10^6, 10^8$ $\Omega^{-1}\mathrm{m}^{-1}$ hardly show differences in our simulations, the differences in η_{rad} are clearly noticeable for the different values of σ.

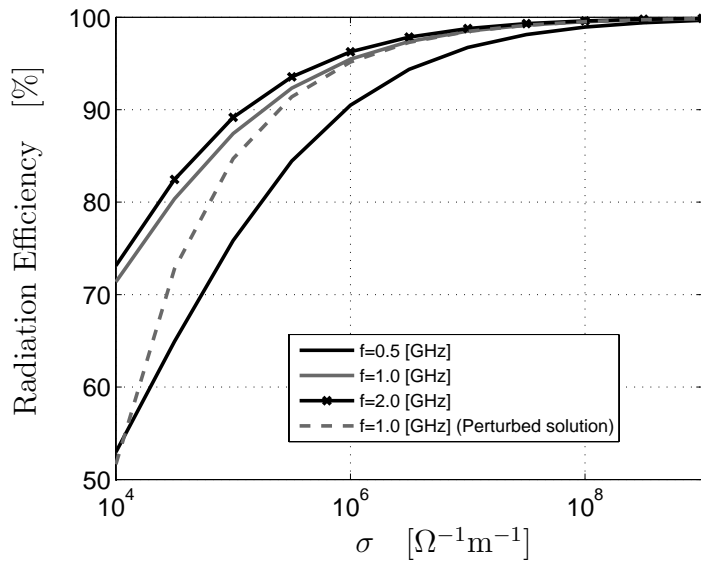As proposed for lossy waveguides in [172, pp. 44–46] an approximation of P_{diss} for Z_S

Figure 5.13: For a single TSA: η_{rad} as a function of the conductivity σ computed for 0.5, 1, and 2 GHz, $Z_S = (1+j)/2\sigma\delta$.
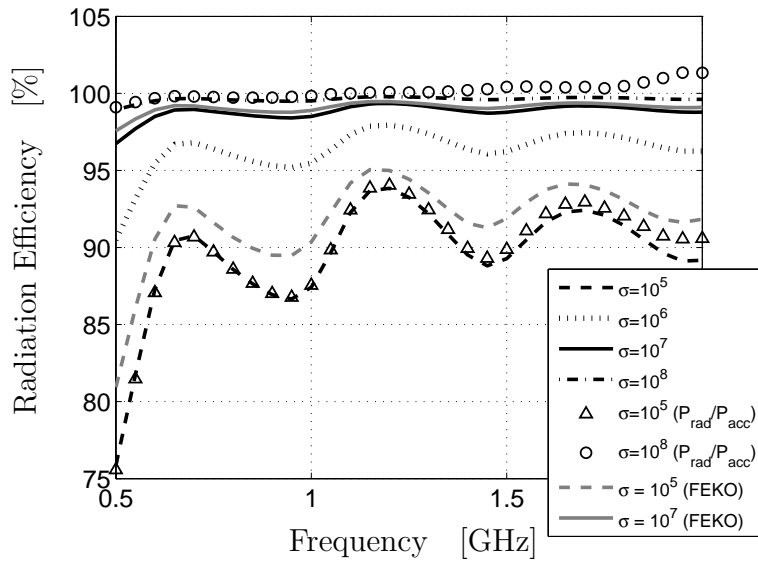

Figure 5.14: For a single TSA: η_{rad} as a function of the frequency for $\sigma = \{10^5, 10^6, 10^7, 10^8\}$ $\Omega^{-1}\text{m}^{-1}$, $Z_S = (1+j)/2\sigma\delta$. First four curves computed with (5.99) and fifth and sixth curve computed with (5.96), where P_{rad} is computed by a composite Simpson rule with steps of 5°.

small may be obtained from (5.99) with $\mathbf{I}^{\text{MoM}}$ replaced by $\mathbf{I}^{\text{PEC}}$. This approximation is first-order accurate and, hence, variations of P_{acc} with respect to the PEC case must be small. Comparing the curves for the perturbed solution and the "exact" solution at 1 GHz in Fig. 5.13, we observe that for higher values of σ the two solutions match. For lower values the perturbed solution underestimates η_{rad}.

For an aluminum TSA, operating at 1 GHz, with $d = 1$ mm and $\sigma = 3 \times 10^7 \ \Omega^{-1}\text{m}^{-1}$, $d/\delta = 344 \gg 1$. Thus $Z_S = (1 + j)/2\sigma\delta = 0.0057(1 + j) \ \Omega$. Fig. 5.13 shows that $\eta_{\text{rad}} = 99.1\%$. Hence T_{sys} increases by 2.4 K for $T_{\text{amb}} = 300$ K.

Fig. 5.14 shows η_{rad} as a function of the frequency for $\sigma = 10^5, 10^6, 10^7, 10^8 \ \Omega^{-1}\text{m}^{-1}$. For $\sigma = 10^5, 10^8 \ \Omega^{-1}\text{m}^{-1}$, η_{rad} is also computed with (5.96) and for $\sigma = 10^5, 10^7 \ \Omega^{-1}\text{m}^{-1}$ with FEKO. We observe that η_{rad} has an oscillatory behavior. which is caused by the frequency dependence of the surface current. At higher frequencies, η_{rad} obtained with (5.96) differs up to 2% from the values obtained with (5.97) and (5.99) and, for $\sigma = 10^8 \ \Omega^{-1}\text{m}^{-1}$, η_{rad} becomes larger than 100%, which points to inaccuracies in the computed P_{rad}. The results obtained by FEKO for $\sigma = 10^7 \ \Omega^{-1}\text{m}^{-1}$ differ at most 0.8% from our results. Note that η_{rad} of a PEC TSA computed by FEKO is 100% as in our simulations. For $\sigma = 10^5 \ \Omega^{-1}\text{m}^{-1}$ the difference is less than 3% except near 0.3 GHz, where it runs up to 5%. These large differences are explained below.
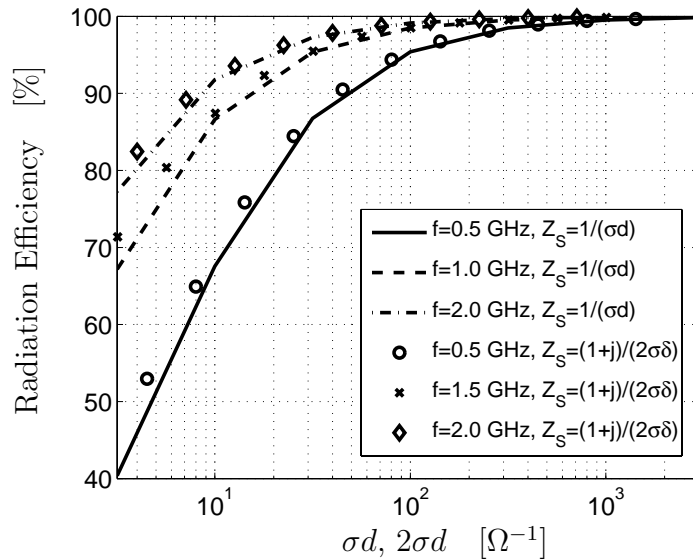

Figure 5.15: For a single TSA: η_{rad} for 0.5, 1, 2 GHz as a function of $2\sigma\delta$ for $Z_S = (1+j)/2\sigma\delta$ (symbols) and as a function of σd for $Z_S = 1/\sigma d$ (solid curves).

Fig. 5.15 shows η_{rad} for 0.5, 1, and 2 GHz as a function of $2\sigma\delta$ and σd for $Z_S = (1+j)/2\sigma\delta$ and $Z_S = 1/\sigma d$, respectively, where σ is varied. For higher values of σd and $2\sigma\delta$ the results match, which follows from P_{diss} being independent of $\mathfrak{Im}\{Z_S\}$ according to (5.103) and (5.104), and from $\mathfrak{Re}\{Z_S\}$ being described by σd and $2\sigma\delta$ for the two surface-impedance expressions. The η_{rad} differences only occur due to MoM differences. A similar observation is valid for IE3D, which employs $Z_S = 1/\sigma d$. Dividing the band into subbands and setting $d = 2\delta$ in each subband (at the center frequency), we obtain the asymptotic value of $\mathfrak{Re}\{Z_S\}$ for $d/\delta \gg 1$, i.e., $1/2\sigma\delta$, which we can employ in the MoM and in the η_{rad} computation.

Table 5.3: For a single TSA: η_{rad} for three different mesh densities and $\sigma = 10^4, 10^7 \ \Omega^{-1}\text{m}^{-1}$ at 1 GHz, $Z_S = (1 + j)/2\sigma\delta$.

	$\sigma = 10^4 \ \Omega^{-1}\text{m}^{-1}$	$\sigma = 10^7 \ \Omega^{-1}\text{m}^{-1}$
10 RWGs/λ_0	68.0%	98.3%
20 RWGs/λ_0	75.0%	98.8%
40 RWGs/λ_0	77.7%	99.0%

Table 5.3 shows that for three mesh densities η_{rad} varies by 10% for $\sigma = 10^4 \ \Omega^{-1}\text{m}^{-1}$ and by 0.7% for $\sigma = 10^7 \ \Omega^{-1}\text{m}^{-1}$. Thus, the mesh density has to be increased in case the conductivity is decreased to maintain a constant accuracy of η_{rad}. This aspect is explained by writing the EFIE for constant Z_S as $-\mathcal{Z}^{-1}\boldsymbol{E}_{\text{tan}}^i/Z_S = (1/Z_S - \mathcal{Z}^{-1})\boldsymbol{J}_S$, where $\mathcal{Z}\boldsymbol{J}_S = \boldsymbol{E}_{\text{tan}}^s(\boldsymbol{J}_S)$. Since the eigenvalues of $\mathcal{Z}^{-1}$ accumulate at zero, they are close to $1/Z_S$ for larger values of Z_S and, hence, the solution of the EFIE is more sensitive to perturbations. Consequently, for lower σ the mesh needs to be denser or numerical integration for P_{rad} can be employed. In the described FEKO simulations the mesh is denser than in our simulations. Taking a coarser FEKO mesh for $\sigma = 10^5 \ \Omega^{-1}\text{m}^{-1}$ reduces the differences with our results in Fig. 5.14 from 3% to 1%.

It is pointed out that, although the above described method guarantees physically meaningful results near $\eta_{\text{rad}} = 100\%$, the overall accuracy of modeling conductor losses using impedance boundary conditions remains a challenging problem, in particular when currents flow across curved surfaces and discontinuities.

5.9   Conclusions

A framework has been presented to numerically analyze the system sensitivity of active antenna arrays operating on receive. Additionally, semi-analytical methods have been developed to describe the noise-coupling effects in active arrays of mutually-coupled antenna elements; they generalize the noise-coupling models as presented by others and increase the fundamental understanding of the receiver sensitivity limiting factors.

It has been shown that the receiver can be "noise decoupled" via the active reflection coefficients of the individual antenna elements. Consequently, and to ease the evaluation of the LNA noise contribution, the full antenna S-parameter matrix can be replaced by a diagonal matrix where the diagonal elements are the active reflection coefficients of the individual array elements. As a result, the total receiver temperature is minimized if the noise contribution for each receiver channel is minimized, which can be achieved by noise matching of the LNA to the active reflection coefficient of the corresponding antenna element (for one specific set of excitation coefficients).

The herein presented "noise-decoupling technique" has been used to represent an antenna array system by an equivalent single-channel receiver. Accordingly, expressions have been developed for the beam sensitivity $A_\mathrm{eff}/T_\mathrm{sys}$ of the antenna system. The model constitutes the parameters: η_coup (coupling efficiency); η_mis (mismatch efficiency); η_rad (radiation efficiency); $G_\mathrm{Eq}^\mathrm{power}$ (equivalent power gain), and; $T_\mathrm{Eq}^\mathrm{LNA}$ (equivalent amplifier noise temperature). The mismatch efficiency reduces both the system available gain and the receiver sensitivity, the latter being caused by a noise mismatch. At the input of the antenna system (the sky), the radiation efficiency also reduces both the system available gain and the receiver sensitivity, the latter being caused by an increase in the receiver and thermal noise temperature.

The aforementioned numerical and semi-analytical methods have been cross-validated and the consistency of the results was demonstrated. Furthermore, for an experimental setup, it has been shown that the absolute noise-power level at the receiver output can be accurately predicted by numerical simulations.

It has been identified that a number of commercial codes are inadequate in computing the dissipative loss of antennas. In fact, the numerically computed η_rad of antennas may highly exceed 100%. This occurs when the radiated power is determined through a numerical

integration of the Poynting vector. The determination of the far field and its numerical integration do not only lead to a high computational cost, but also to substantial (integration) errors, in particular for large arrays with rapidly varying far fields. The remedy is to determine η_{rad} through the dissipated power P_{diss} for which it has been shown that η_{rad} cannot become larger than 100%, independent of numerical errors. Moreover, the data is intrinsically available in a MoM computation and P_{diss} can be computed by two matrix-vector multiplications. Although this method guarantees physically meaningful results near $\eta_{\text{rad}} = 100\%$, the overall accuracy of modeling conductor losses using impedance boundary conditions remains a challenging problem, in particular when currents flow across curved surfaces and discontinuities.

Numerical examples showed that, if η_{rad} is expected to be larger than $\sim 95\%$, the losses can be computed up to first-order accuracy by simply replacing the actual current by the current for PEC surfaces.

For a typical aluminum TSA, operating at 1 GHz, with the thickness of the conductor $d = 1$ mm and conductivity $\sigma = 3 \times 10^7$ $\Omega^{-1}\text{m}^{-1}$, it has been shown that $\eta_{\text{rad}} = 99.1\%$ which means that T_{sys} increases by 2.4 K for $T_{\text{amb}} = 300$ K. An increase by 2.4 K may be significant when the target system temperature is set to 50 K, of which 7–10 K is the maximum allowed contribution due to the antenna including the connection loss with a low noise amplifier at the feedpoint. This demonstrates that it is important to determine this increase in noise temperature accurately.

Chapter 6

Conclusions and Recommendations

This dissertation is a result of five years of research, which was embarked upon in 2004-2005 at ASTRON, Dwingeloo, the Netherlands. The work has been primarily performed in collaboration with the Electromagnetics group of the Eindhoven University of Technology, Eindhoven, the Netherlands, and the Electrical Engineering Department of the Pennsylvania State University, Pennsylvania.

6.1   Conclusions

As described below, this thesis assesses two major shortcomings of commercially available software tools in modeling large antenna arrays for use in low-noise actively beamformed receiving systems.

Firstly, the antennas that are considered in this thesis not only exhibit fine geometrical features, but are also physically large. These multiscale features have serious repercussions on the memory requirements and execution times of electromagnetic field solvers. For integral-equation-based moment-method solvers, the computational burden is further exacerbated when dielectric materials are involved. It is a major challenge to alleviate these problems in order to account for the performance limiting factors of the presently designed antenna arrays. For instance, the arrays of electrically interconnected microstrip-fed Tapered Slot Antenna (TSA) elements have, thus far, been designed by analyzing a single (or

doubly-polarized) antenna element embedded in an infinitely large phased-steered array antenna. However, to refine the design of the antenna array, it is essential to account for the finite-array effects and solve the large problem for the actual (nonuniform) excitation scheme in core, which is beyond the reach of currently available solvers.

Secondly, it is crucial to co-design the antenna in combination with highly integrated electronics for maximizing the receiver sensitivity of the antenna system in its entirety. This requires a dedicated system analysis tool which not only accounts for the antenna array and its external source environment (signal and noise), but also for the low-noise amplifiers and the beamforming circuit. To date, these types of integrated analyses are beyond the scope of most general-purpose codes. In particular, the optimal interfacing reference impedance in most designs is assumed to be the standard 50 Ω, which allows (weakly-coupled) antenna elements to be designed separately from the electronics, but this solution is semi-optimal.

To address the above alluded problems, two main topics have been addressed:

- Extending the capability of the method of moments to solve large antenna array problems.

- Modeling of the receiver sensitivity of actively beamformed antenna array systems.

6.1.1   Conclusions on the Enhanced Moment Method

Various computational techniques have been combined to mitigate the memory overflow problem and to reduce the execution time of conventional integral-equation-based moment methods in analyzing large antenna structures (*cf.* Chapter 4). For instance, instead of employing a large number of independent low-level basis functions for the current, we use the Characteristic Basis Function Method (CBFM) to reduce the Degrees of Freedom (DoF) of the discretized current by employing a relatively small set of physics-based macro-domain basis functions, each of which is constructed as a fixed combination of low-level basis functions. The resulting matrix equation can be solved directly without resorting to iteration. Although this reduces the solve time significantly, the total execution time is dominated by the generation process of the Characteristic Basis Functions (CBFs) and the time to construct the reduced matrix.

The construction of the reduced matrix has been expedited by realizing that the coupling matrix, which represents the reaction integrals between distant groups of CBFs, is of low rank. This has been exploited by using the Adaptive Cross Approximation (ACA) algorithm. The numerical efficiency of this iterative algorithm increases with an increasing separation distance between groups of CBFs, since the rank deficiency of the associated block matrices then also increases. Reciprocity is exploited to fill only half of the reduced matrix (approximately). The matrix fill time is reduced even further by exploiting translation symmetries in the configuration, because many block matrices of the reduced matrix are identical and can be simply copied in the construction of the reduced matrix. The latter is possible because of the (quasi-Toeplitz) translation symmetry that exists between the reaction integrals of group pairs of CBFs. This property can only be exploited if the array structure is meshed such that it facilitates a one-to-one mapping of identical CBFs throughout the array lattice. For this purpose, a specific meshing strategy has been proposed, which is nontrivial for the presently considered overlapping domain decomposition technique, where CBFs between adjacent subdomains partially overlap to model an electrical connection between the subdomains. On the contrary, if one assumes identical sets of CBFs on all array elements, one needs to employ additional sets of independent junction basis functions to synthesize a continuous current across common interfaces, which would unnecessarily increase the size of the matrix equation that needs to be solved.

A novel method has been developed to numerically generate CBFs. First, a small subarray is formed by extracting a single antenna element from the fully meshed array along with its direct electrically interconnected adjacent elements. Afterwards, this subarray is excited in various ways to generate a number of distinct current distributions. Then, these currents are truncated to the mesh of a single element plus a minor extension (a single cell suffices). In this manner, the supports of the CBFs is reduced, thereby eliminating undesired edge-truncation effects at the edges of the outer elements. Finally, the CBFs are reshaped/weighted with the aid of trapezoidal taper functions to ensure that the superposition of partially overlapping CBFs correctly models a continuous junction current across the interconnections between antenna elements.

The above enhanced moment-method technique has been implemented on a regular desktop computer (or notebook) with 2 GB RAM and a CPU clock of 1.73 GHz (single core); dielectric-free arrays of 100+ dual-polarized, or 400+ single-polarized TSA element configurations can be handled. The maximum problem size that a monolevel CBFM approach can handle on this hardware platform is of order 7000 CBFs ($\sim$ 100.000 low-level basis

functions) and is typically solved within a few hours. The exact simulation time and size of the problem that can be analyzed depends on numerous factors, such as the degree of translation symmetry that exists between group pairs of CBFs, the geometrical details of the structure, the number of unique sets of CBFs that need to be generated, the element type, the total number of CBFs to achieve a certain accuracy level, the sparsity of the array, the ACA threshold, etc. For instance, for an array of disconnected equally-spaced dipole antennas, one can compute the radiation patterns and impedance matrix of 800+ dipole antennas within $\sim$ 15 min, while maintaining a relative error level of a few percent with respect to a direct MoM solution (for smaller structures).

The scope and range of application of the above EM code has been enlarged by developing a novel reduced-order model for microstrip-fed TSAs. Even though the microstrip feed forms an integral part of the radiating antenna elements, one can separately characterize the antenna array by EM models, and the feed by circuit models. Afterwards, their solutions are combined to arrive at the total aggregated antenna model. This approach results in a fast optimization of the antenna elements using a dielectric-free EM formulation, while the characterization of the feed circuitry remains unaltered. Although earlier proposed antenna-feed decompositions were found to be inaccurate, we have demonstrated that a relative difference of less than 20% with the measured impedance characteristics is achievable.

Increasing the size of the antenna array will ultimately render the problem unmanageable, even for a CBFM approach. Therefore, to tackle the large arrays of disjoint subarray problems, a perturbation approach has been developed which exploits the relatively low coupling between the subarrays. More specifically, the active antenna impedance matrix of a central subarray has been computed by accounting for the surrounding actively phase-steered subarrays through the use of periodic boundary conditions whose infinite sum is truncated in the spatial domain. If the strength of the coupling between tiles increases, and/or for large scan angles, more tiles need to be included to achieve convergence.

6.1.2   Conclusions on the System Modeling Aspects

A framework has been developed to numerically analyze the system sensitivity of actively beamformed antenna arrays (*cf.* Chapter 5). A scattering formulation is used to model the interaction of transmission-line waves between receiver components. The internal sig-

nal and noise sources are represented externally at the ports of each microwave device by a signal-wave vector and a noise-wave correlation matrix, respectively. The antenna array on receive is modeled by an equivalent circuit model. Both the external nonuniform brightness temperature distribution of the sky and the incident radiation from (partially polarized) celestial signal sources are mapped by the element radiation patterns to the output ports of the array elements and are represented by Thévenin sources. The propagation of transmission-line signal and noise waves throughout the system is analyzed by means of the connection matrix theory. The so-developed system simulator allows to quantify the receiver sensitivity of antenna array receiving systems, as well as to determine the overall system available gain, and to study the noise emitted by the input ports of the amplifiers which re-enters the system coherently through the mutually-coupled antenna elements (noise-coupling phenomenon). The system simulator includes models for microstrip transmission lines and compound structures, such as a Wilkinson power combiner, and has been validated for various cases, among which a practical measurement setup of an actively beamformed antenna system.

Complementary to the above-described numerical approach, semi-analytical methods have been developed that generalize the noise-coupling models as presented by others. These models increase the fundamental understanding of the receiver sensitivity limiting factors. Furthermore, it was found that, to ease the evaluation of the total receiver noise temperature, one can "noise decouple" the receiver by replacing the fully-populated scattering matrix of the antenna array by a diagonal matrix, whose diagonal entries are the active reflection coefficients of the antenna elements. Subsequently, the total noise temperature is evaluated as a weighted sum of uncorrelated channel noise contributions. The noise per channel can be minimized by noise matching the amplifiers to the active impedance of the corresponding antenna element.

The "noise-decoupling technique" described above has been applied to represent the beamformed antenna array by an equivalent single-channel receiving system. This simplification allows the use of the standard IEEE definitions and terms for single-port antennas and to derive formulas for the system sensitivity of the equivalent single-channel receiving system. The results obtained by these expressions have been validated by a numerical calculation.

The radiation efficiency of an antenna has a prominent effect on the receiver sensitivity; it reduces the signal strength in front of the first stage of amplification, but also contributes to the total system noise temperature. Most commercial EM solvers are inadequate in

determining the radiation efficiency for low-loss antennas, because the computed efficiencies often exceed 100%, particularly when the radiation efficiency is computed as a ratio between the radiated power and the antenna's accepted power. In conclusion, whenever a surface current solution is available (as in a MoM approach), it is advised to directly compute the dissipated power of an antenna. This is numerically efficient and does not lead to efficiencies larger than 100%.

6.2   Recommendations

The proposed perturbation method for handling large antenna arrays of disjoint subarrays computes the active impedances of a central subarray only (no patterns), and is therefore of limited use. To determine all the antenna element patterns and the passive input impedance matrix of the entire array, it is recommended to employ a multilevel CBFM approach [173]. This method may ultimately reduce the number of CBFs as few as one per antenna element (the minimum required number), as a result of which one can solve much larger problems.

The domain decomposition technique as presented in this thesis is inherently parallelizable and therefore well-suited to be run on supercomputers or computers equipped with multi-core CPUs [174]. This may be a desired extension in case the complexity and/or the problem increases beyond an unmanageable size.

The impact of the imperfect polarization characteristics of an actively beamformed antenna-array system on the recoverability of the polarization information of the incident field (over a wide field-of-view) is not well understood. The beam-orthogonality measure introduced in this dissertation is an initial step towards comprehension. Preliminary results addressing this issue have been published in [175].

To increase the class of real-world antenna problems that can be solved, it may be worth extending the macro-basis function approach such that dielectric materials can be handled. For instance, the fields (or currents) inside a dielectric material may be synthesized by a superposition of partially overlapping macro-basis functions, each of which represents a closed-form solution to a canonical problem. This concept is explained in [176] and is still in an initial research phase.

To anticipate to the future trends observed in high-frequency electronics, it is recommended to combine macro-basis function approaches with linear embedding techniques [177]. Such a combined approach is numerically efficient, generic, and opens up new possibilities in the analysis and design of packaged active electronics that is highly integrated with waveguiding and/or antenna structures.

6.3   Impact of the Research

The work as presented in this dissertation has led to a number of journal and conference papers as well as to the development of the software tool named CAESAR[1]. An overview has been given at the EuMC 2008 in Amsterdam (see Appendix F and [163]). The combined electromagnetic-microwave simulator has been used at ASTRON for a number of aperture- and focal-plane array related projects. In particular to perform:

- Station configuration and baseline redundancy studies for the LOFAR project (Wim van Cappellen, Parisa Noorishad *et al.*) [178].

- The sensitivity modeling of the APERTIF focal-plane array receiving system (Marianna Ivashina, Oleg Iupikov *et al.*) [179].

- The design and modeling of an EMBRACE precursor called VALARRAY (Rob Maaskant, Mariya Popova, Elena Redkina *et al.*) [89].

- The design and experimental characterization of the THACO hot-cold radiometric measurement facility (Rob Maaskant, Marianna Ivashina *et al.*) [180].

- The analysis of low-frequency rotating magnetic fields to avoid nulls in the field of an RFID system (Rob Maaskant *et al.*) [181].

Furthermore, CAESAR is available to international SKA partners and has specifically been provided to the Universities of Manchester, Cambridge, and the Yebes Observatory. The numerical tool has fostered the development of analytical system models and international collaborations with Professors Per-Simon Kildal and Karl Warnick [157, 158]. As a result of these collaborations, a new set of IEEE standard definitions of antenna figures of

---

[1]CAESAR: Computationally Advanced and Efficient Simulator for ARrays.

merit for beamforming arrays that accounts for the effect of interactions between antenna element mutual coupling and receiver noise on system performance has recently been proposed [182], and presented to the IEEE committee of standards during the AP symposium in Charleston, South Carolina, 2009. It has been shown that these generalized definitions for multi-port antennas reduce to the IEEE standard definitions for a single-port antenna.

Appendix A

The Inverse of the 2-D Operator $\overline{\overline{A}}^{-1}$

With reference to Eq. (3.23), the objective is to find the spectral inverse of the 2-D differential dyadic operator

$$\overline{\overline{\mathcal{A}}} = \left(\overline{\overline{\mathcal{I}}}_t + \frac{\boldsymbol{\nabla_t}\boldsymbol{\nabla_t}}{k^2} \right) \tag{A.1}$$

which acts on transverse vectors $\boldsymbol{x}_t = x\hat{\boldsymbol{x}} + y\hat{\boldsymbol{y}}$, that is,

$$\overline{\overline{\mathcal{A}}} \cdot \boldsymbol{x}_t = \boldsymbol{b}_t \tag{A.2}$$

where the transverse vector $\boldsymbol{b}_t$ is the result. The above system of linear equations can be solved for $\boldsymbol{x}_t$ through the application of the inverse dyadic $\overline{\overline{\mathcal{A}}}^{-1}$, i.e.,

$$\boldsymbol{x}_t = \overline{\overline{\mathcal{A}}}^{-1} \cdot \boldsymbol{b}_t \tag{A.3}$$

where $\overline{\overline{\mathcal{A}}}^{-1}$ is the operator, yet to be determined.

In the spectral domain, (A.2) transforms into

$$\left(\overline{\overline{I}}_t - \frac{\boldsymbol{k}_t\boldsymbol{k}_t}{k^2} \right) \cdot \check{\boldsymbol{x}}_t = \check{\boldsymbol{b}}_t \tag{A.4}$$

which can be written as

$$k^2\check{\boldsymbol{x}}_t - \boldsymbol{k}_t \left(\boldsymbol{k}_t \cdot \check{\boldsymbol{x}}_t \right) = k^2\check{\boldsymbol{b}}_t. \tag{A.5}$$

This, in turn, leads to the following set of equations:

$$k^2 \breve{x}_x - k_x \left(k_x \breve{x}_x + k_y \breve{x}_y \right) = k^2 \breve{b}_x \tag{A.6a}$$

$$k^2 \breve{x}_y - k_y \left(k_x \breve{x}_x + k_y \breve{x}_y \right) = k^2 \breve{b}_y \tag{A.6b}$$

In matrix notation, this is written as

$$\begin{pmatrix} 1 - k_x^2/k^2 & -k_x k_y/k^2 \\ -k_x k_y/k^2 & 1 - k_y^2/k^2 \end{pmatrix} \begin{pmatrix} \breve{x}_x \\ \breve{x}_y \end{pmatrix} = \begin{pmatrix} \breve{b}_x \\ \breve{b}_y \end{pmatrix} \tag{A.7}$$

which has the solution

$$\begin{pmatrix} \breve{x}_x \\ \breve{x}_y \end{pmatrix} = \frac{k^2}{k_z^2} \begin{pmatrix} 1 - k_y^2/k^2 & k_x k_y/k^2 \\ k_x k_y/k^2 & 1 - k_x^2/k^2 \end{pmatrix} \begin{pmatrix} \breve{b}_x \\ \breve{b}_y \end{pmatrix} \tag{A.8}$$

where the inverse of the matrix has been used. The inverse operator $\overline{\overline{A}}^{-1}$ is found by expanding the matrix equation (A.8) as

$$\breve{x}_x = k_z^{-2} \left(k^2 \breve{b}_x - k_y \left[k_y \breve{b}_x - k_x \breve{b}_y \right] \right) \tag{A.9a}$$

$$\breve{x}_y = k_z^{-2} \left(k^2 \breve{b}_y + k_x \left[k_y \breve{b}_x - k_x \breve{b}_y \right] \right) \tag{A.9b}$$

where one recognizes that $k_y \breve{b}_x - k_x \breve{b}_y = (\hat{\boldsymbol{z}} \times \boldsymbol{k}_t) \cdot \breve{\boldsymbol{b}}_t$. Hence, it is easily observed that (A.9) can be compactly written as

$$\breve{\boldsymbol{x}}_t = k_z^{-2} \left[k^2 \overline{\overline{I}}_t - (\hat{\boldsymbol{z}} \times \boldsymbol{k}_t)(\hat{\boldsymbol{z}} \times \boldsymbol{k}_t) \right] \cdot \breve{\boldsymbol{b}}_t \tag{A.10}$$

with

$$\overline{\overline{A}}^{-1} = k_z^{-2} \left[k^2 \overline{\overline{I}}_t - (\hat{\boldsymbol{z}} \times \boldsymbol{k}_t)(\hat{\boldsymbol{z}} \times \boldsymbol{k}_t) \right] \tag{A.11}$$

which is the inverse operator of (A.1) in the spectral domain.

Appendix B

Numerical Integration over Triangular Supports

The numerical integration of a vector function $\boldsymbol{g}\left(\boldsymbol{r}\right)$ over a canonical triangular support can be performed through multidimensional Gaussian quadrature rules that are exact for polynomials up to a certain specified order.
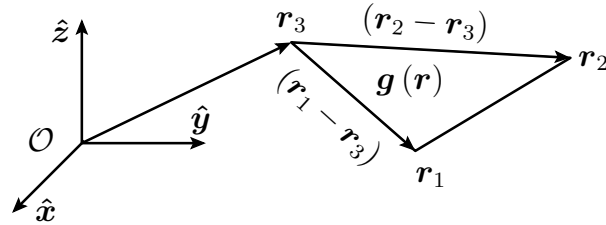

Figure B.1: Vector function $\boldsymbol{g}\left(\boldsymbol{r}\right)$ subject to integration over a triangular support.

Let the three corner vertices of a triangle T be denoted by $\boldsymbol{r}_1$, $\boldsymbol{r}_2$ and $\boldsymbol{r}_3$, as in Fig. B.1. Then, the surface of a triangle can be parameterized in terms of local coordinates (ξ, η), i.e.,

$$\begin{aligned}
\boldsymbol{r}(\xi, \eta) &= \boldsymbol{r}_3 + \xi\left(\boldsymbol{r}_1 - \boldsymbol{r}_3\right) + \eta\left(\boldsymbol{r}_2 - \boldsymbol{r}_3\right) \\
&= \xi\boldsymbol{r}_1 + \eta\boldsymbol{r}_2 + \left(1 - \xi - \eta\right)\boldsymbol{r}_3
\end{aligned} \tag{B.1}$$

for $0 \leq \eta \leq 1$ and $0 \leq \xi \leq 1 - \eta$.

The function $\boldsymbol{g}\left(\boldsymbol{r}\right)$ is then integrated over the triangular surface with area A as

$$\iint_T \boldsymbol{g}\left(\boldsymbol{r}\right) \mathrm{d}S = \int_0^1 \int_0^{1-\eta} \boldsymbol{g}\left[\boldsymbol{r}(\xi,\eta)\right] \left\|\frac{\partial \boldsymbol{r}}{\partial \xi} \times \frac{\partial \boldsymbol{r}}{\partial \eta}\right\|_2 \mathrm{d}\xi\, \mathrm{d}\eta$$

$$= \left\|(\boldsymbol{r}_1 - \boldsymbol{r}_3) \times (\boldsymbol{r}_2 - \boldsymbol{r}_3)\right\|_2 \int_0^1 \int_0^{1-\eta} \boldsymbol{g}\left(\xi,\eta\right) \mathrm{d}\xi\, \mathrm{d}\eta$$

$$= 2A \int_0^1 \int_0^{1-\eta} \boldsymbol{g}\left(\xi,\eta\right) \mathrm{d}\xi\, \mathrm{d}\eta \qquad (\text{B.2})$$

where the Jacobian equals twice the area of the triangle A. With reference to Eq. (B.2), the quadrature rule is herein defined as

$$\frac{1}{A} \iint_T \boldsymbol{g}\left(\boldsymbol{r}\right) \mathrm{d}S = 2 \int_0^1 \int_0^{1-\eta} \boldsymbol{g}\left(\xi,\eta\right) \mathrm{d}\xi\, \mathrm{d}\eta = \sum_{p=1}^P w_p\, \boldsymbol{g}\left(\xi_p,\eta_p\right) + \mathcal{O}\left(h^P\right) \qquad (\text{B.3})$$

where the residual error depends upon the maximum edge length h of the triangle. Furthermore, $P-1$ is the order of the quadrature rule, and $\boldsymbol{g}\left(\xi_p,\eta_p\right)$ for $p = 1, 2, \ldots, P$ are the evaluated function values at P quadrature points which are added through a weighted sum with weights $\{w_p\}$.

By introducing $\zeta_p = 1 - \xi_p - \eta_p$ in (B.1), a symmetric 7-point rule ($P = 7$) can be derived that is independent on the ordering of the corner vertices. The results have been adopted from [183] and are listed in Table B.1 in terms of the simplex coordinates (ξ_p, η_p, ζ_p); this is an integration rule that is exact for quintic polynomials in two dimensions [184].

Table B.1: Quadrature points and associated weights for $P = 7$.

ξ_p	η_p	ζ_p	w_p
γ	γ	γ	0.225000000000000
α_1	β_1	β_1	0.132394152788506
β_1	α_1	β_1	0.132394152788506
β_1	β_1	α_1	0.132394152788506
α_2	β_2	β_2	0.125939180544827
β_2	α_2	β_2	0.125939180544827
β_2	β_2	α_2	0.125939180544827

with

α_1	0.059715871789770
β_1	0.470142064105115
α_2	0.797426985353087
β_2	0.101286507323456
γ	0.333333333333333

The results for a symmetric 3-point integration rule ($P = 3$) are listed in Table B.2 and are exact for quadratic polynomials in two dimensions [183].

Table B.2: Quadrature points and associated weights for $P = 3$.

ξ_p	η_p	ζ_p	w_p
α	β	β	0.333333333333333
β	α	β	0.333333333333333
β	β	α	0.333333333333333

with

α	0.666666666666667
β	0.166666666666667

Finally, for a 1-point rule ($P = 1$), one simply obtains

Table B.3: Quadrature points and associated weights for $P = 1$.

ξ_p	η_p	ζ_p	w_p
α	α	α	1.000000000000000

with

α	0.333333333333333

which is, obviously, only accurate if the function $\boldsymbol{g}$ is virtually linear over the facet of the triangle. Note that the above quadrature rule is known as the midpoint integration rule, i.e.,

$$\frac{1}{A} \iint_T \boldsymbol{g}(\boldsymbol{r}) \, \mathrm{d}S \approx \boldsymbol{g}(\boldsymbol{r}_c), \tag{B.4}$$

where $\boldsymbol{g}(\boldsymbol{r}_c)$ is simply the value of $\boldsymbol{g}$ evaluated at the centroid of the triangle.

Appendix C

Surface Impedance Integral

In the process of computing the moment matrix elements, which specifically pertains to the case of a discretized EFIE and current sheet $\mathcal{S}$ with a non-zero surface impedance $Z_S(\boldsymbol{r})$, it is necessary to evaluate integrals of the type [see Eq. (3.76)]

$$I_{mn}^{\pm} = Z_S^{\pm} \iint\limits_{T_m^{\pm}} \boldsymbol{f}_n \cdot \boldsymbol{f}_m \, \mathrm{d}S \tag{C.1}$$

where $Z_S^{\pm}$ is assumed constant over the corresponding triangular support $T_m^{\pm}$ of the testing function $\boldsymbol{f}_m$. It should be noted that $\boldsymbol{f}_n \cdot \boldsymbol{f}_m = 0$ in case the supports of $\boldsymbol{f}_n$ and $\boldsymbol{f}_m$ are non-overlapping. Hence, we consider the case that at least one of the triangular supports of $\boldsymbol{f}_n$ is in common with one of those in $\boldsymbol{f}_m$. A typical situation is shown in Fig. C.1, where the triangular overlapping area $T_m^{\pm}$ is subject to the evaluation of (C.1).
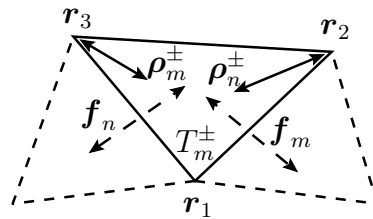
Figure C.1: The case that $\boldsymbol{f}_m$ and $\boldsymbol{f}_n$ have one triangular support in common.

We need to evaluate the two-dimensional integral

$$\iint_{T_m^\pm} \boldsymbol{f}_n \cdot \boldsymbol{f}_m \, \mathrm{d}S = 2A \int_0^1 \int_0^{1-\eta} \boldsymbol{f}_n \cdot \boldsymbol{f}_m \, \mathrm{d}\xi \, \mathrm{d}\eta \tag{C.2}$$

where (B.2) has been used in the mapping to the local (simplex) coordinates (ξ, η). The position vector is parameterized through the relation [*cf.* Eq. (B.1)]

$$\boldsymbol{r}(\xi, \eta) = \xi \boldsymbol{r}_1 + \eta \boldsymbol{r}_2 + (1 - \xi - \eta) \, \boldsymbol{r}_3 \tag{C.3}$$

for $0 \leq \eta \leq 1$ and $0 \leq \xi \leq 1 - \eta$. Note that, on account of (3.70), one can write that

$$\boldsymbol{f}_n \cdot \boldsymbol{f}_m = \pm \frac{\ell_n}{2A_n^\pm} \boldsymbol{\rho}_n^\pm \cdot \frac{\ell_m}{2A_m^\pm} \boldsymbol{\rho}_m^\pm = \pm \frac{\ell_n \ell_m}{4A^2} (\boldsymbol{r} - \boldsymbol{r}_n) \cdot (\boldsymbol{r} - \boldsymbol{r}_m)$$

$$= \pm \frac{\ell_n \ell_m}{4A^2} \Big[(\boldsymbol{r} \cdot \boldsymbol{r}) - (\boldsymbol{r} \cdot \boldsymbol{r}_m) - (\boldsymbol{r}_n \cdot \boldsymbol{r}) + (\boldsymbol{r}_n \cdot \boldsymbol{r}_m) \Big] \tag{C.4}$$

where A is the area of the triangle, and $\boldsymbol{r}_m$ and $\boldsymbol{r}_n$, for $m, n = 1, 2, 3$, are the corresponding corner vertices of the RWGs $\boldsymbol{f}_m$ and $\boldsymbol{f}_n$, respectively[1]. Also, the plus or minus signs should be chosen in accordance with the directions of $\boldsymbol{\rho}_n^\pm$ and $\boldsymbol{\rho}_n^\pm$. The substitution of (C.4) in (C.2) yields,

$$\iint_{T_m^\pm} \boldsymbol{f}_n \cdot \boldsymbol{f}_m \, \mathrm{d}S = \pm \frac{\ell_n \ell_m}{2A} \int_0^1 \int_0^{1-\eta} \Big[(\boldsymbol{r} \cdot \boldsymbol{r}) - (\boldsymbol{r} \cdot \boldsymbol{r}_m) - (\boldsymbol{r}_n \cdot \boldsymbol{r}) + (\boldsymbol{r}_n \cdot \boldsymbol{r}_m) \Big] \, \mathrm{d}\xi \, \mathrm{d}\eta \quad \text{(C.5)}$$

where we will express every term in the integrand on the right-hand-side of (C.5) in local coordinates. With the aid of (C.3), the first term gives

$$(\boldsymbol{r} \cdot \boldsymbol{r}) = \xi^2 \|\boldsymbol{r}_1\|_2^2 + 2\xi\eta \, (\boldsymbol{r}_1 \cdot \boldsymbol{r}_2) + 2\xi \, (1 - \xi - \eta) \, (\boldsymbol{r}_1 \cdot \boldsymbol{r}_3)$$
$$+ \eta^2 \|\boldsymbol{r}_2\|_2^2 + 2\eta \, (1 - \xi - \eta) \, (\boldsymbol{r}_2 \cdot \boldsymbol{r}_3) + (1 - \xi - \eta)^2 \, \|\boldsymbol{r}_3\|_2^2 \tag{C.6}$$

so that

$$\int_0^1 \int_0^{1-\eta} (\boldsymbol{r} \cdot \boldsymbol{r}) \, \mathrm{d}\xi \, \mathrm{d}\eta = \frac{1}{12} \Big[\|\boldsymbol{r}_1\|_2^2 + \|\boldsymbol{r}_2\|_2^2 + \|\boldsymbol{r}_3\|_2^2 + (\boldsymbol{r}_1 \cdot \boldsymbol{r}_2) + (\boldsymbol{r}_1 \cdot \boldsymbol{r}_3) + (\boldsymbol{r}_2 \cdot \boldsymbol{r}_3) \Big] \quad \text{(C.7)}$$

where we made use of the following integrals

---

[1]Note that, in Fig. C.1, we have chosen for $\boldsymbol{r}_m = \boldsymbol{r}_3$ and $\boldsymbol{r}_n = \boldsymbol{r}_2$.

$$\int_0^1 \int_0^{1-\eta} \eta \, \mathrm{d}\xi \, \mathrm{d}\eta = \frac{1}{6} \qquad \text{(C.8a)}$$

$$\int_0^1 \int_0^{1-\eta} \xi \, \mathrm{d}\xi \, \mathrm{d}\eta = \frac{1}{6} \qquad \text{(C.8b)}$$

$$\int_0^1 \int_0^{1-\eta} \xi \eta \, \mathrm{d}\xi \, \mathrm{d}\eta = \frac{1}{24} \qquad \text{(C.8c)}$$

$$\int_0^1 \int_0^{1-\eta} \eta^2 \, \mathrm{d}\xi \, \mathrm{d}\eta = \frac{1}{12} \qquad \text{(C.8d)}$$

$$\int_0^1 \int_0^{1-\eta} \xi^2 \, \mathrm{d}\xi \, \mathrm{d}\eta = \frac{1}{12} \qquad \text{(C.8e)}$$

$$\int_0^1 \int_0^{1-\eta} \eta(1 - \xi - \eta) \, \mathrm{d}\xi \, \mathrm{d}\eta = \frac{1}{24} \qquad \text{(C.9a)}$$

$$\int_0^1 \int_0^{1-\eta} \xi(1 - \xi - \eta) \, \mathrm{d}\xi \, \mathrm{d}\eta = \frac{1}{24} \qquad \text{(C.9b)}$$

$$\int_0^1 \int_0^{1-\eta} (1 - \xi - \eta) \, \mathrm{d}\xi \, \mathrm{d}\eta = \frac{1}{6} \qquad \text{(C.9c)}$$

$$\int_0^1 \int_0^{1-\eta} (1 - \xi - \eta)^2 \, \mathrm{d}\xi \, \mathrm{d}\eta = \frac{1}{12} \qquad \text{(C.9d)}$$

Furthermore, if we use that $\boldsymbol{r}_1 + \boldsymbol{r}_2 + \boldsymbol{r}_3 = 3\boldsymbol{r}_c$, where $\boldsymbol{r}_c$ is the centroid of the triangle, Eq. (C.7) can be rewritten as

$$\int_0^1 \int_0^{1-\eta} (\boldsymbol{r} \cdot \boldsymbol{r}) \, \mathrm{d}\xi \, \mathrm{d}\eta = \frac{9}{12} \|\boldsymbol{r}_c\|_2^2 - \frac{1}{12} \Big[(\boldsymbol{r}_1 \cdot \boldsymbol{r}_2) + (\boldsymbol{r}_1 \cdot \boldsymbol{r}_3) + (\boldsymbol{r}_2 \cdot \boldsymbol{r}_3) \Big]. \qquad \text{(C.10)}$$

Following the above approach, the remaining terms in (C.5) are computed as

$$\int_0^1 \int_0^{1-\eta} (\boldsymbol{r}_n \cdot \boldsymbol{r}) \, \mathrm{d}\xi \, \mathrm{d}\eta = \frac{1}{2} (\boldsymbol{r}_n \cdot \boldsymbol{r}_c) \qquad \text{(C.11)}$$

$$\int_0^1 \int_0^{1-\eta} (\boldsymbol{r}_m \cdot \boldsymbol{r}) \, \mathrm{d}\xi \, \mathrm{d}\eta = \frac{1}{2} (\boldsymbol{r}_m \cdot \boldsymbol{r}_c) \qquad \text{(C.12)}$$

$$\int_0^1 \int_0^{1-\eta} (\boldsymbol{r}_n \cdot \boldsymbol{r}_m) \, \mathrm{d}\xi \, \mathrm{d}\eta = \frac{1}{2} (\boldsymbol{r}_n \cdot \boldsymbol{r}_m) \qquad \text{(C.13)}$$

Upon combining the above results, the surface integration in (C.2) is analytically computed as

$$\iint_{T_m^\pm} \boldsymbol{f}_n \cdot \boldsymbol{f}_m \, \mathrm{d}S = \pm \frac{\ell_n \ell_m}{2A} \Big[\frac{9}{12} \|\boldsymbol{r}_c\|_2^2 - \frac{1}{12} \left[(\boldsymbol{r}_1 \cdot \boldsymbol{r}_2) + (\boldsymbol{r}_1 \cdot \boldsymbol{r}_3) + (\boldsymbol{r}_2 \cdot \boldsymbol{r}_3) \right]$$

$$- \frac{1}{2} (\boldsymbol{r}_n \cdot \boldsymbol{r}_c) - \frac{1}{2} (\boldsymbol{r}_m \cdot \boldsymbol{r}_c) + \frac{1}{2} (\boldsymbol{r}_n \cdot \boldsymbol{r}_m) \Big] \qquad \text{(C.14)}$$

with the specific choice $\boldsymbol{r}_m = \boldsymbol{r}_3$ and $\boldsymbol{r}_n = \boldsymbol{r}_2$ in Fig. C.1.

Appendix D

Adaptive Integration Rule

As the separation distance d between a pair of RWGs increases, the order of the quadrature rule, used to compute the mutual reaction Z_{mn}, can be decreased such that the total number of correctly computed most significant digits in Z_{mn} remains constant as a function of d. This so-called adaptive integration rule reduces the total matrix fill time and avoids computing the smaller matrix elements too accurately with respect to those having a larger magnitude. Figure D.1(a) illustrates an identical pair of RWGs of typical dimensions whose

(a)	(b)
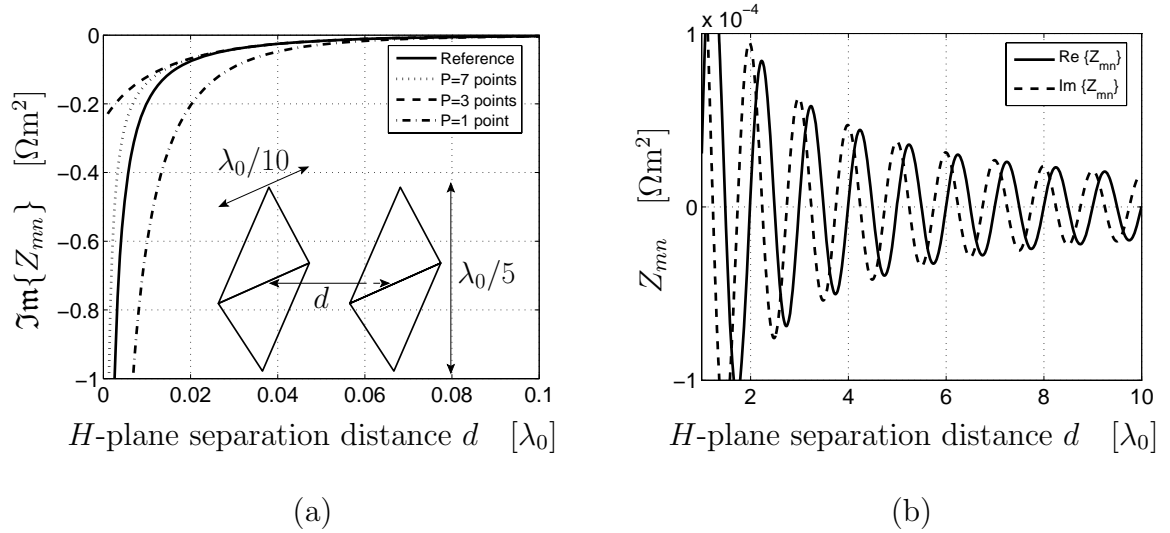
Figure D.1: Mutual reaction Z_{mn} as a function of the H-plane separation distance d in wavelengths between a pair of identical RWG basis functions. (a) Reactive part of Z_{mn} for $0 < d \leq 0.1\lambda_0$. (b) Mutual reaction Z_{mn} for $\lambda_0 < d \leq 10\lambda_0$

mutual reaction Z_{mn} is computed for $0 < d \leq 0.1\lambda_0$ with the aid of quadrature rules of several different orders. The reference solution (solid line) corresponds to the singularity subtraction technique, herein applied to observation points out of the plane of the source triangles ($w_0 \neq 0$), along with a numerical integration scheme employing $P = 7$ quadrature points per triangle.

The calculation of the self term Z_{11}, for which $w_0 = 0$, has been performed for $P = 7$ quadrature points per triangle, and gives $Z_{11} = 0.00078104817011 - 0.23429503364064j$. When the residual integral term is computed using only $P = 1$ quadrature point per triangle, the result is $Z_{11} = \mathbf{0.000}78104817011 - \mathbf{0.234}29503364064j$, where the correctly computed most significant digits are bold faceted. Clearly, 4 digits are still correctly computed because the residual function is smooth over the support of the triangle (two continuous derivatives).

It is observed in Table D.1 that the accuracy of the computed mutual reactance $\mathfrak{Im}\{Z_{mn}\}$ increases with increasing P. Moreover, the singularity subtraction technique should be avoided when $d \gtrsim \lambda_0$, since a fully numerical scheme with $P = 7$ yields identical results.

Table D.1: Numerically computed reaction integral between two RWG basis functions using the singularity subtraction method. The reference case (2nd column) is computed for $P = 7$ quadrature points/triangle and has been compared to the case $P = 1$ (3rd column). The bold-faceted fonts indicate the correctly computed digits with respect to the reference case.

d $[\lambda_0]$	Sing. Sub. Method, $P = 7$ points/triangle	Sing. Sub. Method, $P = 1$ point/triangle
0.00100000	**0.00078104197314** - **0.22917607455055**j	0.00078610727973 - 0.32521267439367j
0.00215443	**0.00078101940656** - **0.20886104043088**j	0.00078608463093 - 0.30248938488623j
0.00464159	**0.00078091466634** - **0.17345422793983**j	0.00078597950910 - 0.25825512349353j
0.01000000	**0.00078042860351** - **0.12158942069287**j	0.00078549167521 - 0.183082222229693j
0.02154435	**0.00077817461474** - **0.06253254417039**j	0.00078322947139 - 0.089426602720982j
0.04641589	**0.00076775799789** - **0.01913502385877**j	0.00077277484099 - 0.02404808744107j
0.10000000	**0.00072037859484** - **0.00308045802141**j	0.00072522150358 - 0.00339130280859j
0.21544347	**0.00052044833380** - **0.00052562278952**j	0.00052453611188 - 0.00053621429395j
0.46415888	**-0.00005840301341** - **0.00037831517370**j	-0.00005686352945 - 0.00038153307444j
1.00000000	**0.00003079590323** + **0.00018340252761**j	0.00003030367453 + 0.00018273633513j

Table D.2 lists the results for the numerical integration rules $P = 7$, and $P = 3$.

Table D.2: Numerically computed reaction integral between two RWG basis functions for $P = 7$ quadrature points/triangle (2nd column), and $P = 3$ (3rd column). The bold-faceted fonts indicate the correctly computed digits with respect to the reference case (*cf.* Table D.1).

d $[\lambda_0]$	$P = 7$ quadrature points/triangle	$P = 3$ quadrature points/triangle
0.00100000	0.00078104197314 - 1.27973459836940j	0.00078073471895 - 2.71949372527937j
0.00215443	0.00078101940656 - 0.59718950042474j	0.00078071215641 - 1.21026808963206j
0.00464159	0.00078091466634 - 0.28312800729213j	0.00078060743498 - 0.51221968262360j
0.01000000	**0.0**0078042860351 - **0.13**911512019398j	0.00078012145935 - 0.19716078784996j
0.02154435	**0.00**077817461474 - **0.06**345978538627j	**0.00**077786787506 - **0.06**809348230503j
0.04641589	**0.00076**775799789 - **0.019**15352017020j	**0.00076**745313051 - **0.019**07922819892j
0.10000000	**0.00072**037859484 - **0.00308**067413149j	**0.00072**008230759 - **0.00309**375009953j
0.21544347	**0.00052044**833380 - **0.00052**563220320j	**0.00052**018957161 - **0.00052**699714509j
0.46415888	**-0.00005840301**341 - **0.00037831517**233j	**-0.00005**853025482 - **0.00037835**121929j
1.00000000	**0.00003079590323** + **0.00018340252764**j	**0.00003081**508513 + **0.00018340**497534j
1.29154967	**0.00013394257461** - **0.00005491635234**j	**0.00013394**096463 - **0.00005492**715183j
1.66810054	**-0.00010286663212** - **0.00004542236708**j	**-0.00010287**023830 - **0.00004541**720557j
2.15443469	**0.00007552407900** + **0.00004365892383**j	**0.00007552**638941 + **0.00004365**605522j
2.78255940	**-0.00006528696198** + **0.00001761845065**j	**-0.00006528665279** + **0.00001762**060343j
3.59381366	**-0.00003108346068** - **0.00004217829633**j	**-0.00003108**456823 - **0.00004217**763151j
4.64158883	**-0.00003241050330** - **0.00002442645284**j	**-0.00003241**101071 - **0.00002442**587361j
5.99484250	**-0.00000015901707** + **0.00003143059463**j	**-0.00000015**855790 + **0.00003143**062323j
7.74263683	**-0.00002433192286** - **0.00000061072693**j	**-0.00002433**194195 - **0.00000061**045236j
10.00000000	**0.00000030887338** + **0.00001884444768**j	**0.00000030**903815 + **0.00001884**445065j

Finally, table D.3 lists the results for the numerical integration rules $P = 1$.

Table D.3: Numerically computed reaction integral between two RWG basis functions for the integration rule $P = 1$ quadrature points/triangle. The bold-faceted fonts indicate the correctly computed digits with respect to the reference case (*cf.* Table D.1).

d [λ_0]	$P = 1$ quadrature point/triangle
0.00100000	0.00078610727973 - 8.24510869446270j
0.00215443	0.00078608463093 - 3.69063644440655j
0.00464159	0.00078597950910 - 1.57809944632013j
0.01000000	0.00078549167521 - 0.60461395780803j
0.02154435	0.00078322947139 - 0.17878934481940j
0.04641589	**0.0**0077277484099 - **0.0**3304734678172j
0.10000000	**0.000**72522150358 - **0.003**76708089761j
0.21544347	**0.0005**2453611188 - **0.0005**4160777267j
0.46415888	**-0.00005**686352945 - **0.00037**977735184j
1.00000000	**0.00003**030367453 + **0.00018**361969457j
1.29154967	**0.00013**412228796 - **0.00005**464231270j
1.66810054	**-0.00010**281406287 - **0.00004**561356462j
2.15443469	**0.00007**547641059 + **0.00004**376853317j
2.78255940	**-0.00006**531172440 + **0.00001**755096314j
3.59381366	**-0.00003**105052632 - **0.00004**220621965j
4.64158883	**-0.00003**239601862 - **0.00002**444794161j
5.99484250	**-0.00000017**455333 + **0.00003**143115045j
7.74263683	**-0.00002433**198351 - **0.00000006**2005029j
10.00000000	**0.00000030**328733 + **0.00001884**467602j

From the above it is concluded that, in order to compute the moment matrix elements with at least 4–6 digits accuracy, which is generally considered (more than) adequate, it suffices to select a numerical integration scheme with $P = 7$ when $d < \lambda_0/10$, $P = 3$ when $\lambda_0/10 \leq d < \lambda_0/5$, and $P = 1$ when $d \geq \lambda_0/5$.

Appendix E

On the Voltage-Gap Source Model in Moment Methods

In method-of-moments formulations one can use distributed or concentrated sources to model a voltage source. The term "gap" is often used to refer to the region of the voltage source[1]. To realize a concentrated source, the limiting case is taken where the dimension of the gap tends to zero. Because the incident electric field as a function of position becomes a delta function, this model is mostly referred to as the delta-gap source model.

The use of the term "gap" maybe misleading. One can think that the gap consists of air (or vacuum). This confusion can give rise to questions like: "Is a base-driven monopole electrically interconnected to the ground plane where a voltage-gap is located?". To avoid misunderstandings, we will deliberately avoid the term "delta gap" when referring to a voltage source. In this respect, the voltage, current and field relations as proposed in [81] for a Rao-Wilton-Glisson (RWG) source model may also lead to confusion, although the port model appears to yield consistent results. In fact, the formulation seems ambiguous because it is unclear whether a total E-field is assumed to exist in a gap of infinitesimal width, or that an incident E-field is impressed in a short-circuited conductor.

To realize a voltage source, one can choose a suitable magnetic current distribution to

---

[1]This appendix is partly based on:

[38]: R. Maaskant and M. J. Arts, "Reconsidering the voltage-gap source model used in moment methods," *IEEE Antennas Propag. Mag.*, accepted for publication.

enclose the gap. This "frill" current should be distributed such that it generates an impressed electric field which, in combination with the scattered electric field, gives rise to the correct total electric field (and voltage) across the gap. This will lead to the correct gap capacitance and input impedance in general. Basically, the impressed electric field (source field) should incorporate the effect of the "gap" from the start. In [185] one takes the static solution for the electric field across the gap as an excitation field. Whenever possible, we prefer to model the voltage source as an ideal voltage source of zero internal impedance. Consequently, a possible physical gap must remain part of the actual structure. Similarly, we may need to model a transmission-line section to feed an antenna, but we will excite the structure using an ideal voltage source of zero internal impedance.

When a concentrated voltage source is used, the incident field can be chosen such that all the elements of the voltage excitation vector are zero, except one. Furthermore, because one is usually interested in relative quantities, such as the port voltage-current ratio (input impedance of the antenna), gain patterns, etc., the non-zero entry can be set to unity because the correct sign and amplitude of the corresponding current should follow from the moment-method solution [186, p. 130].

As we employ voltage-source excitations, the input-admittance matrix can be computed directly, i.e., without having to construct and invert an input impedance matrix first. The antenna input admittance can be computed through a stationary formula whose solution is known to be second-order accurate. Basically, the admittance is then determined through an integral formula involving the solution for the current. We will derive a stationary formula for the mutual admittance between two accessible ports through the Lorentz reciprocity theorem. It turns out that the formula is identical to Eq. (6-12) in [32, p. 109], except for a minus sign. This is an important observation because the formula may be used as a reference formula in various numerical test cases, or in semi-analytical approaches.

Furthermore, instead of setting one entry of the voltage excitation vector to unity, we will relate this entry to the actual applied voltage, while assuring that the voltage-current and field relations are consistent with standard network models. More specifically, a voltage-source model for the edge-based RWG basis function is derived, whose use in the moment method approach is shown to yield the correct formula for the (antenna) input admittance; the latter being validated through the reaction concept.

E.1   The Voltage-Source Model

Fig. E.1(a) shows the standard network convention that the current I^{ant} enters a load (dipole antenna) as a result of exciting the antenna with a voltage source of strength V^{ant}, that is, the current exits the plus terminal of the voltage source (notice the different convention in [81]), so that $Z^{\text{ant}} = V^{\text{ant}}/I^{\text{ant}}$, I^{ant} representing the total current through the source (vectors indicate positive directions).
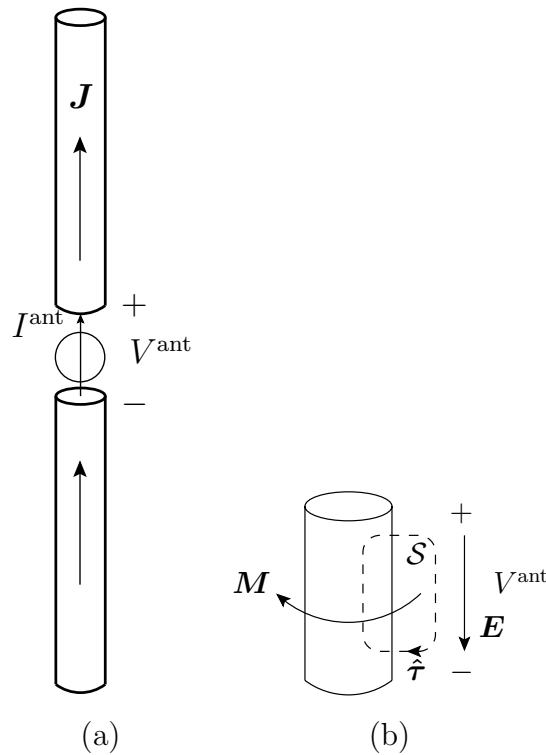
Figure E.1: (a) Standard network conventions for V^{ant} and I^{ant}, such that $Z^{\text{ant}} = V^{\text{ant}}/I^{\text{ant}}$. (b) Voltage source model realized using a magnetic frill current $\boldsymbol{M}$ encircling a PEC cylinder.

An ideal voltage source can be realized by letting a magnetic frill current $\boldsymbol{M}$ encircle a perfectly conducting (PEC) cylinder as depicted in Fig. E.1(b). To determine the voltage between the end caps of the cylinder, we define a surface $\mathcal{S}$ with boundary $\partial\mathcal{S}$ as indicated in Fig. E.1. Then, from Maxwell's equations,

$$\oint_{\partial\mathcal{S}} \boldsymbol{E} \cdot \hat{\boldsymbol{\tau}} \, \mathrm{d}\ell = -\iint_{\mathcal{S}} (j\omega\boldsymbol{B} + \boldsymbol{M}) \cdot \hat{\boldsymbol{n}} \, \mathrm{d}S \tag{E.1}$$

where, in view of the contour integration in the $\hat{\boldsymbol{\tau}}$ direction, the unit normal $\hat{\boldsymbol{n}}$ to surface $\mathcal{S}$ is pointing into the paper. Because of the boundary condition that $\boldsymbol{E} = \boldsymbol{0}$ inside the PEC cylinder, the integral over the external total E-field yields the antenna voltage, i.e.,

$$V^{\mathrm{ant}} = \int_+^- \boldsymbol{E} \cdot \hat{\boldsymbol{\tau}} \, \mathrm{d}\ell = - \iint_{\mathcal{S}} \boldsymbol{M} \cdot \hat{\boldsymbol{n}} \, \mathrm{d}S \tag{E.2}$$

where $\mathcal{S}$ is assumed to be small enough such that the total magnetic flux through $\mathcal{S}$ is solely determined by the concentrated source distribution $\boldsymbol{M}$. The source distribution depends on the specific geometrical details of the feed region [185].

E.2   The Mutual Admittance Between Two Antennas

We will derive a stationary formula for the mutual port admittance between two antennas through the application of the Lorentz reciprocity theorem. Afterwards, it will be demonstrated that this admittance formula reduces to the standard definition of the input admittance using a moment method approach.

The mutual admittance Y_{21}^{ant} between two antennas is defined as

$$Y_{21}^{\mathrm{ant}} = \left. \frac{I_2^{\mathrm{ant}}}{V_1^{\mathrm{ant}}} \right|_{V_2^{\mathrm{ant}}=0} \tag{E.3}$$

where antenna 1 is excited by a voltage source with amplitude V_1^{ant}, and where the short-circuited port current I_2^{ant} is measured at antenna 2.

To derive a stationary formula for Y_{21}^{ant}, the antenna structure as depicted in Fig. E.2 is assumed to have the two accessible ports 1 and 2. The pair of perfectly conducting leads (dark gray) are contained in the domain $\mathcal{D}_1$. The radiating antenna structure occupies a volume $\mathcal{D}_2$ with complex-valued constitutive parameters $\{\mu_0, \varepsilon\}$. The background medium is vacuum.

In situation a we excite the short-circuited port 1 by a magnetic-frill current $\boldsymbol{M}_1$. Port 2 is also short-circuited, but not excited. The resultant electromagnetic fields, which are generated throughout the entire space, are denoted by $\{\boldsymbol{E}^a, \boldsymbol{H}^a\}$.

Henceforth, we will treat the antenna problem as a scattering problem. For scattering problems, we express the total electric field as a superposition of the incident and scattered
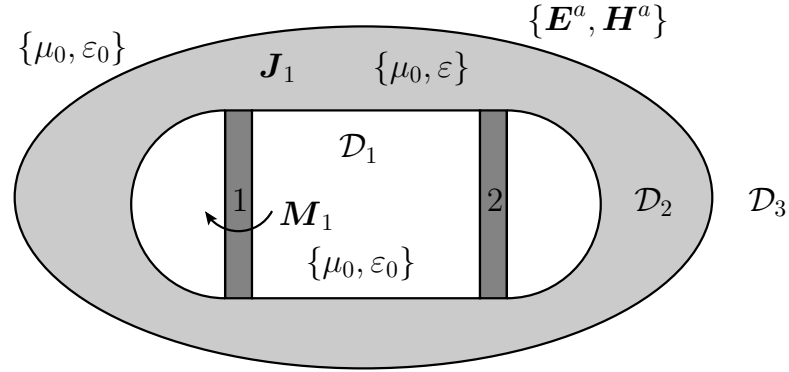
Figure E.2: Situation a; the generated electromagnetic fields $\{\boldsymbol{E}^a, \boldsymbol{H}^a\}$ in case antenna 1 is excited by a magnetic frill current $\boldsymbol{M}_1$.

fields, i.e., $\boldsymbol{E}^a = \boldsymbol{E}^{i,a}(\boldsymbol{M}_1) + \boldsymbol{E}^{s,a}(\boldsymbol{J}_1)$. After the application of the volume equivalence principle, the incident electric field $\boldsymbol{E}^{i,a}$ is generated by the impressed magnetic-frill current $\boldsymbol{M}_1$ in vacuum, but in the absence of the equivalent electric current $\boldsymbol{J}_1$. Likewise; the scattered field $\boldsymbol{E}^{s,a}$ is generated by the impressed electric current $\boldsymbol{J}_1$ in vacuum, but in the absence of $\boldsymbol{M}_1$. Similarly, the total magnetic field is written as $\boldsymbol{H}^a = \boldsymbol{H}^{i,a}(\boldsymbol{M}_1) + \boldsymbol{H}^{s,a}(\boldsymbol{J}_1)$.

In situation b, we only consider the impressed magnetic-frill source $\boldsymbol{M}_2$ at the location of port 2 (in vacuum), as illustrated in Fig. E.3. In the absence of electric current sources,
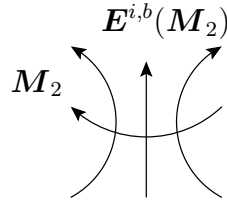
Figure E.3: Incident electric field as generated by $\boldsymbol{M}_2$ at the location of port 2, in vacuum.

the total electromagnetic fields in situation b are: $\boldsymbol{E}^b = \boldsymbol{E}^{i,b}(\boldsymbol{M}_2)$ and $\boldsymbol{H}^b = \boldsymbol{H}^{i,b}(\boldsymbol{M}_2)$.

To determine the mutual admittance Y_{21}^{ant}, we make use of the Lorentz reciprocity theorem, which is given as [30, p. 117]

$$\iiint\limits_{\mathcal{D}_1 \cup \mathcal{D}_2} \left[\boldsymbol{E}^a \cdot \boldsymbol{J}_2 - \boldsymbol{H}^a \cdot \boldsymbol{M}_2 \right] \mathrm{d}V = \iiint\limits_{\mathcal{D}_1 \cup \mathcal{D}_2} \left[\boldsymbol{E}^b \cdot \boldsymbol{J}_1 - \boldsymbol{H}^b \cdot \boldsymbol{M}_1 \right] \mathrm{d}V \qquad \text{(E.4)}$$

where the volume $\mathcal{D}_1 \cup \mathcal{D}_2$ encloses the entire antenna system (all sources). There are only

magnetic sources in situation b, so that $\boldsymbol{J}_2 = \boldsymbol{0}$, and (E.4) reduces to

$$-\iiint_{\mathcal{V}_2} \boldsymbol{H}^a \cdot \boldsymbol{M}_2 \, \mathrm{d}V = \iiint_{\mathcal{D}_1 \cup \mathcal{D}_2} \left[\boldsymbol{E}^b \cdot \boldsymbol{J}_1 - \boldsymbol{H}^b \cdot \boldsymbol{M}_1 \right] \mathrm{d}V \qquad (\text{E.5})$$

where $\mathcal{V}_2$ is the source volume in situation b, i.e., the support of $\boldsymbol{M}_2$. For simplicity, we assume that $\boldsymbol{M}_2$ is a current filament encircling the cylindrical lead at port 2, and this mimics, within $\mathcal{D}_1$, an ideal voltage-source of zero-internal impedance in accordance with the voltage-source model in Fig. E.1(b). The radius of the magnetic current loop is assumed to be electrically small, so that the voltage source alone has a negligible radiation loss in free space; it primarily generates an $\boldsymbol{E}^b = \boldsymbol{E}^{i,b}$ field, while $\boldsymbol{H}^b = \boldsymbol{H}^{i,b} \approx \boldsymbol{0}$, so that (E.5) reduces to

$$-\iiint_{\mathcal{V}_2} \boldsymbol{H}^a \cdot \boldsymbol{M}_2 \, \mathrm{d}V = \iiint_{\mathcal{V}_1} \boldsymbol{E}^{i,b} \cdot \boldsymbol{J}_1 \, \mathrm{d}V \qquad (\text{E.6})$$

where $\mathcal{V}_1$ constitutes the volumetric support of $\boldsymbol{J}_1$.

The left-hand side of (E.6) can be evaluated with the aid of Fig. E.4. From the quasi-static
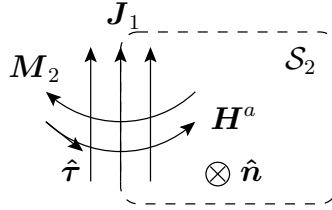
Figure E.4: The generated magnetic field $\boldsymbol{H}^a$ in situation a, which is "tested" along the magnetic current $\boldsymbol{M}_2$ in situation b, at port 2.

field assumptions for electrically small magnetic-current sources, we have that $\boldsymbol{H}^{i,a}(\boldsymbol{M}_1) \approx \boldsymbol{0}$, so that $\boldsymbol{H}^a = \boldsymbol{H}^{i,a}(\boldsymbol{M}_1) + \boldsymbol{H}^{s,a}(\boldsymbol{J}_1) \approx \boldsymbol{H}^{s,a}(\boldsymbol{J}_1)$. Furthermore, if $\boldsymbol{M}_2$ closely surrounds the cylindrical conductor surface at port 2, the total magnetic field $\boldsymbol{H}^a$ is primarily determined by the short-circuited current $\boldsymbol{J}_1$ through port 2 (displacement current is zero inside a PEC conductor). The volume integral on the left-hand side of (E.6) can therefore be evaluated as a surface integral times a contour integral (body of revolution approach) as

$$-\iiint_{\mathcal{V}_2} \boldsymbol{H}^a \cdot \boldsymbol{M}_2 \, \mathrm{d}V = -\underbrace{\iint_{\mathcal{S}_2} \boldsymbol{M}_2 \cdot \hat{\boldsymbol{n}} \, \mathrm{d}S}_{V_2^{\mathrm{ant}}} \underbrace{\oint \boldsymbol{H}^a \cdot \hat{\boldsymbol{\tau}} \, \mathrm{d}\ell}_{I_2^{\mathrm{ant}}}$$

$$= V_2^{\mathrm{ant}} I_2^{\mathrm{ant}} \qquad (\text{E.7})$$

where $\hat{\boldsymbol{\tau}}$ has been chosen in the direction of $\boldsymbol{H}^a$, and $\hat{\boldsymbol{n}}$ should be chosen accordingly, i.e., in the same direction (*cf.* Fig. E.4 for the case that $\hat{\boldsymbol{\tau}}$ is normal to $\mathcal{S}$). Also, we made use of (E.2) and the observation that the total short-circuited current through port 2 is I_2^{ant}. Substituting (E.7) in (E.6), and dropping the superscript b, yields

$$V_2^{\text{ant}} I_2^{\text{ant}} = \iiint\limits_{\mathcal{V}_1} \boldsymbol{E}^i(\boldsymbol{M}_2) \cdot \boldsymbol{J}_1 \, \mathrm{d}V. \tag{E.8}$$

Note that I_2^{ant} represents the total current through voltage source 2 in case element 1 is excited by a voltage source, while voltage source 2 is switched off (zero amplitude).

Next to the situations a and b, we could excite port 2 by a magnetic current $\boldsymbol{M}_2$ and subsequently compute the induced current $\boldsymbol{J}_2$ from a moment-method approach. If only PEC materials are considered, the current resides at the surface of the conductor, and the boundary-integral equation for the tangential components of the electric field across the PEC surface $\mathcal{S}_1$ reads $\boldsymbol{E}_{\text{tan}}^i(\boldsymbol{M}_2) = -\boldsymbol{E}_{\text{tan}}^s(\boldsymbol{J}_2)$. Substituting this in (E.8), yields

$$V_2^{\text{ant}} I_2^{\text{ant}} = -\iint\limits_{\mathcal{S}_1} \boldsymbol{E}^s(\boldsymbol{J}_2) \cdot \boldsymbol{J}_1 \, \mathrm{d}S. \tag{E.9}$$

This result can be divided by $V_1^{\text{ant}} V_2^{\text{ant}}$ to arrive at $Y_{21}^{\text{ant}} = I_2^{\text{ant}}/V_1^{\text{ant}}$. Note that I_2^{ant} is already a short-circuited current, and that the surface currents $\boldsymbol{J}_1$ and $\boldsymbol{J}_2$ are due to the voltage excitations V_1^{ant} at port 1, and V_2^{ant} at port 2, respectively, while the other port is then short circuited. In conclusion, the mutual admittance can be computed as

$$Y_{21}^{\text{ant}} = \frac{-1}{V_1^{\text{ant}} V_2^{\text{ant}}} \iint\limits_{\mathcal{S}_1} \boldsymbol{E}^s(\boldsymbol{J}_2) \cdot \boldsymbol{J}_1 \, \mathrm{d}S. \tag{E.10}$$

Note that (E.10) is identical to Eq. (6-12) in [32, p. 109], except for the minus sign. In this respect, it is regrettable that a minus sign error occurred in Eq. (27) of [87]. It is worth mentioning that Eq. (E.10) has also been used in [31] to compute the mutual admittance between slot antennas through an aperture field integration, although this is a different problem.

E.2.1   Validation of the Mutual Admittance Formula

We will demonstrate that the minus sign in (E.10) is correct for a single antenna. From (E.10), the self admittance is computed as

$$Y^{\mathrm{ant}} = \frac{-1}{(V^{\mathrm{ant}})^2} \iint\limits_{\mathcal{S}} \boldsymbol{E}^s(\boldsymbol{J}_S) \cdot \boldsymbol{J}_S \, \mathrm{d}S \tag{E.11}$$

where $\boldsymbol{J}_1 = \boldsymbol{J}_2 = \boldsymbol{J}_S$ denotes the surface current. The voltage source can be replaced by a current source whenever it has an amplitude which is equal to the port current in case it would have been excited by a voltage source. Then, the induced port voltage would equal the original source voltage. The current must therefore have an amplitude $I^{\mathrm{ant}} = V^{\mathrm{ant}}/Z^{\mathrm{ant}}$. Substituting this in (E.11) gives

$$Z^{\mathrm{ant}} = \frac{-1}{(I^{\mathrm{ant}})^2} \iint\limits_{\mathcal{S}} \boldsymbol{E}^s(\boldsymbol{J}_S) \cdot \boldsymbol{J}_S \, \mathrm{d}S \tag{E.12}$$

which is the correct stationary formula of the antenna input impedance [30, p. 348], which confirms that the incident field $\boldsymbol{E}^i$ must point into the positively defined direction of $\boldsymbol{J}_S$ to yield a positive real part of the impedance.

E.3   The RWG Voltage-Source Model

It is convenient to synthesize a surface current by employing a set of RWG basis functions as they can conform to arbitrarily shaped geometries. We will develop a voltage-source model for an edge-based basis function, more specifically, for a RWG basis function. Following the
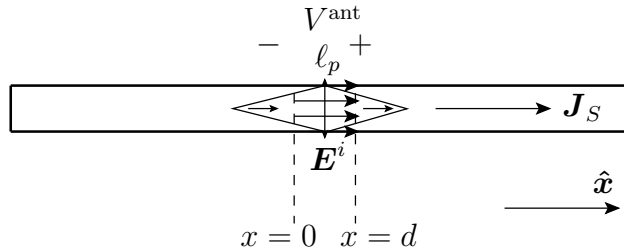
Figure E.5: Voltage-current and field definitions for a RWG voltage generator.

preceding section, we choose $\boldsymbol{E}^i$ to point in the positive current direction. The uniformly

distributed incident electric field $\boldsymbol{E}^i = (V^{\mathrm{ant}}/d)\,\hat{\boldsymbol{x}}$ is assumed to exist for $0 \leq x \leq d$, and resides on the conductor surface only. Although this artificial voltage source (non-physical) barely resembles the incident field as generated by a magnetic-frill current inside the conductor, it is known to yield accurate solutions for a large number of problems.

When the antenna is excited by an incident field $\boldsymbol{E}^i$, the current will distribute itself such that the scattered field $\boldsymbol{E}^s_{\mathrm{tan}}$ cancels $\boldsymbol{E}^i_{\mathrm{tan}}$ in the port region (= support region of $\boldsymbol{E}^i$). Outside the port region, $\boldsymbol{E}^s_{\mathrm{tan}}$ must vanish across the remaining part of the PEC conductor, and outside the source field (where $\boldsymbol{E}^i = \boldsymbol{0}$), we have that the total field $\boldsymbol{E} = \boldsymbol{E}^s(\boldsymbol{J}_S)$. The total electric field $\boldsymbol{E}$ is directed from the plus to minus terminal of the voltage source (see Fig. E.1), so that V^{ant} in Fig. E.5 can be expressed as

$$V^{\mathrm{ant}} = -\int_0^d \boldsymbol{E} \cdot \hat{\boldsymbol{x}}\,\mathrm{d}x = -\int_0^d \boldsymbol{E}^s(\boldsymbol{J}_S) \cdot \hat{\boldsymbol{x}}\,\mathrm{d}x = \int_0^d \boldsymbol{E}^i \cdot \hat{\boldsymbol{x}}\,\mathrm{d}x \qquad (\text{E.13})$$

where the last equality is obtained by assuming that $\boldsymbol{E}^s(\boldsymbol{J}_S) = -\boldsymbol{E}^i$ just "above" the RWG basis functions in the port region.

The last step is to prove that the voltage-generator model as proposed in Fig. E.5 leads to the correct input admittance of an antenna. To perform this check in a moment method context, let the electric-field integral equation (EFIE) for a PEC surface $\mathcal{S}$ be written as

$$\boldsymbol{E}^s_{\mathrm{tan}}(\boldsymbol{J}_S) = -\boldsymbol{E}^i_{\mathrm{tan}} \quad \text{for } \boldsymbol{r} \in \mathcal{S}, \qquad (\text{E.14})$$

and let $\{\boldsymbol{f}_n\}_{n=1}^N$ be the N RWG expansion functions for the surface current $\boldsymbol{J}_S$. Then, by testing (E.14) through Galerkin's approach using the symmetric product[2] $\langle \boldsymbol{a}, \boldsymbol{b} \rangle = \int \boldsymbol{a} \cdot \boldsymbol{b}\,\mathrm{d}S$, the following linear system of equations is obtained:

$$\sum_{n=1}^N Z_{mn} I_n = V_m \quad \text{for } m = 1, 2, \ldots, N \qquad (\text{E.15})$$

with

$$Z_{mn} = \langle \boldsymbol{E}^s(\boldsymbol{f}_n), \boldsymbol{f}_m \rangle = \iint_{\mathcal{S}_m} \boldsymbol{E}^s(\boldsymbol{f}_n) \cdot \boldsymbol{f}_m\,\mathrm{d}S, \qquad (\text{E.16a})$$

$$V_m = -\langle \boldsymbol{E}^i, \boldsymbol{f}_m \rangle = -\iint_{\mathcal{S}_m} \boldsymbol{E}^i \cdot \boldsymbol{f}_m\,\mathrm{d}S. \qquad (\text{E.16b})$$

---

[2]In case the test functions would be complex-valued functions, an identical discretization would be obtained if the EFIE is tested through an Hermitian inner product, but then the test functions need to be the conjugates of the basis functions (a non-Galerkin approach).

The key step herein is to express the moment matrix elements in terms of reactions, since the quantity we are interested in, the self-admittance of an antenna, has also been expressed in terms of a reaction. Since the solution for the current is known in terms of RWGs, we can substitute the RWG expansion $\boldsymbol{J}_S = \sum_{n=1}^{N} I_n \boldsymbol{f}_n$ in (E.11) to obtain

$$Y^{\mathrm{ant}} = \frac{-1}{(V^{\mathrm{ant}})^2} \sum_{m=1}^{N} \sum_{n=1}^{N} I_m \left[\iint_{\mathcal{S}} \boldsymbol{E}^s(\boldsymbol{f}_n) \cdot \boldsymbol{f}_m \, \mathrm{d}S \right] I_n$$

$$= \frac{-1}{(V^{\mathrm{ant}})^2} (\mathbf{I})^T \mathbf{Z} \mathbf{I} \tag{E.17}$$

where $\mathbf{I} = [I_1, \ldots, I_N]^T$ is the coefficient expansion vector for the RWGs, and where the reactions between RWG basis functions are recognized as the entries of moment matrix $\mathbf{Z}$. Since $\mathbf{I}$ is computed through the excitation vector $\mathbf{V}$ as $\mathbf{I} = \mathbf{Z}^{-1}\mathbf{V}$, Eq. (E.17) readily simplifies to

$$Y^{\mathrm{ant}} = \frac{-1}{(V^{\mathrm{ant}})^2} (\mathbf{I})^T \mathbf{V}. \tag{E.18}$$

To ease the numerical computations, it is convenient to reduce the support of $\boldsymbol{E}^i$ to an infinitely small region by letting $d \to 0$ while maintaining its potential difference (voltage). A possible solution to (E.13) is

$$\boldsymbol{E}^i = V^{\mathrm{ant}} \delta(\boldsymbol{r} - \boldsymbol{r}_\ell) \hat{\boldsymbol{x}} \tag{E.19}$$

where the field has been concentrated along a line of length ℓ crossing the conductor. If the delta-field-distribution coincides with a single common edge of a RWG basis function, the excitation vector $\mathbf{V}$ has only one non-zero element. Let V_m in (E.16b) for $m = p$ denote this non-zero element (the port RWG). From (E.16b) and (E.19), we then have that

$$V_p = -V^{\mathrm{ant}} \iint \left(\hat{\boldsymbol{x}} \cdot \boldsymbol{f}_p \right) \delta(\boldsymbol{r} - \boldsymbol{r}_{\mathrm{gap}}) \, \mathrm{d}S = -V^{\mathrm{ant}} \ell_p \tag{E.20}$$

where $\left(\hat{\boldsymbol{x}} \cdot \boldsymbol{f}_p \right) = 1$ (see [26]), and ℓ_p denotes the edge length of the port (the common-edge length of the pth RWG basis function). The total current through the port is defined as $I^{\mathrm{ant}} = I_p \ell_p$. Substituting this result, along with (E.20), in (E.18), yields

$$Y^{\mathrm{ant}} = \frac{1}{(V^{\mathrm{ant}})^2} \frac{I^{\mathrm{ant}}}{\ell_p} V^{\mathrm{ant}} \ell_p = \frac{I^{\mathrm{ant}}}{V^{\mathrm{ant}}} \tag{E.21}$$

which is the correct formula for the antenna input admittance, and this validates the port model in Fig. E.5.

Appendix F

CAESAR Simulation Software

The numerical techniques as presented in this thesis have resulted in the development of a combined electromagnetic-microwave simulation tool. The capabilities of this solver opens up new horizons in understanding the receiver sensitivity limiting factors of actively beam-formed antenna array systems. A general overview of this software has been given at the EuMC 2008 in Amsterdam, and has been included on the following pages for information.

The pertaining reference is [163]:
R. Maaskant, A. G. Tijhuis, R. Mittra, M. V. Ivashina, W. A. van Cappellen, and M. J. Arts, "Hybridization of efficient modeling techniques for fast analysis of large-scale antenna structures in the context of the Square Kilometre Array project," in *Proc. 38th European Microwave Conference*, Amsterdam, Oct. 2008, pp. 837-840.

Hybridization of Efficient Modeling Techniques for Fast Analysis of Large-Scale Antenna Structures in the Context of the Square Kilometre Array Project

R. Maaskant [1], A. G. Tijhuis [†2], R. Mittra [‡3] M. V. Ivashina [1], W. A. van Cappellen [1], M. J. Arts [1]

The Netherlands institute for radio astronomy (ASTRON)
P.O. Box 2, 7990 AA Dwingeloo, The Netherlands
[1]maaskant@astron.nl

[†]*Faculty of Electrical Engineering, Eindhoven University of Technology*
P.O. Box 513, 5600 MB Eindhoven, The Netherlands
[2]a.g.tijhuis@tue.nl

[‡]*Electromagnetic Communication Laboratories, Pennsylvania State University*
University Park, PA 16802, USA
[3]mittra@engr.psu.edu

Abstract— **We provide an overview of the modeling techniques that have been combined to solve large-scale antenna problems within the framework of the Square Kilometre Array (SKA) project. These numerically efficient techniques have been integrated into a software tool named CAESAR [1], which enables us to solve large antenna problems, both at antenna, and at system level. The latter is essential in determining the receiver sensitivity of the entire instrument, which is the main figure of merit. In the present paper we summarize how the conventional method of moments (MoM) has been enhanced using a hybridization of the Characteristic Basis Function Method (CBFM) in conjunction with a number of acceleration techniques so as to greatly reduce the overall execution time without compromising the accuracy. Representative examples are shown of realistically large and complex antenna systems that have been examined only recently.**

I. Introduction

The Square Kilometer Array (SKA) project is a world-wide project to design and construct a revolutionary new radio telescope with a collecting area of order 1 million square meters in the wavelength range from 3 m to 1 cm [1]–[3]. ASTRON[2] conducts the development of the aperture array concept, both by designing and examining small-scale prototype arrays, thereby demonstrating the feasibility of the instrument and revealing the potentials of various cost-effective array technologies. Concurrently, dedicated simulation software is being developed to facilitate this research phase in an accurate and time-efficient manner [4].

The antenna characterization is carried out with the aid of the method of moments (MoM), which discretizes a continuous integral equation for the unknown surface/volume current density by employing an equally large set of basis and test functions. Typically, a subsectional basis is employed to locally represent/expand the unknown current on the domain that supports this vector basis function, as well as to test it using identical vector functions (Galerkin's method). The primary advantage of employing subsectional basis functions is that they can be chosen to conform to arbitrarily shaped geometries. The penalty, however, is that the size of the moment matrix becomes excessively large when a fine discretization of the corresponding integral equation for electrically large problems is required to accurately represent this current.

At present, roughly two classes of solution strategies can be identified to solve the resultant large matrix equation, either based on: (i) iterative techniques; or, (ii) iteration-free techniques. Iteration-free approaches become particularly attractive when a (direct) solution is required for a large number of excitations (MRHS). For instance, for antenna type of problems, N linearly independent array excitations need to be solved to determine the full N-port antenna impedance matrix; hence, an iteration-free method would require N matrix-vector products, whereas a standard iterative (Krylov subspace) solver may then require $\sim N^2$ matrix-vector products. Furthermore, by using an iteration-free approach, convergence problems are avoided that are typically associated to iterative solvers.

Iteration-free techniques rely on a strong compression of the moment matrix by employing numerically generated large-domain basis functions so that the resultant reduced matrix equation can be solved directly, e.g., by means of a standard LU decomposition technique. In the Characteristic Basis Function Method (CBFM), the corresponding macro-domain basis functions (CBFs) conform to arbitrarily shaped geometries since these CBFs are constructed as fixed combinations (aggregations) of subsectional basis functions [5]. Hence, a large degree of geometrical flexibility is maintained when employing a macro basis which in itself is derived from a subsectional basis. In addition, existing computer codes can be reused/upgraded by only minor modifications. Techniques similar to CBFM are, e.g., the eigencurrent approach [6] and

---

[1]Computationally Advanced and Efficient Simulator for ARrays
[2]Netherlands institute for radio astronomy

the synthetic functions approach [7].

Throughout this paper we summarize a number of numerically efficient techniques that have been used to solve a variety of SKA related problems using only moderate computing power.

II. EXAMPLES

All computations have been carried out in double precision arithmetic on a Dell Inspiron 9300 Notebook, equipped with an Intel Pentium-M processor operating at 1.73 GHz, and 2.0 GB of RAM.

A. LOFAR LBA Station Configuration Studies Using CBFM

With the aid of CBFM, the beam pattern of an array of 96 dual-polarized inverted-V dipole antennas (LOFAR station) has been studied for a number of different array configurations, ranging from sparse to dense, and from regular to irregular [8]. For illustration, the calculated array beam pattern ($\theta = 30^0$, $\varphi = 0^0$ scan) is shown in Fig. 1 for one of the regular array configurations.
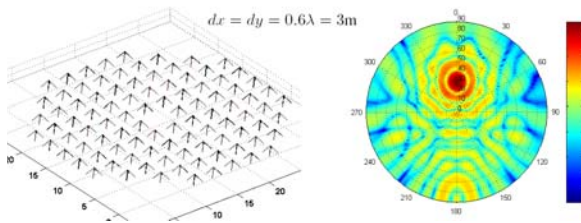
Fig. 1. Station configuration study for the LOFAR LBA project.

The antenna impedance matrix for each array configuration was computed by solving the respective reduced matrix equation

$$\mathbf{Z}^{red}\mathbf{I}^{red} = \mathbf{V}^{red} \tag{1}$$

for the unknown CBF expansion coefficient vectors $\mathbf{I}^{red}$ that belong to the equally large, though distinct, reduced excitation vectors $\mathbf{V}^{red}$ (both $\mathbf{I}^{red}$ and $\mathbf{V}^{red}$ are column-augmented matrices).

In (1), a reduced matrix block $\mathbf{Z}_{mn}^{red}$ is computed as

$$\mathbf{Z}_{mn}^{red} = \mathbf{J}_m^T\mathbf{Z}_{mn}^{MoM}\mathbf{J}_n, \tag{2}$$

i.e., the fully populated moment matrix block $\mathbf{Z}_{mn}^{MoM}$, which holds the reactions between the subsectional basis/test functions supported by the nth and m^{th} subdomain[3], respectively, is compressed by left-right multiplication of $\mathbf{Z}_{mn}^{MoM}$ by the corresponding n^{th} and m^{th} set of CBFs $\mathbf{J}_m$ and $\mathbf{J}_n$, respectively. Each column of $\mathbf{J}_q$ holds the expansion coefficients of the subsectional basis representing one CBF supported by the qth subdomain. Superscript T in (2) denotes the transposition operator.

[3]This domain comprises both a co- and cross-polarized element

Similarly, the reduced excitation vector $\mathbf{V}_m^{red}$ for the mth subdomain is computed as

$$\mathbf{V}_m^{red} = \mathbf{J}_m^T\mathbf{V}_m^{MoM}. \tag{3}$$

Next, we compare the size of the full moment matrix (MoM) to the size of the reduced moment matrix (CBFM), as well as the corresponding total execution times. The results are listed in Table I.

TABLE I
SYSTEM MATRIX COMPRESSION AND TOTAL EXECUTION TIME.

	#RWGs	#MoM Blocks	#CBFs	Matrix Compression	Total Exec. Time
MoM	6336	1	0	0%	39 min. 16 sec.
CBFM	6336	179	768	98.8%	1 min. 12 sec.

As opposed to MoM, one observes that the execution time has dropped significantly for a CBFM approach. Also, the original moment matrix has been strongly reduced, even though the problem is relatively small, implying that the computational overhead of generating CBFs is relatively large.

We remark that CBFM has been used in combination with a number of additional acceleration techniques as detailed hereafter, including the exploitation of the block Toeplitz (translation) symmetry between pairs of groups of CBFs. In this respect, note that not all 96×96 CBF group interactions have to be computed to construct $\mathbf{Z}^{red}$, but only 179 as a result of the large degree of translation symmetry that a regular spaced array possesses with identical elements supporting equal sets of CBFs.

B. ACA and its Solution Accuracy for the LOFAR HBA Array

In the previous subsection, a significant acceleration has been achieved by approximating (2) as

$$\mathbf{Z}_{mn}^{red} \approx \mathbf{J}_m^T\widetilde{\mathbf{Z}}_{mn}^{MoM}\mathbf{J}_n, \tag{4}$$

where $\widetilde{\mathbf{Z}}_{mn}^{MoM}$ is a low-rank approximation of $\mathbf{Z}_{mn}^{MoM}$. Matrix $\mathbf{Z}_{mn}^{MoM}$ can be constructed on-the-fly and numerically efficient using the Adaptive Cross Approximation algorithm (ACA) [9]. This is accomplished without *a priori* knowledge of the actual full matrix block $\mathbf{Z}_{mn}^{MoM}$. It is well-known that the effective rank becomes smaller of matrix blocks representing reaction terms between electrically distant groups of basis functions. For those groups, the rank-revealing ACA algorithm becomes highly effective, even though it will only reduce the computational complexity by a constant factor (instead of by an order).

The accuracy of the combined CBFM–ACA approach is demonstrated through an example of a 4×4 dual-polarized array of LOFAR High Band Antennas. For this purpose, the impedance and radiation characteristics, obtained by a direct MoM approach, have been overlaid with the solutions obtained by a combined CBFM–ACA approach (Fig. 2). One can observe an excellent agreement, both for the computed mutual impedances, as well as for the computed embedded
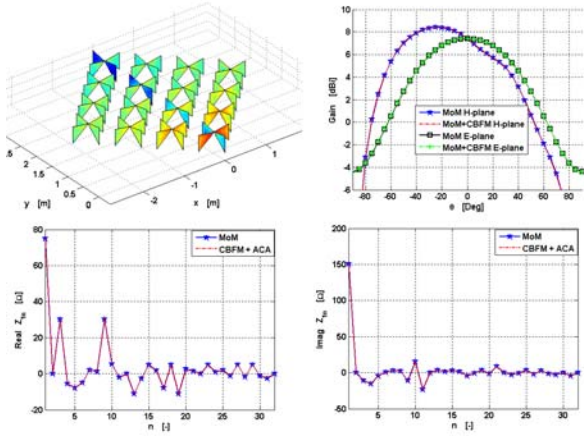
Fig. 2. Top-left: Array of LOFAR HBA antennas. Top-Right: The embedded element pattern of a corner antenna element in the E-and H-plane. Bottom-Left: mutual resistance, and Bottom-Right: mutual reactance between the corner and the remaining antenna elements.
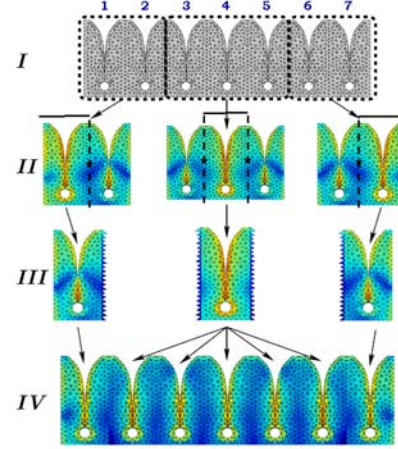

Fig. 3. Trapezoidal post-windowing technique for CBFs to synthesize currents on electrically interconnected antenna arrays.

element pattern of a corner-excited HBA antenna. For this particular case, the relative error ϵ of the antenna impedance matrix $\mathbf{Z}^{ant}$ is 1.1%, with the error defined as a ratio of 2-norms:

$$\epsilon = \frac{||\mathbf{Z}^{ant} - \widetilde{\mathbf{Z}}^{ant}||^2}{||\mathbf{Z}^{ant}||^2}, \qquad (5)$$

and where $\widetilde{\mathbf{Z}}^{ant}$ is the approximated matrix.

Not surprisingly, the speed advantage of the ACA algorithm has to be traded against the solution accuracy. This trade-off can be controlled by means of the ACA threshold [9], which directly influences the accuracy of $\widetilde{\mathbf{Z}}^{ant}$. In the present example, an ACA threshold level of 250 has been used.

C. Arrays of Interconnected Tapered Slot Antennas

In CBFM we decompose the entire computational domain into smaller subdomains, each of them supporting a set of CBFs. These CBFs are generated numerically, and preferably for relatively small antenna structures that have been extracted from the original antenna array, with the restriction that these small antenna structures should closely resemble their original electromagnetic array environment.

However; the generation of CBFs becomes non-trivial for electrically interconnected (antenna) structure, since the structure is, in essence, electromagnetically inseparable. Furthermore, the CBFs have to be generated such as to synthesize a continuous current flow across the boundaries between adjacent antenna elements. A possible solution to the latter problem is to let CBFs partially overlap, or to use special bridge-functions [7], [10].

In [10] we proposed a trapezoidal post-windowing technique to generate CBFs for electrically interconnected (antenna) structures. The pertaining CBF generation procedure has been graphically visualized in Fig. 3.

With reference to Fig. 3, we first extract representative subarrays from the fully meshed array (Step I). Afterwards, each subarray is excited a number of times so as to generate a set of induced surface currents (Step II). Next, these currents are truncated by a trapezoidal windowing function to eliminate the undesired edge-singular currents, and to retain an overlap with adjacent domains. Finally, the so-generated CBFs (Step III) are mapped onto their corresponding array elements (Step IV). Note that, when CBFs partially overlap, they combine properly because the superposition of all taper functions sum to unity.

The aforementioned CBF windowing method has been applied to compute the impedance matrix of 576 TSA element array. Figure. 4 illustrates the array composed of 9 disjoint antenna tiles. The surface current has been synthesized using 375.000 RWG subsectional basis functions which constitute the 4320 CBFs. By exploiting translation symmetry, only 8394 out of 331776 mutual moment blocks had to be constructed, and in an time-efficient manner using the ACA algorithm. The total execution time amounted to 254 min. 44 sec. per frequency point. The execution time can be further reduced by constructing a reduced matrix for only one of the antenna tiles while accounting for the coupling effect between the neighboring phase-steered array tiles [11].

D. Antenna System Modeling

In interferometric receiver systems for radio astronomy, antenna output signals are correlated to create a (steerable) beam in the sky and to achieve a certain receiver sensitivity in that direction. In practical systems, noise is generated at different stages within the receiver, and generally, microwave components are not power-matched to one another. As a result, the overall sensitivity depends upon the array receiver in its entirety.

For the purpose of analyzing the overall receiver system, a dedicated microwave simulator has been developed
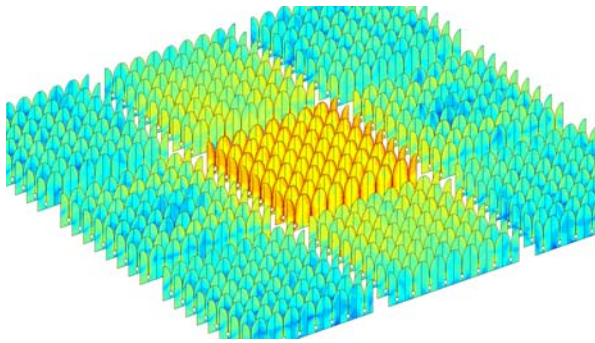
Fig. 4. Array of 9 disjoint subarrays (3x3), each of them composed of 64 TSA elements (8x8). The center tile is excited to illustrate the coupling effects. The magnitude of the surface current distribution is shown (log scale) as computed by a direct CBFM approach.

and integrated with the electromagnetic solver [12]. All microwave components, including the antenna, Low Noise Amplifiers (LNAs) and beamforming network, are characterized in terms of signal-noise wave covariance matrices, together with their scattering matrices. The cascaded compound is computed by applying the connection matrix theory as described in [14], [15].

The use of the hybridized methods enabled us to conduct a number of studies. For instance, it has been demonstrated that one has to noise match the LNAs to the active scan impedance in order to achieve minimum receiver noise in phased array antennas [13]. Another example is a microwave circuit model of a microstrip TSA feed that has been developed and combined with the antenna impedance characteristics obtained by full-wave EM simulations [16]. Figure 5 illustrates that a dielectric-free MoM code can be used to model the antenna structure separately from the feed structure.
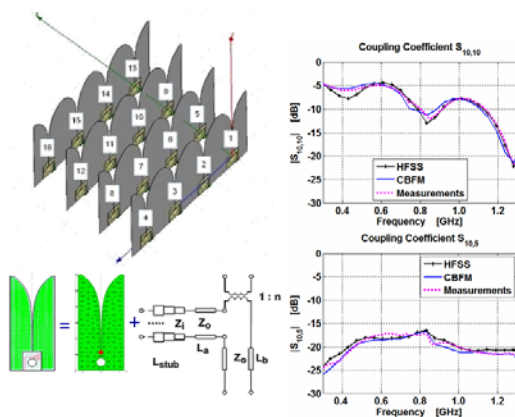
Fig. 5. Combining a microwave circuit model for the feed with a full-wave dielectric-free antenna array model.

Validation of the combined models has been performed through measurements and simulations (HFSS). A very good

agreement is obtained showing that realistically complex and electrically large antenna array structures can be modeled accurately and fast.

REFERENCES

[1] P. J. Hall, "The square kilometre array: an engineering perspective" Reprinted from experimental astronomy, vol. 17, no. 1–3, 2004, ISBN: 1-4020-3797-x, Springer 2005.
[2] A. B. Smolders and M. P. van Haarlem, "Perspectives on radio astronomy: technologies for large antenna arrays," Conf. Proc., ASTRON, ISBN: 90-805434-2-x, April 1999.
[3] Website: http://www.skatelescope.org/
[4] R. Maaskant, R. Mittra, and W. van Cappellen, "Efficient numerical analysis of prototype antennas for the Square Kilometer Array (SKA) using the Characteristic Basis Function Method (CBFM)," *IEEE AP-S International Symposium USNC/URSI Meeting*, Albuquerque, New Mexico, Jul. 9–14, 2006.
[5] V. Prakash and R. Mittra, "Characteristic basis function method: A new technique for efficient solution of method of moments matrix equations," *Micr. Opt. Technol.* vol. 36, pp. 95–100., Jan. 2003.
[6] D. J. Bekers, S. J. L. van Eijndhoven, A. A. F. van de Ven, P. Borsboom, and A. G. Tijhuis, "Eigencurrent analysis of resonant behavior in finite antenna arrays," *IEEE Trans. Microw. Theory Techn.*, vol. 54, no. 6, pp. 2821–2829., Jun. 2006.
[7] L. Matekovits, V. A. Laza, and G. Vecchi, "Analysis of large complex structures with the synthetic-functions approach," *IEEE Trans. Antennas Propagat.*, vol. 55, no. 9, pp. 2509–2521, Sep. 2007.
[8] W. A. van Cappellen, S. J. Wijnholds, and J. D. Bregman, "Sparse antenna array configurations in large aperture synthesis radio telescopes," *3rd European Radar Conference*, pp. 76–79., Sept. 2006.
[9] R. Maaskant, R. Mittra, and A. G. Tijhuis, "Fast solution of large-scale antenna problems using the Characteristic Basis Function Method and the Adaptive Cross Approximation algorithm," submitted to *IEEE Trans. Antennas Propagat.*, Nov. 2007.
[10] R. Maaskant, R. Mittra, and A. G. Tijhuis, "Application of trapezoidal-shaped Characteristic Basis Functions to arrays of electrically interconnected antenna elements," *Proc. Electromagnetics in Advanced Applications*, ICEAA 2007, pp. 567–571, 17-21 Sept.
[11] R. Maaskant, R. Mittra, and A. G. Tijhuis, "Fast solving of multi-scale antenna problems for the Square Kilometre Array (SKA) radio telescope using the Characteristic Basis Function Method (CBFM) – an array of electrically large subarrays," Submitted to the *ACES journal*, Feb. 2008.
[12] R. Maaskant, and B. Yang, "A combined electromagnetic and microwave antenna system simulator for radio astronomy," *Proc. European Conference on Antennas and Propagation (EuCAP)*, Nice, France, Nov. 2006.
[13] R. Maaskant, B. Woestenburg, "Applying the active antenna impedance to achieve noise match in receiving array antennas," *IEEE AP-S International Symposium*, Hawaii, USA, pp. 5889–5892, June 2007.
[14] J. A. Dobrowolski, "Introduction to computer methods for microwave circuit analysis and design," Artech House, Bosten, 1991.
[15] R. Maaskant, E. E. M. Woestenburg, M. J. Arts, "Generalized method of modeling the sensitivity of array antennas at system level," *Proc. 34th Microwave Conference*, vol. 3, pp. 1541–1544, Oct. 2004.
[16] M. V. Ivashina, E. A. Redkina, and R. Maaskant, "An accurate model of a wide-band microstrip feed for slot antenna arrays," *IEEE AP-S International Symposium*, Hawaii, USA, pp. 1953–1956, June 2007.

Bibliography

[1] K. G. Jansky, "Directional studies of atmospherics at high frequencies," *Proc. IRE.*, vol. 20, pp. 1920–1932, Dec. 1932.

[2] ——, "Electrical disturbances apparently of extraterrestrial origin," *Proc. IRE.*, vol. 21, pp. 1387–1398, Oct. 1933.

[3] J. D. Kraus, Ed., *Radio Astronomy, 2nd edition.* Durham, NH: Cygnus-Quasar Books, Nov. 2005.

[4] G. Reber, "Cosmic static," *Astrophys. J.*, vol. 91, pp. 621–624, Jun. 1940.

[5] H. van Woerden and R. G. Strom, "The beginnings of radio astronomy in the Netherlands," *Journal of Astronomical History and Heritage*, vol. 9, no. 1, pp. 3–20, 2006.

[6] C. A. Muller and J. H. Oort, "The interstellar hydrogen line at 1,420 Mc/s and the estimate of galactic rotation," *Nature*, vol. 168, pp. 357–358, Sep. 1951.

[7] H. I. Ewen and E. M. Purcell, "Radiation from galactic hydrogen at 1420 Mc/s," *Nature*, vol. 168, pp. 356–357, Sep. 1951.

[8] M. E. J. Jeuken, M. E. H. Knoben, and K. J. Wellington, "Dual frequency, dual polarized feed for radio astronomy," *NTZ*, vol. 25, pp. 374–376, 1972.

[9] J. K. M. Jansen, M. E. J. Jeuken, and C. W. Lambrechtse, "The scalar feed," *Int. J. Electron. Commun. (AEU)*, vol. 26, pp. 22–30, 1972.

[10] E. Raimond and R. Genee, Eds., *The Westerbork Observatory, Continuing Adventure in Radio Astronomy.* Dordrecht, The Netherlands: Kluwer Academic Publishers, 1996.

[11] P. J. Hall, Ed., *The Square Kilometre Array: an Engineering Perspective.* Spring Street, New York: Springer, Reprinted from experimental astronomy, 2005.

[12] C. Carilli and S. Rawlings, Eds., *Science with the Square Kilometre Array.* Amsterdam, The Netherlands: Elsevier, Dec. 2004.

[13] The SKA website. [Online]. Available: http://www.skatelescope.org/

[14] SKA Science Working Group. (2009, Oct.) The square kilometre array design reference mission: SKA-mid and SKA-lo (v. 0.4). 091001_DRM_v0.4.pdf. [Online]. Available: http://www.skatelescope.org/PDF/

[15] R. T. Schilizzi, P. Alexander, J. M. Cordes, P. E. Dewdney, R. D. Ekers, A. J. Faulkner, B. M. Gaensler, P. J. Hall, J. L. Jonas, and K. I. Kellermann. (2007, Dec.) Preliminary specifications for the square kilometre array. 100_Memo_Schilizzi.pdf. [Online]. Available: http://www.skatelescope.org/PDF/memos/

[16] The LOFAR website. [Online]. Available: http://www.lofar.org/

[17] W. A. van Cappellen, L. Bakker, and T. A. Oosterloo, "Experimental results of a 112 element phased array feed for the westerbork synthesis radio telescope," in *Proc. IEEE AP-S International Symposium*, Charleston, South Carolina, Jun. 2009, pp. 1–4.

[18] M. Ruiter and E. van der Wal, "EMBRACE, a 10000 element next generation aperture array telescope," in *Proc. 39th European Microwave Conference*, Rome, Sep. 2009, pp. 1–4.

[19] The SKADS website. [Online]. Available: http://www.skads-eu.org/

[20] J. G. bij de Vaate, L. Bakker, E. E. M. Woestenburg, R. H. Witvers, G. W. Kant, and W. van Cappellen, "Low cost low noise phased-array feeding systems for SKA pathfinders," in *13th Int. Symp. on Antenna Tech. and Applied Electromagnetics (ANTEM)*, Banff, AB, Canada, Feb. 2009.

[21] R. Maaskant, "Antenne-inrichting, antenne-array, samenstel voor het assembleren van een antenne-array en een elektronische inrichting omvattende een antenne," Dutch filed as NL1 034 102, Oct. 1, 2008.

[22] E. de Lera Acedo, E. Garcia, V. González-Posadas, J. L. Vázquez-Roy, R. Maaskant, and D. Segovia, "Study and design of a differentially-fed tapered slot antenna array," *IEEE Trans. Antennas Propag.*, vol. 58, no. 1, pp. 68–78, Jan. 2010.

[23] R. Maaskant, M. Popova, and R. van de Brink, "Towards the design of a low cost wideband demonstrator tile for the SKA," in *Proc. European Conference on Antennas and Propag. (EuCAP)*, Nice, France, Nov. 2006, pp. 1–4.

[24] W. Yu, X. Yang, Y. Liu, L.-C. Ma, T. Su, N.-T. Huang, R. Mittra, R. Maaskant, Y. Lu, Q. Che, R. Lu, and Z. Su, "A new direction in computational electromagnetics: solving large problems using the parallel FDTD on the BlueGene/L supercomputer providing teraflop-level performance," *IEEE Antennas Propag. Mag.*, vol. 50, no. 2, pp. 26–44, 2008.

[25] A. Vasylchenko, Y. Schols, W. de Raedt, and G. Vandenbosch, "Quality assessment of computational techniques and software tools for planar-antenna analysis," *IEEE Antennas Propag. Mag.*, vol. 51, no. 1, pp. 23–38, Feb. 2009.

[26] S. Rao, D. Wilton, and A. Glisson, "Electromagnetic scattering by surfaces of arbitrary shape," *IEEE Trans. Antennas Propag.*, vol. 30, no. 3, pp. 409–418, May 1982.

[27] J. C. Maxwell, "A dynamical theory of the electromagnetic field," *Philosophical transactions of the royal society of London*, vol. 155, pp. 459–512, 1865.

[28] J. W. Arthur, "The fundamentals of electromagnetic theory revisited," *IEEE Antennas Propag. Mag.*, vol. 50, no. 1, pp. 19–65, Feb. 2008.

[29] A. T. de Hoop and G. de Jong, "Power reciprocity in antenna theory," *Proc. IEE.*, vol. 121, no. 10, pp. 1051–1056, 1974.

[30] R. F. Harrington, *Time-Harmonic Electromagnetic Fields.* New York and London: McGraw-Hill Book Company, 1961.

[31] J. H. Richmond, "A reaction theorem and its application to antenna impedance calculations," *Proc. IRE.*, vol. 9, pp. 515–520, Nov. 1961.

[32] R. F. Harrington, *Field Computation by Moment Methods.* New York: The Macmillan Company, 1968.

[33] V. H. Rumsey, "Reaction concept in electromagnetic theory," *Phys. Rev.*, vol. 94, pp. 1483–1491, Jun. 1954.

[34] A. T. de Hoop, "The n-port receiving antenna and its equivalent electrical network," *Philips Res. Repts.*, vol. 30, pp. 302–315, 1975.

[35] C.-T. Tai, "Kirchhoff theory: Scalar, vector, or dyadic?" *IEEE Trans. Antennas Propag.*, vol. 20, no. 1, pp. 114–115, Jan. 1972.

[36] J. A. Stratton, *Electromagnetic Theory*. New York and London: McGraw-Hill Book Company, 1941.

[37] R. Maaskant, D. J. Bekers, M. J. Arts, W. A. van Cappellen, and M. V. Ivashina, "Evaluation of the radiation efficiency and the noise temperature of low-loss antennas," *IEEE Antennas Wireless Propag. Lett.*, vol. 8, no. 8, pp. 1536–1225, Jan. 2009.

[38] R. Maaskant and M. Arts, "Reconsidering the voltage-gap source model used in moment methods," *IEEE Antennas Propag. Mag.*, accepted for publication.

[39] T. B. A. Senior, "Some extensions of babinet's principle in electromagnetic theory," *IEEE Trans. Antennas Propag.*, vol. 25, no. 3, pp. 417–420, May 1977.

[40] S. Tretyakov, *Analytical Modeling in Applied Electromagnetics*. Boston and London: Artech House, 2003.

[41] D. J. Bekers, private communication, 2009.

[42] EM Software and Systems. (2005, Dec.) FEKO users manual suite 5.1. UserManual.pdf. [Online]. Available: http://www2.ifh.ee.ethz.ch/ fieldcom/pps-antenna/doc/

[43] U. Jakobus, "Comparison of different techniques for the treatment of lossy dielectric/magnetic bodies within the MoM formulation," *Int. J. Electron. Commun. (AEU)*, vol. 54, no. 1, p. 110, 2000.

[44] D. J. Bekers, S. J. L. van Eijndhoven, and A. A. F. van de Ven, "Modeling and analysis of a long thin conducting stripline," *J. Eng. Math.*, vol. 49, no. 4, pp. 373–390, 2004.

[45] C. Craeye, "Including spatial correlation of thermal noise in the noise model of high-sensitivity arrays," *IEEE Trans. Antennas Propag.*, vol. 53, no. 11, pp. 3845–3848, Nov. 2005.

[46] C. Craeye, B. Parvais, and X. Dardenne, "MoM simulation of signal-to-noise patterns in infinite and finite receiving antenna arrays," *IEEE Trans. Antennas Propag.*, vol. 52, no. 12, pp. 3245–3256, Dec. 2004.

[47] S. Yuferev and N. Ida, "Selection of the surface impedance boundary conditions for a given problem," *IEEE Trans. Magn.*, vol. 35, no. 3, pp. 1486–1489, May 1999.

[48] W. T. Shaw and A. J. Dougan, "Curvature corrected impedance boundary conditions in an arbitrary basis," *IEEE Trans. Antennas Propag.*, vol. 53, no. 5, pp. 1699–1705, May 2005.

[49] M. C. van Beurden, "Integro-differential equations for electromagnetic scattering," Ph.D. dissertation, Eindhoven University of Technology, Eindhoven, 2003. [Online]. Available: http://alexandria.tue.nl/extra2/200312216.pdf

[50] J. G. V. Bladel, *Electromagnetic Fields*. New Jersey: IEEE Press Series on Electromagnetic Wave Theory, Second Edition, 2007.

[51] M. N. Sadiku, *Numerical Techniques in Electromagnetics, First Edition*. Boca Raton, Florida: CRC Press, Inc., 1992.

[52] T. Sarkar, A. Djordjević, and E. Arvas, "On the choice of expansion and weighting functions in the numerical solution of operator equations," *IEEE Trans. Antennas Propag.*, vol. 33, no. 9, pp. 988–996, Sep. 1985.

[53] A. D. T. Sarkar and E. Arvas, "A note on the choice of weighting functions in the method of moments," *IEEE Trans. Antennas Propag.*, vol. 33, no. 4, pp. 436–441, Apr. 1985.

[54] K. F. Warnick and W. C. Chew, "Error analysis of the moment method," *IEEE Antennas Propag. Mag.*, vol. 46, no. 6, pp. 38–53, 2004.

[55] R. Harrington and J. Mautz, "Theory of characteristic modes for conducting bodies," *IEEE Trans. Antennas Propag.*, vol. 19, no. 5, pp. 622–628, Sep. 1971.

[56] A. F. Peterson, D. R. Wilton, and R. E. Jorgenson, "Variational nature of Galerkin and non-Galerkin moment method solutions," *IEEE Trans. Antennas Propag.*, vol. 44, no. 4, pp. 500–503, Apr. 1996.

[57] D. G. Dudley, "Comments on "variational nature of Galerkin and non-Galerkin moment method solutions"," *IEEE Trans. Antennas Propag.*, vol. 45, no. 6, pp. 1062–1063, Jun. 1997.

[58] J. H. Richmond, "On the variational aspects of the moment method," *IEEE Trans. Antennas Propag.*, vol. 39, no. 4, pp. 473–479, Apr. 1991.

[59] J. F. Lee, "Conforming hierarchical vector elements," in *Proc. IEEE AP-S International Symposium*, San Antonio, Texas, Jun. 2002, pp. 66–69.

[60] G. Vecchi, "Loop-star decomposition of basis functions in the discretization of the EFIE," *IEEE Trans. Antennas Propag.*, vol. 47, no. 2, pp. 339–346, Feb. 1999.

[61] T. Eibert, "Iterative-solver convergence for loop-star and loop-tree decompositions in method-of-moments solutions of the electric-field integral equation," *IEEE Antennas Propag. Mag.*, vol. 46, no. 3, pp. 80–85, Jun. 2004.

[62] M. Yang and J. M. Song, "Error in projection of plane waves using the RWG basis functions," in *Proc. IEEE AP-S International Symposium*, Albuquerque, New Mexico, Jul. 2006, pp. 2873–2876.

[63] B. Delaunay, "Sur la sphère vide," *Izvestia Akademii Nauk SSSR, Otdelenie Matematicheskikh i Estestvennykh Nauk*, vol. 7, pp. 793–800, 1934.

[64] E. W. Weisstein. Taylor series. MathWorld – A Wolfram web Resource. [Online]. Available: http://mathworld.wolfram.com/TaylorSeries.html

[65] D. R. Wilton, S. M. Rao, A. W. Glisson, D. H. Schaubert, O. M. Al-Bundak, and C. M. Butler, "Potential integrals for uniform and linear source distributions on polygonal and polyhedral domains," *IEEE Trans. Antennas Propag.*, vol. 32, no. 3, pp. 276–281, Mar. 1984.

[66] L. Rossi and P. J. Cullen, "On the fully numerical evaluation of the linear-shape function times the 3-D Green's function on a plane triangle," *IEEE Trans. Antennas Propag.*, vol. 47, no. 4, pp. 398–402, Apr. 1999.

[67] R. D. Graglia, "Static and dynamic potential integrals for linearly varying source distributions in two- and three-dimensional problems," *IEEE Trans. Antennas Propag.*, vol. 35, no. 6, pp. 662–669, Jun. 1987.

[68] ——, "On the numerical integration of the linear shape functions times the 3-D Green's function or its gradient on a plane triangle," *IEEE Trans. Antennas Propag.*, vol. 41, no. 10, pp. 1448–1455, Oct. 1993.

[69] S. Caorsi, D. Moreno, and F. Sidoti, "Theoretical and numerical treatment of surface integrals involving the free-space Green's function," *IEEE Trans. Antennas Propag.*, vol. 41, no. 9, pp. 1296–1301, Sep. 1993.

[70] T. F. Eibert and V. Hansen, "On the calculation of potential integrals for linear source distributions on triangular domains," *IEEE Trans. Antennas Propag.*, vol. 43, no. 12, pp. 1499–1502, Dec. 1995.

[71] P. Arcioni, M. Bressan, and L. Perregrini, "On the evaluation of the double surface integrals arising in the application of the boundary integral method to 3-D problems," *IEEE Trans. Microw. Theory Tech.*, vol. 45, no. 3, pp. 436–439, Mar. 1997.

[72] M. G. Duffy, "Quadrature over a pyramid or cube of integrands with a singularity at a vertex," *SIAM. J. Numer. Anal.*, vol. 19, no. 6, pp. 1260–1262, Dec. 1982.

[73] D. J. Taylor, "Accurate and efficient numerical integration of weakly singular integrals in Galerkin EFIE solutions," *IEEE Trans. Antennas Propag.*, vol. 51, no. 7, pp. 1630–1637, Jul. 2003.

[74] A. G. Polimeridis and T. V. Yioultsis, "On the direct evaluation of weakly singular integrals in Galerkin mixed potential integral equation formulations," *IEEE Trans. Antennas Propag.*, vol. 56, no. 9, pp. 3011–3019, Sep. 2008.

[75] M. A. Khayat and D. R. Wilton, "Numerical evaluation of singular and near-singular potential integrals," *IEEE Trans. Antennas Propag.*, vol. 53, no. 10, pp. 3180–3190, Oct. 2005.

[76] R. D. Graglia and G. Lombardi, "Machine precision evaluation of singular and nearly singular potential integrals by use of gauss quadrature formulas for rational functions," *IEEE Trans. Antennas Propag.*, vol. 56, no. 4, pp. 981–998, Apr. 2008.

[77] P. Y.-Oijala and M. Taskinen, "Calculation of cfie impedance matrix elements with RWG and $n \times$RWG functions," *IEEE Trans. Antennas Propag.*, vol. 51, no. 8, pp. 1837–1846, Aug. 2003.

[78] L. N. Trefethen and D. Bau, Eds., *Numerical Linear Algebra.* Philadelphia: Society for Industrial and Applied Mathematics (SIAM), 1997.

[79] D. Bekers, "Finite antenna arrays – an eigencurrent approach," Ph.D. dissertation, Eindhoven University of Technology, Eindhoven, 2004. [Online]. Available: http://alexandria.tue.nl/extra2/200411410.pdf

[80] R. E. Collin and F. J. Zucker, *Antenna Theory – Part 1.* New York and London: McGraw-Hill Book Company, 1969.

[81] S. N. Makarov, *Antenna and EM Modeling With MATLAB.* New York: John Wiley and Sons, Inc., 2002.

[82] M. F. Cátedra, J. G. Cuevas, and L. Nuno, "A scheme to analyze conducting plates of resonant size using the conjugate-gradient method and the fast Fourier transform," *IEEE Trans. Antennas Propag.*, vol. 36, no. 12, pp. 1744–1752, Dec. 1988.

[83] C. Marasini, "Efficient computation techniques for Galerkin MoM antenna design," Ph.D. dissertation, Eindhoven University of Technology, Eindhoven, 2008.

[84] B. M. Kolundžija, J. S. Ognjanović, and T. K. Sarkar, *WIPL-D: Electromagnetic Modeling of Composite Metallic and Dielectric Structures.* Norwood: Artech House, 2000.

[85] R. Maaskant and B. Yang, "A combined electromagnetic and microwave antenna system simulator for radio astronomy," in *Proc. European Conference on Antennas and Propag. (EuCAP)*, Nice, France, Nov. 2006, pp. 1–4.

[86] G. H. Golub and C. F. van Loan, *Matrix Computations.* London: 3rd ed. Baltimore, MD: Johns Hopkins, 1996.

[87] R. Maaskant, R. Mittra, and A. G. Tijhuis, "Fast analysis of large antenna arrays using the characteristic basis function method and the adaptive cross approximation algorithm," *IEEE Trans. Antennas Propag.*, vol. 56, no. 11, pp. 3440–3451, Nov. 2008.

[88] ——, "Fast solution of multi-scale antenna problems for the square kilomtre array (SKA) radio telescope using the characteristic basis function method (CBFM)," Applied Computational Electromagnetics Society (ACES) Journal, vol. 24, no. 2, pp. 174–188, Apr. 2009.

[89] R. Maaskant, M. V. Ivashina, O. Iupikov, E. A. Redkina, S. Kasturi, and D. H. Schaubert, "Analysis of large microstrip-fed tapered slot antenna arrays by combining electrodynamic and quasi-static field models," *IEEE Trans. Antennas Propag.*, accepted for publication.

[90] A. Neto, S. Maci, G. Vecchi, and M. Sabbadini, "A truncated Floquet wave diffraction method for the full wave analysis of large phased arrays – part ii: Generalization to 3-D cases," *IEEE Trans. Antennas Propag.*, vol. 48, no. 3, pp. 601–611, Mar. 2000.

[91] C. Craeye, A. G. Tijhuis, and D. H. Schaubert, "An efficient MoM formulation for finite-by-ininite arrays of two-dimensional antennas arranged in a three dimensional structure," *IEEE Trans. Antennas Propag.*, vol. 51, no. 9, pp. 2054–2056, Sep. 2003.

[92] A. K. Skrivervik and J. R. Mosig, "Analysis of finite phased arrays of microstrip patches," *IEEE Trans. Antennas Propag.*, vol. 41, no. 9, pp. 1105–1114, Aug. 1993.

[93] B. Tomasic and A. Hessel, "Analysis of finite arrays – a new approach," *IEEE Trans. Antennas Propag.*, vol. 47, no. 3, pp. 555–564, Mar. 1999.

[94] O. A. Çivi, P. H. Pathak, H.-T. Chou, and P. Nepa, "A hybrid uniform geometrical theory of diffraction – moment method for efficient analysis of electromagnetic radiation/scattering from large finite planar arrays," *Radio Sci.*, vol. 35, no. 2, pp. 607–620, Mar. 2000.

[95] E. Garcia, C. Delgado, F. S. de Adana, F. Cátedra, and R. Mittra, "Incorporating the multilevel fast multipole method into the characteristic basis function method to solve large scattering and radiation problems," in *Proc. IEEE AP-S International Symposium*, Honulullu, Hawaii, Jun. 2007, pp. 1285–1288.

[96] G. A. E. Vandenbosch and A. R. Van de Cappelle, "Use of combined expansion scheme to analyze microstrip antennas with the method of moments," *Radio Sci.*, vol. 27, no. 6, pp. 911–916, Dec. 1992.

[97] J. Heinstadt, "New approximation technique for current distribution in microstrip array antennas," *Micr. Opt. Technol.*, vol. 29, pp. 1809–1810, Oct. 1993.

[98] G. A. E. Vandenbosch and F. J. Demuynck, "The expansion wave concept – part ii: A new way to model mutual coupling in microstrip arrays," *IEEE Trans. Antennas Propag.*, vol. 46, no. 3, pp. 407–413, Mar. 1998.

[99] V. Prakash and R. Mittra, "Characteristic basis function method: A new technique for efficient solution of method of moments matrix equations," *Micr. Opt. Technol.*, vol. 36, pp. 95–100, Jan. 2003.

[100] R. Maaskant, R. Mittra, and A. G. Tijhuis, "Application of trapezoidal-shaped characteristic basis functions to arrays of electrically interconnected antenna elements," in *Proc. Int. Conf. on Electromagn. in Adv. Applicat. (ICEAA)*, Torino, Sep. 2007, pp. 567–571.

[101] J. Yeo, V. Prakash, and R. Mittra, "Efficient analysis of a class of microstrip antennas using the characteristic basis function method (CBFM)," *Micr. Opt. Technol.*, vol. 39, pp. 456–464, Dec. 2003.

[102] R. Mittra, J.-F. Ma, E. Lucente, and A. Monorchio, "CBMOM–an iteration free MoM approach for solving large multiscale em radiation and scattering problems," in *Proc. IEEE AP-S International Symposium*, Washington DC, Jul. 2005, pp. 2–5.

[103] G. Tiberi, A. Monorchio, G. Manara, and R. Mittra, "Hybridizing asymptotic and numerically rigorous techniques for solving electromagnetic scattering problems using the characterisitic basis functions (CBFs)," in *Proc. IEEE AP-S International Symposium*, Columbus, Ohio, Jun. 2003, pp. 22–27.

[104] L. Matekovits, V. A. Laza, and G. Vecchi, "Analysis of large complex structures with the synthetic-functions approach," *IEEE Trans. Antennas Propag.*, vol. 55, no. 9, pp. 2509–2521, Sep. 2007.

[105] L. Matekovits, G. Vecchi, G. Dassano, and M. Orefice, "Synthetic function analysis of large printed structures: the solution space sampling approach," in *Proc. IEEE AP-S International Symposium*, Boston, Massachusetts, Jul. 2001, pp. 568–571.

[106] W. B. Lu, T. J. Cui, Z. G. Qian, X. X. Yin, and W. Hong, "Accurate analysis of large-scale periodic structures using an efficient sub-entire-domain basis function method," *IEEE Trans. Antennas Propag.*, vol. 52, no. 11, pp. 3078–3085, Nov. 2004.

[107] D. J. Bekers, S. J. L. van Eijndhoven, A. A. F. van de Ven, P. P. Borsboom, and A. G. Tijhuis, "Eigencurrent analysis of resonant behavior in finite antenna arrays," *IEEE Trans. Microw. Theory Tech.*, vol. 54, no. 6, pp. 2821–2829, Jun. 2006.

[108] E. Suter and J. R. Mosig, "A subdomain multilevel approach for the efficient MoM analysis of large planar antennas," *Micr. Opt. Technol.*, vol. 26, no. 4, pp. 270–277, Aug. 2000.

[109] I. Stevanovic and J. R. Mosig, "Subdomain multilevel approach with fast MBF interactions," in *Proc. IEEE AP-S International Symposium*, Monterey, California, Jun. 2004, pp. 367–370.

[110] C. Craeye, "A fast impedance and pattern computation scheme for finite antenna arrays," *IEEE Trans. Antennas Propag.*, vol. 54, no. 10, pp. 3030–3034, Oct. 2006.

[111] P. D. Vita, A. Freni, L. Matekovits, P. Pirinoli, and G. Vecchi, "A combined AIM-SFX approach for large complex arrays," in *Proc. IEEE AP-S International Symposium*, Honulollu, Hawaii, Jun. 2007, pp. 3452–3455.

[112] E. Bleszynski, M. Bleszynski, and T. Jaroszewicz, "AIM: Adaptive integral method for solving large-scale electromagnetic scattering and radiation problems," *Radio Sci.*, vol. 31, no. 5, pp. 1225–1251, Sep. 1996.

[113] M. Bebendorf, "Approximation of boundary element matrices," *Numer. Math.*, vol. 86, no. 4, pp. 565–589, Jun. 2000.

[114] K. Zhao, M. N. Vouvakis, and J. F. Lee, "The adaptive cross approximation algorithm for accelerated method of moments computations of EMC problems," *IEEE Trans. Electromagn. Compat.*, vol. 47, no. 4, pp. 763–773, Nov. 2005.

[115] S. Kurz, O. Rain, and S. Rjasanow, "The adaptive cross-approximation technique for the 3-D boundary-element method," *IEEE Trans. Magn.*, vol. 38, no. 2, pp. 421–424, Mar. 2002.

[116] W. H. Press, B. P. Flannery, S. A. Teukolsky, and W. T. Vetterling, *Numerical recipes – the art of scientific computing.* Cambridge: Cambridge University Press, 3rd edition, 1988.

[117] C. Delgado, M. F. Catedra, and R. Mittra, "Efficient multilevel approach for the generation of characteristic basis functions for large scatters," *IEEE Trans. Antennas Propag.*, vol. 56, no. 7, pp. 2134–2137, Jul. 2008.

[118] A. O. Boryssenko, private communication, 2004.

[119] A. K. Skrivervik and J. R. Mosig, "Analysis of printed array antennas," *IEEE Trans. Antennas Propag.*, vol. 45, no. 9, pp. 1411–1418, Sep. 1997.

[120] D. H. Schaubert and A. O. Boryssenko, "Subarrays of Vivaldi antennas for very large apertures," in *Proc. 34th European Microwave Conference*, Amsterdam, Oct. 2004, pp. 1533–1536.

[121] D. H. Schaubert, S. Kasturi, M. W. Elsallal, and W. A. van Cappellen, "Wide bandwidth Vivaldi antenna arrays – some recent developments," in *Proc. European Conference on Antennas and Propag. (EuCAP)*, Nice, France, Nov. 2006, pp. 1–4.

[122] R. Maaskant and B. Woestenburg, "Applying the active antenna impedance to achieve noise match in receiving array antennas," in *Proc. IEEE AP-S International Symposium*, Honulollu, Hawaii, Jun. 2007, pp. 5889–5892.

[123] C. Craeye, private communication, 2007.

[124] J. Laviada, F. Las-Heras, M. R. Pino, and R. Mittra, "Solution of electrically large problems with multilevel characteristic basis functions," *IEEE Trans. Antennas Propag.*, vol. 57, no. 10, pp. 3189–3198, Oct. 2009.

[125] S. Kasturi and D. H. Schaubert, "Effect of dielectric permittivity on infinite arrays of single-polarized Vivaldi antennas," *IEEE Trans. Antennas Propag.*, vol. 54, no. 2, pp. 351–358, Feb. 2006.

[126] A. B. Smolders and M. P. van Haarlem, Eds., *Perspectives on radio astronomy: technologies for large antenna arrays*. ISBN: 90-805434-2-x: Conf. Proc., ASTRON, 1999.

[127] M. N. Vouvakis, S.-C. Lee, K. Zhao, and J.-F. Lee, "A symmetric FEM-IE formulation with a single-level IE-QR algorithm for solving electromagnetic radiation and scattering problems," *IEEE Trans. Antennas Propag.*, vol. 52, no. 11, pp. 3060–3070, Nov. 2004.

[128] C. Craeye and X. Dardenne, "Fast numerical analysis of finite arrays of antennas in finite dielectric volumes," in *Proc. Int. Conf. on Electromagn. in Adv. Applicat. (ICEAA)*, Torino, Sep. 2007, pp. 17–21.

[129] L. Matekovits, G. Vecchi, M. Bercigli, and M. Bandinelli, "Synthetic-functions analysis of large aperture-coupled antennas," *IEEE Trans. Antennas Propag.*, vol. 57, no. 7, pp. 1936–1943, Jul. 2009.

[130] J. Shin and D. H. Schaubert, "A parameter study of stripline-fed Vivaldi notch-antenna arrays," *IEEE Trans. Antennas Propag.*, vol. 47, no. 5, pp. 879–886, May 1999.

[131] D. H. Schaubert, "Endfire slotline antennas," in *JINA Conf.*, Nice, France, Nov. 1990, pp. 253–265.

[132] J. B. Knorr, "Slotline transitions," *IEEE Trans. Microw. Theory Tech.*, vol. 22, no. 5, pp. 548–554, May 1974.

[133] A. B. Smolders and M. J. Arts, "Wide-band antenna element with integrated balun," in *Proc. IEEE AP-S International Symposium*, Atlanta, USA, Jun. 1998, pp. 1394–1397.

[134] M. V. Ivashina, E. A. Redkina, and R. Maaskant, "An accurate model of a wide-band microstrip feed for slot antenna arrays," in *Proc. IEEE AP-S International Symposium*, Hawaii, USA, Jun. 2007, pp. 1953–1956.

[135] B. Schüppert, "Microstrip-slotline transitions: modeling and experimental investigation," *IEEE Trans. Microw. Theory Tech.*, vol. 36, no. 8, pp. 1272–1282, Aug. 1988.

[136] K. C. Gupta, R. Garg, and I. Bahl, Eds., *Microstrip lines and slotlines*. Norwood, MA: Artech House, 1979.

[137] M. Arts, M. Ivashina, O. Iupikov, L. Bakker, and R. van den Brink, "Design considerations of tapered slot phased array feeds for reflector antennas," in *Proc. European Conference on Antennas and Propag. (EuCAP)*, Barcelona, Spain, Apr. 2010, pp. 1–4.

[138] A. van Ardenne, J. D. Bregman, W. A. van Cappellen, G. W. Kant, and J. G. bij de Vaate, "Extending the field of view with phased array techniques: results of european SKA research," *Proc. IEEE*, vol. 97, no. 8, pp. 1531–1542, Aug. 2009.

[139] R. Maaskant, E. E. M. Woestenburg, and M. J. Arts, "A generalized method of modeling the sensitivity of array antennas at system level," in *Proc. 34th European Microwave Conference*, Amsterdam, Oct. 2004, pp. 1541–1544.

[140] M. V. Ivashina, R. Maaskant, and B. Woestenburg, "Equivalent system representation to model the beam sensitivity of receiving antenna arrays," *IEEE Antennas Wireless Propag. Lett.*, vol. 7, no. 1, pp. 733–737, Jan. 2008.

[141] K. Kurokawa, "Power waves and the scattering matrix," *IEEE Trans. Microw. Theory Tech.*, vol. 13, no. 2, pp. 194–202, Mar. 1965.

[142] J. A. Dobrowolski, *Introduction to Computer Methods for Microwave Circuit Analysis and Design.* Warsaw University of Technology: Artech House, 1991.

[143] H. Hillbrand and P. Russer, "An efficient method for computer aided noise analysis of linear amplifier networks," *IEEE Trans. Circuits Syst.*, vol. 23, no. 4, pp. 235–238, Apr. 1976.

[144] W. van Etten, "Stochastische signaaltheorie," Eindhoven University of Technology, Eindhoven, The Netherlands, Course Notes 13e editie, 5H130, 1999.

[145] L. W. Couch II, *Digital and Analog Communication Systems.* 6th ed., Upper Saddle River, NJ: Prentice-Hall, Inc., 2001.

[146] A. van der Ziel, Ed., *Noise, Sources, Characterization, Measurement.* Englewood Cliffs, NJ: Prentice-Hall, Inc., Jan. 1970.

[147] J. P. Hamaker, "Instrumental techniques of aperture synthesis," Netherlands Institute for Radio Astronomy, Dwingeloo, The Netherlands, Course Notes, Second printing, March, 2001.

[148] J. P. Weem and Z. Popovic, "A method for determining noise coupling in a phased array antenna," in *Microwave Symposium Digest. (IEEE MTT-S)*, Phoenix, Arizona, May 2001, pp. 271–274.

[149] J. P. Hamaker, J. D. Bregman, and R. J. Sault, "Understanding radio polarimetry – I. mathematical foundations," *Astron. Astrophys. Suppl. Ser.*, vol. 117, pp. 137–147, May 1996.

[150] L. E. Brennan and J. D. Mallett, "Efficient simulation of external noise incident on arrays," *IEEE Trans. Antennas Propag.*, vol. 24, no. 5, pp. 740–741, Sep. 1976.

[151] J. C. Arnbak, J. Dijk, M. H. A. J. Herben, and J. T. A. Neesen, "Radio en radar," Eindhoven University of Technology, Eindhoven, The Netherlands, Course Notes Second printing, 5N040, 1987.

[152] P. Bolli, F. Perini, S. Montebugnoli, G. Pelosi, and S. Poppi, "Basic element for square kilometer array training (BEST): Evaluation of the antenna noise temperature," *IEEE Antennas Propag. Mag.*, vol. 50, no. 2, pp. 58–65, 2008.

[153] S. W. Wedge and D. B. Rutledge, "Wave techniques for noise modeling and measurement," *IEEE Trans. Antennas Propag.*, vol. 40, no. 11, pp. 2004–2012, Nov. 1992.

[154] H. Bosma, "On the theory of linear noisy systems," Philips Research, Eindhoven, The Netherlands, Philips Research Reports, Supplement 10, 2005.

[155] B. Yang, "A generic numerical technique for modeling an array antenna receiving system," Netherlands Institute for Radio Astronomy, Dwingeloo, The Netherlands, Tech. Rep. SKA-ASTRON-RP-034, 2006.

[156] K. F. Warnick and M. A. Jensen, "Effects of mutual coupling on interference mitigation with a focal plane array," *IEEE Trans. Antennas Propag.*, vol. 53, no. 8, pp. 2490–2498, Aug. 2005.

[157] M. V. Ivashina, M. Kehn, P.-S. Kildal, and R. Maaskant, "Decoupling efficiency of a wideband Vivaldi focal plane array feeding a reflector antenna," *IEEE Trans. Antennas Propag.*, vol. 57, no. 2, pp. 373–382, Feb. 2009.

[158] N. M. Kehn, M. V. Ivashina, P.-S. Kildal, and R. Maaskant, "Definition of unifying decoupling efficiency of different array antennas-case study of dense focal plane array feed for parabolic reflector," *Int. J. Electron. Commun. (AEU)*, doi: 10.1016/j.aeue.2009.02.011.

[159] "IEEE standard definitions of terms for antennas." *IEEE Std 145-1993*, Jun 1993.

[160] A. Waldman and G. J. Wooley, "Noise temperature of a phased array receiver," *The Microwave Journal*, pp. 89–96, 1966.

[161] E. E. M. Woestenburg, "Noise matching in dense phased arrays," Netherlands Institute for Radio Astronomy, Dwingeloo, The Netherlands, Tech. Rep. Tech. Rep. RP-083, 2005.

[162] ——. (2008, Feb.) Definition of array receiver gain and noise temperature. 98_Memo_Woestenburg.pdf. [Online]. Available: http://www.skatelescope.org/PDF/memos/

[163] R. Maaskant, A. G. Tijhuis, R. Mittra, M. V. Ivashina, W. A. van Cappellen, and M. J. Arts, "Hybridization of efficient modeling techniques for fast analysis of large-scale antenna structures in the context of the square kilometre array project," in *Proc. 38th European Microwave Conference*, Amsterdam, Oct. 2008, pp. 837–840.

[164] P.-S. Kildal, M. Franzen, M. V. Ivashina, and W. van Cappellen, "Measurement of embedded element efficiencies of wideband dense arrays in reverberation chamber," in *Proc. European Conference on Antennas and Propag. (EuCAP)*, Edinburg, UK, Nov. 2007, pp. 1–4.

[165] K. F. Warnick and B. D. Jeffs, "Gain and aperture efficiency for a reflector antenna with an array feed," *IEEE Antennas Wireless Propag. Lett.*, vol. 5, no. 1, pp. 499–502, 2006.

[166] D. M. Pozar and B. Kaufman, "Comparison of three methods for the measurement of printed antenna efficiency," *IEEE Trans. Antennas Propag.*, vol. 36, no. 1, pp. 136–139, Jan. 1988.

[167] W. L. Schroeder and D. Gapski, "Direct measurement of small antenna radiation efficiency by calorimetric method," *IEEE Trans. Antennas Propag.*, vol. 54, no. 9, pp. 2646–2656, Sep. 2006.

[168] J. S. Petko and D. H. Werner, "Numerical evaluation of antenna radiation characteristics through an oblique Fibonacci based sampling technique," in *Proc. IEEE AP-S International Symposium*, Charleston, South Carolina, Jun. 2009, pp. 1–4.

[169] R. E. Matick, Ed., *Transmission Lines for Digital and Communication Networks*. New York: McGraw-Hill, 1969.

[170] A. R. Kerr. (1999, Jan.) Surface impedance of superconductors and normal conductors in em simulators. memo245.pdf. [Online]. Available: http://www.alma.nrao.edu/memos/html-memos/alma381/

[171] E. A. Soliman, G. A. E. Vandenbosch, E. Beyne, and R. P. Mertens, "Full-wave analysis of multiconductor multislot planar guiding structures in layered media," *IEEE Trans. Microw. Theory Tech.*, vol. 51, no. 3, pp. 874–886, Mar. 2003.

[172] D. Pozar, Ed., *Microwave Engineering*. Massachussets: Addison-Wesley Publishing Company, 1990.

[173] R. Maaskant, R. Mittra, and A. G. Tijhuis, "Multi-level characteristic basis function method (CBFM) for the analysis of large antenna arrays," *Special Issue on: CEM for Modeling Large Finite Antenna Arrays, The Radio Science Bullentin*, submitted for publication.

[174] D. J. Ludick and D. B. Davidson, "Investigating efficient parallelization techniques for the characteristic basis function method (CBFM)," in *Proc. Int. Conf. on Electromagn. in Adv. Applicat. (ICEAA)*, Torino, Sep. 2009, pp. 400–403.

[175] T. D. Carozzi, G. Woan, and R. Maaskant, "Polarization diversity for SKA wide-field polarimetry," in *Widefield Science and Technology for the SKA – SKADS Conference 2009*, Brussel, Nov. 2009, pp. 1–6.

[176] R. Mittra, "New directions in computational electromagnetics for solving real-world antenna and scattering problems," in *Proc. European Conference on Antennas and Propag. (EuCAP)*, Barcelona, Spain, Apr. 2010, pp. 1–4.

[177] A. M. van de Water, "LEGO – linear embedding via Green's operators," Ph.D. dissertation, Eindhoven University of Technology, Eindhoven, 2007. [Online]. Available: http://alexandria.tue.nl/extra2/200711874.pdf

[178] W. A. van Cappellen, S. J. Wijnholds, and J. D. Bregman, "Sparse antenna array configurations in large aperture synthesis radio telescopes," in *Proc. 3rd European Radar Conference*, Manchester, UK, Sep. 2006, pp. 76–79.

[179] M. V. Ivashina, O. Iupikov, R. Maaskant, W. A. van Cappellen, and T. Oosterloo, "An optimal beamforming strategy for wide-field surveys with phased-array-fed reflector antennas," *IEEE Trans. Antennas Propag.*, submitted for publication (minor revisions).

[180] R. Maaskant and B. Enthoven, "Design of a hot-cold test facility," Netherlands Institute for Radio Astronomy, Dwingeloo, The Netherlands, Tech. Rep. SKA-ASTRON-RP-397, 2009.

[181] R. Maaskant and K. kegel, "System and method for detecting objects, and magnetic field generator for use in such a system or method," Dutch filed as WO2 007 030 004, Sep. 9, 2005.

[182] K. F. Warnick, M. V. Ivashina, R. Maaskant, and E. E. M. Woestenburg, "Unified definitions of efficiencies and system noise temperature for receiving antenna arrays," *IEEE Trans. Antennas Propag.*, accepted for publication.

[183] D. A. Dunavant, "High degree efficient symmetrical Gaussian quadrature rules for the triangle," *Int. Journal of Numerical Methods in Engineering*, vol. 21, pp. 1129–1148, 1985.

[184] J. E. Flaherty, "Finite element analysis," Rensselaer Polytechnic Institute, New York, NY, Course Notes, 2000.

[185] D. J. J. van Rensburg and D. A. McNamora, "On quasi-static source models for wire dipole antennas," *Micr. Opt. Technol.*, vol. 3, no. 11, pp. 396–398, 1990.

[186] D. B. Davidson, *Computational Electromagnetics for RF and Microwave Engineering.* Cambridge: Cambridge University Press, 2005.

Summary

Analysis of Large Antenna Systems

The research presented in this thesis has been conducted within the framework of the Square Kilometre Array (SKA) project. SKA is a next generation radio telescope that will have a receiver sensitivity two orders of magnitude larger than the most sensitive radio telescope currently in operation. To meet the specifications, various low-cost low-noise actively beamformed receiving array antennas are being considered. A major problem in designing these systems is that the present-day commercially available electromagnetic solvers need an excessive amount of memory and simulation time to solve electrically large antenna problems. Moreover, it is essential to be able to analyze the receiver sensitivity of large antenna array systems to understand the sensitivity limiting factors. No dedicated commercial software tools exist that can analyze the receiver sensitivity of entire antenna systems specifically for radio astronomy.

The thesis subject deals with two major challenges: (i) To accurately compute the impedance and radiation characteristics of realistically large and complex antenna arrays using only moderate computing power, particularly, of single and dual-polarized arrays of 100+ Tapered Slot Antenna (TSA) elements that are electrically interconnected. If the collection of these elements forms a subarray of a larger system, it is also of interest to analyze an array of disjoint subarrays. (ii) To characterize the system sensitivity of actively beamformed arrays of strongly coupled antenna elements.

To address the above challenges, a conventional method-of-moments approach to solving an electric-field integral equation is enhanced using the Characteristic Basis Function Method (CBFM) to handle electrically large antenna problems. The generation of the associated reduced matrix equation is expedited by combining the CBFM with the Adaptive Cross Approximation (ACA) technique. Furthermore, because an overlapping domain decom-

position technique is employed, Characteristic Basis Functions (CBFs) are generated that partially overlap to ensure the continuity of the current between adjacent subdomains that are electrically interconnected. While generating the CBFs, edge-singular currents are avoided by a post-windowing technique. Finally, a meshing strategy is proposed to optimally exploit the quasi-Toeplitz symmetry of the reduced moment matrix. The numerical accuracy and efficiency has been determined for numerous cases, among which a dual-polarized interconnected TSA array of 112 elements that has been fabricated and subsequently validated by measurements.

The receiver system has been modeled by both a numerical and a semi-analytical method. The models account for a nonuniform brightness temperature distribution of the sky, mismatch effects, noise that emanates from amplifiers inputs and re-enters the system coherently through the mutually coupled antennas (noise coupling), beamformer weights, etc. Results are shown for a practical setup and design rules are derived which demonstrate that minimum receiver noise can be reached by noise matching the low-noise amplifiers to the active antenna reflection coefficient, rather than the passive one. Finally, it is demonstrated that the radiation efficiency of antennas is an important quantity that can degrade the system sensitivity severely. Nevertheless, a number of commercial software tools have shown to be inadequate as the computed efficiency exceeds 100%. A method is proposed which is numerically efficient and robust since it guarantees an efficiency below 100%.

Curriculum Vitae

Rob Maaskant was born in Rotterdam on April 14th, 1978. He obtained his B.Sc. degree in Electrical Engineering from the Polytechnic Institute of Technology in Breda, in 2000. He graduated on a novel type of class-D audio push-pull amplifier, which has resulted in an international patent. His M.Sc. Thesis project was carried out at the Netherlands Institute for Radio Astronomy (ASTRON) and the degree was obtained in Aug. 2003 (*cum laude*) on the semi-analytical modeling of currents on tapered slot antennas, under supervision of Prof. dr. A. G. Tijhuis from the Eindhoven University of Technology, and Dr. M. V. Ivashina from ASTRON.

Since 2003, he has been employed at ASTRON as an antenna research engineer, where he has designed novel type of antennas within the FARADAY, AMPHORA, SKADS, and RFID projects. This work has resulted in four patents. Furthermore, the THACO hot-cold radiometric measurement facility, which has been designed by him, is currently being used by DRAO (Canada).

Since 2005, he has been developing various numerical and semi-analytical models for the analysis of actively beamformed antenna systems within the framework of the Square Kilometre Array (SKA). The results have led to this Ph.D. Dissertation and have been published in 13 journal and 17 conference papers (two under review). This research has been carried out in collaboration with the promotors Prof. dr. A. G. Tijhuis (Eindhoven University of Technology) and Prof. R. Mittra (the Pennsylvania State University), and the co-promotor Ir. W. van Cappellen (ASTRON).

The newly developed mathematical methods have been implemented in the CAESAR software, which is a combined electromagnetic and microwave simulator for the analysis of electrically large antenna systems. He has developed the CAESAR software with the help

of the students: Bill Yang (TU Delft), Oleg Iupikov (Sevastopol University), and Elena Redkina (Sevastopol University), who he guided. The software is being used by the University of Manchester; the University of Cambridge, and the Fundacion General de Alcala - Instituto Geografico Nacional (FG-IGN, radio observatory in Yebes, Spain) with whom ASTRON signed a Memorandum of Understanding.

He has been a visiting scientist at the Amherst University of Technology in the winter of 2004 (group of Prof. D. H. Schaubert), at the Pennsylvania State University in the summer of 2007 (group of Prof. R. Mittra), and at the Chalmers University of Technology in 2008 (group of Prof. P.-S. Kildal).

He is serving as a reviewer for the ACES journal, the IEEE Transactions on Antennas and Propagation, the European Microwave Conference (EUMC), and the International Symposium on Electromagnetic Theory. He has been invited to give guest lectures at the Chalmers University of Technology and the Brigham Young University. He has co-chaired a session at the EUMC, and was an invited speaker in the special session on EM modeling methods in the Netherlands. Next to conferences, he has presented at the 2004 and 2005 international FPA workshops in Dwingeloo, the Netherlands; the SKADS workshop, October, 2007, Paris; and the Marie Curie Actions SKA workshop, November 2007, ASTRON.

He has won the paper award: 'best team contribution' at the ESA Antenna Workshop, 2008.

From July 2010, he will be employed as a part-time postdoctoral researcher at Chalmers (group of Prof. P.-S. Kildal). From January 2011, he will be employed full time by Chalmers.

Acknowledgments

First and foremost, I would like to express my profound gratitude to my first and second promotors Prof. dr. A. G. Tijhuis (Eindhoven University of Technology) and Prof. dr. R. Mittra (Pennsylvania State University), respectively, for their patience and significant amount of time spent for me, their encouragements to complete this dissertation, their invitations to contribute to journal and conference papers, their critical opinion to be thorough and yet productive, and for their advice and recommendations from which my scientific career has benefited greatly. I admire their impressive knowledge and capabilities to solve physical and engineering problems through mathematics.

Without a doubt, the Netherlands Institute for Radio Astronomy (ASTRON) has enabled the development of my technical knowledge and the realization of this dissertation. AS-TRON has enriched my international vision through an indispensable and vast network of international partners they collaborate with, which makes that my work is recognized beyond national boundaries. I owe a lot to the former R&D director of ASTRON, Prof. ir. A. van Ardenne, who has been my first contact person at ASTRON. He offered me the possibility to perform a M.Sc. project at ASTRON, and I appreciate his positive attitude regarding my ambitions to undertake a Ph.D. project afterwards. The latter has been effectuated by my co-promotor and head of the antenna group at ASTRON, Ir. W. A. van Cappellen, and current R&D director, Dr. C. M. de Vos, who both supported my activities morally and financially. Moreover, they provided me with a substantial freedom, which helped considerably to complete this dissertation successfully. Thanks for entrusting this responsible task to me, and your acknowledgement that my work has contributed – either directly or indirectly – to the scientific projects that ran in parallel. In this respect, I particularly wish to thank Ir. J. G. bij de Vaate who involved me in the PACMAN and SKADS projects. He always believed in me, and thanks for your cheering mindset.

entire career at ASTRON. Thank you for the numerous insightful discussions.

I am particularly grateful to the technical discussions with Prof. dr. P.-S. Kildal (University of Gothenburg, Chalmers), Dr. M. Ng. Kehn, and Dr. M. V. Ivashina on the decoupling efficiency. This synergetic teamwork has led to a number of journal and conference papers. I am looking forward to continuing this collaboration in Sweden and to experience the contagious enthusiasm of Prof. dr. P.-S. Kildal and his group.

Prof. dr. K. F. Warnick, thanks for inviting me to the Brigham Young University and the collaboration that we have started during the last part of my thesis. I am looking forward to continuing this fruitful collaboration; it has already led to a joint journal publication. Similarly, I am looking forward to continue to work on radio polarimetry with Dr. T. D. Carozzi from the University of Glasgow.

I wish to thank a number of jury members for carefully reading my thesis and providing me with their comments. The pertaining committee members are: Prof. dr. A. G. Tijhuis, Prof. dr. R. Mittra, Ir. W. A. van Cappellen, Prof. dr. ir. G. A. E. Vandenbosch, Prof. dr. ir. A. B. Smolders, and Prof. ir. A. van Ardenne.

Finally, I recall the warm interaction with the members of the Electromagnetics Group at the Eindhoven University of Technology, as well as your participation in our annual Christmas "borrel", thank you. Likewise, I wish to thank my colleagues at ASTRON who I have not mentioned by name, but did contribute to the stimulating research environment and did play a role in my career as a young researcher.

Last but not least, I am indebted to my adorable wife Marianna and my lovely daughter Daniëlla (born in September, 2004) for sharing the daily load that I brought home for dinner. Admittedly, I have sacrificed too many weekends and vacations for my work, my sincere apologies for that. Improving my self-efficiency is a good way to free some time for my family, without having to compromise my productiveness. Furthermore, our parents have demonstrated to be fantastic *loco parentis* in case of common business trips. Thank you for offering us this flexibility, as well as for designing the cover of this dissertation.